TABLE OF CONTENTS

ABSTRACT ..... **II**

RÉSUMÉ ..... **IV**

ACKNOWLEDGEMENTS ..... **VI**

TABLE OF CONTENTS ..... **VII**

TABLE OF FIGURES ..... **XII**

LIST OF TABLES ..... **XVII**

CHAPTER I : INTRODUCTION **1**

1.1 DEFINITION OF THE ICING AND CORROSION PROBLEMS **1**

1.2 PREVENTION OF ICE ACCUMULATION AND CORROSION **3**

1.3 ORIGINALITY OF THE PRESENT STUDY **6**

1.4 OBJECTIVES AND AIMS OF THE THESIS **7**

1.5 SIGNIFICANCE OF THE RESEARCH WORK **8**

1.6 OUTLINE OF THE THESIS **9**

CHAPTER II : BACKGROUND AND LITERATURE REVIEW **11**

PART I: HYDROPHOBICITY AND ICEPHOBICITY **11**

2.1 INTRODUCTION **11**

2.2 ICING IN NATURE **11**

2.3 ICE-REPELLENCY **13**

2.4 MEASURMENTS OF ADHESION OF ICE **15**

2.5 HOW TO REDUCE ICE ADHESION? **16**

2.6 WETTING PROPERTY (SURFACE WETTABILITY) **16**

2.6.1 SURFACE HYDROPHOBICITY **17**

2.7 SURFACE PASSIVATION **22**

2.8 COATING STABILITY AND DURABILITY **24**

2.8.1 UV DEGRADATION **24**

2.8.2 EFFECT OF pH **24**

PART II: ALUMINUM ALLOYS AND CORROSION **25**

2.9 CORROSION AND PASSIVATION OF ALUMINUM ALLOYS 25

2.9.1 A BRIEF INTRODUCTION TO ALUMINIUM 25

2.9.2 CLASSIFICATION OF ALUMINUM ALLOYS 26

2.9.3 ALUMINUM CORROSION AND PROTECTION SOLUTIONS 29

2.9.3.1 CHARACTERISTICS OF ALUMINUM ALLOY CORROSION 30

2.9.3.2 TYPES OF CORROSION ON ALUMINUM ALLOYS 32

2.9.3.3 CURRENT SOLUTIONS TO THE CORROSION PROBLEM 33

2.9.4 SILANE COUPLING AGENTS 36

2.9.4.1 APPLICATIONS OF SILANE COUPLING AGENTS 39

2.9.5 BIS-TRIETHOXYSILYLETHANE (BTSE) 39

2.9.6 SURFACE SUBSTRATE PRE-TREATMENT 40

2.10 CONCLUSION 41

CHAPTER III : EXPERIMENTS AND TEST PROCEDURES 42

3.1 INTRODUCTION 42

3.2 METHODOLOGY 42

3.2.1 SUBSTRATE PRE-TREATMENT AND CLEANING PROCEDURE 42

3.2.2 CHEMICAL SOLUTIONS (PREPARED DEPOSITION BATHS) 44

3.2.2.1 PREPARATION OF *SAMS* COATINGS (TOP LAYER) 44

3.2.2.2 PREPARATION OF ANTICORROSIVE COATINGS (UNDER LAYER) 46

3.3 CHEMICAL, STRUCTURAL AND AGING CHARACTERIZATION 47

3.3.1 MORPHOLOGICAL ANALYSES 47

3.3.1.1 ATOMIC FORCE MICROSCOPY (AFM) 47

3.3.1.2 SCANNING ELECTRON MICROSCOPY (SEM/EDX) 48

3.3.1.3 OPTICAL PROFILOMETRY AND OPTICAL MICROSCOPY 49

3.3.2 X-RAY PHOTOELECTRON SPECTROSCOPY (XPS) 50

3.3.3 OPTICAL EMISSION SPECTROMETER 51

3.3.4 ELLIPSOMETRY: COATING THICKNESS MEASUREMENT 51

3.3.5 WETTABILITY TESTS 52

3.3.6 ICE ACCRETION TESTS 53

3.3.6.1 CALCULATION OF ICE ADHESION 54

3.3.7 QUV ACCELERATED WEATHERING TESTER 55

3.3.8 ELECTROCHEMICAL MEASUREMENTS 56

3.3.9 CYCLIC CORROSION EXPOSURE TESTING (CCT) 59

3.4 CONCLUSION 41

CHAPTER IV : HYDROPHOBICITY, ICEPHOBICITY AND STABILITY OF SINGLE LAYER *SAMS* COATINGS 61

4.1 INTRODUCTION 61

4.2 SAMPLE PREPARATION AND EFFECT OF DIFFERENT PRE-/POST-TREATMENTS 61

4.3 EFFECTS OF IMMERSION TIME AND ALKYL CHAIN LENGTH 62

4.3.1 SURFACE ENERGY CALCULATION 66

4.4 WETTING PROPERTY AND COATING STABILITY 67

4.4.1 STUDY OF SAMPLE HYDROPHOBICITY 67

4.4.2 COATING STABILITY IN DIFFERENT PH CONDITIONS 70

4.4.3 X-RAY PHOTOELECTRON SPECTROSCOPY (XPS) ANALYSIS RESULTS 73

4.4.4 SURFACE CHARACTERIZATIONS (PRIOR TO TEST): ATOMIC FORCE MICROSCOPY (AFM), SCANNING ELECTRON MICROSCOPY (SEM/EDX) AND OPTICAL MICROSCOPY SURVEYS 76

4.4.5 SURFACE CHARACTERIZATIONS (AFTER TEST) 78

4.4.6 X-RAY PHOTOELECTRON SPECTROSCOPY (XPS) RESULTS (AFTER TEST) 83

4.5 EFFECT OF UV RADIATION ON HYDROPHOBIC PROPERTIES 85

4.5.1 X-RAY PHOTOELECTRON SPECTROSCOPY (XPS) RESULTS 83

4.6 COATING STABILITY AT AMBIENT CONDITIONS 85

4.7 ICEPHOBIC PROPERTIES AND STABILITY OF PREPARED *SAMS* COATINGS 85

4.7.1 STUDY OF HYDROPHOBICITY FOLLOWING ICE DETACHMENT 85

4.7.2 RESULTS OF ICE ADHESION STRENGTH 86

4.7.3 X-RAY PHOTOELECTRON SPECTROSCOPY (XPS) RESULTS (PRIOR AND FOLLOWING ICE DETACHMENT) 89

4.8 CONCLUSIONS 89

CHAPTER V : ANTI-CORROSIVE PERFORMANCE OF SINGLE LAYER *SAMS* COATINGS: POTENTIODYNAMIC POLARIZATION, ELECTROCHEMICAL IMPEDANCE SPECTROSCOPY AND CYCLIC CORROSION EXPOSURE 90

5.1 INTRODUCTION 90

5.2 CORROSION RESISTANCE OF SINGLE LAYER *SAMS* COATINGS 90

5.2.1 ANTI-CORROSIVE PERFORMANCE OF SINGLE LAYER COATINGS 90

5.2.2 CYCLIC CORROSION TESTS OF PREPARED SINGLE LAYER COATINGS 95

5.2.3 CORROSION RESISTANCE OF SINGLE LAYER *SAMS* COATINGS AFTER ONE WEEK OF IMMERSION IN SALINE SOLUTION 101

5.2.4 ELECTROCHEMICAL IMPEDANCE SPECTROSCOPY (EIS) OF PREPARED SINGLE LAYER COATINGS ON ALUMINUM 102

5.2.5 CORROSION RESISTANCE OF SINGLE LAYER *SAMS* COATINGS AFTER UV-AGEING TEST 110

5.3 CONCLUSIONS 111

CHAPTER VI : HYDROPHOBICITY, ICEPHOBICITY AND DURABILITY OF DOUBLE LAYER COATING SYSTEM ON ALUMINUM SUBSTRATE 112

6.1 INTRODUCTION 112

6.2 WETTING PROPERTY AND COATING STABILITY 113

6.2.1 HYDROPHOBICITY OF DOUBLE LAYERS COATING SYSTEM 113

6.2.2 COATING THICKNESS AND SURFACE ENERGY CALCULATION 114

6.2.3 COATING STABILITY AND DURABILITY IN DIFFERENT CONDITIONS 116

6.2.4 SURFACE CHEMICAL COMPOSITION ANALYSIS VIA X-RAY PHOTOELECTRON SPECTROSCOPY (XPS) 120

6.2.5 SURFACE CHARACTERIZATIONS (PRIOR TO TEST) 122

6.2.6 SURFACE CHARACTERIZATIONS (AFTER STABILITY TEST): SCANNING ELECTRON MICROSCOPY AND OPTICAL MICROSCOPY 124

6.2.7 X-RAY PHOTOELECTRON SPECTROSCOPY (XPS) RESULTS (AFTER STABILITY TEST) 127

6.3 DURABILITY OF SINGLE AND DOUBLE LAYER COATINGS AT AMBIENT CONDITIONS 127

6.4 EFFECT OF UV RADIATION ON HYDROPHOBIC PROPERTIES OF SINGLE AND DOUBLE LAYER *SAMS* COATINGS 128

6.4.1 X-RAY PHOTOELECTRON SPECTROSCOPY (XPS) RESULTS AFTER UV EXPOSURE 130

6.5 ICE-PHOBIC PERFORMANCE AND DURABILITY OF SINGLE AND DOUBLE LAYER *SAMS* COATINGS 131

6.5.1 ICE ADHESION STRENGTH 131

6.5.2 SAMPLE HYDROPHOBIC PROPERTY FOLLOWING ICE DETACHMENT 133

6.5.3 X-RAY PHOTOELECTRON SPECTROSCOPY (XPS) RESULTS (PRIOR AND FOLLOWING ICE DETACHMENT) 134

6.6 CONCLUSIONS 136

CHAPTER VII : ANTI-CORROSIVE PERFORMANCE OF DOUBLE LAYER *SAMS* COATING SYSTEMS: POTENTIODYNAMIC POLARIZATION, ELECTROCHEMICAL IMPEDANCE SPECTROSCOPY AND CYCLIC CORROSION TESTING 138

7.1 INTRODUCTION 138

7.2 CORROSION RESISTANCE OF PREPARED DOUBLE LAYER *SAMS* COATINGS 138

7.2.1 ANTI-CORROSIVE PERFORMANCE OF DOUBLE LAYER COATINGS 138

7.2.2 CYCLIC CORROSION TESTS OF PREPARED DOUBLE LAYER COATINGS 142

7.2.3 CORROSION RESISTANCE OF DOUBLE LAYER *SAMS* COATINGS ON AL AFTER ONE WEEK OF IMMERSION IN SALINE SOLUTION 147

7.2.4 ELECTROCHEMICAL IMPEDANCE SPECTROSCOPY (EIS) OF DOUBLE LAYER COATINGS ON ALUMINUM SUBSTRATE 148

7.2.5 CORROSION RESISTANCE OF DOUBLE LAYER *SAMS* COATINGS AFTER THE UV-AGING TEST 154

7.3 CONCLUSIONS 155

CHAPTER VIII : CONCLUSIONS AND RECOMMENDATIONS 158

8.1 CONCLUSIONS 158

8.2 RECOMMENDATIONS FOR FUTURE WORKS 164

REFERENCES 166

TABLE OF FIGURES

Fig.1.1. Atmospheric icing (left), flash over in iced overhead transmission lines (center) and destroyed transmission pylon (right) caused by accumulated ice, the Quebec ice storm 1998 [3-5]……..…3

Fig.2.1. Schematic representation of a liquid droplet on a surface illustrating the quantities in Young's equation……..……18

Fig.2. 2. Examples from nature: (a) Pond skater walking on water and (b) lotus effect……...19

Fig.2.3. Schematics representation of configurations described by the (a) Wenzel and (b) Cassie–Baxter regime with air pockets…….....20

Fig.2.4. Schematic illustration of the relationship between advancing, receding, and tilt angles……..21

Fig.2.5. Different steps of *SAMs* coating on an oxide surface…….……...23

Fig.2.6. Potential *vs.* pH diagram for Al/H_2O system at 25 ^oC and at 1 atm [205]…….....31

Fig.2.7. Filiform corrosion tests performed on trivalent chromium (pre-treated) and $KMnO_4$ post-oxidized aluminum samples without drying (a), with drying (b), and chromated samples (c)……34

Fig.2.8. Self-assembled monolayer film of alkylsilane molecules on AA substrate……..36

Fig.2.9. Proposed mechanism for silane bonding to a metal substrate……...37

Fig.2.10. TEOS molecule and its spatial configuration……..38

Fig.3.1. Chemical structure of a) Octadecyltrimethoxysilane (18C), b) Triethoxy(octyl)silane (8C), and c) Trichlorooctadecylsilane (18C+Cl)……45

Fig.3.2. (a) Atomic force microscope (*AFM*), CIGELE and (b) Silicon nitride probe fixed on cantilever……48

Fig.3.3. Image of scanning electron microscope (SEM) used in the present study……49

Fig.3.4. Optical profilometer (left) and optical microscope (right), NRC-ATC laboratory……...49

Fig.3.5. X-ray photoelectron spectroscopy (XPS) instruments, CIGELE laboratory…….....50

Fig.3.6. ARL 4460 Optical Emission Spectrometer, NRC-ATC laboratories…….....51

Fig.3.7. Contact angle goniometer (DSA100, Krüss), NRC-ATC and CIGELE laboratories. (Inset: a static CA measured)……..……52

Fig.3.8. Advancing and receding CA_s on a sample with a high hysteresis (advancing (θ_A) and receding (θ_R) CAs)……..53

Fig.3.9. (a) Top view of wind tunnel used and (b) a view of ice accumulations in the tunnel……..…….54

Fig.3.10. (a) Sample covered with artificial glaze ice, (b) centrifuge adhesion test machine, and (c) sample with coating in centrifuge set-up measuring ice adhesion where (1) sample, (2) aluminum beam, (3) counter-weight……...54

Fig.3.11. QUV accelerated weathering tester apparatus, CIGELE laboratory (left) and inside of sample chamber (right)……...56

Fig.3.12. Three-electrode flat cell used in the present study for electrochemical measurements……..……57

Fig.3.13. Schematic presentation of cathodic and anodic polarization curves of a metal in the active state in a reducing acidic solution [202]…….…..58

Fig.3.14. A programmable cyclic corrosion test chamber (*Ascott*), NRC-ATC…….……59

Fig.4.1. Contact angle values (deg.) of prepared samples, immersed for 15 min in the corresponding diluted solutions……..…...63

Fig.4.2. Contact angle values (deg.) of prepared samples, immersed for 60 min in the corresponding non-diluted baths……..…...64

Fig.4.3. Surface energy values (mNm^{-1}) of different *SAMs* coatings on Al alloy versus stirring time (min)……...……66

Fig.4.4. Contact angle of Al sample coated with 18C-*SAMs vs.* immersion time in acidic (pH=4.01), basic (pH=10.01), nano-pure and tap water. At the end of the test, the lowest and highest values of free surface energy (ε) are 21.31 (±0.63) and 33.35 (±0.63) mNm^{-1}, respectively……..……...70

Fig.4.5. Contact angle of Al sample coated with 8C-*SAMs vs.* immersion time in acidic (pH=4.01), basic (pH=10.01), nano-pure and tap water. At the end of the test, the lowest and highest values of free surface energy (ε) are 24.21 (±1.23) and 32.18 (±1.25) mNm^{-1}, respectively……..……...71

Fig.4.6. Contact angle of Al sample coated with 18C+Cl *SAMs vs.* immersion time in acidic (pH=4.01), basic (pH=10.01), nano-pure and tap water. At the end of the test, the lowest and highest values of free surface energy (ε) are 23.17 (±1.24) and 35.54 (±0.63) mNm-1, respectively……..……...72

Fig.4.7. Water droplet images on an Al surface coated with18C-*SAMs*: a) before [ε:6.08 (±1.13) mNm-1] and b) after 700-h immersion in nano-pure water [(ε:21.12 (±1.23) mNm^{-1}]……...73

Fig.4.8. XPS spectra of aluminum sample coated with 8C-*SAMs* coating…….74

Fig.4.9. XPS spectra of aluminum sample coated with 18C-*SAMs* coating.……...……75

Fig.4.10. XPS spectra of aluminum sample coated with 18C+Cl *SAMs* coating…….……75

Fig.4.11. AFM images of: a) bare polished standard AA2024 (R_{rms}: ~ 28 nm), b) as-received AA2024 (R_{rms}: ~ 177 nm) and aluminum surface coated with different *SAMs* of c) 18C (R_{rms}: ~ 25 to 28 nm) and d) 18C+Cl (R_{rms}: ~ 73 nm) before any test……..……76

Fig.4.12. Microscope images of: a) bare standard AA2024 (x100), b) as-received AA2024 (x100), and aluminum surface coated with *SAMs* of c) 8C (x100), d) 18C (x100) and e) 18C+Cl (x100, inset (x1000)), prior to test……..……..…77

Fig.4.13. EDX spectra and SEM images of bare standard AA2024 prior to test……...……78

Fig.4.14. Microscope images of a) bare standard aluminum alloy 2024 (x100) and coated AA2024 with *SAMs* of b) 8C (x100), c) 18C (x100) and d) 18C+Cl (x100), after 580-h stability test (basic media)……..……..79

Fig.4.15. SEM images of a) bare standard AA2024 and coated AA2024 with *SAMs* of b) 8C, c) 18C and d) 18C+Cl, prior to test……..……...80

Fig.4.16. SEM images of a) bare standard AA2024 and coated AA2024 with *SAMs* of b) 8C, c) 18C and d) 18C+Cl after 580-h stability test (basic condition). The image (e) shows the magnified spot present on surface (d). ……..……..…..81

Fig.4.17. Coating durability (CA *vs.* UV cycle) for flat AA2024 coated with different *SAMs* (left) with 4-h condensation and (right) without condensation step. ……..……83

Fig.4.18. Stability of flat AA2024 coated with different *SAMs* coatings kept at ambient condition. At the end of the test, the lowest and highest values of free surface energy (ε) are 6.62 (±0.45) and 14.46 (±0.66) mNm^{-1}, respectively. ……..……..85

Fig.4.19. Contact angle values as a function of icing/de-icing cycles for samples coated with 8C, 18C and 18C+Cl *SAMs* layers. ……..…….86

Fig.4.20. Shear stress of ice detachment *vs.* icing/de-icing cycle for aluminum surface coated with 8C, 18C and 18C+Cl *SAMs* layers. ……..……..88

Fig.5.1. Polarization curves of bare and coated AA2024 with 8C-, 18C- and 18C+Cl *SAMs* coating. The bare AA6061 curve presents for comparison purpose. ……..……..93

Fig.5.2. Optical images of unmodified and coated AA2024 with different *SAMs* before and after 120 cycles of cyclic corrosion test. ……96

Fig.5.3. Optical images of bare and coated AA2024 with different *SAMs* after 120 cycles of cyclic corrosion test: a) standard AA2024, b) control AA2024, c) 8C-*SAMs*, d) 18C+Cl *SAMs* and e) 18C-*SAMs* coatings. ……..……98

Fig.5.4. Portion of the corroded area of modified and unmodified Al samples exposed to the cyclic corrosion test. ……..……99

Fig.5.5. Depth of corroded area measured on standard AA2024 after cyclic corrosion tests via a and b) optical profilometry and c-e) AFM techniques. ……..……..……...100

Fig.5.6. Potential and current density of bare and coated AA2024 samples with different *SAMs* after one week immersion in 3.5% NaCl solution. ……..101

Fig.5.7. Impedance plots of bare AA2024 and coated AA2024 with 8C-*SAMs* in 3.5% NaCl aqueous solution. Bode phase angle (phase angle *vs.* logarithmic frequency) and frequency (logarithmic total impedance *vs.* logarithmic frequency). ……..……103

Fig.5.8. Impedance plots of coated AA2024 with 18C-*SAMs* in 3.5% NaCl aqueous solution. Bode phase angle (phase angle *vs.* logarithmic frequency) and frequency (logarithmic total impedance *vs.* logarithmic frequency). ……..……104

Fig.5.9. Impedance plots of coated AA2024 with 18C+Cl *SAMs* in 3.5% NaCl aqueous solution. Bode phase angle (phase angle *vs.* logarithmic frequency) and frequency (logarithmic total impedance *vs.* logarithmic frequency). ……..……..105

Fig.5.10. Impedance plots of bare and coated AA2024 with dissimilar *SAMs* in 3.5% NaCl aqueous solution. Bode phase angle (phase angle *vs.* logarithmic frequency) and frequency (logarithmic total impedance *vs.* logarithmic frequency). ……..……106

Fig.5.11. The equivalent circuit used to model EIS data. R_s is the solution resistance, R_{ct} is the polarization resistance and CPE is a constant phase element. ……..……..107

Fig.5.12. Potential and current density of bare and coated AA2024 with different *SAMs* after UV-ageing Test with condensation step. ……..……..110

Fig.6.1. Contact angle values (deg.) of prepared single 18C-*SAMs* and double layer BTSE/18C-*SAMs* coatings on AA2024 samples (bare samples as reference……..……114

Fig.6.2. Contact angle *vs*. immersion time in different pH conditions for Al sample coated with 18C-*SAMs* coating. ……..…118

Fig.6.3. Contact angle *vs.* immersion time in different pH conditions for Al sample coated with BTSE/18C-*SAMs* layers. ……..……118

Fig.6.4. Water droplet images on a coated aluminum sample with BTSE/18C-*SAMs* before (a) and after (b) an ~820-h immersion in nano-pure water. ……..……119

Fig.6.5. Al samples immersed in basic solution (a) initially and (b) after finishing the stability test. ……..……119

Fig.6.6. XPS spectra of Al sample coated with BTSE layer [Al K_α X-ray source, 1486.6 (eV)]. ……..……120

Fig.6.7. XPS spectra of Al sample coated with 18C-*SAMs* alone [Al K_α X-ray source, 1486.6 (eV)]. ……..…….121

Fig.6. 8. XPS spectra of Al sample coated with BTSE/18C-*SAMs* coating [Al K_α X-ray source, 1486.6 (eV)]. ……..……..121

Fig.6.9. C1s spectra of Al sample coated with as-prepared BTSE/18C-*SAMs*…..……..122

Fig.6.10. AFM images of: (a) bare standard AA2024 (R_{rms}: ~ 28 nm), (b) as-received AA2024 (R_{rms}: ~ 177 nm) and aluminum surface coated with (c) single 18C-*SAMs* (R_{rms}: ~ 25 nm) and (d) BTSE/18C-*SAMs* (R_{rms}: ~ 33 nm) prior to test. ……..……123

Fig.6.11. Microscopic images of: (a) bare standard AA2024 (x1000) and as-prepared coated Al surface with (b) 18C-*SAMs* (x1000) and (c) BTSE/18C-*SAMs* (x1000), prior to test……..124

Fig.6.12. Optical microscope images of (a) bare standard AA2024 (x1000) and coated Al surface with (b) 18C-*SAMs* (x1000) and (c) BTSE/18C-*SAMs* (x1000), after 700-h immersion in water…….…….125

Fig.6.13. Backscattered SEM images of (a) bare and coated Al surface with (b) 18C-*SAMs* and (c) BTSE/18C-*SAMs* after 700-h immersion in water. ……..……126

Fig.6.14. EDX results and SEM images of bare standard AA2024 after stability test (immersion in water). ……..……..……126

Fig. 6.15. Stability of flat AA2024 sample coated with 18C-*SAMs* and BTSE/18C-*SAMs* coatings kept at ambient condition. At the end of the test, the lowest and highest values of free surface energy (ε) are 9.18 (±0.12) and 8.83 (±0.36) mNm^{-1}, respectively……..……128

Fig.6.16. Coating stability (CA *vs.* UV cycle) for flat AA2024 coated with 18C-*SAMs* and BTSE/18C-*SAMs* (left) without condensation step and (right) with 4-h condensation……..……..…….130

Fig.6.17. Shear stress of ice detachment *vs.* icing/de-icing cycle for coated Al surface with 18C-*SAMs* and BTSE/18C-*SAMs* layers. ……..……..132

Fig.6.18. Contact angle values as a function of icing/de-icing cycles for coated Al samples with 18C-*SAMs* and BTSE/18C-*SAMs* layers. ……..……...134

Fig.7.1. Polarization curves of bare and coated AA2024 with 18C-*SAMs* and BTSE/18C-*SAMs* thin films in 3.5 wt.% NaCl solution. ……..140

Fig.7.2. Optical images of unmodified AA2024 a) before and b) after 85 cycles of cyclic corrosion test and modified AA2024 with c) 18C-*SAMs* and d) BTSE/18C-*SAMs* after cyclic corrosion cycles. ……..……143

Fig.7.3. Optical images of bare and coated AA2024 with single and double layer *SAMs* thin film after 120 cycles of cyclic corrosion test: a) standard AA2024, b) control AA2024, c) 18C-*SAMs* and d) BTSE/18C-*SAMs* coatings. ……...144

Fig.7.4. SEM images of a) bare Al and coated Al with SAMs of b)18C and c) BTSE/18C coatings after 85 cycles of cyclic corrosion test.. ……...145

Fig.7.5. Portion of the corroded area of modified and unmodified Al samples exposed to the cyclic corrosion test. ……146

Fig.7.6. Potential and current density of bare and coated AA2024 samples with single and double layer *SAMs* thin films after one week immersion in 3.5% NaCl solution……**.....**147

Fig.7.7. Impedance plots of bare and coated AA2024 with 18C-*SAMs* and BTSE/18C-*SAMs* in 3.5% NaCl aqueous solution. Bode phase angle (phase angle *vs.* logarithmic frequency) and frequency (logarithmic total impedance *vs.* logarithmic frequency). ……..……150

Fig.7.8. The Randle's equivalent circuit used to model EIS data of single (left) and double layers (right). R_s is the solution resistance, CPE1 and CPE2 are constant phase elements corresponding to under and top layers, respectively and R_{ct} and R_{pf} are the charge transfer and polarization resistances, respectively……..……152

LIST OF TABLES

Table 2.1 Physical properties of atmospheric ice [60, 61, 64, 65]……..…12

Table 2.2 Aluminum alloy designation according to the Al Association (AA) [197, 202, 203]…….28

Table 2.3 Chemical composition (wt. %) of several typical AAs based on ASM Material Data Sheet. Other elements were also detected at lower levels [172]. ……..…..29

Table 2.4 Silane coupling agents (monofunctional silanes). ……..……...38

Table 2.5 Silane coupling agents (Bisfunctional silanes). ……..……..38

Table 3.1. Designate chemical composition of the AA2024-T3 alloy [172, 202, 264-267]…….. ……..….43

Table 4.1. Different coating treatment applied for self-assembling on AA2024 substrates (8C-*SAMs*, 18C-*SAMs* and 18C+Cl *SAMs* coatings). ……..…..…64

Table 4.2. Contact angle and free surface energy [ε (mNm^{-1})] of AA2024 coated with different self-assembled organosilanes. ……...…65

Table 4.3. Contact angle and free surface energy [ε (mNm^{-1})] values of flat AA2024 samples coated with different *SAMs vs.* stirring time. ……...……..……65

Table 4.4. XPS results of Al surface coated with 18C-*SAMs* and BTSE/18C-*SAMs* coating before and after stability test. ……...……...……..82

Table 4.5. XPS analysis results of aluminum samples coated with 18C-*SAMs* coating before and after UV exposure (without 4 hrs condensation step)…….....84

Table 4.6. The ice adhesion strength and *ARF* values of different *SAMs* coatings on Al...……...87

Table 4.7. XPS analysis results of Al samples coated with 8C and 18C-*SAMs* before and after icing/de-icing cycles. …….……89

Table 5.1. Potentiodynamic results of bare AA2024 and coated AA2024 with 8C-, 18C- and 18C+Cl *SAMs* film in 3.5 wt.% NaCl solution……..…….92

Table 5.2. Potentiodynamic results of bare and coated AA2024 samples with different *SAMs* after one week immersion in 3.5% NaCl solution. ……..……102

Table 5.3. ElS parameters data obtained for bare and coated Al samples after 2-h immersion in 0.1 M $NaHCO_3$ + 3.5% NaCl solution. …….....108

Table 5.4. Charge transfer resistance and surface coverage values calculated for bare and *SAM*s modified aluminum. ……..……...…109

Table 5.5. Potentiodynamic results of coated AA2024 with different *SAMs* after UV-aging test.……..……...…..111

Table 6.1. Contact angle (degree) and free surface energy [ε (mNm^{-1})] of AA2024 coated with single and double layer *SAMs* coatings. ……...……...115

Table 6.2. XPS results of Al surface coated with 18C-*SAMs* and BTSE/18C-*SAMs* coating before and after stability test.……...127

Table 6.3. XPS analysis of coated Al samples with 18C-*SAMs* and BTSE/18C-*SAMs* before and after UV exposure test. ……....131

Table 6.4. The ice adhesion strength and *ARF* values of Al sample coated with BTSE/18C-*SAMs* layers. ……..…....132

Table 6.5. The elemental composition of aluminum samples coated with 18C-*SAMs* and BTSE/18C-*SAMs* before and after icing/de-icing cycles….……..…….…..135

Table 7.1. Potentiodynamic results of bare and coated AA2024 with 18C-*SAMs* and BTSE/18C-*SAMs* thin films in 3.5 wt.% NaCl solution. ……..…..139

Table 7.2. Potentiodynamic results of bare and coated AA2024 samples with single and double layer *SAMs* thin films after one week of immersion in 3.5% NaCl solutio…….….148

Table 7.3. ElS parameters data obtained for bare and coated aluminum samples after 2-h immersion in 0.1 M $NaHCO_3$ + 3.5% NaCl solution. ……..……....152

Table 7.4. Charge transfer resistance and surface coverage values calculated for bare, single and double layer coatings on Al substrate. ……..…153

Table 7.5. Potentiodynamic results of coated AA2024 with single and double layer thin films after UV-aging test. ……..155

CHAPTER I

INTRODUCTION

1.1 Definition of the Icing and Corrosion Problems

Atmospheric icing happens when the surfaces of exposed structures are subjected to contact with super-cooled water drops or snow particles. Ice and wet-snow accumulation on exposed surfaces can seriously impair the operation and integrity of outdoor civilian, industrial or military structures, electric power lines, telecommunication networks, aircraft, transportation, antennae, and so forth, in cold climate countries subjected to extreme weather conditions [1]. Ice adhesion may lead to serious risks to the security of such systems as well as significant damage or financial losses in various sectors of the economy, as was the case during the 1998 and 2007 ice storms in Canada and the U.S.A (Fig.1.1) [1-6]. The ice storm of 1998 was the worst ever to hit Canada, based on the criteria of the amount of ice accumulation, the duration of the storm, and the population affected [7, 8]. Each year, numerous failures due to ice or snow accumulation are reported from Canada, the United States, Russia, Japan and elsewhere. In the specific case of power transmission lines, ice and wet snow can cause severe trouble due to their high adherence to both metallic and insulator surfaces resulting in cable sagging and short circuits due to static ice overloads on cables (Fig.1.1). Transmission lines are often subjected to wind-induced dynamic oscillations, the so called galloping. Aerodynamically unstable ice on power lines is an important factor in initiating the occurrence of galloping while decreasing the damping rate. In extreme cases it leads to high mechanical stress on conductors, insulating supports, cables and towers. The galloping finally leads to collapse of structures and reduces the life time of transmission lines. Meanwhile, when the accumulated ice suddenly drops off, extreme mechanical tensions are generated on a conductor resulting in increase of the possibility of no clearance between adjacent cables or cables and towers [9].

Fig.1.1. Atmospheric icing **(left)**, flash over in iced overhead transmission lines **(center)** and destroyed transmission pylon **(right)** caused by accumulated ice, the Quebec ice storm 1998 [3-5].

Flashover on ice-covered insulators is a complex phenomenon which causes damage to insulators and reduces their lifetime [4, 10-12]. The need for reliable transmission and distribution networks in severe icing conditions, thus, highlights the importance of ice adhesion studies. Therefore, a variety of de-icing and anti-icing techniques were developed over the last several decades [1, 7, 8, 13-15]. Different types of ice can be classified into three basic categories: hard rime, soft rime, and glaze [16-18]. Of most economical concern are glaze, hard rime and wet snow. Previous studies presented the possibility of distinguishing among them by temperature measurement [19]. Ice can be formed in dry or wet atmospheric conditions, accumulating on insulator surfaces from freezing rain, freezing drizzles, in-cloud icing, icing fog, wet snow or frost, and strongly adhering to any surface [3]. Prevention of ice accretion on surfaces requires reduction of adhesion strength between ice and subjected surface. Over the past decades, researchers have tried to improve on so-called de-icing methods such as thermal, mechanical and chemical methods to remove the ice/snow build-ups and are currently in use. Several research works are also underway to develop hydrophobic coatings with icephobic properties on outdoor surface structure [20-24].

On the other hand and in connection with the subject of the present study, which deals with reduction of ice accumulation on aluminum alloys (AAs) surfaces, it should be remembered that corrosion is always a serious issue when it comes to using metallic substrates outdoors. Aluminum alloys with a wide range of properties are used extensively in many industrial sectors

due to their strength, ductility, formability, workability, etc. In view of the fact that all modern AAs use various types of metallic additives to improve their strength and properties, this inevitably leads to the increased susceptibility of such alloys to electrochemical corrosion. Accordingly, while developing durable anti-icing coatings on Al surfaces, their anticorrosive resistance should necessarily be kept in mind as an important issue regarding coating durability and stability.

1.2 Prevention of Ice Accumulation and Corrosion

Prevention of ice build-up and adhesion has long been a technological challenge. Ice, with its broad range from snow to glaze, can stick to everything. Hydrogen bonds, *Van der Waals* forces, and non-polar covalent bonds are the main contributors in adhesion of ice to a surface [25-28]. Currently, most de-icing techniques (so-called active de-icing, e.g. chemical, mechanical and thermal de-icing techniques) are applied extensively without fully preventing ice accumulation. Among these techniques one can cite freezing-point depressants for highways (salt, chemical sprays, etc.) [29] and de-icing fluids for aircraft (ethylene and propylene glycols) [30]. Although very efficient, the main disadvantage of the de-icing methods is that they must be used after ice build-up and thus during a period when damage can still occur on accumulated ice structures. The other disadvantages of de-icing methods are: frequency of application, significant negative environmental impacts (toxicity) and cost. Other methods, specifically applicable to transmission lines, such as mechanical vibration of cables, Joule heating of the conductors [29] and electrolysis [25], are effective but consume a considerable amount of energy and require surveillance of the lines and on-site intervention. Moreover, mechanical de-icing can lead to surface damage resulting in the gradual degradation of the system itself. Various anti-icing fluids, e.g. ethylene glycol (EG) and propylene glycol (PG) are used to prevent ice build-up on aircraft, however, they need frequent application in large quantities [31] making their use both time-consuming and expensive. Furthermore, such de-icers are often toxic and environmentally unsafe [32, 33]. None of the above-mentioned techniques prevents ice from creating or accumulating in

the first place. Preventing ice accumulation or reducing considerably its adhesion force may be accomplished by producing anti-icing or icephobic coatings [34-37]. Recently, several coatings for such applications have been tested and reported [13]. Icephobic coatings must necessarily fulfill both of the following requirements: to provide a significant reduction in ice adhesion, and to ensure a reasonably long service-life (*durability*) [35]. Even though there is, as yet, no material which completely prevents ice or snow build-up on its surface [13], however, some coatings are believed to bring reduced adhesion or accumulation of ice. They are environmentally friendly compared to de-icing fluids and are cheaper than active methods which are energy-consuming and expensive to operate [2]. Icephobic coatings, indeed, inhibit ice accumulation rather than eliminating it after its accretion. Superhydrophobic coatings with a small value of contact angle hysteresis showed a remarkable reduction of ice adhesion strength [38] and was developed and reported by the CIGELE research group using different techniques [21, 22, 39-42]. The delayed water freezing on superhydrophobic surfaces is also believed to reduce ice accumulation [39, 43]. To prepare the superhydrophobic coatings, however, there is a common two-step process: surface roughening followed by applying a low surface energy material. The rough structures created on the coating can be damaged and removed during icing/de-icing tests [23, 24, 38-40, 44, 45]. The coating durability is an important feature in the lifetime of a coating under extreme environmental conditions. Several studies reported on the fabrication of hydrophobic coatings via different methods, however, few investigated the durability of such coatings under simulated environmental conditions, e.g. ice-accumulation, UV degradation and rainwater. Therefore, in this research work, the prepared coatings are immersed in distilled and tap water as well for several hours in order to evaluate the durability of such coatings. The UV-degradation is, in fact, a critical aging process when coatings are exposed to atmospheric weathering conditions. Rainwater, with an average pH of 4-6, is another environmental parameter which needs to be simulated in outdoor conditions. Meanwhile, to compare the effect of acidic, basic and natural solutions, the prepared coatings were immersed in various pH solutions. Reduced ice accumulation on any metallic surfaces is always accompanied by corrosion which is a serious issue when it comes to outdoor use. Corrosion is defined by the

breaking down of fundamental properties in a material due to chemical reactions with its surroundings. Typically, environmental parameters such as moisture and electrolytes are capable of penetrating through coatings to form an electrochemical galvanic cell with the anodic versus cathodic sites, resulting in the corrosion of the Al alloy [46]. Corrosion may be observed to concentrate locally in the form of pits or cracks on the surfaces. Different types of corrosion, more or less visible to the naked eye, can occur on Al, e.g. galvanic corrosion, uniform corrosion, pitting corrosion, trans-granular and inter-granular corrosion, exfoliation corrosion, filiform corrosion and so forth each having its own characteristics and conditions [46, 47]. The use of hexavalent chromium for surface treatment of metals has a long history. Both for environmental reasons and worker safety concerns, however, the replacement of such coatings became a major priority and research activities increased to develop alternative non-toxic treatment processes. In addition to using cerium salts and zirconates, self-assembled monolayers often made from amphiphilic hydrocarbon molecules, can be used to protect Al surfaces against corrosion [26, 48]. However, the complex surface chemistry of a metal is certain to have significant effects on the coating process and properties of such resulting thin films [49]. Three categories of molecules are commonly used for self-assembled monolayers**;** these include fatty acids with carboxylic end groups forming electrostatic interactions with metal substrates, alkylthiols that link to the steel substrate through iron-sulfur bonding, and alkylsilanes that react with the metal oxide from the metal and metal alloy substrates [49]. For alkylsilanes, the metal alloy surface becomes much more hydrophobic due to film formation, while the corrosion resistance of the substrate was found to increase. The surface properties of metals are often affected by surface cleaning and the treatment protocols applied. Siloxane-anchored *SAM*s began attracting interest as surface modifiers since early 1980s [50]. Organofunctional silanes are hybrid organic-inorganic compounds which can be used as coupling agents across the organic-inorganic interface [48]. Bis-silanes can be used as an efficient corrosion inhibitor because of the presence of a long alkyl chain and cross-linking agents in their molecular structure [51, 52]. Alkanoic acid molecules such as stearic acid can be formed as a well-ordered self-assembled layer on different metallic substrates. As it was mentioned earlier, to date**,** the most successful coating used on Al is based

on hexavalent chromium [53] which provides ideal alloy protection against pitting and filiform corrosion [54]. Such processes were also observed in vanadate- and/or cerium-oxide- based conversion coatings [55]. One alternative approach is to fabricate coatings by oxidizing Al with the permanganate anion, followed by Mn (IV) deposition [55]. The corrosion characteristics of the permanganate-based coatings are identical with those of the chromate-based system with the exception for alloys containing high levels of Cu or Zn, as in the aircraft alloys of AA2024 and AA7075**.**

Consequently, in this project, organic anticorrosive coatings on AA2024 surfaces have been prepared, with due attention to the literature. Furthermore, the combination of corrosion protection with ice repellent properties has been developed**.**

1.3 Originality of the Present Study

As chapter II describes in more detail, the studies cited in the previous section were focused on the fabrication of hydro- and/or superhydrophobic coatings in order to reduce adhesion of ice or on fabrication of anti-corrosive coatings to reduce the corrosion rate of a substrate. Much research has been conducted so far on characteristics, properties and performance of anti-icing coatings. The originality of this research is that it is focused for the first time on the preparation and study of icephobic coatings with anti-corrosive properties by a simple and easy-to-use method as well as reasonable stability. This combination on a metallic substrate such as Al has not yet been reported and/or systematically studied. In other words, the purpose of this research work is the preparation of icephobic coatings with anti-corrosive properties by using an approach other than those reported in the literature. Meanwhile, anticorrosive performances of various coatings, more specifically those which are environmentally friendly alternatives to the currently in-use toxic chromate-based coatings, are considered. Since the majority of anti-corrosive coatings are not hydrophobic, but rather hydrophilic, our selection is seriously narrowed, if icephobicity is considered too. Therefore, another layer(s) is inevitably required to obtain hydrophobic and icephobic properties. On the

other hand, many hydrophobic coatings on metallic or non-metallic substrates have been introduced in the past decades. However, their anticorrosive performances are neither sufficient nor well studied. For instance, alkylsilanes were previously proposed as potentially icephobic coatings; however, several issues associated with such coatings remain unclear. Therefore, it seems that improving anticorrosive performance with icephobicity is a real challenge.

A combination of both low surface energy and good anticorrosive performance on an AA2024 metallic substrate was expected to be achieved by preparing double layer coating systems, where each layer plays its own role. This approach, introduced for the first time, has never been applied on any substrates so far, neither in CIGELE, nor other research groups. There is, indeed, no literature available in this field. In addition, the fabrication of such coating systems by the self-assembly method as well as their hydro- and icephobic properties and performance under various outdoor conditions such as UV degradation, immersion in various pH solutions etc., have not been studied so far. Such coatings would be a very interesting alternative system for replacing the well-studied and toxic Cr-coatings, as they are considered as environmentally friendly alternatives (detailed in the following chapters). The *SAM*s approach is advantageous for industrial large-scale production. The experimental results obtained will help to understand and develop large-scale production of organic icephobic coatings with anticorrosive properties for industrial applications, e.g. the aerospace industry, offshore oil companies, etc., in order to replace toxic chromate-coating with a cheap, simple-to-prepare and easy-to-apply technique. Since AAs with a wide range of properties are used in many and varied sectors of the economy or engineering structures, there are many other industries that are interested in new and affordable coatings with improved anticorrosive performance.

1.4 Objectives and Aims of the Thesis

The present research aims to introduce, develop and systematically study new environmentally friendly double layer coating systems (with special emphasis on flat AA2024 surfaces) that possess anticorrosive and icephobic properties together in lab-scale conditions. In

other words, the work in this thesis investigates the feasibility of combining low surface energy and anticorrosive performance in double layer coating systems via *SAMs* deposition, where each layer plays its own role. The goals of this research work are achieved by the following sub-objectives:

1. Studying several coatings as candidates for the top layer by applying a number of low surface energy materials, e.g., alkylsilane-based layers (CH_3- terminated group) on AA2024 surfaces by simple immersion in their corresponding solutions (known as the *wet-chemistry technique*), with different pre-/post-treatment.
2. Selecting the most efficient alkylsilane-based coating as the top layer in order to deposit later on an under layer.
3. Systematically investigating, morphologically and compositionally, the organosilane-based coating as a candidate for the under layer which provides reasonable density and thus improved anti-corrosive performance.
4. Studying the ice adhesion performance on such coating systems when subjected to a number of icing/de-icing cycles in orders to assess their stability in real-world conditions, e.g. hydro- and ice-phobicity.
5. Investigating their outdoor durability and stability by evaluating their wetting properties under different conditions, e.g. UV exposure, immersion in various pH solutions, etc.
6. Furthermore, systematically studying the corrosion resistance of such single and double layer coating systems via potentiodynamic polarization measurements, electrochemical impedance spectroscopy (*EIS*) and the cyclic corrosion test as well.

1.5 Significance of the Research Work

As it was mentioned earlier, the present research work intends to introduce, develop and study environmentally friendly double layer coating systems on outdoor structures made of AA2024 with anti-corrosive and icephobic properties together. Consequently, their

hydrophobicity, icephobicity, stability as well as their corrosion resistance were studied by means of facilities available at the CIGELE/ INGIVRE[1] and the NRC- ATC[2**]. There is an increasing demand in the area for the development of new environmentally friendly, inexpensive and easy-to-apply protective chemicals on different Al alloys. Of the enterprises involved, at least two major companies in the province of Quebec may potentially benefit from these research results: Hydro Quebec, which is involved in developing anti-icing techniques and coatings with reduced ice accumulation on metal surfaces, and also Rio Tinto Alcan, another big representative of industry, for whom improved corrosive resistance of the Al alloy surface has been of constant interest for several decades now.

1.6 Outline of the Thesis

The thesis is ordered in eight chapters as follows:

- Chapter **I** presents a summary of icing and corrosion problems and a short introduction to the prevention of corrosion or ice accumulation on metallic surfaces.
- Chapter **II** presents a fundamental review of the literature and background studies on hydrophobicity, superhydrophobicity, icephobicity as well as AAs and the corrosion concept, which should be of help to the reader.
- Chapter **III** explains the experimental procedures for preparing single and double layer coating systems. It also describes in detail the facilities and techniques available at CIGELE and NRC-ATC and used for characterizing the prepared coatings, e.g. Atomic Force Microscope (*AFM*), Scanning Electron Microscope (*SEM/EDS*), X-ray photoelectron spectroscopy (*XPS*), Cyclic Corrosion Exposure Testing (CCT) and so on.

[1] The Industrial Chair on Atmospheric Icing of Power Network Equipment and The Canada Research Chair on Engineering of Power Network Atmospheric Icing.

[**] The National Research Council of Canada-Aluminium Technology Centre.

- Chapter **IV** describes in detail the experimental results obtained for the prepared single *SAM*s coatings on flat AA2024 in terms of hydrophobic properties, stability and surface characterizations, e.g. morphological and chemical analysis by using a variety of techniques and methods.
- Chapter **V** presents the experimental results obtained for the prepared single *SAM*s coatings on flat AA2024 and AA6061 in terms of corrosion resistance in different conditions.
- Chapter **VI** provides in detail the experimental results obtained for the prepared double layer coating systems on flat AA2024 in terms of hydrophobicity, icephobicity, stability and surface characterizations, e.g. morphological and chemical analysis by using a number of techniques and methods.
- Chapter **VII** presents the experimental results obtained on the double layer coating systems prepared on flat AA2024 in terms of their anticorrosive performance versus different settings.
- Chapter **VIII** includes general conclusions and recommendations for future studies based on this research work including the obtained results and their discussion.

Finally, the references cited in this thesis are presented at the end.

CHAPTER II
BACKGROUND AND LITERATURE REVIEW

PART I: HYDROPHOBICITY AND ICEPHOBICITY

2.1 Introduction

Atmospheric icing, in general, occurs when freezing water is deposited on surfaces at or below the freezing point. This natural phenomenon may result from freezing rain, wet snow, supercooled clouds, etc. or even from splashing water. Atmospheric icing on equipment may impact on their operation diminishing their safety and productivity. It is especially hazardous to aircraft, notably when it builds up on helicopter blades. It also affects power and communications lines, antennae, and pavements, either directly or from trees destroyed by the weight of the ice. A number of new technologies and modern versions of old technologies have been used successfully to minimize icing in the electric power industry and ground transportation systems. Controlling ice-formation by means of its physical removal, whether by heating or through the application of the appropriate chemicals, might be possible. However, it would prove to be an expensive proposition and not broadly practicable. This chapter presents a brief review of the occurrence of icing in nature and its consequences, hydro-and superhydrophobicity, corrosion and anticorrosion properties, icephobicity and interface chemistry, showing the anti-icing and anti-corrosive properties of hydrophobic coatings developed via different techniques and based on the specialized literature available in these areas.

2.2 Icing in Nature

Ice and wet snow accretion on structures is a significant problem faced by design engineers in cold climate countries, e.g. Canada and the United States [56]. Atmospheric icing,

according to the *ISO-12494 standard* [57], is described as any process of ice build-up or snow accumulation on the surface of an object exposed to the atmosphere in contact with supercooled water drops or snow particles [58, 59]. Atmospheric icing is further classified by different types of ice, based upon the method of deposition and deposits characteristics, for instance: glaze, rime and hoar frost [60]. According to the meteorological conditions, atmospheric icing is usually classified based on two formation processes:

A) ***Precipitation icing (freezing precipitation and wet snow):*** forms when a warm layer of air (above 0 °C) is trapped between two layers of cold air (below 0 °C) during precipitation of freezing rain. Precipitation starts falling in the form of snow and**,** upon reaching the warm air, the snow particles melt to become water. Finally, they come across the low-level cold air, becoming supercooled water droplets [61].

B) ***In-cloud icing:*** occurs when supercooled water droplets in clouds come into contact with an exposed structure. This type of icing relates to aircraft flying through clouds or equipment installed at a high altitude [62, 63]. When the flux of water droplets towards an object is less than the freezing rate, the ice growth is called "*dry*". However, when the water flux increases, the ice growth will tend to be "*wet"*. The appearance and physical properties of accumulated ice are shown in Table 2.1 [57, 60, 63]. In addition to the properties mentioned in Table 2.1, other parameters may be used to explain the nature of accreted ice, e.g. shear strength.

Table 2.1 Physical properties of atmospheric ice [60, 61, 64, 65].

Type of ice	**Density (kgm^{-3})**	**Adhesion /Cohesion**	**General appearance**	
			Color	**Shape**
Glaze	900	Strong	Transparent	Evenly distributed/icicles
Wet snow	300-600	Weak (forming) Strong (frozen)	White	Evenly distributed/eccentric
Hard rime	600-900	Strong	Opaque	Eccentric, pointing wind-ward
Soft rime	200-600	Low to medium	White	Eccentric, pointing wind-ward

Meanwhile, the density of accreted ice varies widely from low *(soft rime)* to medium *(hard rime)* or to high *(glaze)* [64, 66-70]. Ice build-up on high voltage distribution lines may lead to mechanical failure of the cables, resulting from static load of accreted ice or dynamic stresses of ice shedding, or loss of insulation, electric arcs and insulator flashovers between power lines and metallic supports [19, 71-75]. All result in long-term power outages and major costs**,** as was made evident from the 1998 ice storm. For six days, freezing rain coated Eastern Ontario, Québec, New Brunswick and some parts of the United States with 7-11 cm of ice and over four million people lost power during the storm. Long-term power outages were indeed caused by huge accumulation of ice on power lines or by trees falling on transmission towers, bringing them down. The 1998 ice storm was the most expensive natural disaster in North America [10, 76]. Transmission lines are often subjected to wind-induced oscillations, so called galloping. Galloping is, basically, caused by different pressure distributions among the cable surface, arising from dissimilarity of wind velocities passing the top and bottom of the cross-section. The ice accretion on power lines is an important factor for occurrence of galloping. Although galloping leads only in extreme cases to collapse of the structure, it may significantly reduce the lifetime of transmission lines. The glaze ice is dense; it applies larger static or dynamic forces to the transmission lines, conducts electricity more easily and is more dangerous with regard to the performance of the components of electric networks. Over the past decades, researchers have tried to improve methods of reducing or eliminating ice adhesion to a surface. De-icing methods using techniques such as conductor heating or mechanical de-icing using a roller are possible for overhead lines ranging from 25 to 245 kV. However, such methods cannot be easily applied to lines with twin or quad conductors at rated voltages of 315 to 735 kV respectively. Another de-icing method is based on circulation of short circuit current (ISC) [77, 78].

2.3 Ice-Repellency

As explained earlier, ice can bond strongly to nearly all types of surfaces, making it difficult to remove. While the majority of techniques actively used are active de-icing, i.e.

mechanical removal, none of them can be easily or reasonably applied to different structures as they are destructive to most surfaces, highly demanding of energy and not environmentally-friendly (in the case of anti-icing fluids) [37]. Fabrication of any surfaces to which ice would not adhere can be considered as an ideal solution to being used instead of de-icing techniques. Such surfaces are known as "*icephobic*" surface. These ice-repellent surfaces can be created by an appropriate morphological modification of the surface followed by the application of a coating whose chemical components would have a weak chemical interaction with ice. It was shown that Al surfaces treated with self-assembled monolayers of silane or fluorocarbon will display reduced ice adhesion [34]. The mechanisms involved in the strong adhesion of ice to materials can be divided into three main categories [26, 61, 79, 80]**,** namely, electrostatic forces [26, 79, 81, 82], chemical bonds including hydrogen bonds, dipole-dipole bonds, and secondary attractive forces [83], and finally diffusion or mechanical penetration. In ideal cases, all interactions must be eliminated to obtain zero or reduced ice adhesion [84]. The primary chemical bonding or valence forces are effective only at typical bond lengths of 0.15-0.2 nm and decrease rapidly with distance [85, 86]. Hydrogen bonding is also involved in ice adhesion [87], however, hydrogen-bond energies, namely 8.4-41.8 $kJmol^{-1}$ [87], are comparable with the weaker primary bonds and generally exceed the *Lifshitz-van der Waals* attraction forces [26, 83, 88]. The electrostatic forces between a charge at the ice surface and the charge induced on a substrate have been found to significantly dominate the adhesion of ice to surfaces with an interaction energy of up to 500 mJm^{-2} [26, 80]. The force required to detach ice from a surface is termed ice adhesion force. A number of parameters and conditions may influence the ice adhesion to a surface, including purity of materials, surface uniformity, substrate properties, the conditions under which the ice formed, air temperature, freezing rate, water contact area, etc. [13, 80]. In addition, in the presence of microscopic pores in a solid, a water drop can enter and freeze inside the pores. After freezing, the expansion of water leads to a strong mechanical interlocking between the ice and substrate. Generally, adhesion failure may occur at five points, these being at the true interface, within either of the bulk phases or at either of the two regions adjacent to the true interfaces [13]. Altering the ice/solid interface by dirt, dust, grease, chemical

nature of materials, etc. may change ice adhesion [89, 90]. The surface property is different when compared to the interior or bulk. The extra energy associated with the surface, the so-called surface free energy, arises from an imbalance between the interior and the exterior. This leads molecules to seek the interior, minimizing the surface energy (designated as 'γ' and with dimension of Nm^{-1} or Jm^{-2}). Consequently, a liquid tends to form a spherical droplet, the form which displays a minimum area-to-volume ratio, and thus minimum surface free energy [91]. The surface energy of metals has been the subject of numerous theoretical and experimental investigations [92-94].

2.4 Measurements of Adhesion of Ice

A variety of methods and devices are available and employed to measure adhesion of ice [6], for instance, the peel test and the blister test [87], impact tests [13], laser techniques [95], the cone or tensile test, scratch methods [96], electromagnetic tensile tests [97] etc., each of which has its own advantages and disadvantage [5, 6, 28, 87, 96-98]. Beams *et al.* [100] and Raraty *et al.* [101] applied a rotating centrifugal force method to measure the shear strength of ice on metal surfaces. The main factors in ice adhesion measurement are, indeed, the reliability and reproducibility of the results. Therefore, a common technique to measure ice adhesion is to conduct a comparative study by creating ice on surface of both a reference and sample in question as well in the same condition and providing the results in shear strength change percentage. Ice is a polycrystalline material with many dislocations especially at temperatures above -6 ºC which is a result of always being under stress due to volume changes in ice while it forms and cools. The interface is accordingly always under stress. Meanwhile, accumulation of dislocations is also a result of differences in thermal coefficients of expansion and contraction of the ice-solid [13]. The shear strength of refrigerated ice on Cu substrate is ~1.72 MPa and the same variable for artificial ice was found to be 0.85 MPa for Cu and 1.52 MPa for Al [99]. A poor adhesion occurs with low energy surfaces or contaminants.

2.5 How to Reduce Ice Adhesion?

Reduced adhesion of ice requires reducing substrate wettability, in that way making it more hydrophobic. This property implies reducing both its reactivity and surface forces, making it become more inert and incompatible with water. A high energy surface, exhibiting high interfacial energy, has a high level of attraction for a contacting fluid and a low energy surface is the opposite, i.e. relatively inert [87, 89]. A well polished surface reduced the shear stress while a sanded surface increased the adhesion by 149 %. Polymeric hydrocarbons and fluorocarbons, as in the case of Teflon® (polytetrafluoroethylene) and polyethylene, demonstrate low attraction to ice adhesion which is due to low energy surfaces of ~489.5 $kJmole^{-1}$ [87]. The hydrophobic waxes and Teflon® decreased the adhesion of ice by over 50 % [13]. The relatively low adhesion of ice to silicones is explained by structural characteristics which keep their oxygen atoms well screened by methyl groups [87]. In most studies, icephobic products are chosen according to their hydrophobic properties, presenting water-repulsion qualities [102-104]. In hydrophilic surfaces, the interfacial forces are strong and step formation is inhibited with a subsequent lower concentration of interfacial defects. The adhesion failure, thus, occurs in the bulk ice, *i.e.* cohesion [13]. However, on hydrophobic films, dislocations occurring during the removal of ice tend to collapse into the surface due to lower interfacial forces, producing interfacial defects. This explains why adhesion failure occurs at or very close to the interface.

2.6 Wetting Property (Surface Wettability)

It is well-known that a liquid-like or a transition layer exists on ice, both on free surfaces and at interface with solids [87, 105, 106]. A wetting phenomenon may occur at the point where all three states, whether solid, liquid or vapor, are in contact; this also includes the behavior displayed by the intersection of the three interfaces, namely, solid-liquid, solid-vapor, and liquid-vapor [107, 108]. In addition, the physical roughness of a texture plays a secondary role in adhesion. Where wetting is sufficient, roughness can enhance adhesion by increasing the

contact area for an exchange of forces by "*tooth*" or "*anchor*" effects [83, 86, 107]. When wetting is incomplete, pockets of air are left in hollows and adhere to the surfaces which reduce bonding. Therefore, poor wetting or occlusion of air may be a way of bringing poor ice adhesion. Wetting depends on the attraction between a liquid and a solid which reflects as surface energy or '**γ**' [107]. The surface energy of water is 72 mJm^{-2}. This is due to the role of hydrogen bonding to hold it together**,** as in mercury, in which the metallic bonding does this function [83, 87]. For metals, oxides, nitrides, silica and diamond, known as hard solids, the surface energies are 500-5000 mJm^{-2}. For soft solids**,** *e.g.* waxes and most organic compounds and liquids (excluding liquid metals), however, the surface energies are between 0.1 and 100 mJm^{-2}. From a practical point of view, any liquid will spread out over high energy surfaces. If surface energy is low, as for waxes and various polymers, self-satisfied forces provide little inducement for liquids to spread out. Though the surface energy of solids is not as readily measured as it is for liquids, however, the values can be obtained through specialized measurements, e.g. CA, thermodynamics, calorimetric heat of solution, etc. [85, 86].

2.6.1 Surface Hydrophobicity

Wettability is expressed by the contact angle, CA (θ), formed by the liquid and the substrate. Contact angle measurement is an easy-to-adopt method for surface and surface energy analysis. Young and Laplace found that each surface has a specific energy which is called surface energy and is proportional to the number of atoms present on the outermost layer, as shown in Fig. 2.1 [13, 28]. In this figure, the γ_{SV}, γ_{SL} and γ_{LV} are the interfacial free energies per unit area of the solid-vapor, solid-liquid**,** and liquid-vapor interfaces, respectively. The equilibrium of surface energy can determine the entire shape of a droplet on a solid. The CA values vary inversely to attraction and ease of wetting of materials, ranging from 0º to 180º, theoretically. When θ is larger than 90º, the surface is called a hydrophobic surface, with less attraction to water, and when θ is smaller than 90 º, the surface is called a hydrophilic surface indicating considerable attraction to liquids. The contact angle, indeed, is the macroscopic

indicator of the surface energy balance. To date, several methods have been developed to characterize surface hydrophobicity, including contact angle, tilt angle, etc. [86, 109-111].

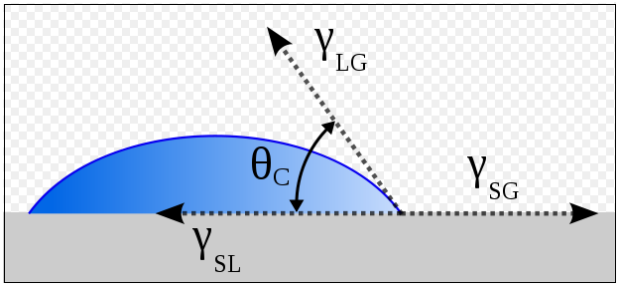

Fig.2.1. Schematic representation of a liquid droplet on a surface illustrating the quantities in Young's equation**.**

However, the static CA measurement is the main technique for characterization of surface hydrophobicity and therefore to study the surface energy. Disorders, impurities, and other defects or energetic effects close to the material surface can give rise to increased surface energy [28]. The CA values may be found to be as large as 115^{o} for water on waxy or -CH_3 surfaces [87, 109], or 154^{o} for mercury on steel [110]. It is impossible to achieve CA of 180^{o} as hydrophilic sites are always present on practical hydrophobic surfaces. Meanwhile, the *Lifshitz-van der Waals* or *London forces* would always act across the interface between two materials. Accordingly, it is impractical to fabricate a surface which water would not wet at all and to which ice would not adhere [13, 107, 109]. When θ is equal to 180^{o}, no wetting and hence low adhesion occurs. When θ is equal to 90^{o}, it displays poor wetting and fair to poor adhesion. The greater the CA, preferably larger than 150^{o}, the better the water-repellency and self-cleaning abilities. Such surfaces are called as superhydrophobic or ultrahydrophobic surfaces [33, 36]. Superhydrophobic surfaces are observed in nature, for example, the lotus plant (or *Nelumbo nucifera*), which also demonstrates the self-cleaning action of some leaf surfaces [112]. Figure 2.2 shows some examples of superhydrophobic surfaces in nature [113-120]. The CA value of a lotus leaf is about 164^{o} (Fig.2.2b) [121]. Pond skaters (*Gerris remigis*) have the ability to stand and walk upon a water surface without getting wet (Fig. 2.2a) which is due to presence of a special hierarchical structure on the pond skater's legs covered with cuticle wax [122].

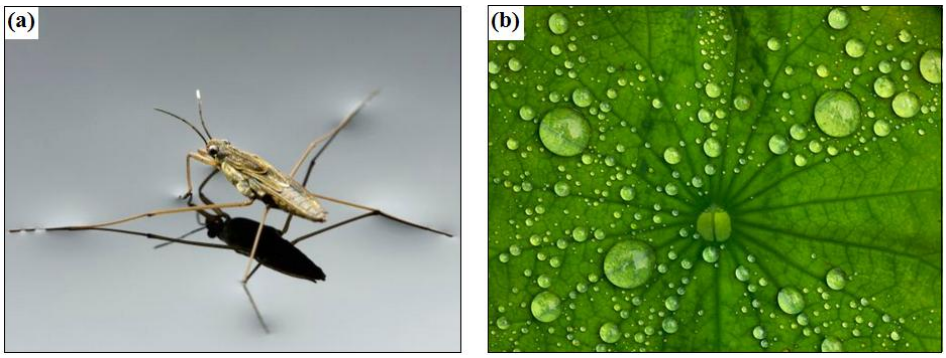

Fig.2.2. Examples from nature: (a) Pond skater walking on water and (b) lotus effect.

One of the ways to increase the hydrophobic or hydrophilic properties of a surface is to increase surface roughness, so roughness-induced hydrophobicity or hydrophilicity has become the subject of extensive investigations [33, 109, 111, 116, 123-143]. Wenzel [135] suggested a simple model predicting how the CA of a liquid with a rough surface is different from that with a smooth surface. The Wenzel regime is defined by Equation.2.1 for the contact angle on a rough surface:

$$Cos\theta' = rCos\theta \qquad \textbf{2.1}$$

where:

- θ' : Apparent contact angle (°)
- r : Roughness factor
- θ : Contact angle of flat surface (°)

The Wenzel model predicts that a hydrophobic surface with increasing roughness becomes even more hydrophobic, while a hydrophilic surface with increasing roughness becomes more hydrophilic [135]. Cassie and Baxter [127] showed that a gaseous phase including water vapor or air may be trapped in the cavities of a rough surface, resulting in a composite solid-liquid-air interface, as opposed to the solid-liquid interface. These two models describe two possible wetting regimes on rough surfaces: Wenzel and Cassie-Baxter regimes as

shown in Fig.2.3. The Cassie-Baxter model is characterized by a big CA and a very small contact angle hysteresis.

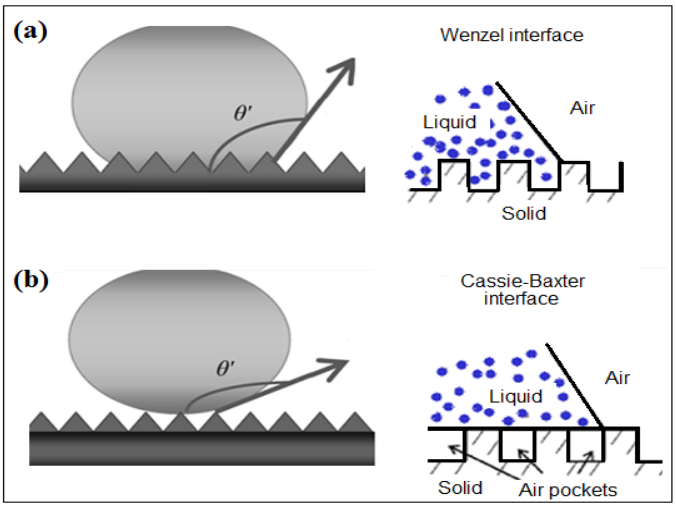

Fig.2.3. Schematics representation of configurations described by the (a) Wenzel and (b) Cassie–Baxter regime with air pockets.

In the Cassie-Baxter model [127] the contact angle values are determined by the fractions of solid and air facing the drop, as describes in Equation 2.2:

$$Cos\theta' = f.(Cos\theta + 1) - 1 \qquad \textbf{2.2}$$

where:

- θ' : Apparent contact angle (°)
- f : Surface fraction (the ratio of surface top-post to projected surface)
- θ : Contact angle of flat surface (°)

As explained earlier, artificial superhydrophobic surfaces are fabricated by combining rough surface morphology and low-surface-energy coatings via two general approaches, i.e. chemical and physical methods such as lithography, vapor deposition and plasma techniques, sol-gel processing, electrochemical methods, *SAM*s of organosilanes, etc. [33, 111, 144-160]. For instance, a CA value of 160° was found using Plasma-enhanced chemical vapor deposition

(PECVD) of fluoroalkylsilanes on an Al surface [127, 161, 162]. The combination of high surface roughness with the low-energy surface of FAS molecules [CF_3-$(CF_2)_7CH_2CH_2Si(OCH_3)_3$] gives a contact angle value of 158° [163]. A CA value of 162° was obtained after being modified with octadecyltrichlorosilane (ODTS) [164]. The superhydrophobicity can be further classified by contact angle hysteresis [111, 165]. The dynamic CA or contact angle hysteresis (CAH) can be measured when a water droplet is allowed to advance in one direction on a surface with the difference calculated between advancing contact angle **(**the CA at the wetting edge of droplet, θ_A**)** and the receding contact angle (the CA at the de-wetting edge of droplet, θ_R), as presented in Fig.2.4 [111, 166]. The tilt angle, used to study the superhydrophobic surfaces, refers to the critical angle between the substrate and the horizontal, below which the water droplet begins to move after elevation of one end of the substrate [167]. Surface roughness, combination of micro-/nano-roughness can affect the sample wettability. This is to say when the CA is less than 90^o, increasing roughness causes decrease of CA, while it increases when the CA is greater than 90^o [86, 107, 168].

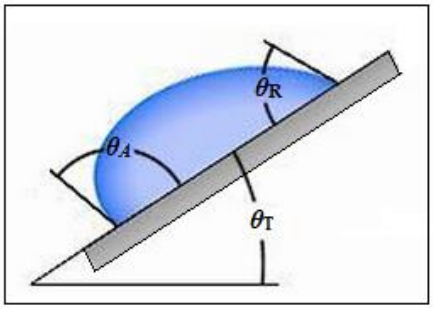

Fig.2.4. Schematic illustration of the relationship between advancing, receding, and tilt angles.

The bouncing drop method may also be used to characterize the CAH. When a liquid drop lands on a surface without wetting it, it bounces with remarkable elasticity, hence, the bouncing ability of the water droplet can also reflect the CAH [111, 169, 170]. Superhydrophobicity means not only a high contact angle, but also a low hysteresis of the contact angle. It was demonstrated that a water drop can slide off a surface even if the CA is very low, even less than 20^o, provided that the CAH is less than 4-5^o. On the other hand, a

water drop can slide off a surface even if the CAH is higher, provided that the CA is greater than 160^{o} [143]. For a monolayer anchored to a substrate by the polar acid, alcohol and ester groups, wettability is governed by the end groups exposed (-CH_3, -CHF_2, and so forth) together with decreases for substituents on an organic carbon chain substance in the order of N>O>Cl>H>F [83, 107]. It is the combination between surface roughness and low-surface-energy coating that leads to superhydrophobicity. Various applications of superhydrophobic surfaces in micro- and nano-materials and devices were recently reported [33, 163, 171]. The low hysteresis of contact angle of a superhydrophobic surface is responsible for the self-cleaning properties too, which means a water droplet can easily roll off the surface and remove dust from the surface. In addition, fabrication of superhydrophobic coatings on metallic substrates has provided a solution to the corrosion problem.

2.7 Surface Passivation

It is possible to alter the surface energy and wettability of surfaces by coating a surface with an appropriate coating, even if it is only as thin as a few layers of molecules; this is called the "*passivation process*" [28, 172]. A typical passivation process used in industries is the cleaning of stainless steel tanks with sodium hydroxide, citric acid and nitric acid. These steps help to restore the film by removing metal particles, dirt, and welding-generated compounds or oxides. In the case of corrosion, passivation is the spontaneous formation of a hard and non-reactive surface film that inhibits further corrosion. This layer is usually an oxide or nitride layer having the thickness of a few molecules. Some corrosion inhibitors help to formation of a passivation layer on the metals surfaces to which they are applied. Another common passivation procedure is based on self-assembly of a number of organic molecules which is one of the most successful approaches to chemical modification and hydrophobization of numerous hydrophilic surfaces[31, 172]. Such self-assembled coatings in general have a polar unit on one side, known as the head, and a non-polar long saturated hydrocarbon chain on the other side, known as the tail. A typical hydrocarbon molecule used for passivation is stearic acid. Self-

assembling monolayers (*SAMs*) are broadly used for hydrophobization of different surfaces through a combined process of hydrolysis, adsorption and polymerization, forming dense and well-organized layers, as shown in Figure 2.5 [31, 172, 173]. A fully-grafted-*SAM*s surface which exposes its CF_3 or CH_3 groups atop is considered as low-surface-energy coating [174].

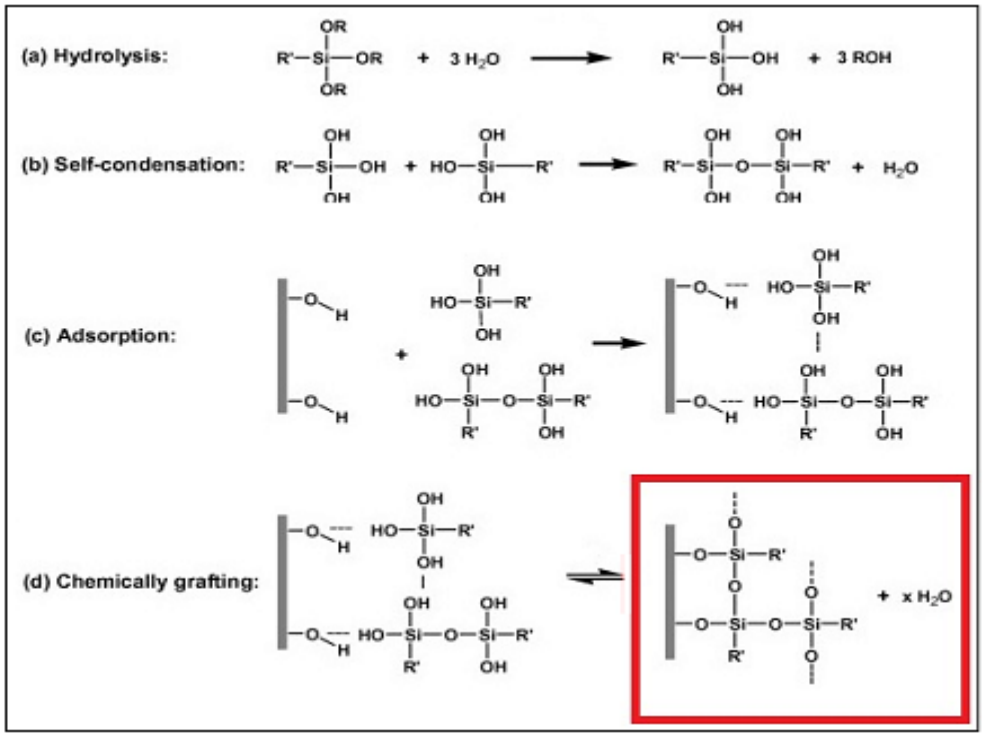

Fig.2.5. Different steps of *SAM*s coating on an oxide surface.

The water CAs ranging from 100^o to 120^o were obtained on flat surfaces coated with F-containing *SAM*s layers [175, 176]. Decrease of surface energy can be placed in the following order: $-CH_2 > -CH_3 > -CF_2 > -CF_2H > -CF_3$ [28, 177]. Both the static and dynamic contact angles of *SAM*-coated surfaces are strongly affected by the degree of self-assembly of fluoroalkylsilane or alkylsilane molecules [13, 173]. Another alternative approach is to apply insulating low-surface-energy coatings with higher thicknesses, e.g. diamond-like carbon (*DLC*) or room-temperature-vulcanizing (*RTV*) silicones. Dimethyl-n-octadecylcholorsilane, belongs to the self-assembled monolayer family, adheres strongly to the Al surfaces due to their thickness and formation of covalent bonds between Si and Al, resulting in improved

service life under periodic icing/de-icing cycles [34]. Octadecyltrichlorosilane is an organo-metallic chemical which is used in the semiconductor industry to form thin films of *SAM*s.

2.8 Coating Stability and Durability

Stability of any coating is a critical issue for various industrial applications since they must be enough durable against different conditions such as UV-exposure, acidic rain, dust and contaminations, corrosion, atmospheric icing, marine conditions, etc. A number of research groups have studied the stability of hydrophobic coatings under different conditions [18, 23, 24, 39, 40, 45, 172, 178-194].

2.8.1 UV Degradation

Sunlight is a major cause of damage to a number of materials, including coatings, textiles, plastics and other organic materials. The type of damage such as loss of physical properties, cracking, peeling, fading, and color change varies and depends on the material sensitivity and the sunlight spectrum [178, 182]. Ultraviolet (UV) light has been recognized as the main cause of damage of coatings since the ultraviolet radiation can cause chemical reactions with coatings due to its level of energy [178]. The Zanini *et al.* result showed that the CA of the coated samples under simulated aging decreased from 122° to 55° or from 175° to 0°. Likewise, in the case of some superhydrophobic coatings, e.g. SiO_2 nano-particle coated surfaces, following UV radiation, they retain their superhydrophobicity after several hours of UV exposure.

2.8.2 Effect of pH

In order to investigate the influence of rainwater and marine conditions on hydrophobic coatings, the surfaces should be immersed in various pH solutions, e.g. 4, 6, 7 and 10 [172, 180, 183-188, 190-194]. It was shown that the surfaces keep their hydrophobicity after immersion in pH solutions, except for the sample immersed in tap water which is due to ionic contamination. It was confirmed that the hydrophobic property of plasma-polymerized

fluorocarbon coatings on stainless steel was reduced after several days of immersion in distilled water [186]. The XPS results revealed that the reduction in fluorine concentration after immersion in water led to a decrease of hydrophobicity.

PART II: ALUMINUM ALLOYS AND CORROSION

Reduced accumulation of ice on metallic substrates, e.g. Al and its alloys, always comes with corrosion, which is a serious problem in outdoor applications. Since in all modern AAs, other metallic additives are used to improve the strength of the material, these metal additives precipitate during the solidification processes and create second-phase particles in the Al matrix. This composition of the Al matrix and second-phase particles, inevitably leads to increased un-sustainability of the electrochemical corrosion (local galvanic corrosion) of such alloys, more especially, for AAs in close contact with water. Corrosion is defined by the breaking down of fundamental properties in a material due to chemical reactions with its surroundings. Most structural alloys corrode by exposure to moisture in the air. Accordingly, anticorrosive performance of any icephobic coating on AAs becomes a significant issue in evaluating the durability and stability of the coating.

2.9 Corrosion and Passivation of Aluminum Alloys

2.9.1 A Brief Introduction to Aluminum

Aluminum and its alloys are the most frequently used non-ferrous metal in aerospace, marine industries, automotive applications, and so on, because of their low density, favorable mechanical properties, good thermal and electrical conductivity, and resistance to corrosion. Pure Al has a low tensile strength, however when combined with thermo-mechanical processing to manufacture Al alloys**,** it displays a significant improvement in mechanical properties, especially when tempered. Aluminum and its alloys have a natural corrosion protection from the thin oxide layer (Al_xO_y) which forms when the metal is exposed to air. However, if exposed to

certain conditions, e.g. salt, acid, corrosive gases etc., it may corrode and consequently becomes costly. For instance, in 2013, the cost of corrosion related to the aircraft industry in North America was around 13 billion dollars [195]. Many studies revealed that hydrophobic coatings may cause an increase in corrosion resistance of surfaces [183, 184, 189, 196]. It was demonstrated that anodized Al could inhibit the corrosion of an Al surface up to 61%, which increases to 96% by depositing a superhydrophobic coating [189]. Aluminum is widely distributed in the oxide form called Alumina (Al_2O_3). It comprises 15% of the Earth's shell and is second to silica in abundance. Therefore, there is a virtually unlimited supply of Al [197]. Aluminum was discovered by Sir Humphrey Davy in 1809, but was not isolated as a metal until 1825 by H. C. Oersted. An economical industrial process was found in 1886 when two scientists, Hall and Heroult, independently developed the same electrolytic process to reduce alumina to Al metal and this process is still widely used nowadays [197]. Aluminum has many properties, making it desirable for various applications. It has a low density (2.7 g cm^{-3}), good thermal and electrical conductivity, high ductility, low cost compared to comparable metals due to its abundance, and the high-purity form of the metal has good corrosion resistance in the ambient atmosphere [198]. The presence of an amorphous oxide layer (Al_xO_y) which forms naturally on Al surface upon exposure to atmosphere explains why the surface is resistant to further oxidation and causes the surface to be "*passive*" or corrosion resistant. The resistance of Al to rainwater or beverages was first assessed at the beginning of the 1890s [172, 239]. The natural oxide layer, however, has a limited thickness of 1 to 3 nm and flaws exist in the natural oxide film, which can act as sites for film breakdown [197, 199-201].

2.9.2 Classification of Aluminum Alloys

Pure aluminum in general has inadequate mechanical strength, making it not practical to use for commercial applications. Alloying and numerous treatments are possible to improve Al properties including cold working and heat treating. Alloying implies adding and dissolving one or more dissimilar metals into the Al. Major elements used for alloying Al are copper, zinc,

manganese, silicon**,** and magnesium and nickel. Aluminum alloys can be classified as "*Cast Alloys"*, since they are cast directly into desired forms by one of the many methods, e.g. sand casting, gravity die casting, or pressure die casting; or the as "*Wrought Alloys"*, where the alloy is made into ingots or billets [197, 202, 203]. These are then hot or cold-worked mechanically into wires, extrusions, sheets, forgings, foils and tubes [197, 202]. The specifications and properties for Al and its alloys are covered by different standard codes that allow standardization for specific applications [202, 203]. This also covers temper designations to signify any cold or heat working applied to the Al alloy.

The cast and wrought alloys classes, in brief, are summarized as follows:

1) The high-strength Al-Cu alloys (2000 series), used mostly in the aero craft industry.
2) Al-Mn alloys (3000 series), used mainly in the canning industry.
3) Al-Mg alloys (5000 series), used for structural and architectural applications.
4) Al-Mg-Si alloys (6000 series), used typically as most common extrusion alloys, used in the building industry.
5) Al-Zn-Mg alloys (7000 series), used largely in the construction of aero craft and military vehicles [197, 202, 203].

The strongest Al alloys are less corrosion resistant due to galvanic reactions with alloyed copper or zinc. In this research work, the AA2024-T3 (an alloy used extensively to manufacture aircraft) is used. The composition of this alloy makes it noticeably prone to corrosion processes. The T3 temper designation indicates that the AA has been thermally treated after precipitation hardening (cold-worked and naturally aged) [202, 203]. It was shown that the most populated category of second-phase inter-metallic particles contain Al, Cu, and Mg exclusively, though the analysis was unable to distinguish conclusively between Al_2CuMg, AlCuMg, $A1_5Mg_2Cu_5$, and $A1_6Mg_4Cu$ chemical types [47]. However, in AA2024-T3, approximately 60% of second-phase inter-metallic particles greater than about 0.5 to 0.7 μm are Al_2CuMg, so-called the S phase. This fraction corresponds to 2.7% of the total alloy surface area which is the main reason for localized corrosion [47]. The S phase particles in the AA2024 appeared to be active with respect

to the Al matrix resulting in severe de-alloying and thus leading to the formation of Cu-rich particle remnants. The composition of the Al-Cu-Fe-Mn particles is believed to be Al_6(Cu,Fe,Mn). These particles are typically small in size, ≤ 4 μm, and regular in shape, whereas the S phase particles are irregularly shaped and coarse usually ≥10 μm [55].

Table 2.2 Aluminum alloy designation according to the Al Association (AA) [197, 202, 203].

Wrought Alloy Designations	
Aluminum, 99.00% purity minimum or greater	1xxx
Aluminum Alloys Grouped by Major Alloying Elements	
Copper	2xxx
Manganese	3xxx
Silicon	4xxx
Magnesium	5xxx
Magnesium and Silicon	6xxx
Zinc	7xxx
Other Elements	8xxx
Un-used Series	9xxx
Cast Alloy Designations	
Aluminum, 99.00% purity minimum or greater	1xx.x
Aluminum Alloys Grouped by Major Alloying Elements	
Copper	2xx.x
Silicon with Copper and/or Magnesium	3xx.x
Silicon	4xx.x
Magnesium	5xx.x
Zinc	7xx.x
Tin	8xx.x
Other Elements	9xx.x
Un-used Series	6xx.x

Aluminum, together with Mg, is selectively dissolved from S phase particles leaving behind Cu-rich remnants which are no longer attached to the metal surface [47]. A maximum in the density of pitting due to selectively dissolved particles was observed at pH 4.2 [47, 172, 202]. This pH is close to minimum solubility of Al which occurs at approximately pH 5. Micro-structural heterogeneity also arises as a result of impurities which are involuntarily introduced

during melting processing; making AAs susceptible to localized corrosion. Some of the most common alloys**,** together with their chemical composition are listed below in Table 2.3.

Table 2.3 Chemical composition (wt. %) of several typical AAs based on ASM Material Data Sheet. Other elements were also detected at lower levels [172].

Alloy	Cu	Mg	Si	Mn	Cr	Zn	Fe	Ti
AA2014-T6	3.9-5.0	0.2-0.8	0.5-1.2	0.4-1.2	<0.1	<0.25	<0.7	<0.15
AA2024-T3	3.8-4.9	1.2-1.8	<0.5	0.3-0.9	<0.1	<0.25	<0.5	<0.15
AA3003-H14	0.05-0.2	-	<0.6	1.0-1.5	-	<0.1	<0.7	-
AA6061-T6	0.15-0.4	0.8-1.2	0.4-0.8	<0.15	0.04-0.35	<0.25	<0.7	<0.15
AA6063-T5	<0.1	0.45 - 0.9	0.2 - 0.6	<0.1	<0.1	<0.1	<0.35	<0.1
AA7075-T6	1.2-2.0	2.1-2.9	<0.4	<0.3	0.18-0.28	5.1-6.1	<0.5	<0.2

2.9.3 Aluminum Corrosion and Protection Solutions

Alloying Al may increase the mechanical strength, making it more useful for industry; however, the corrosion resistance of the AA is decreased substantially. The verb "*corrode*" is derived from the Latin word "*rodere*" that means "*to gnaw*" [172, 209, 232]. This word entered French (and other European languages) in the Middle Ages. The noun "*corrosion*" was derived at the beginning of the 19th century from "*corrosio*" to designate the act of gnawing [172, 209]. The first reported corrosion experiments on Al started around 1890 [209]. Corrosion in metals is defined as a destructive and unintentional oxidation of a metal caused by an electrochemical reaction between a metal and its surroundings [198, 202]. This is a complex electrochemical process in nature, related to the atomic structure of matter, and typically begins at the surface. In metals, the electrical environment of atoms is made up of free electrons capable of moving throughout the metal. Environmental factors such as moisture or electrolytes are, in general, able to penetrate through the coating layer to form an electrochemical galvanic cell, resulting in corrosion of the Al alloy [49]. At the interface between metal and electrolyte, the transfer of electrical charges transfers to electrochemical reactions [172, 202]. Four practical conditions,

reported in the literature [47], must be met in order to initiate corrosion**,** particularly filiform corrosion**;** (i) a high relative humidity of 60% to 80% RH, (ii) the presence of halide ions at the coating-substrate interface, (iii) the presence of defects in the coating, and (iv) the permeability of the coating to water and oxygen. As was explained earlier, galvanic corrosion is an electrochemical process which occurs when two different metals or alloys come into electrical contact with each other and are immersed in an electrolyte. As a result, a galvanic couple gets set where the more active metal acts as an anode and corrodes and a cathodic reaction occurs at the more noble metal. Corrosion may be observed to concentrate locally in the form of pits or cracks on Al surfaces. Corrosion is a significant problem in a modern industrial society. An industrial nation may spend up to five percent of its gross national product (*GNP*) for corrosion prevention, maintenance as well as the replacement of products lost or contaminated by the corrosion effects [172, 198, 202, 203]. Additional costs may indirectly affect the industry such as plant shutdowns, planning and development, and over-design should also be factored into the economic scenario [172, 202-204].

2.9.3.1 Characteristics of Aluminum Alloy Corrosion

The corrosion features and characteristics of pure Al are presented in the potential-pH or *Pourbaix diagram* in Figure 2.6 [205]. The *Pourbaix diagram* illustrates the thermodynamic stability of a species as a function of the variables plotted. It is used to predict the spontaneous direction of a reaction. Since this is a thermodynamic diagram, the *Pourbaix diagram* gives no details on the kinetics of a reaction. The two lines, lines (a) and (b), are called the a-line and b-line, respectively. They stand for the stability of water at temperature of 25 °C and pressure of 1 atm. Below the a-line, water is reduced to produce H_2; above the b-line, water is oxidized to produce O_2. The stability region of water in the absence of Al is between the a-line and the b-line. In Figure 2.6, it is evident that the whole domain of Al metal stability lies below that of water. If conditions are adequately acidic, the metal will decompose the water with evolution of H_2 and form Al^{3+}, as seen in Area (I). If conditions are sufficiently alkaline, the metal may

decompose the water with the evolution of H_2 and form aluminate ions (AlO_2^-), as seen in Area (II). A third intermediate condition occurs between pH 4 and 9. In this case, the Al becomes covered with an oxide film ($Al_2O_3.3H_2O$) [172, 202, 203] which is the natural oxide film mentioned earlier. It may act to protect the metal from a surrounding corroding medium and provide kinetic stability. This region is known as "*Passive Region*" and is seen in Area (III). The molecular volume of the oxide film is stoichiometrically 1.5 times that of the metal. These results in the oxide film being under compressive stress, however, in practice, some deformation may occur before rupturing [197, 202, 203]. Breakdown of the oxide film can result from mechanical rupture or chemical attack via anions.

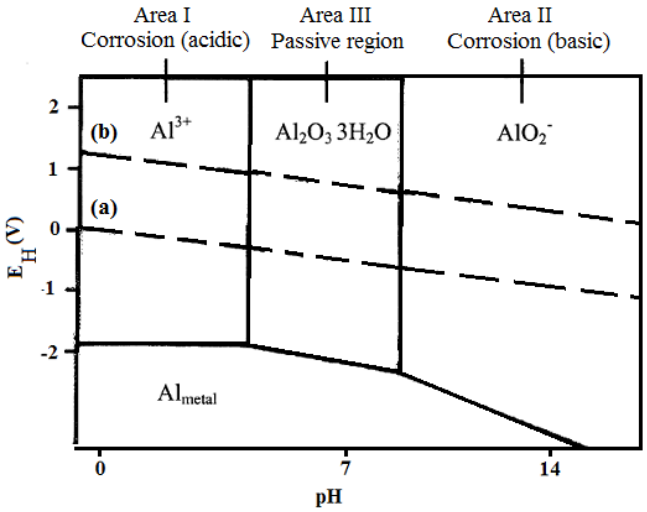

Fig.2.6. Potential *vs.* pH diagram for Al/H_2O system at 25 ^oC and at 1 atm [205].

Aluminum corrosion, in general, is the sum of two electrochemical reactions, i.e. oxidation and reduction, as follows:

$$Al \rightarrow Al^{+3} + 3e^- \qquad \text{(oxidation)} \qquad \textbf{2.3}$$

$$3H^+ + 3e^- \rightarrow 3/2\ H_2 \qquad \text{(reduction)} \qquad \textbf{2.4}$$

$$Al + 3H^+ \rightarrow Al^{+3} + 3/2\ H_2 \qquad \textbf{2.5}$$

(or) $Al + 3H_2O \rightarrow Al(OH)_3 + 3/2\ H_2$ **2.6**

Aluminum corrosion results in the formation of Al hydroxide, $Al(OH)_3\downarrow$, which is insoluble in water and precipitates as a white gel observed in corrosion pits as white gelatinous flakes. Aluminum corrosion may occur when the oxide film is damaged or removed and the surrounding conditions prevent the reformation of this protective oxide film, allowing attack on the exposed metal. It has been suggested that the presence of aggressive ions, e.g. Cl^-, may hinder the re-passivation of the oxide layer, allowing corrosion sites to be generated on the exposed metal. Electrochemical and microscopic studies have in addition confirmed that pre-existing flaws in the oxide film may act as nucleation sites for film breakdown [172, 197-201]. The galvanic coupling is proposed as a mechanism for the alloying element to lower the corrosion resistance involves. In the case of AA2024, as Cu is a more noble metal relative to Al, this causes the preferential dissolution of Al metal [172, 202, 204]. The second mechanism suggested for the poor corrosion performance of alloys involves the differences in the properties and thickness of the oxide film on AA compared to more pure forms of the metal. It has been revealed that the oxide layer above the second-phase particles, more precisely, compounds containing Al-Cu-Mg, and Al-Cu-Fe-Mn-Si, in this alloy may be thinner or even non-existent, which leaves these areas more prone to attack [202, 206, 207].

2.9.3.2 Types of Corrosion on Aluminum Alloys

Different types of corrosion, more or less visible to the naked eye, may occur on aluminum. The predominant type of corrosion depends on a certain number of parameters related to the medium, metal, and the conditions of use. Some types of Al corrosion can be classified among others as pitting corrosion, uniform corrosion, trans-granular and inter-granular corrosion, galvanic corrosion, exfoliation, etc. Each of them has its own characteristics and conditions. Galvanic corrosion, for example, has appeared ever since two different metals were first placed together in a liquid medium, that is to say, since the Bronze Age. From its ranking on the scale of potentials shown on the electro potentials table, Al is more electronegative than

most common metal elements including Fe (steel, stainless steel), and Cu (cuprous alloys). When two dissimilar metals are in direct contact with each other in a liquid, one of the two may corrode through a process of galvanic corrosion. The second metal will not corrode; it may even be protected under these conditions. Galvanic corrosion may occur with any metal, as soon as two of them are in contact in a conductive liquid. It works like a battery built out of two electrodes, namely the cathode, where reduction takes place, and the anode, where oxidation takes place. These two electrodes are plunged into a conductive liquid called an electrolyte, which is normally a diluted acid solution, or a salt solution or even moisture extracted from the environment. The appearance of galvanic corrosion is characteristic; it is not dispersed like pitting corrosion, but highly localized in the contact zone with the other metal. Over all, the following three conditions must be met simultaneously to corrode on AA to undergo corrosion: (i) presence of at least two different types of metal, (ii) presence of an electrolyte, and (iii) electrical continuity between the two metals.

2.9.3.3 Current Solutions to the Corrosion Problem

Since corrosion of metallic substrates represents a significant challenge in modern society and industries, therefore, several researches have aimed at introducing and developing methods for corrosion inhibition. Numerous solutions currently exist including: i) chemical conversion coatings (CCC) involving simple chemical treatments to build protective coatings; (ii) sacrificial anodic coatings, e.g. metal sprays like zinc, or metal painting to protect the substrate surface from being exposed to a corrosive environment; (iii) cathodic protection, or lowering the potential sufficiently, so that corrosion will not occur according to the *Pourbaix diagram* either by placing the system in the stable region or placing it in the passive region; and (iv) anodising, which artificially builds a thicker, but porous, passive oxide layer that acts similarly to the natural oxide layer of the metal. The conversion coatings are mostly from chromate solutions to form Cr (VI) or Cr (III) moieties on the metal surfaces, though newer methods involve applying phosphate-based solutions to form phosphate coatings [172, 197, 202]. These solutions, however, may not be acceptable in practical applications due to various reasons. Both for

environmental reasons and for worker safety concerns, however, the replacement of this chromium treatment became a major priority to develop alternative non-toxic treatment processes [53, 172, 242]. The term "*conversion coating*", as used in the metal finishing industry, refers to the conversion of a metal surface into a surface which will more easily accept applied coatings, so offering corrosion resistance in the event that the secondary coating is breached. A cold applied version of CC, which reacts in a few seconds, has been available for several decades for the processing of large scale items**,** such as aircraft [54]. Vanadate as well as cerium-oxide based conversion coatings are also providing such performances [55]. One environmentally-friendly alternative approach is to produce coatings by oxidizing Al with the permanganate anion, followed by Mn (IV) deposition. Permanganates, which have long been used to purify drinking water, are attractive for large-scale applications, in contrast to Cr (VI) compounds which may be used as a safe alternative to CCCs; they can be successfully used to protect Al alloys [55]. Drying permanganate-based coatings on Al surface provides superior filiform corrosion protection**,** as shown in Figure 2.7 [54].

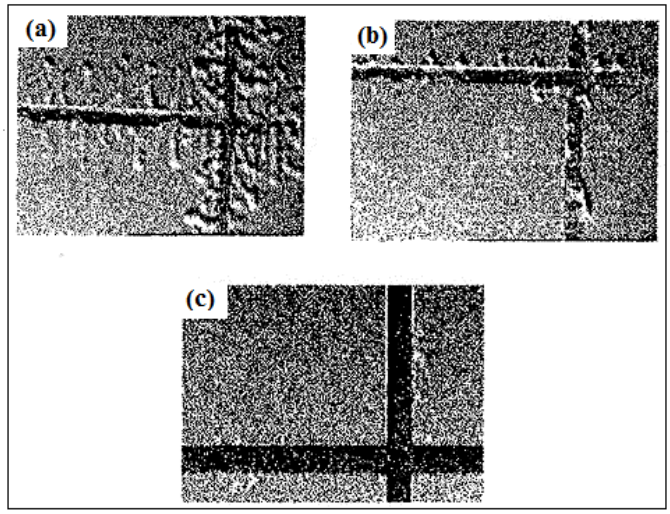

Fig.2.7. Filiform corrosion tests performed on trivalent chromium (pre-treated) and $KMnO_4$ post-oxidized Al without drying (a), with drying (b), and chromated samples (c).

However, PCCs coatings on most of the irregularly shaped Al-Cu-Fe-Mn particles present cracks, which developed during drying due to the thickness of the PCC. Most defects are concentrated in the vicinity of large inter-metallic particles. Painting metals or using sacrificial

coatings, not only serves as an esthetic treatment of the metal, but also serves to form a coating or barrier against corrosion elements. On the other hand, cathodic protection of a metal surface is environmentally friendly and effective too, creating little or no waste products, but it is too expensive to supply the electric current for large exposed surfaces, thus making it impractical for industrial applications. Anodising gives thicker, but more porous, oxide layers which have to be plugged. Comparable solutions for the paint adhesion problem have been achieved by chromate and phosphate-based conversion coatings. However, more strict environmental laws concerning the waste and disposal of hard metals, and the toxic and carcinogenic effects of the Cr (VI) species have initiated a desire to search for an effective, yet more environmentally-friendly alternative to the current chromic acid anodizing or phosphoric acid anodizing processes used [172, 211]. The CIGELE laboratory has been working on permanganate conversion coatings or alkylsilanes-based coatings [172, 190-194]. In addition to cerium salts and zirconates, coating Al surfaces with silane molecules containing a long aliphatic chain, e.g octadecyltrimethoxysilane, may increase significantly the barrier properties of the silanic coating [48]. Such coatings, although not uniform, tend to cover the entire Al surface with fewer defects, as found in the case of self-assembled-monolayers (*SAM*s) on different metal substrates [48]. Self-assembled monolayers are expected to function as a barrier against the permeation of corrosion accelerants such as moisture and electrolytes into the metal substrate, thereby improving the corrosion resistance of the substrate. A *SAM*s film tends to hinder both the cathodic oxygen reduction and the anodic oxidation of Al to a limited extent [48]. The fatty acids and the phosphonic acid tend to bond with Al_2O_3 from the Al substrates through electrostatic interactions, while the long alkyl chains interact together by means of *van der Waals* interactions to form stable monolayer films.

A molecule known to be structurally close to octadecylsilane is stearic acid (*SA*). For alkylsilanes, a two-dimensional hydrolysis-condensation reaction occurs between the silane and the Al substrate, leading to a polymerized monolayer film, as illustrated in Figure 2.8.

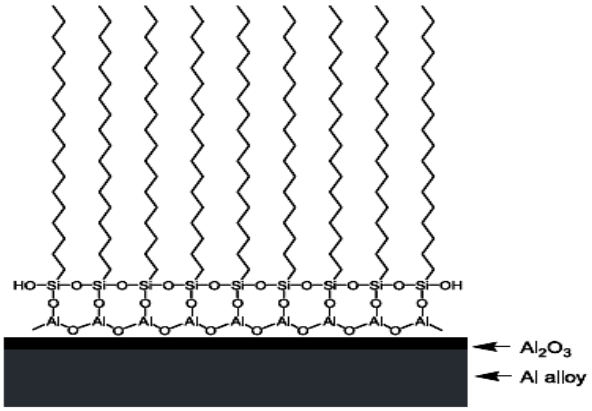

Fig.2.8. Self-assembled monolayer film of alkylsilane molecules on AA substrate.

Over the past several years, organofunctional silanes, known as "*coupling agents"* for metals, have been given more consideration as a *"green"* corrosion inhibitor alternative [48, 172, 190-194, 212-215, 243]. These organofunctional silanes are known as "*Silane Coupling Agents"* or "*Silanes"*. Organofunctional silanes are, indeed, hybrid organic-inorganic compounds which can be used as coupling agents across the organic-inorganic interfaces. It was found that 1,2-bis-trioxymethyl-silyl-ethane (BTSE) coating, 250 to1700 nm, can be used as a corrosion inhibitor [48, 51, 52]. Non-functional silanes or di-silyl derivatives bear a close likeness to functional silanes in structure, except for the fact that they have hydrolysable Si-O-C bonds on both ends of the carbon chain.

2.9.4 Silane Coupling Agents

Coupling Agents are defined as materials which improve the chemical resistance, more especially to water, of the bond across the interface [172, 216-218]. The most commonly-used silane coupling agents have the structure Y-R'-Si-$(OR)_3$, where they are mono-functional, i.e. having only one silicon moiety. Y is an organo-functional group such as chlorine, amine, epoxy or mercapto, R' is a hydrocarbon chain, and OR represents an hydrolysable alkoxy groups, e.g. methoxy or ethoxy species, which upon contact with water produces silanol (Si-OH) groups as presented in Fig.2.7 [172, 216-218]. The silicon moiety gives the metal-bonding ability and the

possibility of polymerization by condensation of excess silanol groups, not bonded to the metal. The silanol groups are the functional groups which interact with the metal oxide surface, leaving the Si-R'-Y side of the silane to be free to react in subsequent steps, e.g. adding a second silane or painting [172]. This is well-known as "*Right-Side-Up"* bonding [219].

1. Hydrolysis of silane:

$$(OR)_3—Si—R'Y + 3\ H_2O \text{ -» } (OH)_3—Si—R'Y + 3\ ROH \qquad \textbf{2.7}$$

2. Condensation and polymerization of silane to free hydroxyls in oxide layer (Fig. 2.9):

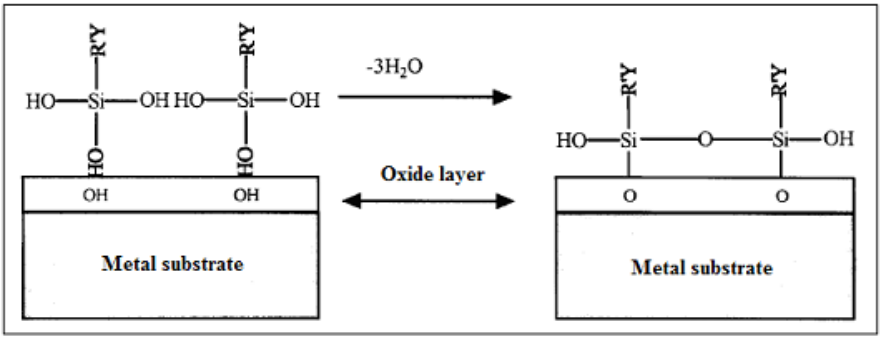

Fig.2.9. Proposed mechanism for silane bonding to a metal substrate.

The "*Upside-Down"* bonding occurs when the organofunctional group Y is bonded to the metal oxide, leaving no functional group other than the silanol groups for further reaction [219]. Some examples of silanes are shown in Tables 2.4 and 2.5. Silanes with varying Y groups may be chosen for subsequent steps. If an appropriate functional group is chosen, it may participate in further bonding with other silanes, producing a more cross-linked film. This cross-linking aids in hydrophobic properties of the silane film. Organofunctional silanes can bond with a metallic surface via the formation of oxane bonds. This reaction may be expressed by the general equation [52]:

$$Me\text{-}O\text{-}Si\text{-}R + H_2O \rightarrow Me\text{-}OH + HO\text{-}Si\text{-}R \qquad \textbf{2.8}$$

Table 2.4 Silane coupling agents (monofunctional silanes).

Monofunctional silanes		
Organofunctional group	**Name**	**Chemical structure**
Vinyl	Vinyl silane (VS)	$CH_2=CHSi(OC_2H_5)_3$
Epoxy	γ- Glycidopropyl-trimethoxy silane	$CH_2OCHCH_2O\ CH_2\ CH_2\ CH_2Si(OC_2H_5)$
Primary amine	γ- Amino propyltrimethoxy silane	$H_2N\ CH_2\ CH_2CH_2Si(OC_2H_5)_3$
Phenyl	Phenyl silane	$C_6H_5Si(OCH_3)_3$

Table 2.5 Silane coupling agents (Bisfunctional silanes).

Bisfunctional silanes		
Organofunctional group	**Name**	**Chemical structure**
--	Bis-triethoxysilyl ethane (BTSE)	$(H_5C_2O)_3SiCH_2CH_2Si(OC_2H_5)_3$
Amine	Bis-(triethoxysilylpropyl) amine (BTSPA)	$(H_5C_2O)_3Si(CH_2)_3NH(CH_2)_3Si(OC_2H_5)_3$
Sulfur	Bis-(triethoxysilylpropyl) tetrasulfide (BTSPS)	$(H_5C_2O)_3Si(CH_2)_3S_4(CH_2)_3Si(OC_2H_5)_3$

Tetraethyl orthosilicate, ($C_8H_{20}O_4Si$), Fig.2.10, is another organosilane can be used on Al surface against corrosion and as an under-layer that can be then covered with a *SAM*s layer.

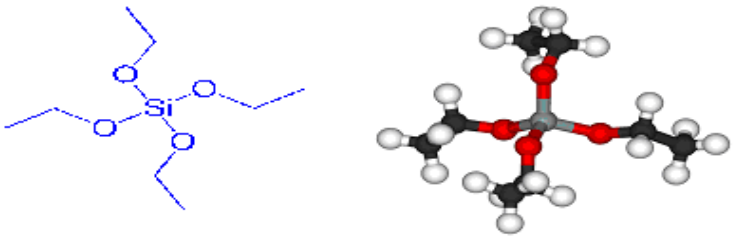

Fig.2.10. TEOS molecule and its spatial configuration.

2.9.4.1 Applications of Silane Coupling Agents

There is a long history for binding dissimilar materials with philosophical thoughts recorded by Plato [220]. Organosilanes initially received interests as coupling agents in the 1940's, when there was a need for new techniques to bond glass fibers as reinforcements in organic resins. A water-resistant bond was needed. In 1947, allyltriethoxysilane on glass fibers gave polyester composites with twice the bond strength of those fibers treated with ethyltrichlorosilane [216]. In 1962, the effectiveness of silanes, as coupling agents, paralleled the reactivity of its organofunctional group with the resin [221]. Since then, numerous articles have been published on role of silanes as coupling agent or a primer for painting. However, silanes were considered as corrosion inhibitors for metals the early 1990's [172, 190-194, 216-218]. This idea depends on the nature of silane to create a well-bonded, hydrophobic, cross-linked barrier, which may protect the metal in an aqueous environment. Much of this work has been done primarily on hot-dipped steel, galvanised steel, iron, zinc, and various AAs using mono functional silanes [222-226]. Early results mixed the efficiency of such coatings for corrosion inhibition of metals, as it depends not only on the choice of silane used, but also on the choice and state of the metal being coated [172, 227]. However, it was shown that some metal/silane combinations are promising and they may even challenge the stability of current chromating processes [172, 190-194, 228].

In this research work, the *"bis-triethoxysilylethane (BTSE)"* is in analyzed as a corrosion inhibitor on AA2024. Such an "*anchoring layer*" can be then covered with a *SAMs* layer, as top layer providing hydrophobic property, forming a thicker and denser coating against corrosion.

2.9.5 Bis-triethoxysilylethane (BTSE)

The BTSE chemical structure is as $(H_5C_{20})_3SiCH_2CH_2Si(OC_2H_5)_3$ [172]. The monomer is bi-functional and has two silicon moieties. For the reason of its bis-functionality, lack of traditional organofunctional group Y, and the presence of six silanol groups in the hydrolyzed form, it is much stronger acid than the mono-functional silanes which follow the formula of Y-

R'-Si$(OR)_3$ [172, 229, 230]. This helps to form more covalent bonds with a metal substrate. Meanwhile, due to the six possible silanol groups present after hydrolysis, further cross-linking between the monomer units may result in a less porous film, with better water resistance. These six silanol groups may also be available for bonding to a second silane having an organo-functional group "Y", which may not have been strongly adhered to the substrate on its own [172, 229, 230]. Based on the silane nature, however, it was demonstrated that the BTSE layer alone may be sufficient to act as an inhibitor [172, 222, 223, 227-230].

2.9.6 Surface Substrate Pre-treatment

Prior to any coating applied to a metallic substrate, the substrate should be sufficiently pre-treated, for instance, it must be cleaned and prepared to deposit the coating and ensure durable bonding to the substrate. Surface contamination has been revealed to cause problems with the durability of such bond [49, 231-233]. In fact, the Al oxide layer is highly adsorbed to contaminants from the ambient environment, thereby affecting the adsorption kinetics of any coating significantly [241]. These results suggest that surface defects may play an important role in the adsorption process and completion of film formation**,** the poor quality of which can be verified by Raman spectroscopy. A pre-treatment may also serve to change the morphology of the surface, making the surface rougher, which may aid the mechanical interlocking of any subsequent coatings [225]. In addition to the flaws that pre-exist in the thin, natural-borne oxide film, it was suggested that the original oxide layer is not conducive for the bonding of organic coatings, as it is usually amorphous with few metal hydroxide sites [172, 197, 234]. Alkaline etching, in general, increases surface roughness. Mechanical polishing is used to create a microscopically rough surface which is shown to create a large surface area that may improve adhesion, and is frequently used prior to any chemical etching [172, 235]. Alkaline etching also increases the amount of free metal basic hydroxyls compared to other forms of metal pre-treatment, for example, acidic or neutral chemical cleaners [229, 230]. These hydroxyls are believed to be

essential for silane bonding [216, 218]. It was suggested that etching products are created after the alkaline etching step in NaOH as pre-treatment according to the following reaction [238]:

$$2\ Al + 2\ NaOH + 2\ H_2O \rightarrow 2\ NaAlO_2 + 3\ H_2 \qquad \textbf{2.9}$$

AlO_2^- in solution may further react with water or acid to form one of the two following forms of etching product:

$$2\ NaA1O_2 + 4\ H_2O \rightarrow 2\ Al(OH)_3\ (\ s\ ) + 2\ NaOH\ \text{(in alkaline media)} \qquad \textbf{2.10}$$

Or

$$AlO^{2-} + H_3O^+ \rightarrow A1OOH_{(S)} + H_2O\ \ \text{(in acidic media)} \qquad \textbf{2.11}$$

However, the alkaline etching pre-treatment proposed for silane deposition has its own advantages and disadvantages. While this process may be essential to build free hydroxyls needed for bonding as well as to increase the total surface area, it may have the side effect of creating etching products which may create a poorly-bonded silane film.

2.10 Conclusion

A review on the principles of wettability, hydrophobicity as well as Al alloys, corrosion and surface pre-treatment and modification were presented in this chapter. The effect of surface pre-treatment in alkaline solution as well as the immersion time and solution concentrations on the physical and chemical characteristic of a thin film was discussed. The durability and stability of hydrophobic coatings under accelerated aging conditions such as UV degradation, immersion in different pH solutions to simulate rainwater conditions and exposure to an environment was explained in detail. The combination of corrosion protection with ice repellent properties via one layer or multilayer approaches have involved considering under layer(s) and upper layer(s).

CHAPTER III

EXPERIMENTS AND TEST PROCEDURES

3.1 Introduction

The objective of this chapter is to describe and discuss in detail the methods used to prepare and characterize various low-surface energy and anticorrosive thin films on AA2024 surfaces by available facilities. The design of experiments including deposition of one-layer and double layer(s) environmentally-friendly coating on Al and their physico-chemical characterization will be described precisely.

3.2 Methodology

3.2.1 Substrate Pre-treatment and Cleaning Procedure

As-received Al alloy 2024 panels with ~2 mm thickness (AA2024-T3, provided by Rio Tinto Alcan, Quebec, Canada) in the form of industrial rolled sheets were cut into smaller plates with dimensions of 1 cm ×1 cm, 2 cm ×2 cm and 5.1 cm × 3.2 cm and were used as substrates in the present study. The nominal chemical composition of AA2024-T3 base alloy is listed in Table 3.1 [172, 202, 264-267]. As it is evident, this alloy is an AA with Cu as the primary alloying element between 3.8-4.9% (wt. %) [268, 269] and is used extensively in applications requiring high strength to weight ratio and good fatigue resistance. Both sides of as-received AA2024 plates were firmly covered by Teflon strip to avoid surface corrosion when they are in direct contact with atmosphere and humidity. The chemical composition of this alloy was in addition validated via optical emission spectrometer. The trace elements obtained according to 2014AD-C107 standard for AA2024 was in close range presented in Table 3.1. This alloy is among the most common Al alloys used in aerospace and transport industries [202, 264-267].

Table 3.1. Designate chemical composition of the AA2024-T3 alloy [172, 202, 264-267].

Elements	Al	Mg	Si	Cu	Cr	Mn	other
Composition (wt. %)	93.50	1.40	0.50	4.10	0.09	0.40	<0.01

Power transmission lines conductors, indeed, are generally made of two parts; a stainless steel core and Al strands around the core, mainly AA1350. Prior to coating, the plates were mechanically polished, first using different grit sand papers from 320 to 4000, then successively finer SiC abrasive papers lubricated with water, and finally aqueous 1.0 μm alumina slurry, in order to obtain mirror-polished surfaces. While the smaller samples were used to evaluate stability and durability of the coatings in aggressive media and conditions, the larger ones were used to evaluate their ice-repellent and anti-corrosive performances as well. Larger Al substrates had two holes on one side to connect to an icing test beam. The polished Al substrates were next cleaned and degreased with soapy water and ultrasonically in different organic solvents as well. More specifically, substrates were cleaned in acetone (99.5%, EMD), methanol (99.8%, MAT), iso-propanol (99.8%, EMD) and rinsed with deionized water, respectively, each for 3 min followed by cleaning in a *Turco Redoline 53D* alkaline solution (pH~10) for 2-3 min. The alkaline solution was used to create freshly cleaned Al oxide layer on each surface substrate following simple chemical reaction between Al oxide layer on Al surface and the *Turco Redoline 53D* alkaline solution OH-anions [270, 271]. This fresh Al oxide layer is obtained by soft etching for removal of an old Al oxide layer, in order to produce a fresh and reproducible layer [252, 253]. The cleaned and polished Al plates were then blow-dried in a N_2 gas flow, and were dried in an oven at 80 °C in air for 3 hrs and were subsequently placed in corresponding chemical baths at room temperature. It is worthy to mention that polished Al surfaces were inspected by optical microscopy, prior to test, demonstrating no evidence of particle-matrix pits or local corrosion. For cyclic corrosion test, some of these cleaned Al samples were labelled as "*Standard*", while some others were labelled as "*control*" samples.

The control samples were only immersed in iso-propanol, as solvent, for 15 min under the same conditions, without addition of alkylsilane compounds.

3.2.2 Chemical Solutions (Prepared Deposition Baths)

3.2.2.1 Preparation of *SAM*s Coatings (Top Layer)

As it was mentioned earlier, numerous approaches have been reported in recent years to fabricate controllable hydrophobic surfaces, such as electrochemical, plasma etching, electrostatic spraying and so forth. There are several problems existing in these methods including expensive approaches, need of complicated equipments and unstable surface properties. Consequently, in the present study, it was decided to use a liquid phase technique known as *wet-chemistry technique* which is easy to use, cheap and fast. The polished flat AA2024 were coated with self-assembled monolayer or multilayer thin films of three dissimilar solutions of well stirred diluted alkylsilane-based layers *(silanisation).* More precisely, Al substrates were coated by Octadecyltrimethoxysilane ($CH_3(CH_2)_{17}Si(OMe)_3$) abbreviated as 18C in the present study, Triethoxy(octyl)silane ($CH_3(CH_2)_7Si(OC_2H_5)_3$) abbreviated as 8C herein and Trichlorooctadecylsilane ($CH_3(CH_2)_{17}SiCl_3$) abbreviated as 18C+Cl in the present study, all purchased from *Sigma-Aldrich Company* and used as-received without any further purification. The molecular structures of 8C, 18C and 18C+Cl are presented schematically in Figure 3.1. The chemical baths used for coating preparation contained 1% (V/V%) of as-received octadecyltrimethoxysilane, triethoxy(octyl)silane and trichlorooctadecylsilane. The solvent was iso-propanol with and without adding deionized water [172, 270-272]. In the case of adding deionized water, the solvent was iso-propanol/water (9 : 1 V/V). All the coating protocols applied in this study are broadly used by others and their description can be found in greater detail elsewhere [270-272]. The immersion time in deposition baths was also vary for different treatments to trace any effects of immersion time and the solvent (explained in details in the next chapter). The isopropanol used in the cleaning and sell-assembling process was ACS grade purchased from EMD® with water content of <0.2%. After sample coating and prior to tests, all the coated samples were removed from the solutions then rinsed with copious amounts of the relevant solvent, iso-propanol, and rinsed ultrasonically for 5s in the solvent followed by

blow-dried with N_2. Prior to surface characterization, they were finally post-dried in oven in air at 80 ^{o}C for 3 h and then at 50 ^{o}C for 5 h to remove any volatile components or residual solvents and to improve layer cross-linking with good barrier properties [172, 270-272].

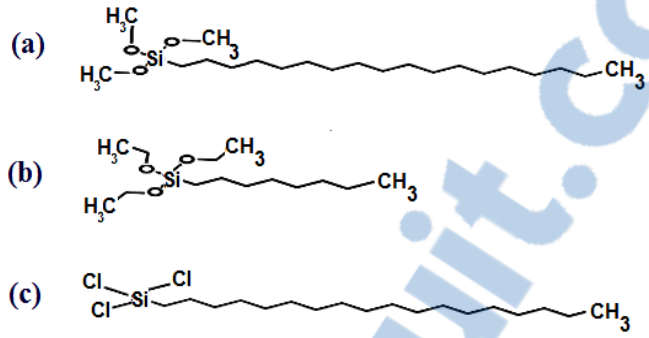

Fig.3.1. Chemical structure of a) Octadecyltrimethoxysilane *(18C)*, b) Triethoxy(octyl)silane *(8C)*, and c) Trichlorooctadecylsilane *(18C+Cl)*.

Each sample was prepared as four duplicates to test the reproducibility of its properties and performance. The results shown later thus present average values measured for four samples, unless otherwise explained. Millipore water with resistivity of ~18 Ωcm was used to prepare aqueous solutions obtained by passing distilled water through an ion exchange resin unite of Barnstead E-pure model system. In case of diluted deposition baths, prior to use, they were vigorously stirred at room temperature to allow for dissolution and/or hydrolysis processes according to the following reactions.

$$R\text{-}Si(OMe)_3 + 3\ H_2O \rightarrow R\text{-}Si(OH)_3 + 3\ MeOH \qquad \textbf{3.1}$$

$$R\text{-}Si(Et)_3 + 3\ H_2O \rightarrow R\text{-}Si(OH)_3 + 3\ EtOH \qquad \textbf{3.2}$$

Alkylsilanes, indeed, covalently react with surface hydroxyl groups of the Al surface forming Al-O-Si bonds while releasing H_2O or HCl as a by-product [172, 270-271]. However, in the case of Trichlorooctadecylsilane in the hydrolysis step of the *SAM*s configuration process, the chloride ions (Cl^-) are released to form hydrochloric acid (HCl). This reaction can be expressed by the following general scheme [250]:

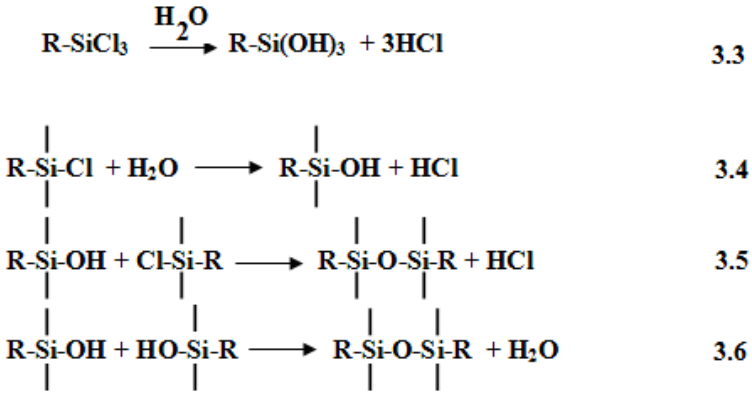

This hypothesis was also confirmed by measuring the pH values of prepared solution that was around 2. Such coatings were formed on AA substrates alone known as single layer coating system or in combination with anticorrosive under layer, explained in the following subsection, and called double layer coating systems in the present study. The initial CA of the prepared samples were measured immediately after organosilane-based deposition.

3.2.2.2 Preparation of Anticorrosive Coatings (Under Layer)

A liquid phase method was used to fabricate under layer(s) as a facile and cheap approach. A smooth under layer was first prepared and then coated with a top monolayer following the same protocol as described above for the alkylsilane single layer samples. The candidate thin layer tested as anticorrosive under layer was organosilane coupling agent of bis-1, 2-(triethoxysilyl) ethane (BTSE, $C_{14}H_{34}O_6Si_2$)) following *SAMs* coating process and the method previously reported by others [52, 229, 258, 261, 262]. In order to provide a maximum amount of silanol groups and consequently, the highest surface density of hydroxyl groups, the pH was kept in the range of 4.5–5.0 [52]. A 4.0% (V/V) BTSE bath was used. The solvent was methanol iso-propanol/water (9 : 6 V/V) and the solution stirred for 5 hrs. Polished and cleaned AA2024 samples were dipped into the BTSE solution for ~100 s [51, 52, 229, 261, 262] at room temperature followed by blow-drying in N_2 gas flow prior to use for silane deposition as an under layer. This offers a practical compromise between silane hydrolysis and condensation,

leading to improved stability of the solution [48, 51, 52, 172, 258]. The BTSE-treated samples were then immersed into selected top layer bath solution (*see section I*) for different immersion times of 1, 5, 15, 30, 60 min, and 5 hours. This series is further denoted as BTSE/alkylsilane coatings. Subsequently, they were annealed in ambient atmosphere at 80 ^{o}C for ~3h to remove any volatile components or residual solvents. These samples were annealed for a further 2 h at 80 ºC to assure all possible poly-condensation in the coatings.

3.3 Chemical, Structural and Aging Characterization

In the present study, surface characterizations and analysis were carried out to investigate the morphology, chemical composition and stability of the prepared coatings.

3.3.1 Morphological Analyses

The surface morphology of bare and coated samples was characterized and analyzed with a Scanning Electron Microscope (SEM) and an Atomic Force Microscope (AFM).

3.3.1.1 Atomic Force Microscopy (AFM)

An atomic force microscope (Veeco) was used to characterize and analyze the surface morphologies of the coated samples (Fig.3.2). In fact, the AFM technique is a very high-resolution type of scanning probe microscopy (SPM), with demonstrated resolution on the order of fractions of a nanometer. Using an AFM, it is possible to measure a roughness of a sample surface at a high resolution. Examples of complementary technologies of the AFM include optical microscope or electronic microscope. To generate the three dimensional (3-D) AFM images, the tapping mode method was used. Conditions were at room temperature under normal air pressure. In this mode, a swing silicon probe (Nanosensors™) designed an image in the topography of the surface. Changes in the cantilever oscillation amplitude were monitored while scanning the surface. A typical tip radius of such AFM probe is less than 10-15 nm and with a

length of 10-15 μm set on a cantilever. AFM images reported in the present study were gathered in various scales from 1 μm ×1 μm to 20 μm ×20 μm with a scan rate ranging from 0.5 to 1 Hz.

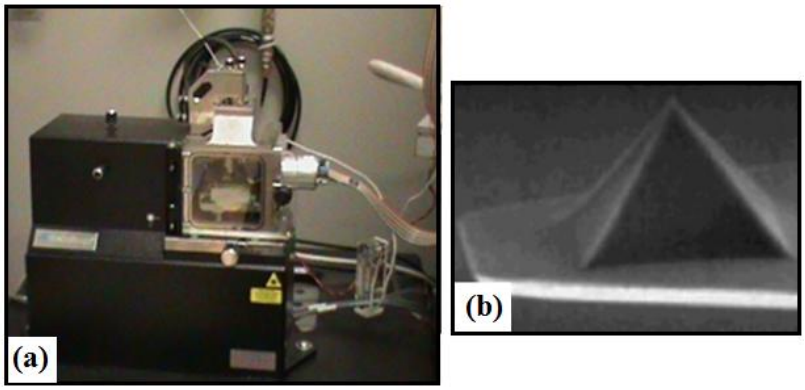

Fig.3.2. (a) Atomic force microscope (AFM) and (b) Silicon nitride probe fixed on cantilever.

3.3.1.2 Scanning Electron Microscopy (SEM)

Scanning electron microscopes together with an energy-dispersive X-ray spectrometer (SEM/EDX) were used to study the morphologies of coated surfaces with their surface chemical composition with accelerating voltages from 500 V to 20 kV (Fig. 3.3). This SEM microscope provides high beam brightness and high resolution images in high magnifications. Before each measurement, samples with low surface conductivity were covered with a very thin film of platinum or carbon to lessen charge build-up *(surface charging effects)* during the scanning. A 20 kV beam was generally used during scanning with magnifications of up to ×1000. Scanning electron microscope was also used to characterize the surface features and microstructures before and after the corrosion tests. SEM measurements (Hitachi FEGSEM-SU 70) in high-vacuum mode) produce a two dimensional (2D) image of the morphological features of the surface in addition to providing the atomic composition of the material by means of energy dispersive X-ray spectroscopy.

Fig.3.3. Image of scanning electron microscope (SEM) used in the present study (ATC lab).

3.3.1.3 Optical Profilometry and Optical Microscopy

Since the AFM technique is an efficient and useful approach to study surfaces with nano-scale roughness features, however, it is complicated to have an appropriate image in the case where there are micro-sized features on a substrate surface. The surface morphology and microstructures of samples before and after corrosion tests was characterized using an optical profilometer machine (STIL confocal profilometer (CHR 150-L) equipped with an optical pen MG140 in CTA laboratory) and optical microscope (CLEMEX JS-2000) (Fig. 3.4). The optical profilometer uses a high resolution non-contact sensor and facilitates the examination of opaque as well as highly reflective surface finishes. Stereomicroscope images were obtained from a Leica Model MZ16 microscope equipped with a camera (Leica Microsystems, Bannockburn, IL, USA).

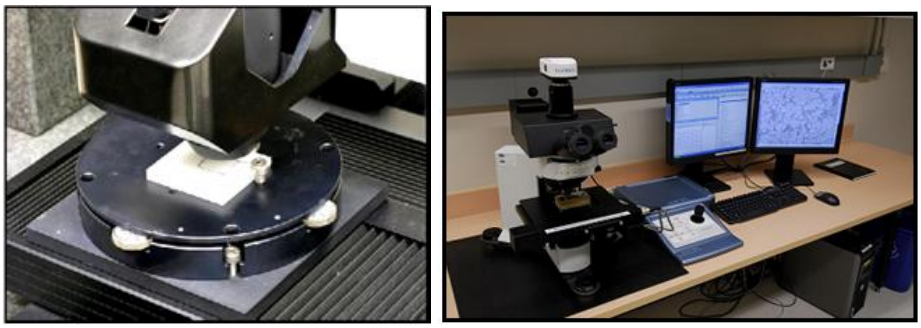

Fig.3.4. Optical profilometer **(left)** and optical microscope **(right)**, NRC-ATC laboratory.

3.3.2 X-ray Photoelectron Spectroscopy (XPS)

A variety of chemical compositions on coated Al surfaces were identified and analyzed by X-ray photoelectron spectroscopy (XPS). The XPS measurements were performed with a Quantum-2000 instrument from PHI and Staib Instruments from GmbH (Germany) and Plasmionique (Canada) (Fig. 3.5) in a UHV system. A monochromatic Al K-α radiation was the X-Ray source (1486.6 eV) produced by electron of 15 kV and P = 400W divergent beam in the case of Quantum-2000 instrument. Emitted photoelectrons were detected by a multichannel detector at a take-off angle of 90^{o} relative to the surface and no ion etching. During analysis, the base pressure was less than 10^{-9} mbar. X-ray photoelectron spectroscopy is a quantitative and semi-qualitative spectroscopic technique that analyzes surface chemical composition for a thickness as low as a few nanometers. In the case of Staib Instruments GmbH, the X-ray source was Mg K polychromatic which operated at anode voltage of 15 kV and P = 300W. The analyzed surface area was 4×4 mm^2 and 2×3 mm^2 with a depth of 6-10 nm.

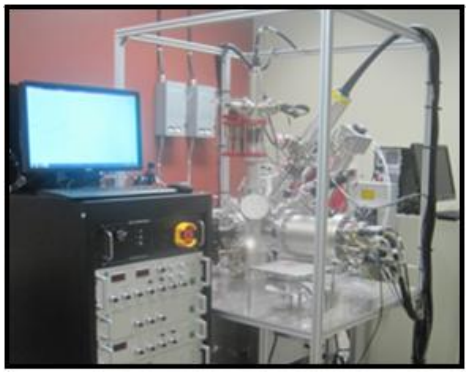

Fig.3.5. X-ray photoelectron spectroscopy (XPS) instruments, CIGELE laboratory.

The overview (*Survol*) measurements were done at Pass Energy of 100 eV, measurement step of 1.0 eV and time/step of 100 ms. For high resolution spectra, the Pass Energy was 20 eV, measurement step of 0.1 eV and the time/step was 50 ms. For each sample, high resolution scans for Al 2p, C ls, O ls and Si 2p were recorded. For each element, the number of scan was adjusted in order to get a good ratio signal/noise. Meanwhile, during the analysis of the XPS data, the peaks position has been calibrated according to the C-C peak of C1s spectrum at 284,6eV.

3.3.3 Optical Emission Spectrometer

Prior to tests, the chemical composition of Al alloy used in the present study was in addition validated by using ARL™ 4460 Optical Emission Spectrometer (Fig. 3.6) available at NRC-ATC, Canada. The results were obtained in accordance with 2024AD-C107 standard for AA2024 [273]. The optical emission spectrometer provides outstanding analytical performance for both alloying and trace elements in metals. The ARL 4460 Optical Emission Spectrometer can analyze a particularly wide range of metals, up to 60 elements simultaneously, in about 50 seconds, with excellent detection limits, reproducibility and accuracy.

Fig.3.6. ARL 4460 Optical Emission Spectrometer, NRC-ATC laboratories.

3.3.4 Ellipsometry: Coating Thickness Measurement

The coating thickness was measured by RC2 UV-VIS-NIR ellipsometer from J.A. Woollam Co. using focusing probes in order to decrease the spot size (~200 microns) and to reduce depolarization of light. It is a dual ellipsometery compensator equipped with QTH/D2 lamps and a CCD detector. Wavelength range of the instrument was 190-1700 nm; however, the 400-1700 nm was used as useable range in the current study due to depolarization. The incidence angles of 25, 30, 35, 55 and 65 degrees were selected in order to further reduce depolarization. The bare Al was modeled as a semi infinite material and the optical constants were fitted with a Kramers-Kronig-consistent spline model. For coated samples, the optical

constants of the Al substrate were fixed to those of bare Al, and only the properties of the *SAM* layer were fitted (thickness and optical constants). The *SAM*s layer was fitted with the Cauchy dispersion. The Cauchy parameters were fitted only for thick layers (>10 nm).

3.3.5 Wettability Tests

The wetting behavior, hydrophobicity and/or hydrophilicity, of the prepared coatings were assessed on a contact angle goniometer following standard procedures by measuring the water contact angle (CA) (Fig.3.7). The contact angle measurements were performed on a fully automated contact angle goniometer, DSA 100, a drop shape analyzer system from Krüss GmbH Co. Contact angles and surface energy were measured using the sessile-drop method. Small water droplets (4 µL in volume) and feed rate of 195 µl min-1 were quietly placed on the surface by an injection mechanism with several convenient syringes, as shown in Fig.3.7 (inset). Another important advantage of the software is to calculate the surface energy by using appropriate techniques. To investigate changes in surface energy upon a prepared coating, water and formamide were used as probe liquids. Surface energy parameters of the probe liquids are the total, dispersive and polar components of the probe liquid surface free energy.

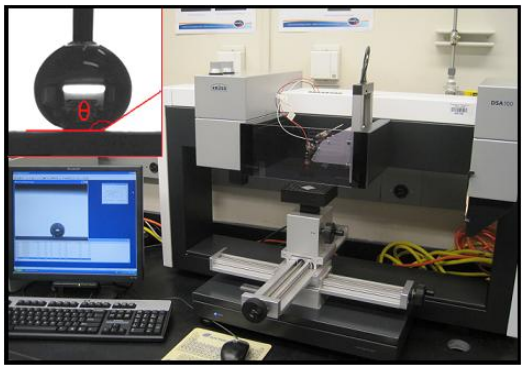

Fig.3.7. Contact angle goniometer (DSA100, Krüss), NRC-ATC and CIGELE laboratories. (Inset: a static CA measured).

The components of the total surface free energy for the prepared coatings were determined from the Owens and Wendt equation. For each sample, contact angle measurements were made on at least five diverse randomly selected spots on a surface. In the case of

superhydrophobic surfaces, the dynamic contact angle or contact angle hysteresis (CAH) value, the difference between the advancing (θ_A) and receding (θ_R) contact angles, as shown in Fig.3.8, can be measured by applying a standard experimental approach to the asymmetric water drops using the tangent-2 method [274, 275].

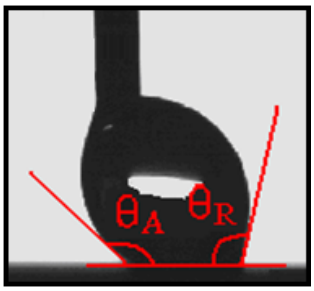

Fig.3.8. Advancing and receding CAs on a sample with a high hysteresis (advancing (θ_A) and receding (θ_R) CAs).

3.3.6 Ice Accretion Tests

Various methods have been introduced and developed so far to measure ice adhesion, but some of them are not applicable for the atmospheric ice formed by the freezing of the super-cooled water drops in contact with structures. In this series of experiments, the ice accumulation conditions were generated in the CIGELE laboratories. The wind tunnel was adjusted and maintained under conditions similar to those in nature which lead to glaze ice accretion during freezing rain, as shown in Figure 3.9. The atmospheric icing wind tunnel was based on injection of room temperature water through three warm nozzles into a cold air stream provided by three nozzles on the spray line [276-279]. The glaze ice was accumulated on coated samples in a wind tunnel at subzero temperature (-10 ± 0.5 ^{o}C) and with adjusted wind velocity, water pressure, air pressure and liquid water content (*LWC*) values to l0 ± 0.1 m s^{-1}, 300 ± 15 kPa, 100 ± 0.1 kPa and ~6.3 gm^{-3}, respectively, to simulate the atmospheric glaze ice created on surfaces in nature. The samples were first placed in a wind tunnel to build up a given thickness of glaze ice accretion by spraying super-cooled micrometer-sized water droplets (average size (*MVD*) of ~63.7 µm). Prior to icing, all samples were placed in the tunnel for approximately 8 to 10 min to cool down.

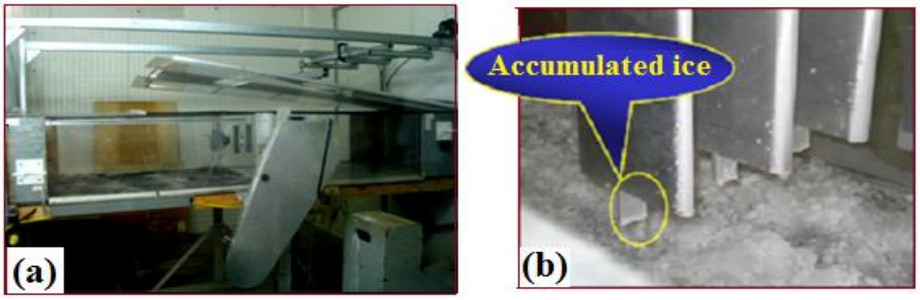

Fig.3.9. (a) Top view of wind tunnel and (b) a view of ice accumulations in the tunnel.

3.3.6.1 Calculation of Ice Adhesion

As a final point, the adhesion of ice to the coatings was tested on the relevant surfaces in order to find out what parameters govern these properties. This series of ice-adhesion evaluation tests was conducted on Al beams with artificially iced samples spun in a home-made centrifuge apparatus and placed in a climatic chamber at -10 ± 0.5 °C [280]. The centrifuge test machine can accelerate an iced sample beam from 0 to 5500 rpm with an acceleration rate of ~300 $rpms^{-1}$ [245]. The samples attached to the beams were iced by freezing drizzle in a wind tunnel at a fixed air temperature of -10 ± 0.5 °C in order to prepare glaze ice of 3 to 5 g weight over the sample area of ~3.2 cm × 3.0 cm on an Al beam. The artificially iced samples were spun in the centrifuge placed in a climatic chamber at -10 °C to determine the rotational speed at which ice detachment from the sample surface occurred. To balance the beam in the centrifuge, a counter-weight was used on the opposite side, as shown in Figure 3.10.

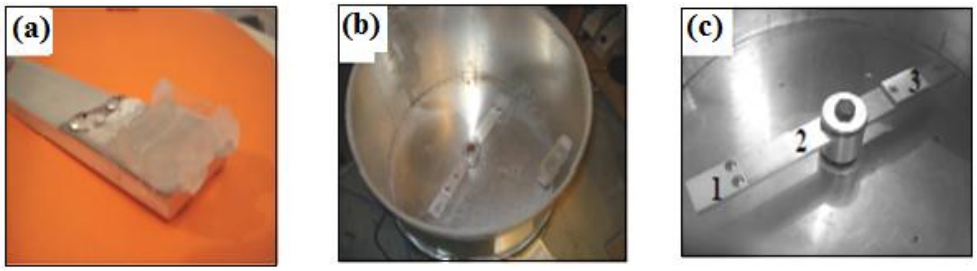

Fig.3.10. (a) Sample covered with artificial glaze ice, (b) centrifuge adhesion test machine, and (c) sample with coating in centrifuge set-up measuring ice adhesion where (1) sample, (2) aluminum beam, (3) counter-weight.

Rotation generates a centrifugal force and when this force is larger than adhesion force of ice, the ice detaches from the sample. At the moment of detachment, the adhesion strength of ice is assumed to be equal to the centrifugal force as $F = mr\omega^2$, where m is the ice mass (kg), r is the beam radius (m) and ω is the rotation speed (rad s^{-1}). The shear stress, correspondingly, was calculated as $\tau = F/A$, where A is the apparent de-iced area of the sample surface (m^2) and F is ice adhesion strength (N). To reduce the influence of potential experimental errors, the adhesion reduction factor (*ARF*) was used rather than absolute values of shear stress. The *ARF* factor is calculated as the ratio of the shear stress of ice detachment on bare Al to that observed on coated samples as $ARF = \tau_{(\text{bare Al})}/\tau_{(\text{coated Al})}$ provided that all the tests**,** for both uncoated and coated samples**,** were run under identical conditions. The *ARF* of bare Al is 1. Further experimental details and procedure description can be found elsewhere [2, 172, 280].

3.3.7 QUV Accelerated Weathering Tester

Several tests were performed to determine the durability, aging behavior and degradation of the different coatings. In brief, sunlight is considered among serious reasons in damage of material surfaces and ultraviolet light has been documented as the cause of most of this damage. Degradation due to UV illumination was assessed using accelerated tests with the QUV/Accelerated Weathering Tester in accordance with ASTM G154, which was among the equipment acquired by CIGELE (Fig. 3.11). This machine was used to simulate damaging outdoor conditions in a controlled laboratory environment. The QUV tester irradiance is 75 % higher than noon summer sunlight [281]. The coated samples were exposed to a UVA-340 fluorescent lamp. The test cycle was 8 hrs at the conditions 0.89 W m^{-2} irradiance and temperature of 60 ºC in the QUV tester following 4 hrs of condensation at 50 ºC in absence of UV exposure. Its programmable methods meet the standard of different organizations *(ASTM, ISO, DIN, etc.)*. It is worthy to highlight the fact that almost each 537-h of artificial UV exposure is equal to one year of sunlight exposure [255, 282].

Fig.3.11. QUV accelerated weathering tester apparatus, CIGELE laboratory **(left)** and inside of sample chamber **(right)**.

3.3.8 Electrochemical Measurements

Potentiodynamic polarization was used to examine the corrosion behavior of bare and coated Al samples. A 300 cm^3 - EG&G PAR flat standard three-electrode cell (London Scientific, London, ON, Canada) was used as the working cell. The exposed surface of working electrode (bare or coated Al sample) was 1 cm^2, if not otherwise mentioned. In the three-electrode system, platinized platinum grid, saturated calomel electrode (*SCE*) and sample were used as counter (CE), reference (RE) and working (WE) electrodes, respectively (Fig. 3.12). Prior to potentiodynamic polarization (PDP) and electrochemical impedance spectroscopy (EIS) measurements, samples were immersed in the solution for 1 to 2 hours in order to reach a steady open circuit potential (E_{ocp}). Prior to test, air bubbled blown through the head space of the electrochemical cell for 30 min before starting the data collection to ensure steady-state conditions. Meanwhile, magnetic stirring was employed at cell bottom to increase mass transfer at the electrode surface. The set-up used to perform the electrochemical measurements was a potentiostat/galvanostat system composed of a *Solartron analytical 1252A* frequency response analyzer (FRA) coupled to a *Solartron SI 1287A* electrochemical interface and were controlled by Corrware® software. Measurements were performed in 3.5% NaCl solutions (ACS crystalline grade 100%, Fisher Scientific®) at room temperature [ASTM47]. Potentiodynamic polarization curves were established and the corrosion potential (E_{corr}), corrosion current density ($j_{corr.}$) and polarization resistance (R_p) were determined using the Tafel extrapolation method

(Fig.3.13).

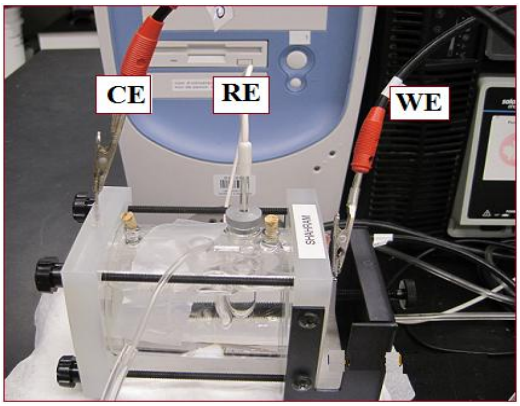

Fig.3.12. Three-electrode flat cell (NRC-ATC lab) used in the present study for electrochemical measurements.

The polarization was started from 250 mV below the open circuit potential *(OCP)* in the cathodic region, through the corrosion potential, and 250 mV above the open circuit potential in the anodic region at a constant rate of 1 mVs^{-1}. Polarization resistance is defined as the slope of the potential-current density curve at the OCP, yielding the polarization resistance (R_p) that can be related to the corrosion current by the Stern-Geary equation [202]:

$$R_P = \frac{1}{(2.3 i_{corr})}\left(\frac{\beta_a \beta_c}{\beta_a + \beta_c}\right) \qquad \textbf{3.10}$$

Where

- R_p is polarization resistance (Ω)
- I_{corr} is corrosion current density (A)
- β_c is the cathodic Tafel slope
- β_a is the anodic Tafel slope

The slopes of log ($i_{corr.}$) *vs.* E_{corr} diagram are determined as the cathodic slope (β_c) and the anodic slope (β_a). The cathodic slope contains information concerning the kinetics of the reduction reaction occurring for a particular system. The particular features of the anodic slope depend strongly on the metal electrolyte system.

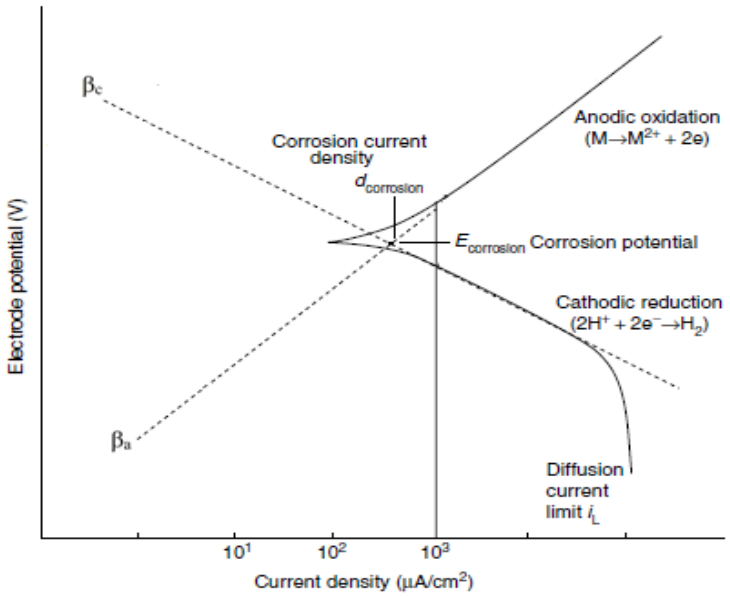

Fig.3.13. Schematic presentation of cathodic and anodic polarization curves of a metal in the active state in a reducing acidic solution [202].

Potentiodynamic polarization values reported in the present study are the average of three to four separate measurements to guarantee the reliability of the results. Decrease in $j_{corr.}$ and increase of R_p in case of coated Al surface suggests reduced corrosion rate of Al, which normally accelerates in aggressive and humid environments or even attachment of bacteria. The electrochemical impedance spectroscopy (EIS) plots and fitted results of surfaces immersed in NaCl solution were used as a final step of electrochemical investigation. More precisely, the corrosion behavior of coated samples were further studied by EIS analysis scanned around OCP at a steady-state with sine-wave (sinusoidal) amplitude of 10 mV perturbation over the frequency range from 100 kHz to 0.1 Hz. In general, impedance spectra are analyzed using an equivalent circuit, taking into account the contribution of each phenomenon, such as electrical double layer, film formation etc. EIS was performed using a three-electrode configuration. The reference electrode was a saturated calomel electrode (*SCE*) and the counter-electrode consisted of a platinum grid electrode. The SCE is relatively stable, inexpensive, and easy to set up and has a well-known electrode potential which used in general aqueous electrochemistry. The SCE is a reference electrode based on the reaction between elemental mercury and mercury (I) chloride (Hg_2Cl_2, "*calomel*") and the aqueous phase in contact with them is a saturated solution of KCl in water. Pt is un-reactive for most purposes and although Pt is expensive, a small wire

is adequate for many purposes.

3.3.9 Cyclic Corrosion Exposure Testing (*CCT*)

Anti-corrosive performance of modified and unmodified Al samples was further investigated by *Cyclic Corrosion Exposure Testing*. A programmable cyclic corrosion test chamber *(Ascott)*, often abbreviated to "***CCT***", was used to reproduce cyclic fog at controlled temperatures and humidity (Fig. 3.14). The cyclic corrosion test chamber, available at NRC-ATC, was used to evaluate and study the prepared coating stability in harsh conditions in accordance with International Organization for Standardization ISO14993:2001 "*Corrosion of metals and alloys-Accelerated testing involving cyclic exposure to salt mist, dry and wet conditions*" (Fig. 3.15). The Al panels (two panels for each) were placed into cyclic corrosion chamber with unmodified side protected by scotch tape and the modified surfaces exposed alternatively to salt mist, dry and wet conditions in accordance with ISO14993 [271]. Test specimens were placed in an enclosed chamber and exposed to a changing climate that comprises of the three repeating cycles as follow:

1) 2hrs exposure to a continuous indirect spray of neutral (pH: 6.5-7.2) salt water solution, which falls-out on to the specimens at a rate of 1 to 2ml/80cm²/hour, in a chamber temperature of 35 ^{o}C.
2) 4 hrs of air drying in a climate of >30 %RH at 60 ^{o}C, and
3) 2 hrs exposure to a condensing water climate (wetting) of 95 to 100 %RH at 50 ^{o}C.

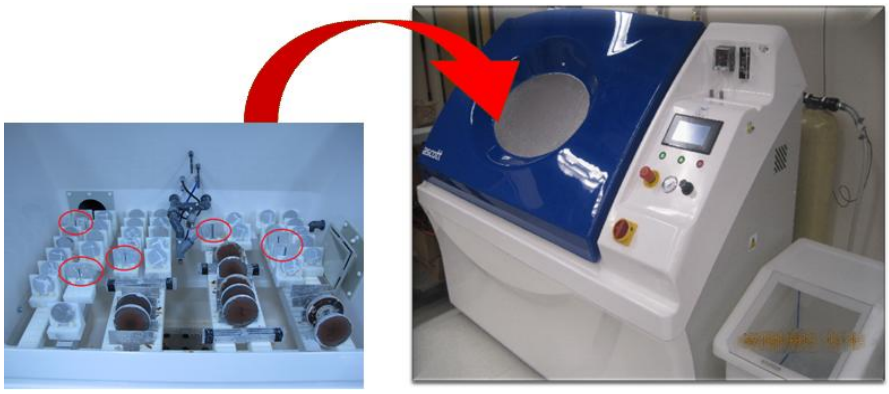

Fig.3.14. A programmable cyclic corrosion test chamber (*Ascott*), NRC-ATC.

3.4 Conclusion

In this chapter, different methods and techniques for preparation and characterization of single and double layer coatings were presented in detail. The hydrophobic and icephobic properties of the prepared samples are measured via CA goniometer and centrifuge adhesion test machine, respectively. The chemical composition of the prepared coatings was studied by XPS analysis. To study the morphology and topography of such prepared coatings, the SEM, AFM and profilometer techniques were used. Their durability was studied by using the QUV tester apparatus. Potentiodynamic polarization was used to examine the corrosion behavior of samples. Finally, their anti-corrosive performance was investigated by Cyclic Corrosion Exposure Testing.

CHAPTER IV

HYDROPHOBICITY, ICEPHOBICITY AND STABILITY OF SINGLE LAYER *SAM*s COATINGS

4.1 Introduction

The objective of this chapter is to study and discuss in detail the effect of different parameters such as immersion time, alkyl length, pre-/post-treatments etc. on prepared coatings as well as to characterize the hydrophobic and icephobic properties of low-surface energy self-assembled monolayer/multilayer thin films on Al alloy 2024. However, the corrosion resistance of such coatings will be discussed in detail in the following chapter.

4.2 Sample Preparation and Effect of Different Pre-/Post-Treatments

Briefly, the mechanically polished AA2024 substrates were cleaned and degreased in organic solvents followed by cleaning in a *Turco Redoline 53D* alkaline solution. The cleaned surfaces were then blow-dried in N_2 gas flow and were kept in oven at 80 °C for 3 hrs. They were then placed in baths with different chemical composition. Different *SAMs* coatings with dissimilar alkyl length and chemical structures have been prepared on Al substrates controlled by a trace of water through liquid phase method. The chemical bath deposition method has been recently used extensively for the purpose of preparing uniform thin films on flat substrates. Even though a number of organic coatings [21-23, 38-40, 42, 45, 172, 173, 190-192, 194, 245, 246] were previously examined in this laboratory, however, the systematic study of their hydrophobicity and stability under different conditions or UV irradiation and their anti-corrosive performance have not yet been undertaken. This research work was hence conducted to investigate these properties on coated AA2024 in details. A solution of as-received

octadecyltrimethoxysilane (18C), triethoxy(octyl)silane (8C) and trichlorooctadecylsilane (18C+Cl) in iso-propanol, with and without adding deionized water were prepared. All details of possible effect of pre-/post-treatment including immersion time in corresponding deposition baths on coating properties can be observed clearly in Tables 4.1 to 4.3. In the case of diluted deposition bath, the baths, prior to use, were vigorously stirred at room temperature for different time intervals, i.e. 5, 30, 60, 120 and 180 min, to complete the dissolution and hydrolysis process as much as possible.

4.3 Effects of Immersion Time and Alkyl Chain Length

As it is evident, by increasing alkyl chain length as well as water content of the reaction system, the surface properties were changed too. Indeed, the hydrolysis/condensation reactions were catalyzed by the amount of water added to the chemical bath solutions. However, for the rest, it was catalyzed by a trace quantity of water in solvent or by moisture in the air. The difference mainly arises from the pre-treatment method adapted and the various immersion times employed for the *SAM*s formation. Indeed, a review of the literature indicates that by increasing the immersion time, the efficiency of formation of *SAM*s on a surface can be described in terms of surface coverage. Therefore, the immersion time parameter plays a significant role in the self-assembly process [247-249]. Figures 4.1 and 4.2 illustrate the contact angle (CA) values of sample surfaces coated with 8C-*SAM*s, 18C-*SAM*s and 18C+Cl-*SAM*s immersed for 15 min and 60 min in their corresponding diluted and non-diluted baths, respectively. The CA values as well as free surface energy of the same coatings are presented in Table 4.2. It is evident that the contact angle values obtained for samples immersed for 15 min in their corresponding diluted solutions were bigger than those obtained on 60 min non-diluted solution baths. This is, of course, due to effect of water added to the chemical baths (diluted solutions) in catalyzing the hydrolysis/condensation reactions. It is obvious that Al samples coated with different alkylsilanes demonstrated improved hydrophobicity when immersed in water-diluted solution and in a shorter period of immersion time. At the same time, the contact

angle values in both cases increased in the following order: 18C+Cl *SAM*s > 18C-*SAM*s > 8C-*SAM*s. Different immersion times of 1 min to 120 min was also used for both water-diluted and non-diluted solution baths; however, the contact angle values corresponding to immersion times of 60 min and 15 min along with alkaline pre-treatment were the biggest ones, demonstrating improved wetting properties on Al substrates. In fact, complex surface chemistry of crystalline metallic substrate of Al definitely brings some significant effects on the molecular *SAMs* process and hence, on the properties of the resulting thin films, as it is evident in Tables 4.1-4.3 (CA and surface energy).

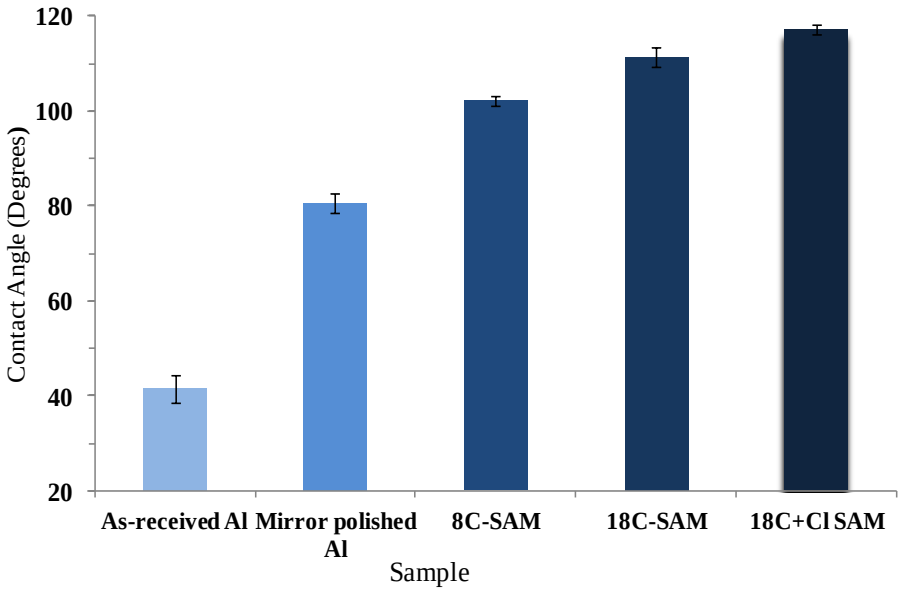

Fig.4.1. Contact angle values (deg.) of prepared samples, immersed for 15 min in the corresponding diluted solutions.

Table 4.3 demonstrates how increasing the stirring time influences the wetting characteristics of different prepared coatings. When the stirring time increased from 5 to 120 minutes, the contact angle values of all dip coated samples increased. More precisely, the contact angle values obtained for 8C-*SAMs*, 18C-*SAMs* and 18C+Cl *SAMs* coatings after 120 min of stirring were 102.5 ± 1^{o}, 112.1 ± 1^{o} and 117.3 ± 2^{o}, respectively. However, a remarkable enhancement of contact angle values was observed for 18C-*SAMs* and 18C+Cl *SAMs* coatings (112.1 ± 1^{o} and 117.3 ± 2^{o}).

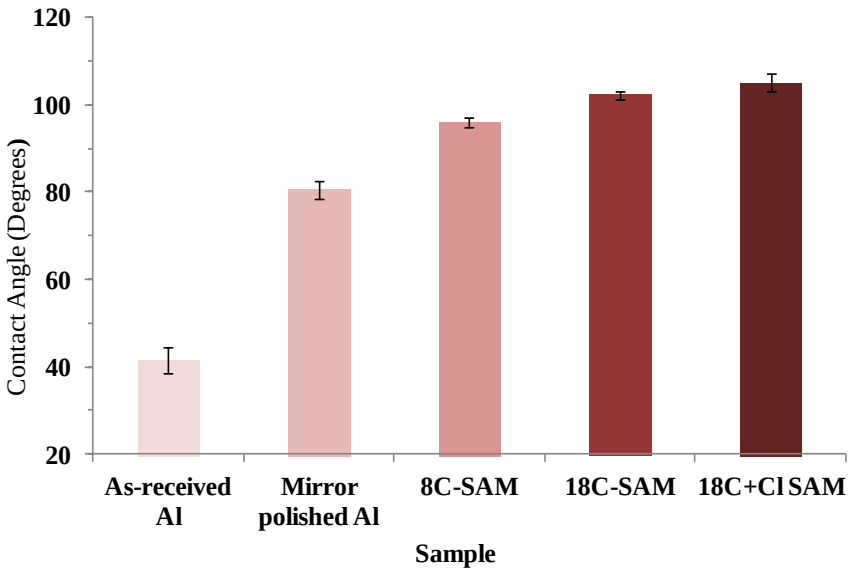

Fig.4.2. Contact angle values (deg.) of prepared samples, immersed for 60 min in the corresponding non-diluted baths.

It is also important to highlight the fact that the contact angle for all *SAM*s coated samples did not changed significantly when they were immersed for a longer period of time (e.g. 180 min). Therefore, the observed results concerning the wetting properties of such *SAMs* coatings are probably due to well-ordered *SAMs* fabrications on a well-immersed Al oxide layer [32, 250].

Table 4.1. Different coating treatment applied for self-assembling on AA2024 substrates (8C-*SAMs*, 18C-*SAMs* and 18C+Cl *SAMs* coatings).

Sample No.	**1**	**2**	**3**	**4**	**5**	**6**	**7**	**8**	**9**
Immersion time in non-diluted bath (min)	1	15	30	60	120	1	30	60	120
Immersion time in diluted bath (min)	1	15	30	60	120	1	30	60	120
Alkaline pre-treatment	+	+	+	+	+	-	-	-	-

Meanwhile, the effect of stirring time of alkylsilane solutions on coating wettability was also examined, demonstrating enhanced CA in the case of samples immersed in the 120-min-stirred solution in advance in all three samples (Tables 4.1-4.3). A few samples were immersed in such baths overnight, however, no significant change in sample contact angle was observed.

Table 4.2. Contact angle and free surface energy [ε (mNm^{-1})] of AA2024 coated with different self-assembled organosilanes.

Surface treatment / Experimental conditions	As-received AA2024	Mirror polished AA2024	8C-*SAM*s	18C-*SAM*s	18C+Cl *SAM*s
Immersed for 60 min in non-diluted bath	------	------	96 ± 1° ε: 16.12 (±0.62)	102.3 ± 1° ε: 12.09 (±0.60)	105.1 ± 2° ε: 10.12 (±1.19)
Immersed for 15 min in diluted bath	------	------	102.2 ± 1° ε: 12.14 (±0.60)	111.4 ± 2° ε: 6.03 (±1.14)	117.1 ± 1° ε: 4.77 (±0.54)
No *SAM*s coating	41.5 ± 3° ε: 46.36 (±1.64)	80.6 ± 2° ε: 23.27 (±1.25)	------	------	------

For an in-depth study of prepared *SAM*s coatings that can suitably interpret the obtained results, other characterization techniques were used, including surface energy calculation, SEM, and XPS analyses of these coatings. This will be presented in the following sections.

Table 4.3. Contact angle and free surface energy [ε (mNm^{-1})] values of flat AA2024 (AA2024) samples coated with different *SAM*s *vs.* stirring time.

Stirring time (min) / *SAM*s coating	5	30	60	**120**	180
18C - *SAM*s	95.4 ± 1° ε: 16.32 (±0.62)	97 ± 2° ε: 15.05 (±1.23)	102.2 ± 1° ε: 12.14 (±0.60)	112.1 ± 1° ε: 5.79 (±0.57)	111.7 ± 1° ε: 6.01 (±0.57)
18C+Cl - *SAM*s	93.7 ± 1° ε: 17.19 (±0.62)	97.2 ± 1° ε: 15.03 (±0.62)	105.1 ± 2° ε: 10.12 (±1.19)	117.3 ± 2° ε: 4.76 (±1.07)	117.1 ± 2° ε: 4.77 (±1.08)
8C - *SAM*s	91.3 ± 1° ε: 19.36 (±0.62)	93.3 ± 2° ε: 17.28 (±1.24)	98.6 ± 1° ε: 14.58 (±0.61)	102.5 ± 1° ε: 12.11 (±0.61)	102.4 ± 1° ε: 12.15 (±0.61)

4.3.1 Surface Energy Calculation

Another significant investigation for the hydrophobic properties of *SAM*s coatings is the determination of surface energy values. It is well known that when the surface energy is lowered, the water repellency is enhanced [32]. The surface energy of a solid surface or a coating is a characteristic relevant to surface chemistry, depending on its chemical composition and atomic arrangements near the surface [41, 172]. Tables 4.1 and 4.3 present the surface energy values of prepared coatings obtained from contact angle measurements. As is evident, for samples immersed 15 min in diluted solutions, Table 4.1, the surface energy values are smaller than samples immersed for 60 min in non-diluted baths. Moreover, the smallest values were obtained for 18C-*SAM*s and 18C+Cl *SAM*s coatings with 15 min of immersion time, i.e. 6.03 ± 1.14 and 4.77 ± 0.54 (mNm^{-1}), respectively. However, in all cases, the surface energies are always smaller than those obtained on bare samples (no *SAM*s coating), i.e. 46.36 ± 1.64 and 23.27 ± 1.25 (mNm^{-1}) for as-received and mirror-polished AA2024, respectively.

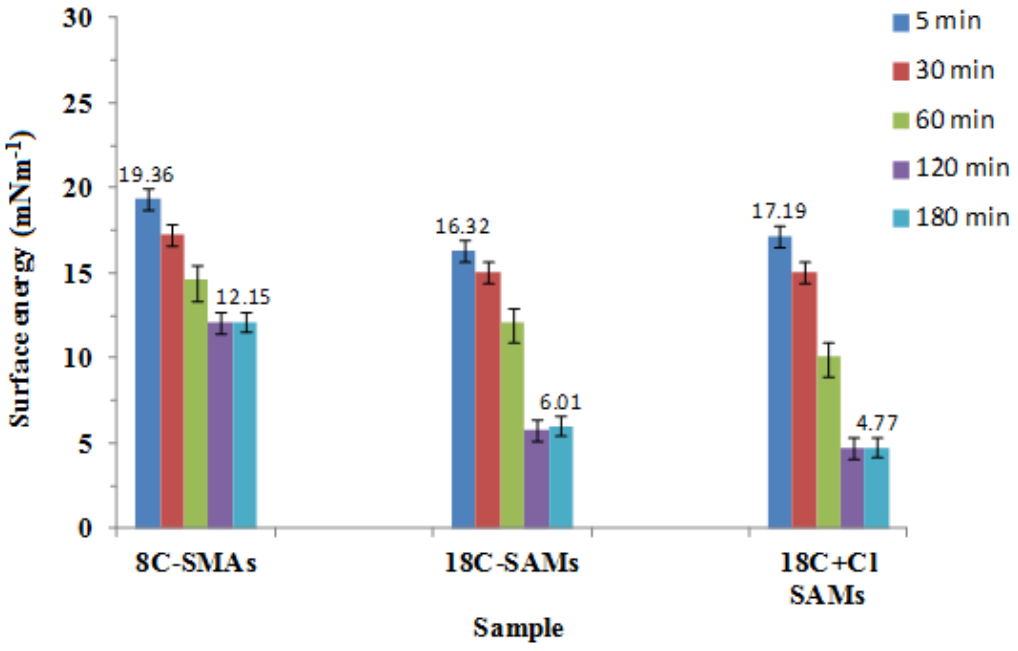

Fig.4.3. Surface energy values (mNm^{-1}) of different *SAM*s coatings on Al alloy versus stirring time (min).

Meanwhile, the surface energy values obtained for coated samples by different *SAM*s for stirring time of 120 min were, in all cases, smaller than those obtained for the others' stirring time, i.e. 12.11 ± 0.61, 5.79 ± 0.57 and 4.76 ± 1.07 for 8C-*SAM*s, 18C-*SAM*s and 18C+Cl *SAM*s on AA2024 substrates, respectively (Fig. 4.3). It can be, thus, concluded that by applying dissimilar organosilanes and pre-/post-treatments on an Al surface, the wetting characteristics of samples were affected seriously as the surface energy values changes. This is known as the "*steric effect*" which will be explained in more detail in the following section.

4.4 Wetting Property and Coating Stability

4.4.1 Study of Sample Hydrophobicity

Organosilanes can be easily grafted to a surface by chemical bond (Si-O-Al) for its hydrolysable group in molecule showing properties of low surface free energy and chemical stability. Under different conditions, organosilanes can form various geometrical structures (monolayers and cross-linked polymeric layers) on the surface [251]. As it was mentioned earlier, three dissimilar organosilanes in alkyl chain length and molecular structure were selected to evaluate effect of alkyl length on surfaces properties, e.g. wetting behavior and corrosion protection performance. When water-diluted solutions were used, the prepared coated surfaces showed larger values of contact angle compare to non-diluted coated samples. With the growth of alkyl chain length, i.e. alkyl tail of octadecyl, the contact angle also increased. It is currently showed that by using water-saturated solvent, the coated surfaces with alkylsilanes were quite flat and without nano-scale protuberances formed on the surfaces compared to non-saturated one [251]. This implies that the alkyl length plays a significant role in surface properties. It is well-known that metallic Al is extremely reactive with atmospheric oxygen, and a thin layer of Al_xO_y (~ 4 nm thickness) forms on exposed Al surface [251]. Pre-treatment of Al alloy, for instance, soaking in alkaline solution, led to the formation of a pseudo-boehmite surface layer (hydrated Al oxide, AlOOH [252]), which after post-heat treatment can transform to Al_2O_3 which is characterized by a IR band at 940 cm^{-1} [253]. Therefore, bare Al is a

hydrophilic substance with water contact angle and surface energy of ~41.5 ± 3^{o} and 46.36 ± 1.64 (mNm^{-1}), respectively. Previous studies showed that Al surface changes significantly by using different surface cleaning and treatment protocols. For example, water contact angles of 50 ^{o}, 60 ^{o} and 10 ^{o} were reported for un-cleaned, acetone-cleaned and alkaline solution-treated aluminum, respectively [172, 252, 253]. The freshly formed Al_xO_y layer on Al surface, created after exposure to air, were then reacted with silane molecules to form a covalently bound coating on Al surface. The initial contact angle values of coated samples in question were measured by means of a water contact angle goniometer. After coating deposition, all samples demonstrate initial values of contact angle, CA $\geq$ 100 ^{o} (Figs.4.4 to 4.6 and 4.7a), which indicates hydrophobic surfaces. It was also observed that without any coating, the bare and mirror polished samples display an average contact angle of 41.5 ± 3 ^{o} and 80.6 ± 2 ^{o}, respectively, indicating a relatively high surface energy. Among these three compounds, the 18C+Cl *SAM*s show the highest values of contact angle, CA: ~118 ^{o}, which is probably due to the erosion of Al substrate during *SAMs* process. The contact angles of Al samples modified by 18C-*SAM*s and 18C+Cl *SAM*s are close. In contrast, the contact angle of 8C-modified Al surface is remarkably small, suggesting a more hydrophilic surface than other two samples. This result suggests that 18C-*SAMs* formed a more closely packed self-assembled thin film on the substrate compared to the 8C-*SAMs* coating. It is also possible that 8C-*SAMs* molecules or at least some of them form a monolayer film on Al surface with alkyl chains anchored onto the substrate, and the functional moieties oriented towards the solution phase, i.e. opposite molecular orientation. Indeed, hydrolysis of -Si-X bond can lead to formation of -Si-OH bond, a fairly hydrophilic functional group. Because these polar groups are oriented away from the surface, as a result, the Al sample becomes more hydrophilic. Meanwhile, the alkyl chains or some of them are anchored on metal surface, and a multiple layer film could be eventually formed on the Al surface. Between each layer, the functional trichlorosilane or trimethoxysilane groups can polymerize together through hydrolysis and condensation reaction. This polymer network would provide extra strength to stabilize layer-to-layer interactions. It is possible to have both molecular orientations and a mixed *SAMs* film was formed through *SAMs* process.

The hydrophobic characteristics of Al substrates coated by three different alkylsilanes are summarized in Tables 4.1 to 4.3. As mentioned earlier, the contact angle of coated surfaces fabricated under condition of adding water was bigger than those without water. When diluted solution was used, the hydrophobic properties of all coated samples were increased. However, as the alkyl chain length decreased, the contact angle, and therefore, the wetting property decreased. In fact, the increase of chain length will decrease the surface energy, so that the surface hydrophobicity increased [251, 252]. Meanwhile, in diluted solution with trace of water, silanes can also react with adjacent silane molecules to form a network structure. With the increase in alkyl length, the so-called "s*teric effect*" of organosilane rises and thus decreases of organosilane activity occurs. Subsequently, the organosilane hydrolysis/polycondensation becomes more difficult causing number of organosilane molecule forming network structure turn down. Therefore, the network structure becomes thin and the corresponding contact angles decrease, with increase of alkyl length. When the aliphatic tail is small, the "*steric effect"* is dominant and when the alkyl length increases to some extents, the surface energy plays a dominant role and therefore, the contact angles increase with the growth of alkyl length. Consequently, the wettability of a sample prepared in a diluted bath is affected by both the "*steric effect"* and surface energy. In other words, by increasing alkyl chain length, the different wettability observed is due to the competition between decrease of reactivity caused by the increase of the "*steric effect"* and that of the alkyl hydrophobicity which in turn is due to difference in alkyl length [251, 252].

The initial values of contact angle (CA > 109 ^{o}) in the case of 18C-*SAM*s and 18C+Cl *SAM*s indicates well coated flat hydrophobic surfaces (Tables 4.1-4.3). It is evident that Al samples coated with different alkylsilanes showed improved wettability when immersed in diluted solution and in a shorter period of immersion time. At the same time, the contact angle values in both cases, diluted and non-diluted, increased as the following order: 18C+Cl *SAM*s > 18C-*SAM*s > 8C-*SAM*s. Therefore, it is possible to conclude that *SAMs* coating process depends strictly on pre-/post-treatment conditions. Now the question is: are these *SAM*s coatings dense enough to prevent aggressive molecules from penetrating through the coatings or not?

4.4.2 Coating Stability in Different pH Conditions

Figures 4.4 to 4.6 show contact angle values of Al samples coated with different silanes as a function of immersion time in nano-pure and tap water as well as basic and acidic media. The acidic and alkaline buffer solutions used in this study were color-coded "*Thermo Scientific™ Orion™ pH Buffers"* contained potassium hydrogen phthalate ($C_8H_5KO_4$, KHP), sodium carbonate (Na_2CO_3)/bicarbonate ($NaHCO_3$) and Methylparaben ($C_8H_8O_3$), respectively. While these samples initially demonstrated the hydrophobic property (CA $\geq$ 100 ^{o}), however, it can be observed that the contact angle values decrease over time and they lose their hydrophobic properties. In other words, the coated surfaces were found to gradually lose their hydrophobic properties completely after ~1100-h of immersion in different media, associated with considerable decrease of their water contact angle values (Fig.4.7a, b). This tendency to lose surface hydrophobic property is probably due to rupture of Si-O-Al bond between silane molecules and the Al oxide layer due to their hydrolysis.

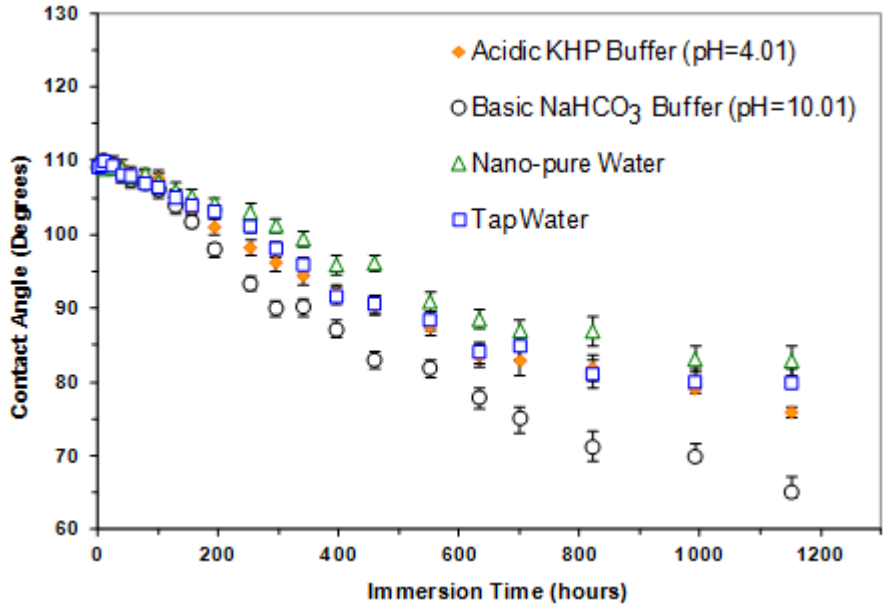

Fig.4.4. Contact angle of Al samples coated with 18C-*SAM*s *vs.*immersion time in acidic (pH=4.01), basic (pH=10.01), nano-pure and tap water. At the end of the test, the lowest and highest values of free surface energy (ε) are 21.31 (±0.63) and 33.35 (±0.63) mNm^{-1}, respectively.

Water molecules can penetrate and hydrolyze the Al-O-Si-R bond, resulting in Al-OH and RSi-OH components. Some alkylsilane tend to form monolayer films with more closely packed and ordered monolayer films, while others will result in films with more defective domains. Generally, films with less defective domains will result in a better corrosion protection of the Al substrate. Alkyl trichlorosilanes are known to undergo faster hydrolysis-condensation reaction compared to trimethoxysilanes. However, this molecule itself contains the corrosive chloride after hydrolysis. Between the two trimethoxysilane compounds, $C_{18}Si(OMe)_3$ and $C_8Si(OMe)_3$, $C_{18}Si(OMe)_3$ has a longer alkyl chain of 18 carbons, while $C_8Si(OMe)_3$ has a shorter alkyl chain of 8 carbons. This chain length difference may lead to some variations in the structures and properties of the thin films that are formed.

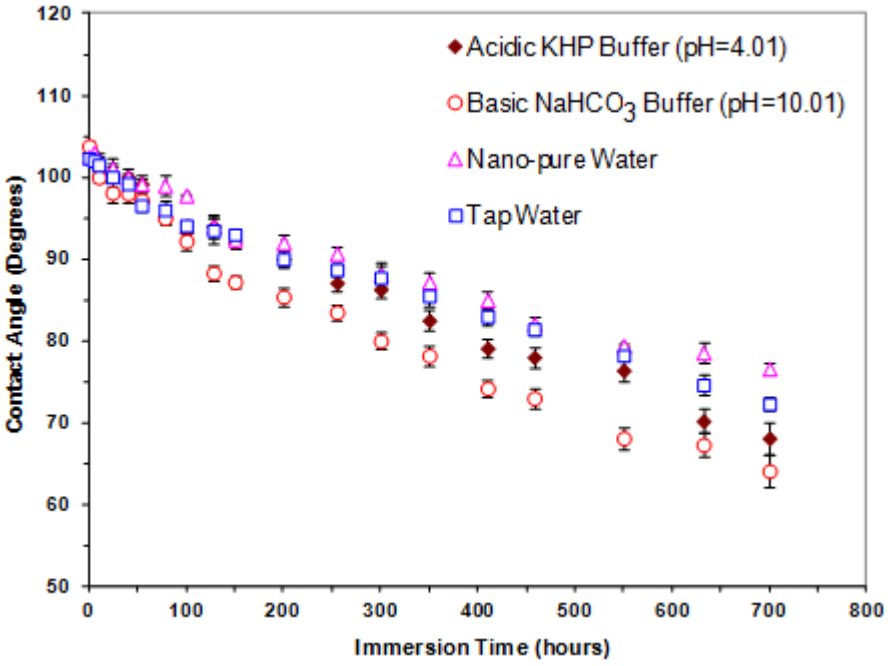

Fig.4.5. Contact angle of Al sample coated with 8C-*SAM*s *vs.* immersion time in acidic (pH=4.01), basic (pH=10.01), nano-pure and tap water. At the end of the test, the lowest and highest values of free surface energy (ε) are 24.21 (±1.23) and 32.18 (±1.25) mNm^{-1}, respectively.

Meanwhile, all three silane compounds are expected to form polysiloxane networks, since they have all three active -Si-X bonds. Packing density is expected to increase with chain length [254]. This eventually decreases the surface hydrophobicity and hence forms a

hydrophilic surface including -OH groups [49]. Hydrolysis of siloxane and Al-O-Si bonds is one of the possible reasons for the silane coatings degradation when they are exposed to aggressive media (gradual uptake of water and formation of hydrated silane coatings) suggesting hydration of the network and disruption of siloxane and alkyl moieties. With different chemical structures, the hydrolysis-condensation kinetics vary from one type of molecule to the other, as do the self-assembled monolayer/multilayer structures and properties.

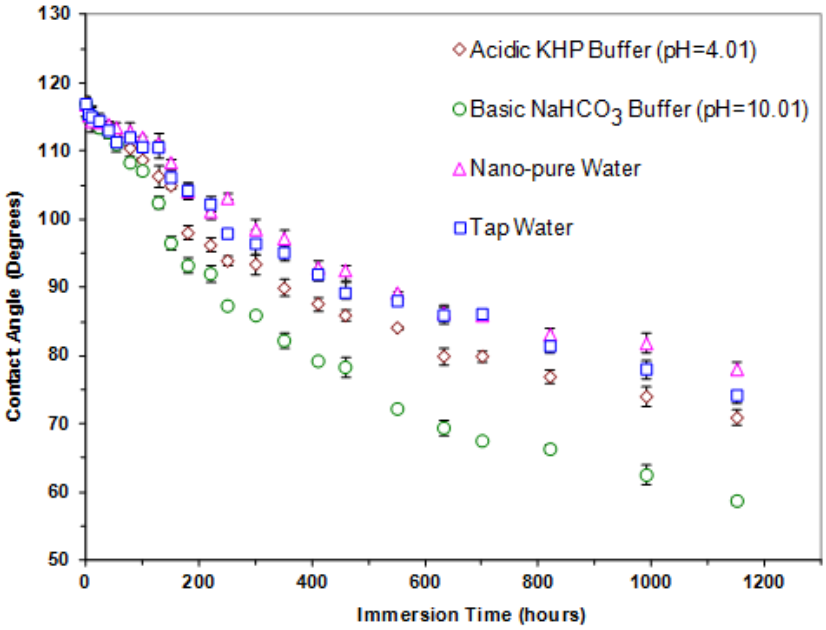

Fig.4.6. Contact angle of Al sample coated with 18C+Cl *SAMs vs.* immersion time in acidic (pH=4.01), basic (pH=10.01), nano-pure and tap water. At the end of the test, the lowest and highest values of free surface energy (ε) are 23.17 (±1.24) and 35.54 (±0.63) mNm^{-1}, respectively.

A large contact angle can be considered as a characteristic for well-covered, complete and homogeneous hydrophobic *SAMs* coating, while a small contact angle is associated with a degraded or incomplete layer. It is clear from Figs.4.5-4.6 that losing hydrophobicity was faster in the case of samples coated with 8C-*SAMs* and 18C+Cl *SAMs* than 18C-*SAMs*. Meanwhile, in all cases, decrease of the CA was quite fast in the case of samples immersed in a basic solution compared to other media. The reason for this observation is the influence of the basic condition on Al oxide layer stability and the rate of Al corrosion in basic media which leads to accelerated

coating deterioration. Meanwhile, losing hydrophobicity as a decrease of contact angle values was slightly faster for samples immersed in tap water compared to samples immersed in nano-pure water, which is most likely due to salts dissolved in tap water, causing an accelerated rate of coating deterioration.

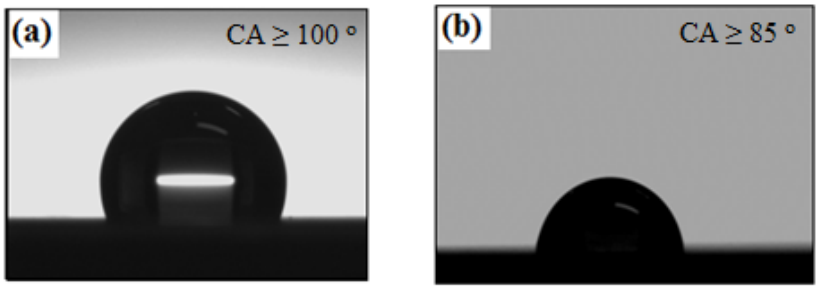

Fig.4.7. Water droplet images on an Al surface coated with18C-*SAM*s: a) before [ε:6.08 (±1.13) mNm^{-1}] and b) after 700-h immersion in nano-pure water [(ε:21.12 (±1.23) mNm^{-1}].

A significant decrease in surface hydrophobicity can be observed clearly in Fig.4.7b, which implies a coating layer decay. These *SAM*s layers, indeed, are believed to be not dense enough or too thin and insufficiently cross-linked to prevent water molecules or other aggressive ions from penetrating through the coating to the surface beneath. In the case of Al samples coated with 18C+Cl *SAM*s, the Cl^- ions cause chloride-induced pitting corrosion which is a source for decreasing contact angle. Therefore, it is possible to conclude that a big challenge in Al surface modification is to avoid use of Cl^- releasing materials either as *SAM*s precursors or in subsequent manipulations of the *SAM*s coated substrates.

4.4.3 X-ray Photoelectron Spectroscopy (XPS) Analysis Results

Surface chemical composition of these *SAM*s thin films was examined by X-ray photoelectron spectroscopy (XPS) studies. Figure 4.8 to 4.10 illustrate XPS spectra of samples immersed for 15-min in diluted silane baths of 8C, 18C and 18C+Cl solutions. The XPS signals of C, O and Si demonstrated covered Al surfaces with low surface energy coatings of each *SAM*s layer. The high-binding-energy peak at 284.6 (eV) corresponds to existence of C-H and

C-C bonds with high concentration implying on presence of alkylsilanes molecules on Al substrates as characteristic of *SAM*s coatings. Meanwhile, the observed peaks at ~281 and ~286 (eV) corresponds to the C-Si and C-Cl groups, respectively, indicating the presence of 18C+Cl *SAM*s molecules on Al substrates.

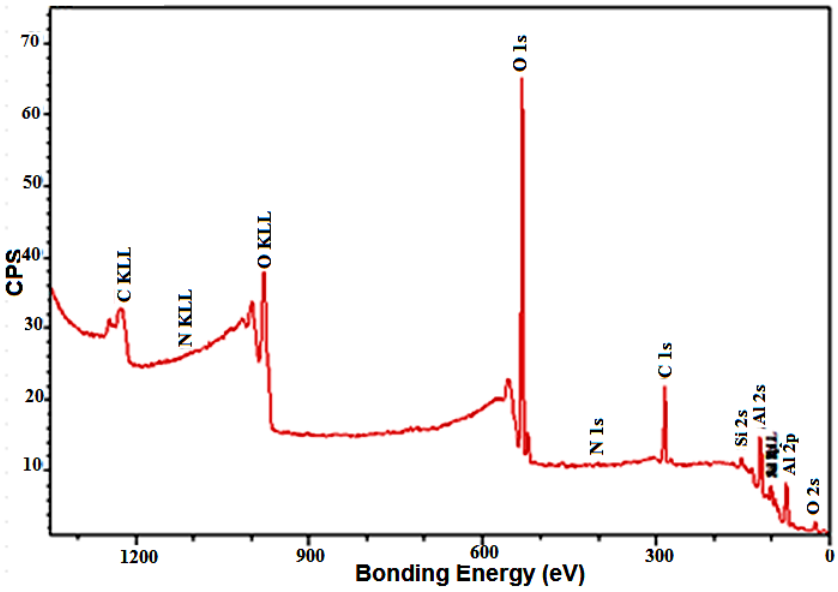

Fig.4.8. XPS spectra of aluminum sample coated with 8C-*SAMs* coating.

Consequently, the XPS results confirmed that the Al surfaces were covered with their corresponding alkylsilane molecules. The existence of silanol groups in contact with the hydroxylated surface of the metal could favour the formation of Al-O-Si interface bonding. The formation of a silane *SAMs* on an oxide surface, indeed, occurs in two steps, conversion to silanol followed by condensation on surface. Methoxy silanes (R-Si-O-CH_3) should convert to silanols (R-Si-OH) before *SAMs* formation via hydrolyzing in a solution. The silanol undergoes a condensation reaction with a hydroxide group on the alloy surface forming the siloxane linkage (metal-O-Si).

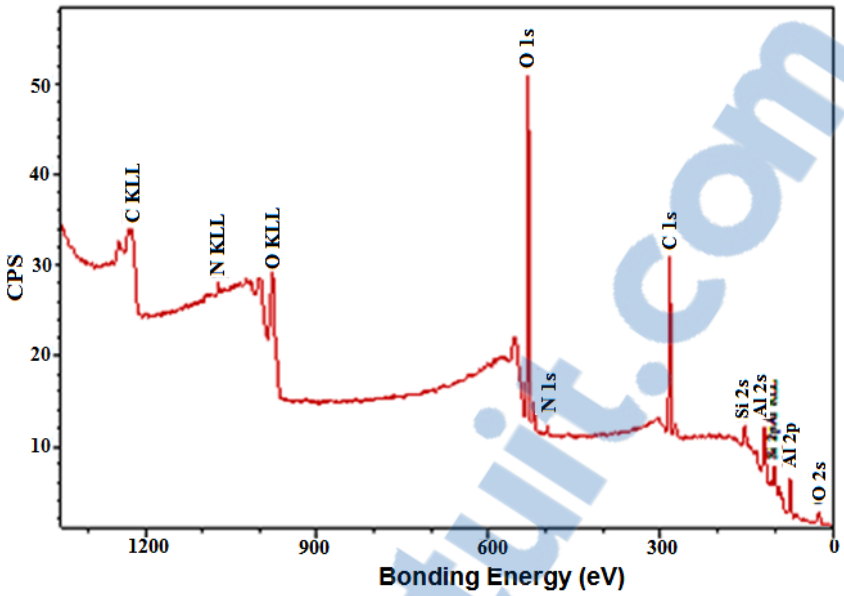

Fig.4.9. XPS spectra of aluminum sample coated with 18C-*SAMs* coating.

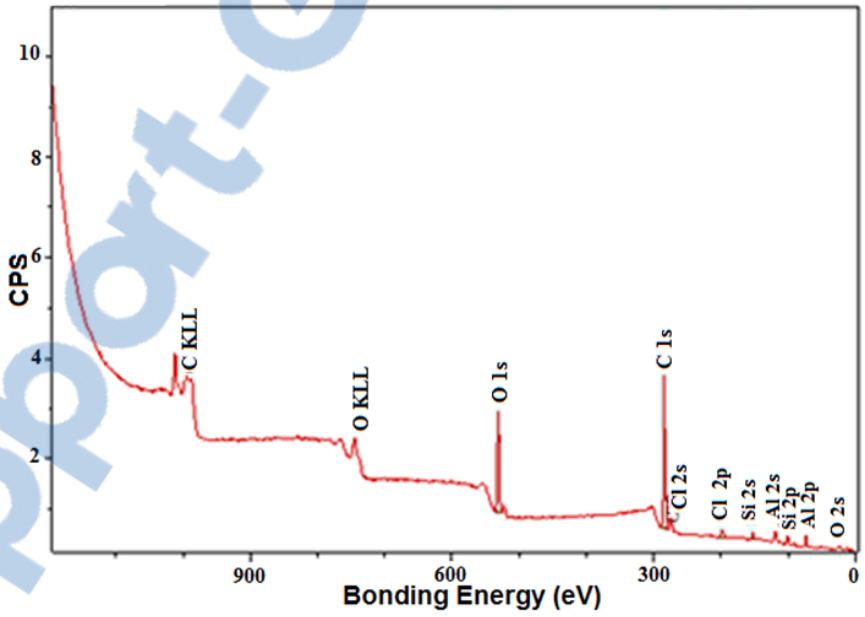

Fig.4.10. XPS spectra of aluminum sample coated with 18C+Cl *SAMs* coating.

4.4.4 Surface Characterizations (Prior to Test)

The AFM, optical microscope image and SEM survey of both series of bare and coated AA2024 surfaces have shown flat uniform surfaces (Figs.4.11 to 4.13). However, dark spots scattered and distributed on Al surface coated with 18C+Cl *SAM*s can be observed easily on as-prepared surface. These spots are severe local corrosion and pitting in either matrix region or around second-phase particles due to Cl^- ion attack. Meanwhile, morphological and chemical compositional studies were conducted on tested samples prior and after sample stability tests to evaluate any change in coating composition. As is evident, the alkyl trichlorosilane molecules (18C+Cl) contain the corrosive Cl^- ions which were released following hydrolysis-condensation reactions, leading to pitting corrosion on the Al substrate.

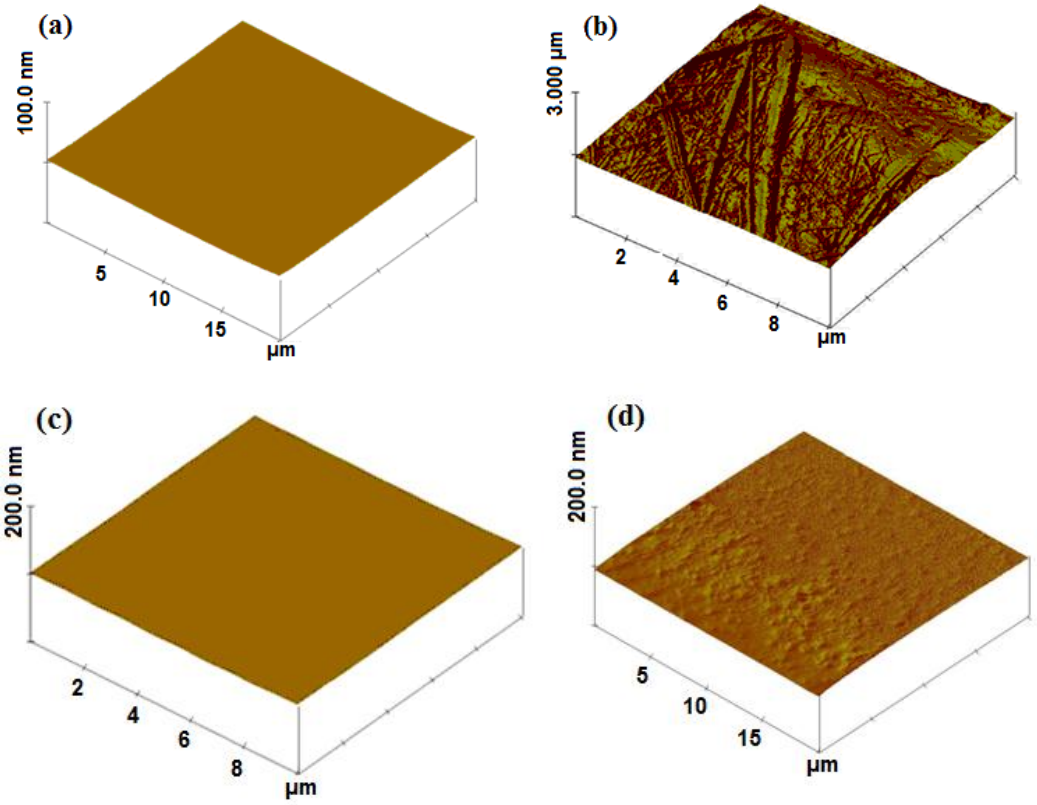

Fig4.11. AFM images of: a) bare polished standard AA2024 (R_{rms}: ~ 28 nm), b) as-received AA2024 (R_{rms}: ~ 177 nm) and aluminum surface coated with *SAM*s of c) 18C (R_{rms}: ~ 25 to 28 nm) and d) 18C+Cl (R_{rms}: ~ 73 nm) before any test.

However, in the case of the two trimethoxysilane compounds, 8C and 18C, there are no corrosive ions of Cl^- which in turn leads to more corrosion protection of Al substrate, as is obvious in Fig. 4.12. Meanwhile, the 18C-*SAMs* has a longer alkyl chain (18 carbons) compared to 8C-*SAMs* which has a shorter alkyl chain (8 carbons) which resulted in improved corrosion protection of Al surface (variations in structures and properties of the film).

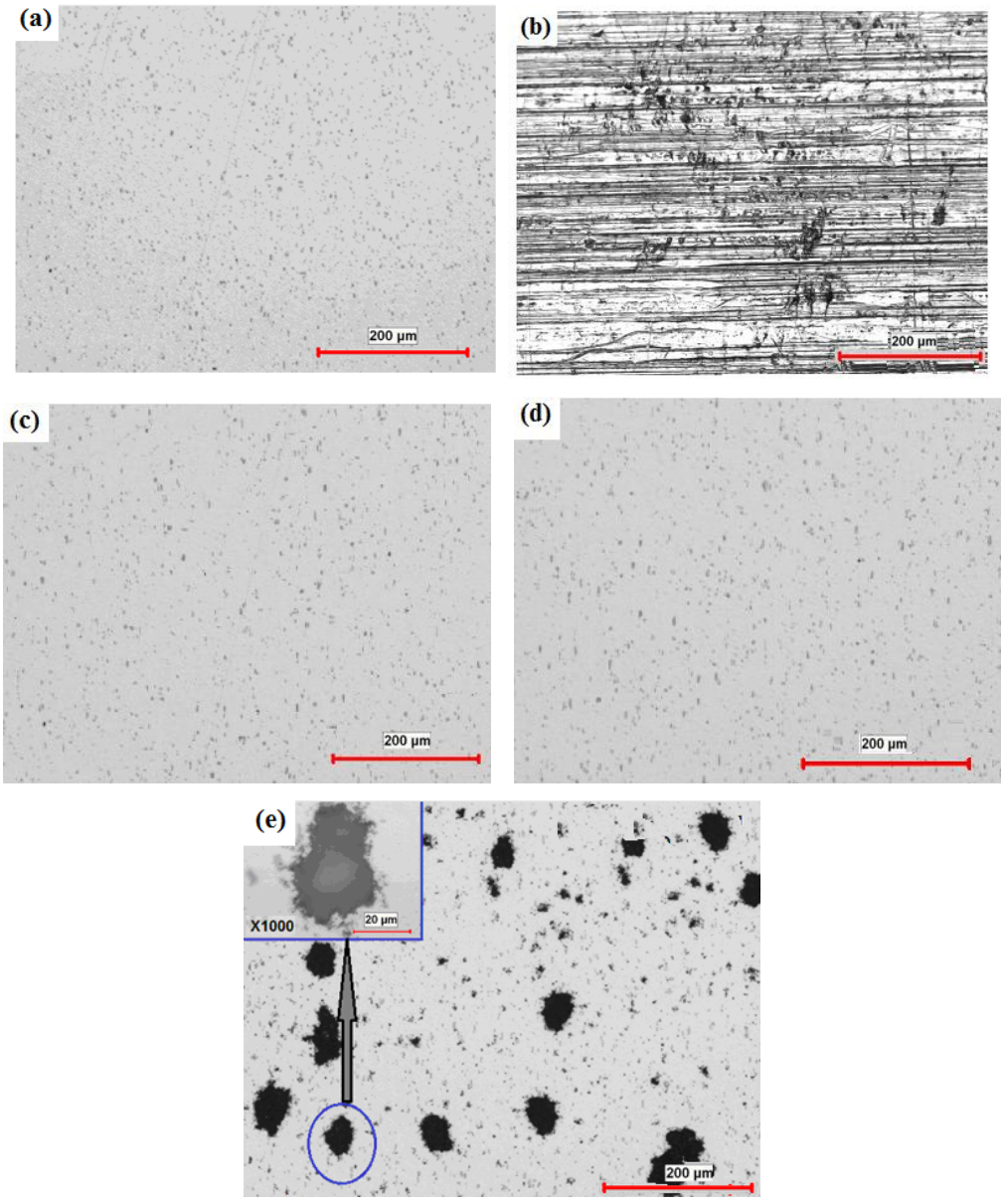

Fig.4.12. Microscope images of: a) bare standard AA2024 (x100), b) as-received AA2024 (x100), and Al surface coated with *SAM*s of c) 8C (x100), d) 18C (x100) and e) 18C+Cl (x100), inset (x1000)), prior to test.

In fact, packing density is expected to increase with chain length [254]. Therefore, it is possible to conclude that the 18C-SAMs layer(s) formed a more closely packed and well-ordered thin film on Al compared to 8C and 18C+Cl thin films which resulted in films with more defective domains (Fig. 4.12). Consequently, the less defective domains in 18C-*SAMs* led to better corrosion protection of the Al substrate. In addition, all the three alkylsilanes are expected to form polysiloxane networks. As it is well known, the aluminum alloy 2024 (AA2024) contains Cu-enriched particles (confirmed by EDX analysis during SEM survey, Fig.4.13) and therefore, chemical state and large number of these particles could influence *SAM*s formation.

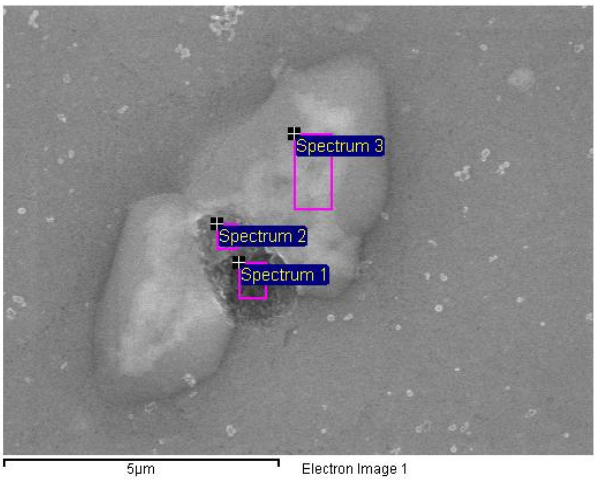

Spectrum	O	Mg	Al	Si	Mn	Cu
Spectrum 1	15.99	2.86	71.68	3.97	0.42	5.07
Spectrum 2	6.14	9.67	67.62	0.70		15.86
Spectrum 3	5.93	10.43	68.61			15.03
Max.	15.99	10.43	71.68	3.97	0.42	15.86
Min.	5.93	2.86	67.62	0.70	0.42	5.07

Fig.4.13. EDX results and SEM images of bare standard AA2024 prior to test.

4.4.5 Surface Characterizations (After Test)

Optical microscope survey and SEM analysis revealed that while earliest corrosion products came into sight on the unmodified samples only after ~20 hours of immersion in humid media, corrosion products, local corrosion and pitting in either matrix region or around second-phase particles was observed after ~85-h and ~310-h exposure to aggressive media in the case of 8C-*SAM*s and 18C-*SAM*s, respectively (Figs.4.14-4.16). An alloy surface tends to be considerably more inhomogeneous than a pure metal surface. A number of inter-metallic

particles with regular or irregular shapes (compounds containing Al-Cu-Mg and Al-Cu-Fe-Mn-Si [172, 189]) were dissolved and removed from the matrix.

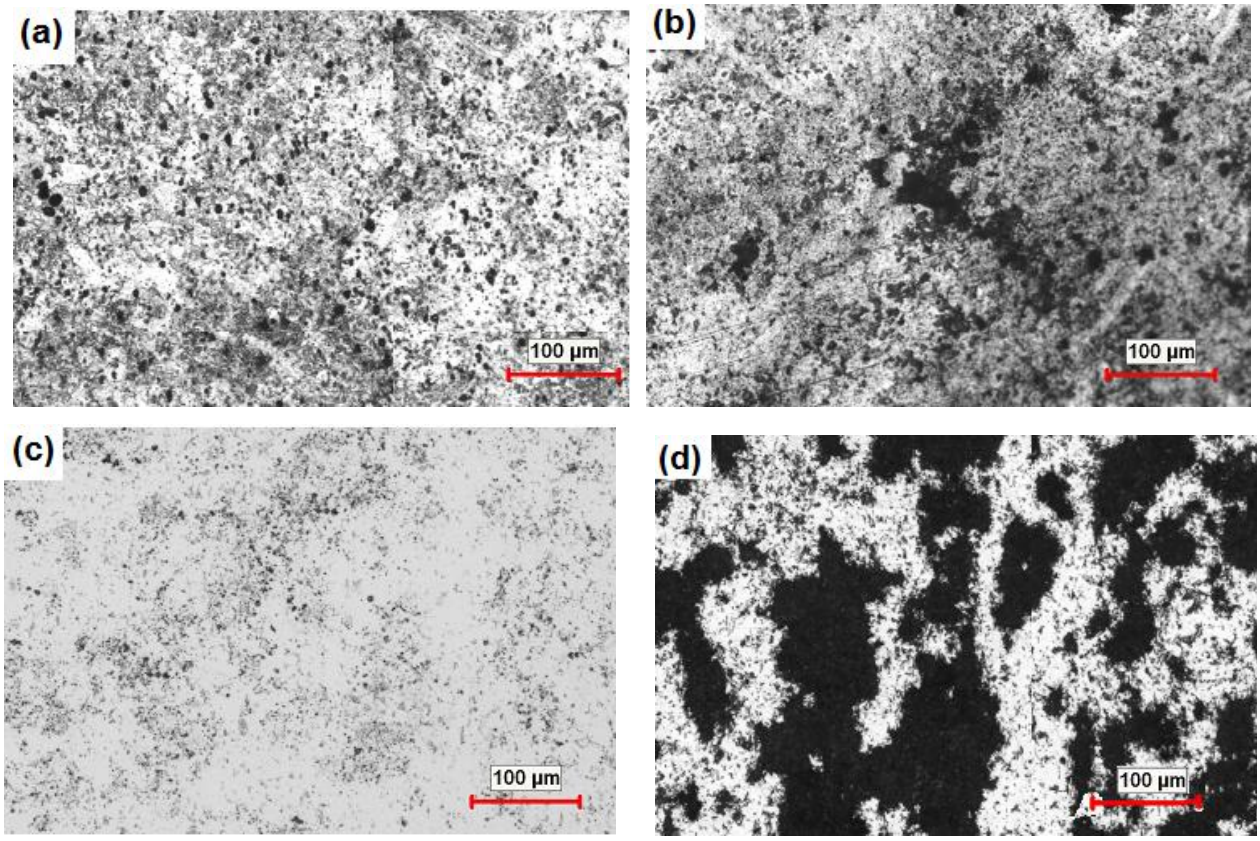

Fig.4.14. Microscope images of a) bare standard Al (x100) and coated Al with *SAM*s of b) 8C (x100), c) 18C (x100) and d) 18C+Cl (x100), after 580-h stability test (basic media).

Significant morphological changes are obvious following immersion test via SEM surveys. With propagation of corrosion, the coating layer eventually loses adhesion with the metal surface, making the metal substrate more vulnerable to the corrosion process. Copper rich alloys, e.g. AA2024, tend to undergo localized corrosion at copper rich particles as can be seen in Fig.4.13 where the Cu At% changes from ~15% on particles to 5% on Al matrix. The copper rich particle in fact acts as a cathode in a galvanic couple between it and the Al matrix. This composition of the Al matrix and second-phase particles, inevitably leads to electrochemical

corrosion. Effective protection of the particles will prevent the cathodic reaction therefore preventing localized corrosion.

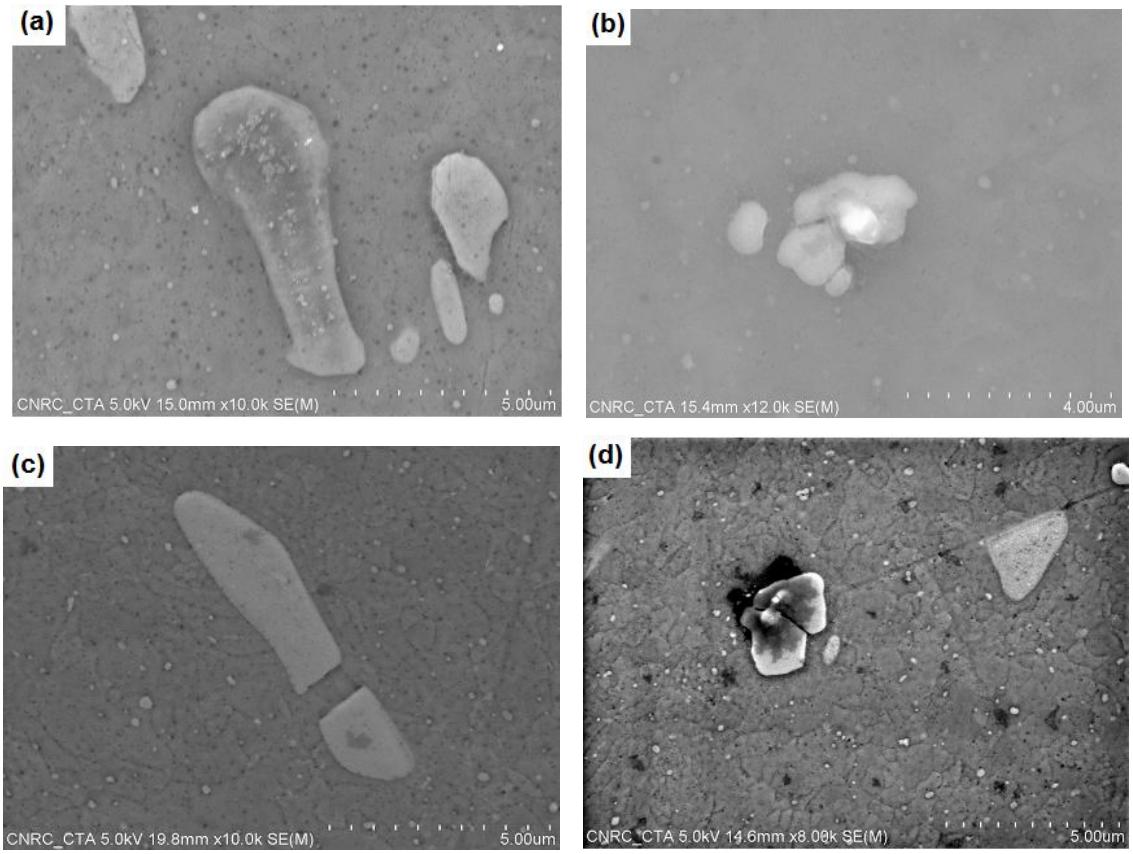

Fig.4.15. SEM images of a) bare standard AA2024 and coated AA2024 with *SAM*s of b) 8C, c) 18C and d) 18C+Cl, prior to test.

As is evident from Figs. 4.14-4.16, the black dots existing on the sample coated with 18C+Cl *SAM*s were severely enlarged, greatly distributed and extended to the limit completely covering the Al surface, due to extensive dissolution and corrosion incurred by immersion in aggressive media.

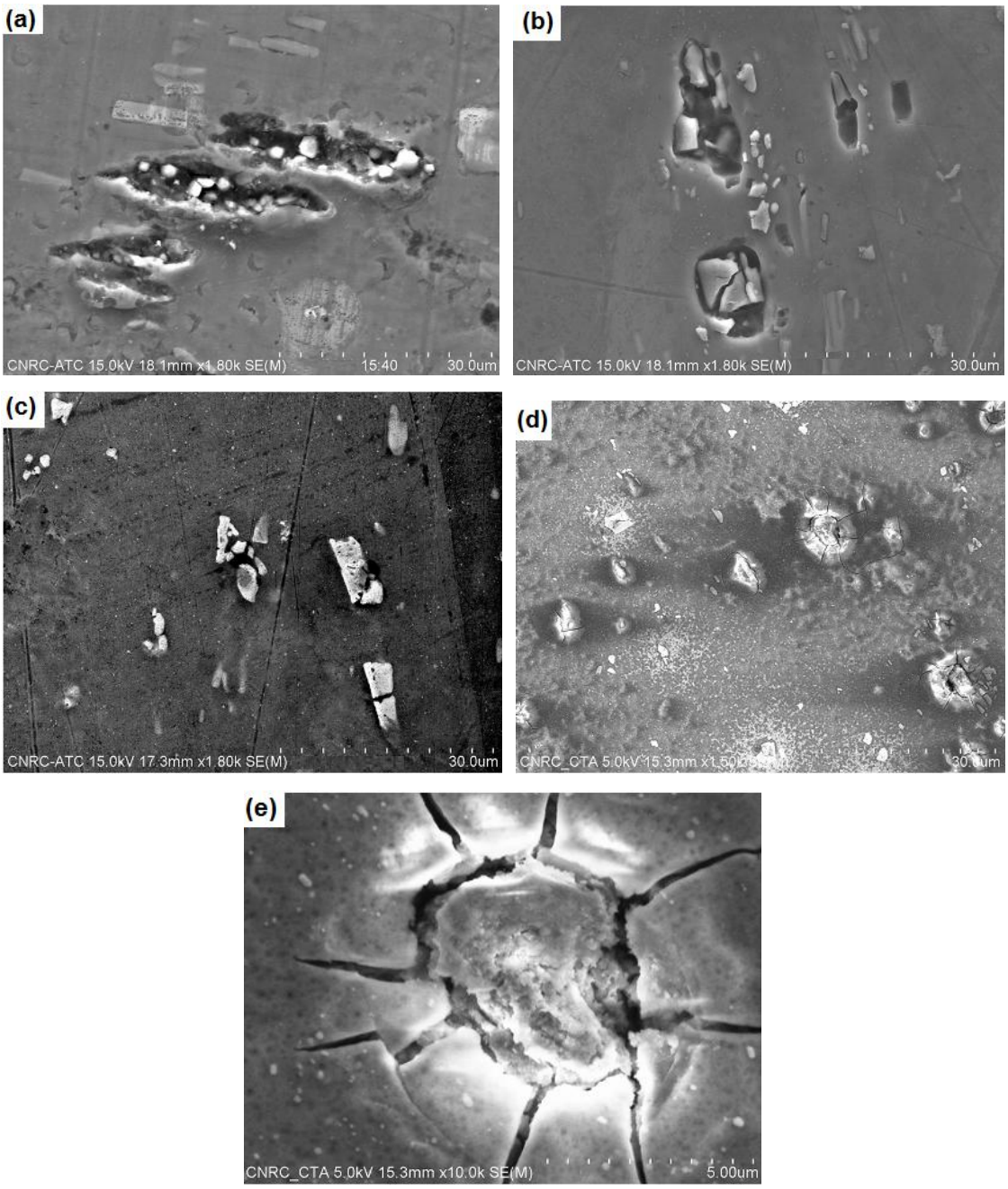

Fig.4.16. SEM images of a) bare standard AA2024 and coated Al with *SAM*s of b) 8C, c) 18C and d) 18C+Cl after 580-h stability test. The image (e) shows the magnified spot present on surface (d).

4.4.6 X-ray Photoelectron Spectroscopy (XPS) Results (After Test)

The X-ray photoelectron spectroscopy analysis was used to investigate chemical composition of acid-tested 18C-*SAM*s surfaces, implying an altered sample surface chemistry

(Table 4.4). While Si 2P peak is detected significantly before sample immersion representing silane layer on aluminum, however, its atomic concentrations decreased considerably after 1100-h immersion in acidic media. This supports the described assumption above by which water molecules hydrolyze the -O-Si-R bond and gradually destroy silane layers on an Al substrate. Thus, the XPS analysis results along with SEM survey imply that both surface morphology and chemistry are altered after the stability tests. Similar processes and explanations are expected in the case of coated Al samples immersed in other aggressive media or coated with 8C-*SAM*s and/or 18C+Cl *SAM*s.

Table 4.4. XPS results of Al surface coated with 18C-*SAM*s and BTSE/18C-*SAM*s coating before and after stability test.

Element	18C-*SAM* coating	
	% At. Concentration	
	Before	After
C 1s	44.08	29.95
O 1s	30.10	42.07
Si 2p	13.15	2.18
Al 2p	12.67	25.15
Na 1s	n/a	0.65

4.5 Effect of UV Radiation on Hydrophobic Properties

In order to evaluate the durability of coatings in a simulated natural weathering process for potential outdoor applications, their aging was studied against UV exposure. Sunlight or more precisely ultraviolet (UVA/B) light is considered as one of the most important causes of coating damage. The samples were exposed to UVA-340 fluorescent lamp according to ASTM G154. It is worthy to highlight the fact that each 537-h of artificial UV exposure is almost equal to one year of sunlight exposure [255]. Figure 4.17 presents contact angle values of coated Al samples with different *SAM*s following UV exposure (above) with and (below) without a 4 hrs condensation step. As is evident, all samples lost their hydrophobicity associated with the

decrease of CA while the number of UV cycles increased, more especially when the condensation step was applied. However, no significant difference was observed from one sample to another one. Meanwhile, the contact angle remains almost constant (Fig.4.17 below) between cycles of 12 to 20 where their contact angle slightly decreased. However, after 20 cycles, the CA decreased dramatically, especially in the case of a sample coated with 8C-*SAM*s, on which it turns completely as hydrophilic surface. Therefore, based on UV exposure results, it is possible to conclude that a realistic stability was observed for coated Al with 18C-*SAM*s and 18C+Cl *SAM*s over almost six months of natural sunlight exposure [255]. The 8C-*SAM*s coatings exhibit the most remarkable UV-induced degradation reaching a nearly 80^{o} water CA. As is evident, all *SAMs* coatings exhibit UV-change in their wetting properties. In particular, 8C-*SAMs* coatings exhibit the most remarkable UV-induced degradation CA ~ 80^{o}.

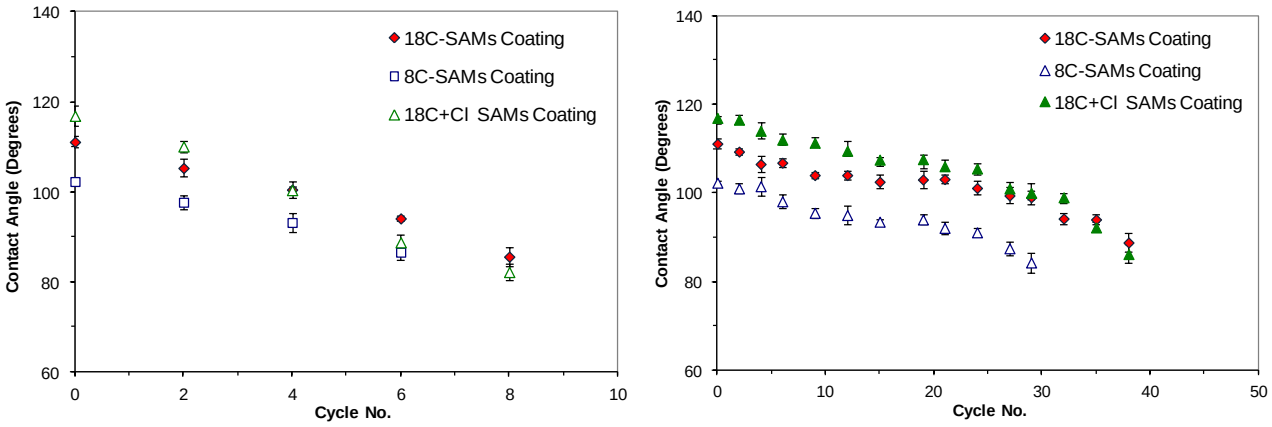

Fig.4.17. Coating durability (CA *vs.* UV cycle) for flat AA2024 coated with different *SAM*s (left) with 4-h condensation and (right) without condensation step.

4.5.1 X-ray Photoelectron Spectroscopy (XPS) Results

The XPS analysis was used in order to examine chemical composition of 18C-*SAM*s coating before and after UV exposure (Table 4.5). It is clear that the Si 2p atomic concentration remains almost the same before and after the test; however, atomic concentration of C 1s decreased from 44.08% to 28.20% and O 1s increased from 30.10% to 45.66%. This is due to the difference in atomic bond strength in *SAM*s molecules resulting in the gradual loss of deposited 18C-*SAM*s coatings on an Al substrate after UV exposure.

Table 4.5. XPS analysis results of aluminum samples coated with 18C-*SAM*s coating before and after UV exposure (without 4 hrs condensation step).

Element	18C-*SAMs* coating	
	% At. Concentration	
	Before	After
C 1s	44.08	28.20
O 1s	30.10	45.66
Si 2p	13.15	11.53
Al 2p	12.67	13.09
Na 1s	n/a	1.52

This is the reason why contact angle decreased over UV cycles. A decrease of contact angle values is due to the gradual loss of the deposited coating after UV exposure. As far as it concerns the origin of UV-induced degradation, UV irradiation can generate electron-hole pairs in the coated surface, some of the holes reacting with oxygen to form surface oxygen vacancies. Meanwhile, water and oxygen may compete to dissociative adsorption onto these vacancies. The defective sites are kinetically more favorable for hydroxyl adsorption than oxygen adsorption. As a result, the surface hydrophilicity is improved. It has also been demonstrated that the surface becomes energetically unstable after the hydroxyl adsorption. Since the oxygen adsorption is thermodynamically favored, it is more strongly bonded on the defect sites than the hydroxyl group [256]. Therefore, the hydroxyl groups adsorbed on the defective sites can be replaced gradually by oxygen atoms when samples UV-irradiated [129]. In the case of 8C-*SAM*s which exhibits considerable UV-induced change in contact angle, this is possibly due to its poor orientation along c-axis which is insufficient to repel water droplets because of the high surface polarity and energy that makes the water cover the surface very easily. Therefore, the subsequent significant increase in UV-active defect sites, which are in contact with the water molecules, results in increased UV-induced hydrophilicity.

4.6 Coating Stability at Ambient Conditions

Finally, a set of Al samples coated with different *SAM*s used in this study were also kept at ambient conditions of T: (18-21 ^{o}C) and humidity of 30 to 53 % RH to evaluate their stability over long period of time. As is clear in Fig.4.18, no significant changes were observed after 240-days of keeping at ambient conditions and all three coated samples illustrates almost similar rate of degradations over time. Therefore, a reasonable stability was observed for coated Al samples with such *SAM*s coatings in all cases at ambient conditions and over time.

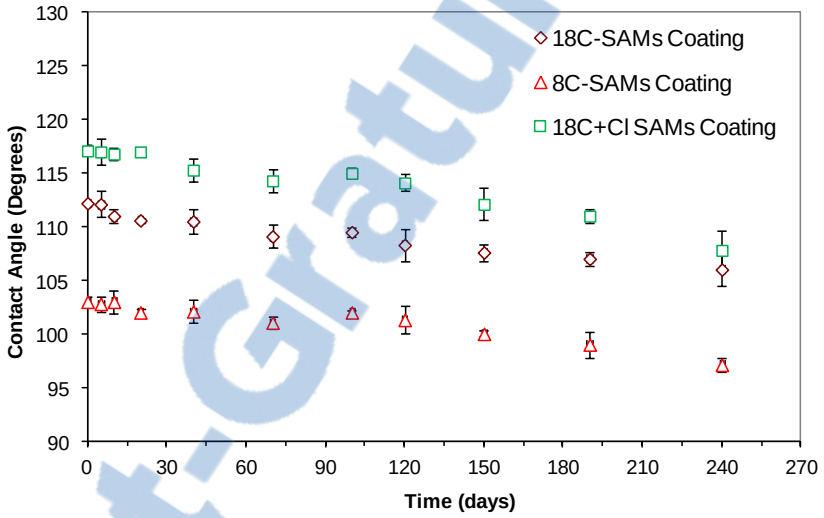

Fig.4.18. Stability of flat AA2024 coated with different *SAM*s coatings kept at ambient condition. At the end of the test, the lowest and highest values of free surface energy (ε) are 6.62 (±0.45) and 14.46 (±0.66) mNm^{-1}, respectively.

4.7 Icephobic Properties and Stability of Prepared *SAM*s Coatings

4.7.1 Study of Hydrophobicity Following Ice Detachment

To study whether hydrophobic properties of prepared coated samples remain following ice detachment, measurements of the contact angle on coated samples after icing/de-icing cycles were conducted. A minor decrease in contact angle values was observed following each icing/de-icing cycle in the case of samples coated with 18C-*SAM*s and 18C+Cl *SAM*s coatings, however, a significant change was observed for sample coated with 8C-*SAM*s (Fig.4.19). After 5 cycles of icing/de-icing, the contact angle values of Al sample coated with 8C-*SAM*s decreased quickly

from ~102^{o} to ~75^{o}. However, in the case of samples coated with 18C-*SAM*s and 18C+Cl *SAM*s, the contact angle values decreased moderately. This behavior is probably due to the "*steric effect*" which prevents well-ordering of *SAM*s molecules structures on Al leading to decrease of hydrophobicity. This behavior originates from competition between decreases in reactivity caused by increasing the *steric effect* on Al [251]. In chemistry, the *steric effect* is defined as an influence on reaction rate determined by the fact that all the atoms within a molecule occupy space; therefore, certain collision paths are either disfavored or favored, when atoms are brought close [257].

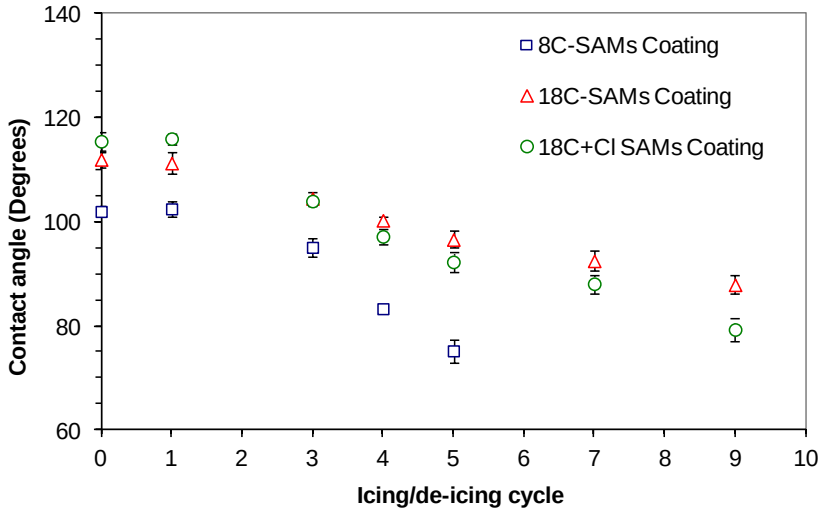

Fig.4.19. Contact angle values as a function of icing/de-icing cycles for samples coated with 8C, 18C and 18C+Cl *SAM*s layers.

In all cases, hydrophobic properties of each coated sample were gradually reduced after icing/de-icing cycles and this confirms partial loss and damage of hydrophobic coating on sample surfaces during and after several icing/de-icing cycles. In other words, water could attack the R-Si-O- bond, hydrolyzing it and thus resulting in loose silanol species and hydrophilic -OH group on the surface.

4.7.2 Results of Ice Adhesion Strength

Table 4.6 shows the initial values of the shear stress of ice detachment and the ice adhesion reduction factor (*ARF*) for coated samples with different *SAM*s prepared. Meanwhile, their

durability in term of anti-ice performance over time and repeated icing/de-icing cycles similar to natural atmospheric icing were studied as well.

Table 4.6. The ice adhesion strength and *ARF* values of different *SAM*s coatings on Al.

Sample	Ice adhesion strength (kPa)	*ARF*
Mirror-polished AA2024	270 ± 20	~ 1.37
As-received AA2024	370 ± 30	1
8C-*SAMs* Coating	220 ± 11	~ 1.68
18C-*SAMs* Coating	190 ± 15	~ 1.94
18C+Cl *SAMs* Coating	185 ± 19	~ 2

The hydrophobic properties of those surfaces were examined after ice removal, as shown earlier in Fig.4.19. Figure 4.20 shows the shear stress of ice detachment as a function of icing/de-icing cycles on sample surfaces tested. For each coating studied, one sample was subjected to 9 successive de-icing tests. As-received and mirror-polished bare Al was used as standard reference showing the initial values of shear stress of ice detachment of ~370 ± 30 kPa and ~270 ± 20 kPa, respectively. Both the 18C-*SAM*s and 18C+Cl *SAM*s coated samples showed close values of shear stress, implying very similar ice adhesion strength (*IAS*) on alkyl-grafted samples. While uncoated flat sample showed average shear stress of ice detachment of ~ 370 ± 30 kPa, its coated counterparts with 8C-*SAM*s, 18C-*SAM*s and 18C+Cl *SAM*s layers showed reduced values of ~ 220, ~ 190 and ~ 185 kPa, respectively. This reduction can be attributed to the presence of the low surface energy coatings on the samples. All flat coated surfaces demonstrated shear stress of ice detachment values of ~ 1.68 to 2 times lower than as-received Al surfaces and about ~ 1.22 to 1.5 times lower than those observed on mirror-polished Al surfaces. However, the adhesion stress of ice detachment values increased for both samples, 18C-*SAMs* and 18C+Cl *SAMs*, after as many as 9 icing/de-icing cycles in a similar manner, as shown in Fig.4.20. This increase in ice adhesion strength is believed to be associated with partial decay of the coatings caused by their contact with water. As contact angle values were decreased after icing/de-icing event, then, it is another confirmation for the reason of partial loss of hydrophobic coating on Al surfaces.

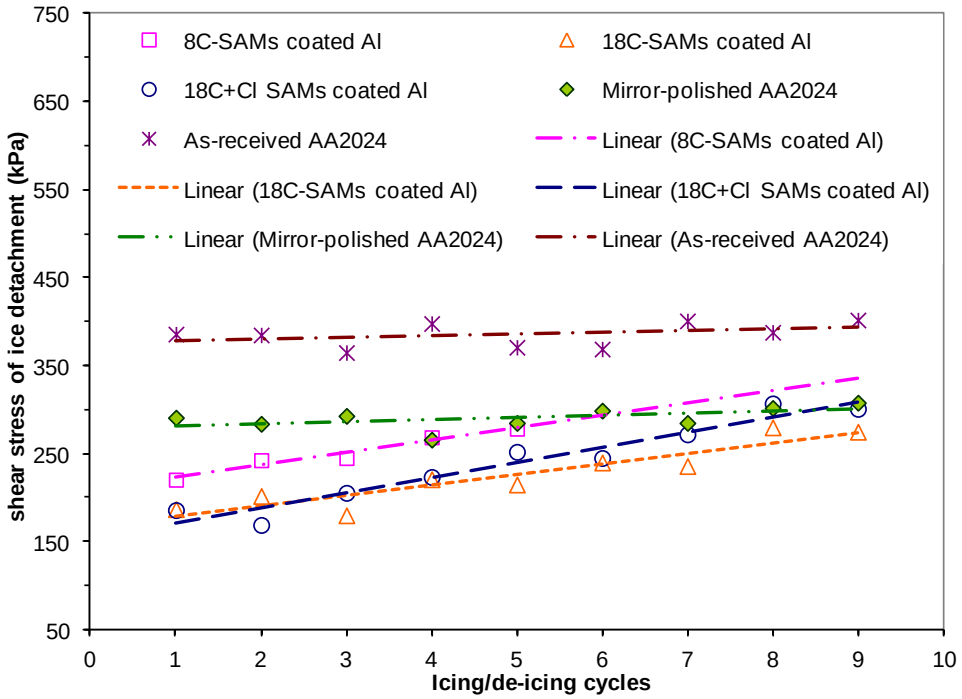

Fig.4.20. Shear stress of ice detachment *vs.* icing/de-icing cycle for Al surface coated with 8C, 18C and 18C+Cl *SAM*s layers.

Though, loss of hydrophobicity and increase in ice adhesion strength values was dramatically and completely different in the case of sample coated with 8C-*SAMs* layers. It raised this fact that the *SAMs* coating of 18C created on Al was well-ordered than *SAMs* fabricated by 8C.

4.7.3 XPS Results: Prior and Following Ice Detachment

While both *SAMs* coatings demonstrated a peak of Si 2p before test (silane layer(s) on Al), however, its atomic concentration decreased significantly after ice detachments (Table 4.7). As it is evident, this decrease is even worse in the case of Al sample coated by 8C-*SAM*s. This supports the described assumption above by which water molecules hydrolyze the -O-Si-R bond and gradually destroy silane layers on an Al substrate. Similar reasons are expected in the case of samples coated with 18C+Cl *SAM*s.

Table 4.7. XPS analysis results of Al samples coated with 8C and 18C-*SAM*s before and after icing/de-icing cycles.

Element	18C-*SAMs* coating		8C-*SAMs* coating	
	% At. Concentration		% At. Concentration	
	Before	After	Before	After
C 1s	44.08	26.16	36.68	17.53
O 1s	30.10	38.02	28.17	35.76
Si 2p	13.15	4.09	10.08	1.16
Al 2p	12.67	29.95	25.07	43.52
Na 1s	n/a	1.78	n/a	2.03

4.8 Conclusions

In the present chapter, a series of experiments was conducted to investigate and study hydrophobic and ice phobic properties of coated AA2024 substrates by dissimilar alkyl-terminated *SAM*s thin films. The hydrophobic, icephobic, surface characteristics and durability of such coatings in different conditions were tested by means of contact angle measurements, demonstrating gradual loss of hydrophobicity over time. Ice-releasing performance of the same surfaces was also examined. All coated surfaces demonstrated initially the shear stress of ice detachment values of ~1.68 to 2 times lower than as-received aluminum surfaces and about ~1.22 to 1.5 times lower than those observed on mirror-polished substrates. The ice adhesion strength values gradually increased after as many as 5 to 9 successive icing/de-icing cycles.

CHAPTER V

ANTI-CORROSIVE PERFORMANCE OF SINGLE LAYER *SAMS* COATINGS: POTENTIODYNAMIC POLARIZATION, ELECTROCHEMICAL IMPEDANCE SPECTROSCOPY AND CYCLIC CORROSION EXPOSURE

5.1 Introduction

The hydrophobic and icephobic properties as well as the stability and durability of single layer SAMs coated Al substrates were discussed in detail in the previous chapter. Therefore, the objective of this chapter is to study anti-corrosive properties of prepared single layer thin films on an Al substrate by means of appropriate instruments. A standard three-electrode flat cell was used as the working cell.

5.2 Corrosion Resistance of Single Layer *SAM*s Coatings

5.2.1 Anti-corrosive Performance of Single Layer Coatings

The high-strength AA2024 is an alloy with Cu as the main alloying element, typically between 3.8-4.9% (wt. %) [268, 269], and is used extensively in applications requiring high strength to weight ratio and good fatigue resistance, e.g. aircraft structures, especially wing and fuselage structures under tension. Environmental species such as moisture and electrolytes can typically penetrate through the polymer coating layer to form an electrochemical galvanic cell with the Al and Cu-rich particles. This leads to corrosion of the Al alloy. Consequently, by corrosion distribution and propagation, the coating layer eventually loses adhesion with the metal surface, making the metal substrate more vulnerable to the corrosion process. Therefore, study and development of anti-icing coatings on Al substrates highlight the necessity of improving their anticorrosive resistance. In other words, the anti-corrosive performance of coated AA2024 should

be studied too. Two main factors are expected to dominate corrosion inhibition:

(i) The higher extent of alkyl interactions in the *SAMs* coatings

(ii) The more efficient silane-aluminum interface bonding of the coatings.

The corrosion resistance of the modified and unmodified AA2024 substrates was initially evaluated by potentiodynamic polarization test in 3.5 wt.% NaCl solution (pH: ~7.9), as shown in Figure 5.1. The E_{corr}, j_{corr} and R_p values derived from corresponding polarization curves using *Tafel* extrapolation are summarized in Table 5.1. It is evident in Fig.5.1 and Table 5.1 that the value of E_{corr} positively increases from -0.68±0.03V and -0.69±0.04V for the bare standard and control AA2024, respectively, to -0.60±0.03V in the case of hydrophobic 18C-*SAMs* coating. However, it shifts slightly to positive values for Al sample coated with 8C-*SAMs* and 18C+Cl *SAMs,* i.e. -0.64±0.03V and -0.65±0.04V, respectively. The positive shift observed in E_{corr} values is obviously due to improvement in protective performance of hydrophobic coating formed on Al substrate. In other words, the potentiodynamic polarization curves demonstrated that the corrosion inhibition of 18C-*SAMs* film was superior to that of the 8C-*SAMs* and 18C+Cl *SAMs* films. The 18C-*SAMs* film also showed a decrease in j_{corr} in the cathodic and anodic regions, which suggested that the coating formed tight silane layers, which prevented ingression of O_2 and its diffusion to the metal surface [268]. In fact, some alkylsilane coatings cover up only those parts of alloy where no Cu-rich domains exist, i.e. n-decyltriethoxysilane [172, 268], and show practically no change in j_{corr} in the cathodic part of potentiodynamic polarization curves. This fact is used generally as an indication for partial coverage of a surface. The slope of anodic current versus E curve was smaller for 18C-*SAMs*-coated Al than other two coatings (8C-*SAMs* and 18C+Cl *SAMs* films) as well as bare substrates. This observation supports the fact that the 18C-*SAMs* film protects the Al alloy surface more effectively. This difference is attributed to the bonding of silane groups to the oxide surface. Therefore, it is likely that 18C-*SAM*s coating exhibited better bonding to both oxide and metallic surfaces, resulting in enhanced corrosion inhibition. It should be noted that anodic dissolution is practically system-specific. Hydrophobicity is claimed to be the most important property against corrosion as it controls the access of water to the metal-coating interface. Therefore, a sufficiently cross-linked network firmly attached to the metallic substrate should be formed to protect the

surface against corrosion. It is possible to say that according to the results obtained from potentiodynamic polarization tests, the 18C-*SAMs* thin film also exhibited a good coverage of Cu-enriched parts of AA2024 surface.

Table 5.1. Potentiodynamic results of bare AA2024 and coated AA2024 with 8C-, 18C- and 18C+Cl *SAM*s film in 3.5 wt.% NaCl solution.

Specimen	$E_{corr.}$ (V *vs.* SCE)	$j_{corr.}$ (μAcm^{-2})	R_p ($k\Omega cm^2$)	E_b-E_{corr} (V *vs.* SCE)
Control AA2024	-0.69 (±0.04)	9.78 (±0.63)	15.57 (±2.20)	-
Standard AA2024	-0.68 (±0.03)	22.89 (±.9.06)	2.96 (±2.71)	-
8C-*SAMs*	-0.64 (±0.03)	4.07 (±1.12)	21.45 (±2.11)	0.07
18C+Cl *SAM*s	-0.65 (±0.04)	5.65 (±0.83)	39.24 (±1.21)	0.038
18C-*SAM*s	-0.60 (±0.03)	0.90 (±0.11)	248.11 (±2.55)	0.12

However, coverage of these parts should be increased more since the localized corrosion still represents the weakest point of the corrosion inhibition of this coating. Oxidation-reduction reactions in the electrolyte can only occur when imperfections or defects are present in the structure of the coatings, allowing electron transfer at the aluminum-*SAMs* coating interface. Indeed, corrosion inhibition is a multifaceted phenomenon depending on the simultaneous effect of various factors such as surface pretreatment of the metallic substrate, ability of silanes to form a highly cross-linked network, and the silane-aluminum oxide interface bonding and finally its inherent hydrophobicity. The potentiodynamic polarization studies revealed so far that the corrosion resistance of the 18C-*SAM*s-modified Al substrates improved moderately compared to both the 8C- and 18C+Cl-*SAM*s-modified samples. However, the 8C-*SAM*s-modified substrate also exhibited slight improve in corrosion resistance compared to the bare and control panels (bare AA6061, control and Standard samples). In this case, the corrosion current density of the 8C-*SAM*s and 18C+Cl-modified samples only decreased very slightly, i.e. less than one order of magnitude. However, more outstanding result was obtained for samples coated by 18C-*SAM*s where exhibited more positive corrosion potential ($E_{corr.}$) compared to the bare and control samples. Increase in

$E_{corr.}$ observed for sample coated with 18C-*SAM*s suggests a closely packed barrier film on the Al surface which was formed from *SAMs* molecules.

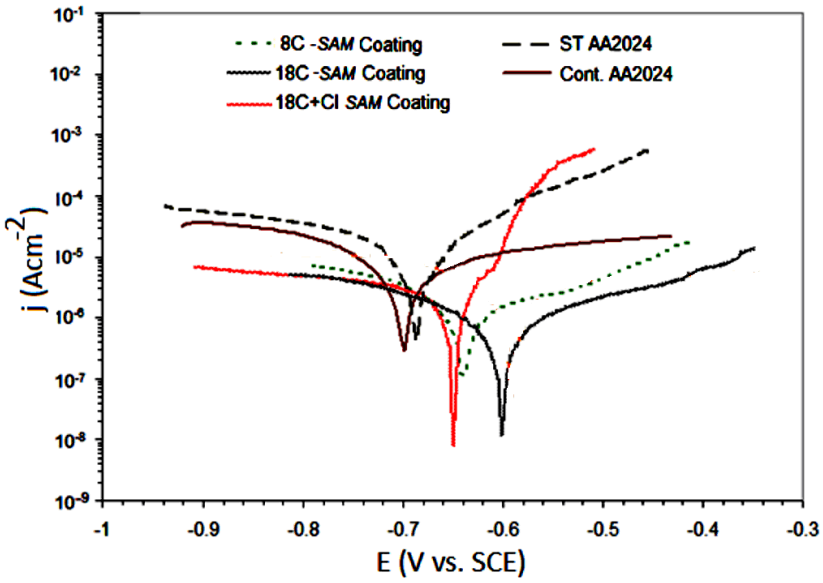

Fig.5.1. Polarization curves of bare and coated Al with 8C-, 18C- and 18C+Cl *SAMs* coating.

However, in the case of 8C-*SAM*s coated sample, due to formation of a disordered or highly defective film on Al surface, poor corrosion resistance was observed. Moreover, all coated specimens displayed somewhat resistance to initiation of corrosion attack shown by the presence of a breakdown potential, E_b, and a passive potential range, E_b-E_{corr}.. It is interesting to mention that although the 18C+Cl-coated sample also exhibited large values of contact angle, however, based on potentiodynamic polarization results, it does not demonstrate significant improvement in either $E_{corr.}$ or $j_{corr.}$ compared to the 18C-*SAM*s coated samples. This is probably due to the fact that the barrier property of the 18C+Cl *SAM*s coating on Al surface was not quite enough to improve surface corrosion resistance. The reason is the presence of a large number of defects in the films compared to the films formed from 18C-*SAM*s [172, 268]. Even though the bare samples also have high corrosion potential, however, this is perhaps due to the presence of an insulating Al_2O_3 layer on Al surface. It is reasonable to expect that 18C+Cl *SAM*s and 8C-*SAM*s films, especially the one formed from C18+Cl *SAM*s, bring worse corrosion resistance to the Al substrate compared to the

18C-*SAM*s coated sample. Upon cathodic polarization, there is a large difference between what observed for coated samples with 8C-*SAM*s or 18C+Cl *SAM*s and those observed for bare surfaces. However, for 18C-*SAMs*, the thin layer inhibited the cathodic process, and thus, the O_2 diffusion to the metal surface was suppressed. Meanwhile, the similarity between the bare and coated surfaces under cathodic polarization indicates that the 8C-*SAM*s and 18C+Cl *SAM*s on Al do not prevent O_2 diffusion to the surface in a significant way. This could be caused by two factors:

(i) The 8C and 18C+Cl *SAM*s are fabricated over the entire Al surface, but the *SAM*s are not dense enough to provide a packed barrier layer, or

(ii) The 8C and 18C+Cl *SAM*s are locally packed densely, but it is not a complete layer.

The *SAMs* layers, in fact, undergo a typical tendency in packing as the chain length increases, suggesting that, at least locally, the molecules in the *SAMs* are densely packed. In addition, the contact angle values are consistent with a well oriented, densely packed 18C-*SAMs* film on Al surface. Therefore, it is possible to conclude that the *SAMs* layer*s* are well ordered and closely packed over portions of the surface. In the case of 8C and 18C+Cl *SAM*s, the Al substrate is not likely covered by a complete mono-/multilayer thin film and a greater numbers of defect sites exist compare to what was found for *SAM*s of 18C. Oxidation of Al is balanced by simultaneous reduction of ions in solution. In aqueous media with pH close to 7 (fresh water), only two reduction reactions can occur: (i) reduction of protons (H^+) or (ii) reduction of oxygen (O_2) dissolved in water. Generally, *SAMs* may not form over Cu-enriched particles if they are not covered by oxide [172]. Indeed a higher redox activity was found over Cu-enriched particles regarding to matrix oxide surface, indicating that cathodic reaction should occur mainly on the Cu-enriched particles. Similarity in cathodic behavior between 8C and 18C+Cl *SAM*s coated samples and close values of $j_{corr.}$ to bare substrates supports our conclusion that there is no *SAMs* cover on Cu-enriched particles. Hence, if these sites were left open, suppression of the cathodic current would not be expected.

The slope of anodic i *vs.* E is less for 18C-*SAMs* and 8C-modified surface than bare surface and 18C+Cl *SAM*s. Therefore, the anodic current density is moderately suppressed on these modified surfaces. These results are a consequence of *SAMs* bonding to the Al surface. Moreover,

the corrosion current density, $j_{corr.}$, of hydrophobic coating of 18C-*SAMs* (9.08×10^{-7} Acm^{-2}) decreased about 2 orders of magnitude as compared to that of bare standard (22.8×10^{-5} Acm^{-2}). However, in the case of Al samples coated with 8C and 18C+Cl *SAMs* [8C-*SAMs* (4.07×10^{-6} Acm^{-2}) and 18C+Cl *SAMs* (5.65×10^{-6} Acm^{-2})], the $j_{corr.}$ did not decrease significantly as compared to bare standard Al surface. These results indicate that hydrophobic coating of 18C-*SAMs* can improve the corrosion resistance of Al surfaces more significantly if compared to two other *SAMs* applied on an Al substrate. The results obtained suggest that the barrier property of the 18C-modified Al samples was improved compared to the unmodified and 8C- or 18C+Cl *SAMs* samples with respect to $E_{corr.}$ and $j_{corr.}$ values. The hydrolysis and condensation reaction is in fact slow, thus, it is possible that under current experimental conditions, the hydrolysis and condensation reaction of such molecules was incomplete, leading to form films with defect areas.

5.2.2 Cyclic Corrosion Tests of Prepared Single Layer Coatings

The corrosion resistances of bare and coated AA2024 samples were further studied by cyclic corrosion exposure testing. Practically, test specimens were placed in an enclosed chamber and exposed to a changing climate. As presented in Figures 5.2 and 5.3, the unmodified flat Al samples exhibited extensive corrosion after only 8 cycles of cyclic corrosion test with appearance of numerous black dots (pits) in micrometer scale. Meanwhile, the size and density of the black dots increased as the cyclic corrosion test cycle number increased which is due to localized corrosion continually expanding. However, the earlier stage of corrosion observable in the case of hydrophobic Al samples coated with 8C-*SAM*s was after 12 cycles of exposure and trace of corrosion was observed in the case of 18C-*SAMs*-modified samples even after 18 cycles of exposure (Figures 5.2 and 5.3). In Figure 5.2, the optical images of unmodified (bare) and modified (*SAM*s coated) samples taken by a digital camera are presented. These observations revealed by the cyclic corrosion test confirmed again the results presented earlier in Figure 5.1 by potentiodynamic polarization curves which implies an improvement in corrosion resistance of modified samples compared to bare samples. Meanwhile, cyclic corrosion tests provided in addition evidence for higher corrosion inhibition of the 18C-*SAM*s coatings, demonstrating

dependence of corrosion inhibition on *SAM*s coating orientation. Pitting corrosion seemed to be a typical mode of surface degradation. It is obvious that the 18C-*SAM*s coating performed like other coatings, however, it blocked more effectively a certain number of active sites. In contrast to 8C-*SAM*s and 18C+Cl *SAM*s-modified samples, the Al panels coated with 18C-*SAM*s exhibited no obvious corrosion before 18 cycles of exposure. It is very likely due to the combined effect of formation of Al-O-Si interface bonding with the Al substrate and the hydrophobicity of the alkyl chains.

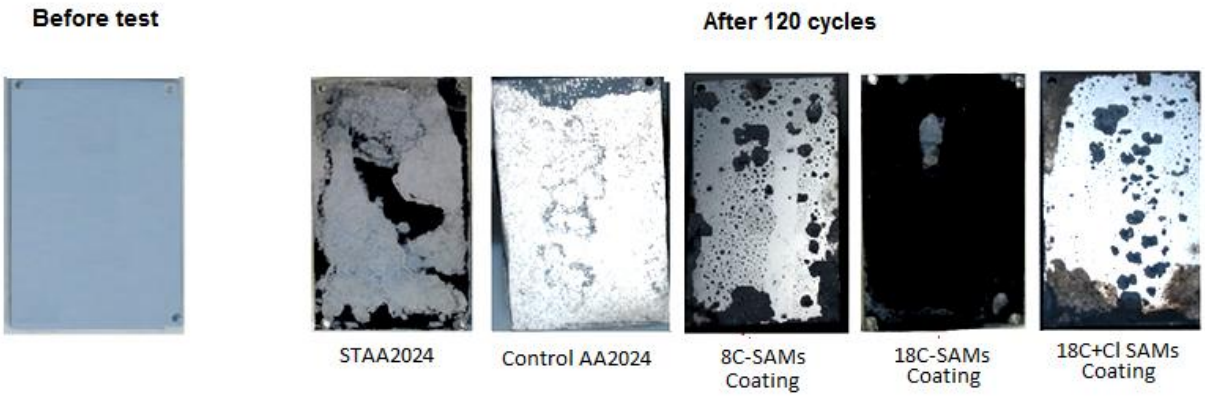

Fig.5.2. Optical images of unmodified and coated AA2024 with different *SAM*s before and after 120 cycles of cyclic corrosion test.

However, as it is obvious, corrosion resistance of the 8C-*SAM*s and 18C+Cl *SAM*s-modified samples did not improve much compared to the unmodified samples and 18C- *SAM*s as well. The optical images of 18C+Cl *SAM*s modified samples after cyclic corrosion exposure bear a very close likeness to 8C-*SAM*s modified sample. Because of the improved barrier property of Al alloy surface modified by 18C-*SAMs*, the corrosion resistance of these samples, as a result, improved compared to the bare samples. In other words, these results validate the fact that the 18C-*SAMs* layer was formed on Al substrate with less defect areas and reasonable density compared to the 8C-*SAM*s or 18C+Cl *SAMs* layer. Therefore it acts as a barrier to prevent easy penetration of corrosion accelerants beneath the Al surface. As a result, a decreasing corrosion rate or further expansion of corrosion to the surrounding areas was observed.

Corrosion inhibition depends on appropriate equilibrium between the numbers of silanol groups and the presence of linear siloxane species in the deposited coatings, both influencing

adhesion and density of the protective coatings [172]. Specifically, for achieving good corrosion inhibition when highly diluted silane solutions are used, the undesired re-esterification reactions, where the Si-OH formed groups interact with the parent alcohol (isopropanol), re-establishing the alkoxy groups, should be avoided. Another interesting result obtained from optical microscope observations is the appearance of small black dots, or pits, in C18+Cl *SAM*s coated panels after and even before exposure. A closer look at these black dots under an optical microscope revealed that they are very small (micrometer scale) locally corroded areas. The C18+Cl *SAM*s molecules could form mixed thin film by either anchoring the alkyl chains to the hydrophobic Al region of the surface, or reacting the silane head groups with the Al_2O_3 domain to form a polysiloxane network. In the latter case, a large amount of corrosive Cl^- ions can be released to the local area of Al surface, leading to the appearance of local corrosion, i.e., the observed black dots on the surface. Therefore, the trichlorosilane coating itself brings the Cl^- ions into the substrate which is a well-known corrosion accelerant for Al alloy substrates. In fact, chloride ions are in direct contact with the aluminum surface, and also, due to a not densely packed monolayer structure, electrolytes such as Cl^- ions or moisture easily penetrate the metal substrate, leading to a worse corrosion resistance. Meanwhile, the size and density of the black dots increased over time. It means that the localized corrosion after chlorosilane modification expands further during the cyclic corrosion test exposure. This is due to the weak barrier property of this thin film to prevent electrolytes and water from penetrating the metal surface to introduce further expansion of corrosion to the surrounding areas.

As in the case of 8C-*SAM*s modified substrates, it is believed that this thin film contains more defect areas compared to 18C-*SAM*s thin film. Through these defect areas, corrosion accelerants such as electrolytes and moisture can readily penetrate through the film to the metal substrate. The trimethoxysilane molecules should have formed a similar multilayer thin film on the Al surface; however, as trimethoxysilane does not contain corrosive ions, i.e. Cl^-, no local corrosion was observed from these modified samples before exposure. The 18C-*SAMs* layer showed a higher contact angle compared to 8C-*SAM*s which is due to formation of compact and well-ordered hydrophobic *SAMs* on Al surface with methyl group termination. Therefore, it is

believed that *SAMs* formation (silanisation) on Al and its surface properties, e.g. wettability and anti-corrosive performance, are strongly influenced by their molecular structure.

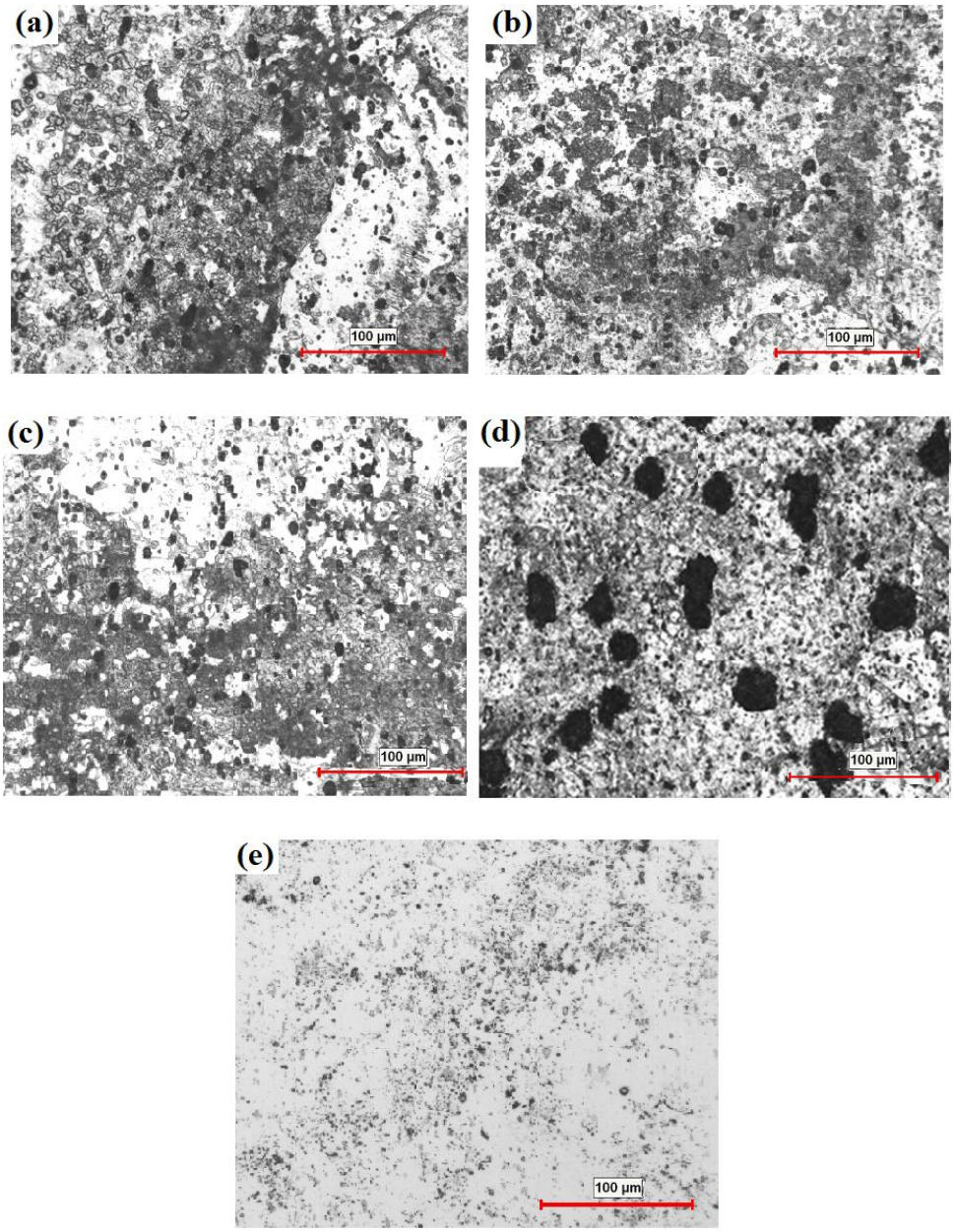

Fig.5.3. Optical images of bare and coated AA2024 with different *SAM*s after 120 cycles of cyclic corrosion test: a) standard AA2024, b) control AA2024, c) 8C-*SAM*s, d) 18C+Cl *SAM*s and e) 18C-*SAM*s coatings.

Based on these observations and the results obtained so far, it is possible to say that different chemical structures of alkylsilanes and hydrolysis and condensation kinetics of the silane head

groups could have dramatic impact on thin film structure and, thus, on the corrosion protection of the resulting films. It is supposed that the 18C-*SAMs* film also contain defect areas through which corrosion accelerants can penetrate to the metallic substrate beneath. However, a reasonable barrier property of 18C-*SAMs* prevents electrolytes or water molecules penetrating to the metal substrate to prevent further expansion of corrosion to the surrounding areas. Figure 5.4 illustrates corroded area percentage of the bare and coated aluminum samples over 120 cycles of cyclic corrosion exposure obtained by using CLEMEX Vision PE (Olympus BX51M) Mosaic Images Feature with a magnification of ×50 over a surface area of ~1631±35 mm^2 (28*24-frames). The gray cast corresponding to the corrosion product was defined. The share of the corroded area was calculated by dividing the dots having a white-to-gray cast by the whole number of dots representing the sample. It is shown in Fig. 5.4 that by increasing the cycle number of cyclic corrosion exposure, the percentage of corroded area for all samples, bare and coated Al substrate, increased, as it was also observed in Fig. 5.3.

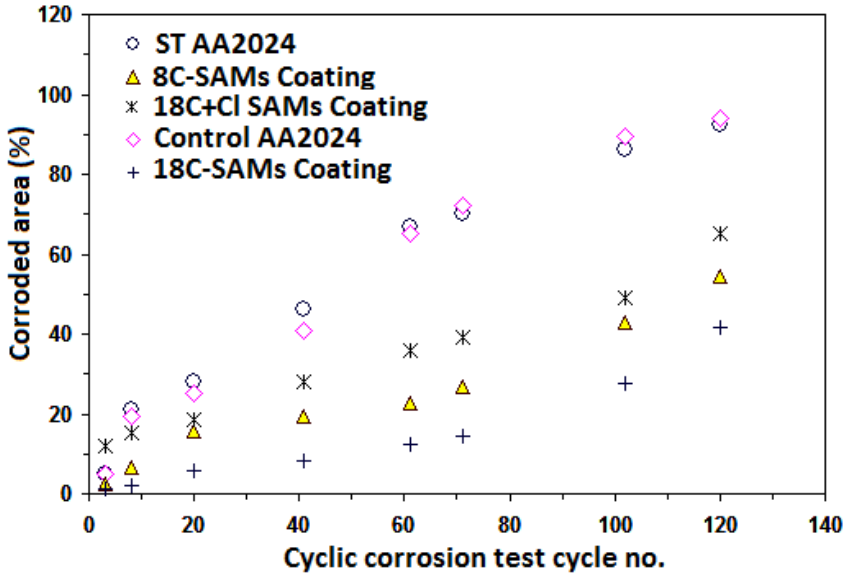

Fig.5.4. Portion of the corroded area of modified and unmodified Al samples exposed to the cyclic corrosion test.

However, as it is evident, in the case of bare standard and control AA2024, after 42 cycles of exposure, a substrate surface area of about ~50% was corroded and completely destroyed. For coated Al samples with 8C-*SAMs* and 18C+Cl *SAMs* coatings, however, this percentage was lower,

e.g. ~19 and ~28%, respectively. The most promising result again was obtained for the Al substrates coated with 18C-*SAMs*, where after 42 cycles of exposure, a surface corroded area of about ~9% was observed. Meanwhile, it is obvious that standard and control AA2024 both are demonstrating a high corrosion rate in all stages as the slope of the curves are too sharp and steep if compare to coated Al samples (even 8C-*SAMs* and 18C+Cl *SAMs* coatings). Meanwhile, the depth of the corroded area measured on standard AA2024 after cyclic corrosion tests via optical profilometry and/or AFM techniques showed a 2µm to 4µm depth (as shown in Fig.5.5). This means that during cyclic corrosion exposure, the Al substrate imposed to being corroded not only by distribution of corrosion on the outermost layer of the surface, but also by digging throughout the surface. In other words, it is possible to say that corrosion was initiated as pitting on the surface and then continued in a three dimensional (x, y, z) propagation and distribution.

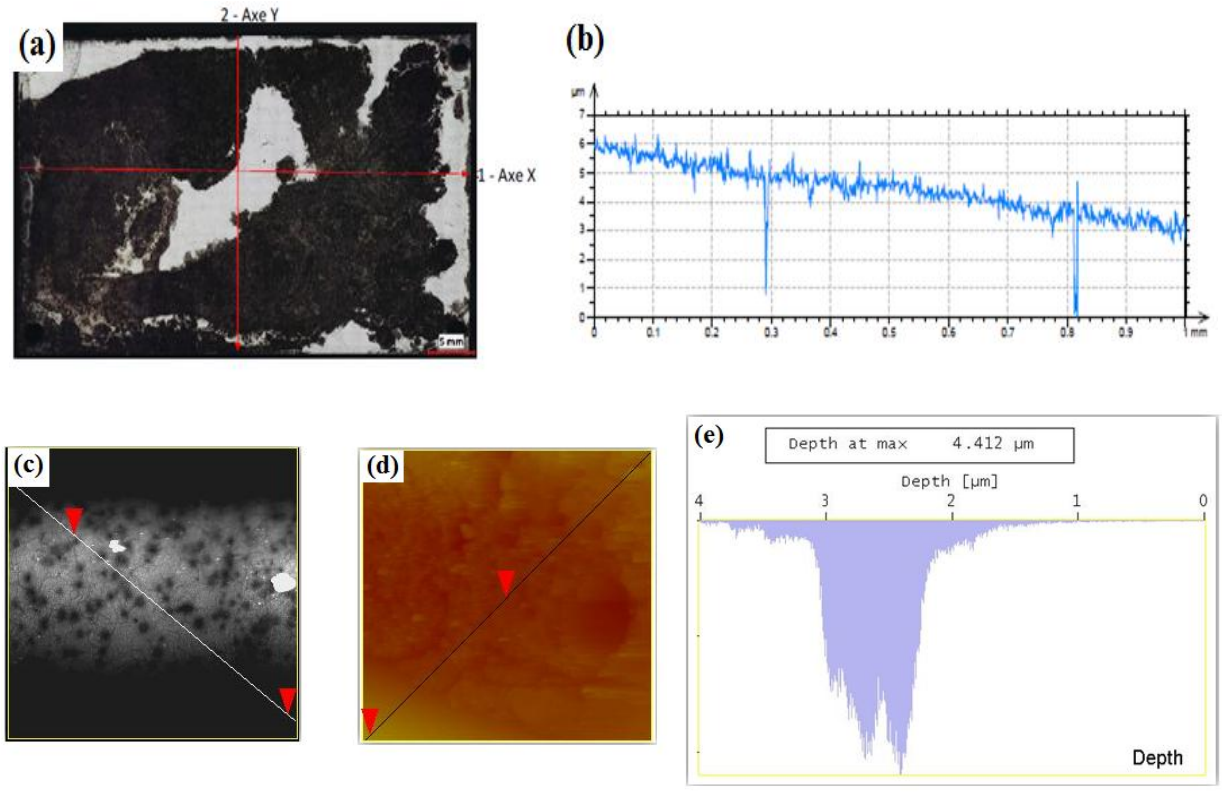

Fig.5.5. Depth of corroded area measured on standard AA2024 after cyclic corrosion tests via a and b) optical profilometry and c-e) AFM techniques.

5.2.3 Corrosion Resistance of Single Layer *SAMs* Coatings After One Week of Immersion in Saline Solution

A series of bare and coated Al samples with different *SAMs* used in this study were kept for one week in a 3.5% NaCl solution and their anti-corrosive performances were measured immediately via potentiodynamic polarization curves, as shown in Figure 5.6. Consequently, the values of $E_{corr.}$ and $j_{corr.}$ derived from corresponding polarization curves using Tafel extrapolation were obtained, see Table 5.2. It is obvious that the corrosion current density, $j_{corr.}$, of hydrophobic coating of 18C-*SAMs* on Al substrate decreased about one order of magnitude as compared to a similar untested one. Furthermore, all coated samples displayed reduced resistance to initiation of corrosion presented by small values of passive potential range (E_b-$E_{corr.}$) as shown in table 5.2.

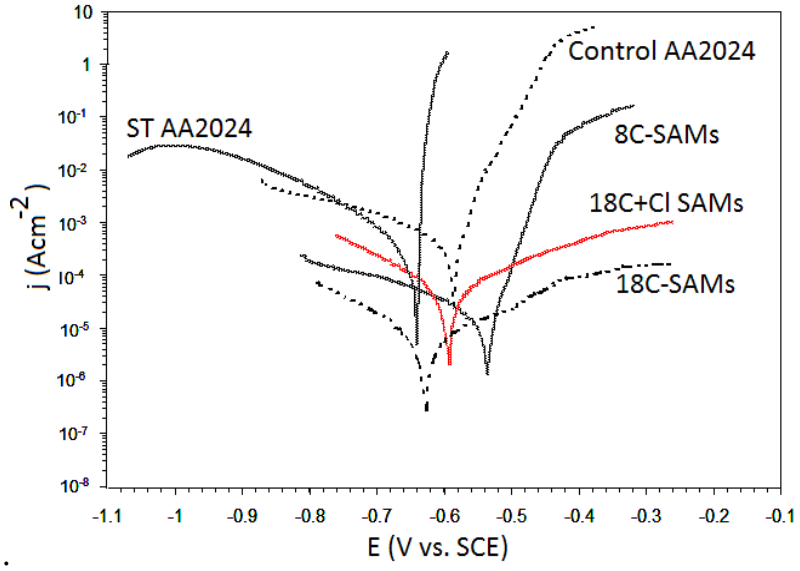

Fig.5.6. Potential and current density of bare and coated AA2024 samples with different *SAM*s after one week immersion in 3.5% NaCl solution.

These results point out that the hydrophobic coatings of different *SAMs* on Al surfaces, indeed, are permeable to electrolytes and moisture and are prone to undergo dissolution in humid or salted environment with aggressive ions of Cl^-. This leads to an accelerated corrosion rate. Based on observed results, it is possible to conclude that the barrier property of *SAMs*-modified Al samples decreased while undergoing saline test with respect to $E_{corr.}$ and $j_{corr.}$ values. This is most

likely due to the presence of defects, holes and imperfection in silane films. It should be noted that in all cases, however, *SAMs*-modified samples exhibited slightly better anti-corrosive performance compared to the unmodified (standard and control AA2024) samples.

Table 5.2. Potentiodynamic results of bare and coated AA2024 samples with different *SAM*s after one week immersion in 3.5% NaCl solution.

Specimen	$E_{corr.}$ (V *vs.* SCE)	$j_{corr.}$ (μAcm^{-2})	E_b-E_{corr} (V *vs.* SCE)
Control AA2024	-0.61 (±0.02)	878 (±121)	-
Standard AA2024	-0.65 (±0.03)	528 (±107)	-
8C-*SAMs*	-0.53 (±0.01)	52.2 (±7.1)	0.033
18C+Cl *SAM*s	-0.62 (±0.04)	89.1 (±9.7)	-
18C-*SAM*s	-0.63 (±0.02)	17.0 (±6.1)	0.09

5.2.4 Electrochemical Impedance Spectroscopy of Prepared Single Layer Coatings

Numerous reports exist on the use of electrochemical impedance spectroscopic (EIS) studies to understand corrosion of silane-coated-aluminum alloy, but none of them were conclusive. Silane molecules with diverse domains such as substrate binding part (siloxanes), electron transport region (aliphatic and aromatic spacer) and terminal functional groups (-SH, -CH_3 groups) are employed in the study in order to tune the electron transfer (ET) behavior or ionic diffusion across a *SAM* modified electrode-electrolyte interface. The ET behavior of coated samples was investigated more by electrochemical impedance spectroscopy (EIS). The electron transfer rate is determined from EIS curves by fitting them to an appropriate equivalent circuit model. Understanding details of structural arrangement, ordering and orientation of organic molecules self-assembled on substrate is necessary from both fundamental and applications point of view. Generally, *SAM*s are obtained by spontaneous chemisorptions of molecules to form a layer on a substrate. Nevertheless, few studies were carried out to investigate their blocking

behavior (barrier property) and electron transfer behavior across the electrode-electrolyte interface. From impedance data and equivalent circuit fitting procedure, the charge transfer resistance (R_{ct}), which provides resistance offered by monolayer film towards ET process across *SAM* modified electrode-electrolyte interface is calculated. By using the R_{ct} values, the surface coverage (Θ) of the corresponding thin films and other kinetics parameters associated with film formation were determined.

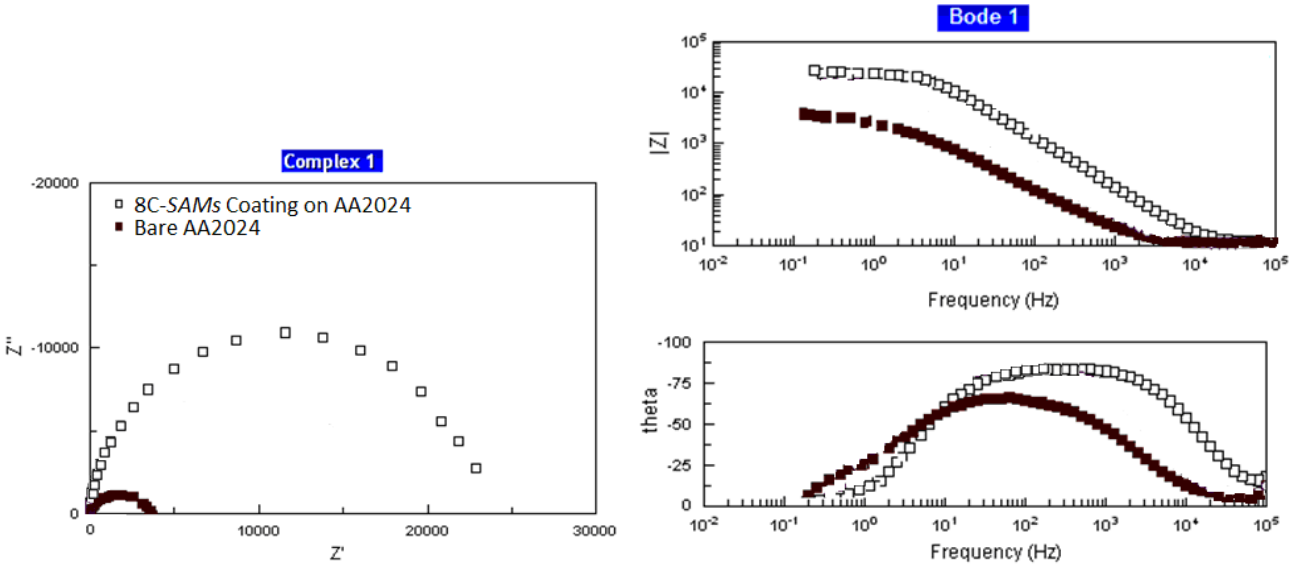

Fig.5.7. Impedance plots of bare AA2024 and coated AA2024 with 8C-*SAM*s in 3.5% NaCl aqueous solution. Bode phase angle (phase angle *vs.* logarithmic frequency) and frequency (logarithmic total impedance *vs.* logarithmic frequency).

Impedance measurements were carried out using an ac signal of 10 mV amplitude versus OCP in a wide frequency ranging from 100 kHz to 0.1 Hz via an electrochemical impedance analyzer at room temperature. In addition, the impedance data were useful to analyze distribution of pinholes and defects present within the *SAM* layer on Al surfaces. The impedance data were fitted to an appropriate equivalent circuit model using a Solartron analytical 1252A frequency response analyzer (FRA) coupled to a Solartron SI1287A electrochemical interface and Corrware® and Zplot® softwares. Typical EIS spectra (Nyquist and Bode plots) of bare as well as dissimilar *SAM*s modified samples immediately after exposure to 3.5% NaCl supporting electrolyte, are

shown in Fig.5.7-5.10. The Bode plots of phase angle and impedance *versus* frequency show characteristic differences between *SAM* modified and bare surfaces.

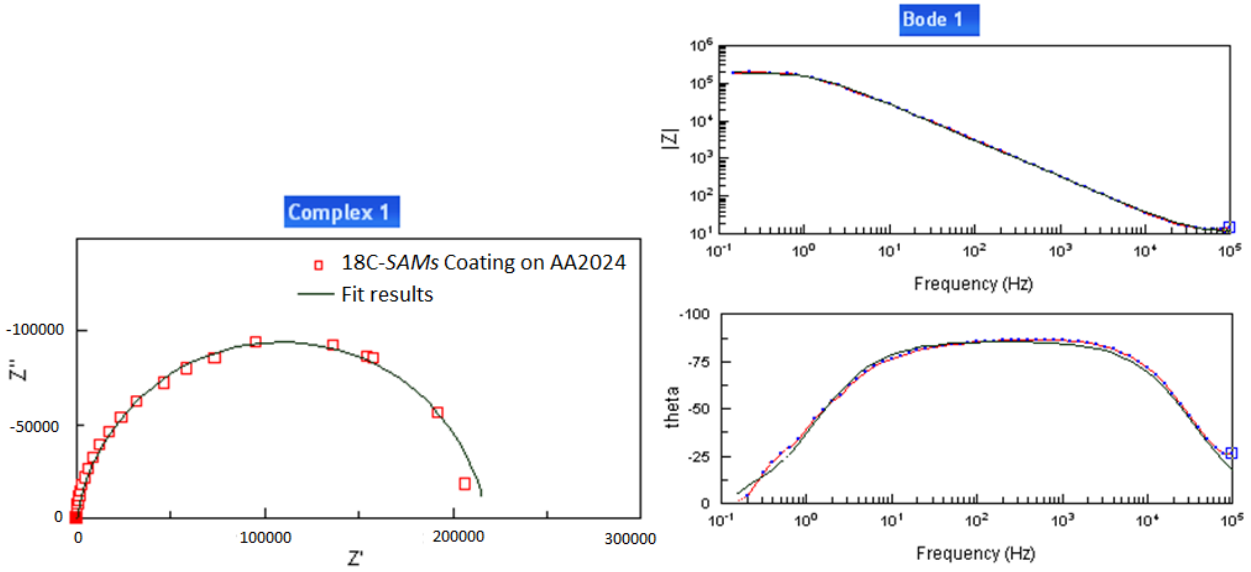

Fig.5.8. Impedance plots of coated AA2024 with 18C-*SAM*s in 3.5% NaCl aqueous solution. Bode phase angle (phase angle *vs.* logarithmic frequency) and frequency (logarithmic total impedance *vs.* logarithmic frequency).

Using impedance measurements and the difference observed in the phase angle, it is possible to classify these *SAM*s into pure and leaky capacitors. The NaCl solution was used in order to evaluate ionic permeation of *SAM*s to very small ions via electrochemical impedance spectroscopy [48, 49, 55, 202,239, 261]. In the meantime, it is well-known that more rapid formation of corrosion products occurs in the aerated solution. It can be seen in Fig.5.7-5.10 that the 18C-*SAMs* shows a higher phase angle, suggesting lower ionic permeation and, thus, this exhibits better insulating properties [48, 49, 202]. On the other hand, *SAM*s of 8C and 18C+Cl display a lower phase angle implying that these films show higher ionic permeation capability, resulting in poor insulating properties of corresponding *SAM*s. This means the presence of diffusional components in the low frequency region which cause permeating ions through these films [202, 239]. Meanwhile, the phase angles of -11.52, -17.38, -12.12 and -26.29 degrees at 100 kHz and -21.21, -6.84, -29.02 and -38.46 at 0.6 Hz and -64.48, -80.44, -81.28 and -88.4 at 100 Hz and 0.751, 0.115, 0.271 and -2.22 at 0.1 Hz were obtained for AA2024, 8C, 18C+Cl and 18C thin films on Al,

respectively. These values showed that the films of 18C behave much like an ideal capacitor while the *SAM*s of 8C and 18C+Cl act as a leaky capacitor through a resistive component arising mainly from presence of defects within the films [48, 49, 261]. Based on total impedance ($|Z|(\Omega cm^2)$) *vs.* frequency (*f*), it can be noted that the impedance values are higher and show good capacitive behavior for 18C-*SAM*s layer than other two layers. The higher phase angle values were obtained in the cases of *SAM* of 18C even at lower frequencies, where the ionic permeation is generally favored. This observation points to the fact that these molecules form more compact and dense layer with few pinholes and defects [48]. In contrast, 8C forms a poor monolayer film with a large number of holes and defects on Al electrode. It can be observed from Nyquist plots that bare AA2024 as well as coated Al samples with 8C and 18C+Cl *SAM*s show very small semicircle thought frequency region. This indicates that the ET process is reversible and essentially diffusion controlled [48, 49, 183, 202].

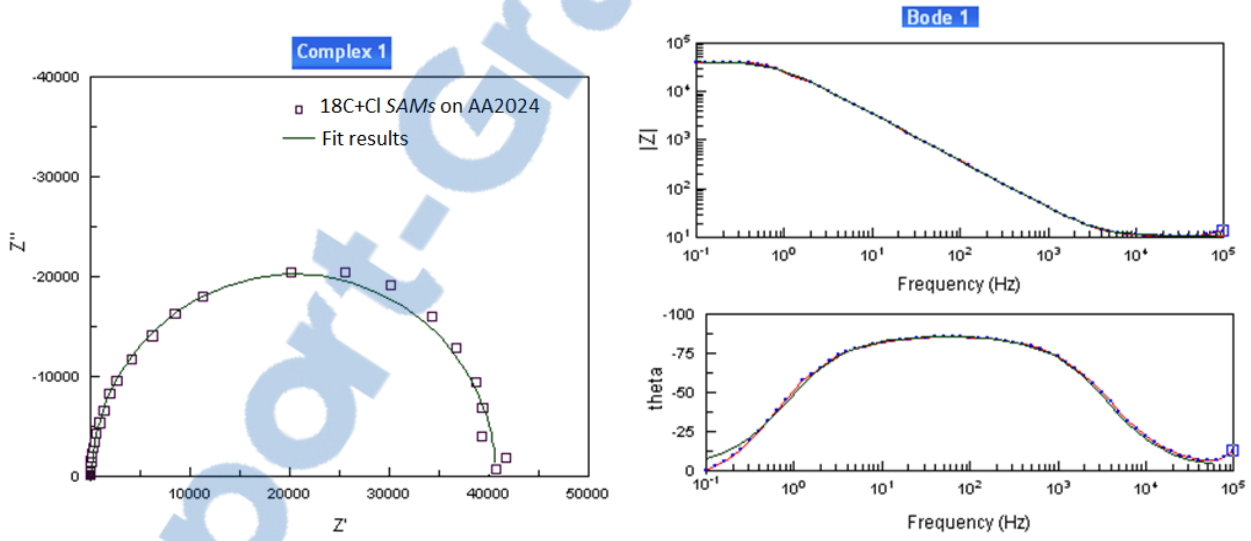

Fig.5.9. Impedance plots of coated AA2024 with 18C+Cl *SAM*s in 3.5% NaCl aqueous solution. Bode phase angle (phase angle *vs.* logarithmic frequency) and frequency (logarithmic total impedance *vs.* logarithmic frequency).

On contrary, layer coated Al of 18C *SAM* exhibit larger semicircle formation over the entire range of frequency indicating that the ET reaction is inhibited by displaying improved blocking behavior. In such cases, the process of ET is considered as charge transfer control process. Formation of quite large semicircles in the case of 18C-*SAMs* on Al (Fig.5.10) confirms

improvement in electrochemical blocking ability of this thin film against diffusion of aggressive molecule [183, 202]. For the bare AA2024 and 8C-*SAMs*, the low frequency impedance log|Z| (V) at 0.1 Hz decreased to ~3.5 and 4.3, respectively, indicating the_corrosion process [202]. For Al samples coated with 18C+Cl compound, log|Z| also decreased to approximately 4.5. However, log|Z| was already at the higher value of ~5.3 for 18C-*SAMs* coating. Decrease of low frequency impedance is often an indication of a more permeable barrier towards electrolyte ions and also the beginning of the corrosion process [48, 202]. The decreased low frequency impedance after film formation by *SAMs* of 8C and 18C+Cl compounds is most likely associated with those black dots, the locally corroded pitting areas of these samples. Since the EIS method is a sensitive technique to probe early stage corrosion, the impedance data obtained from these samples confirmed that local corrosion occurred in the Al sample during the modification process. The formation of a semicircle with a higher charge transfer resistance (R_{ct}) during EIS studies suggest that the film is a compact, well-ordered and with few defects and holes (superior blocking property) [48, 49].

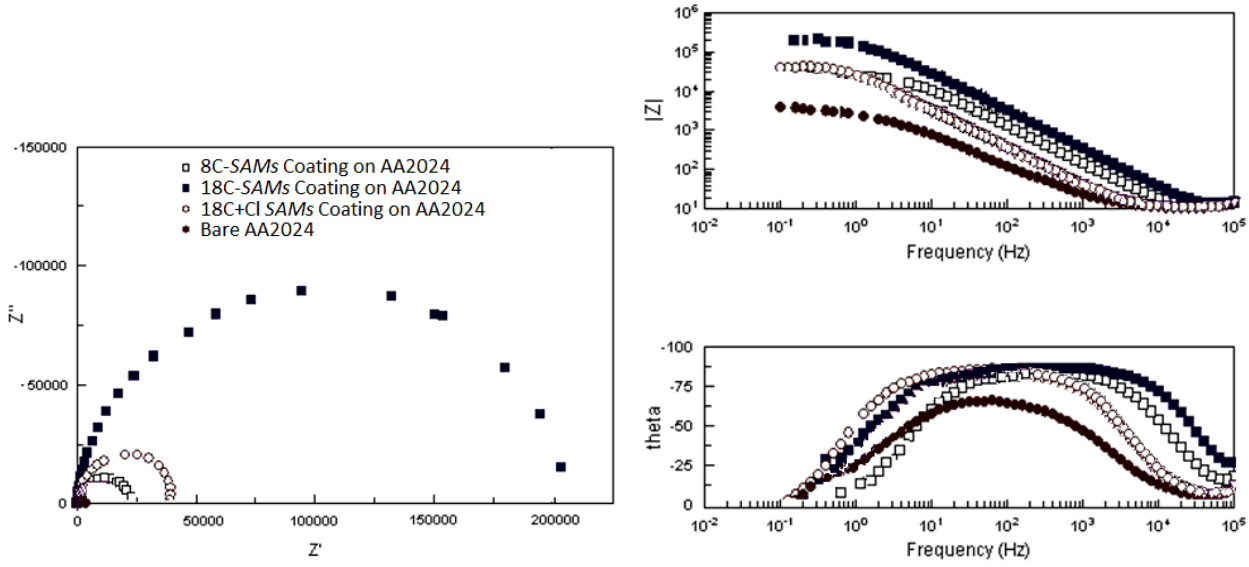

Fig.5.10. Impedance plots of bare and coated AA2024 with dissimilar *SAM*s in 3.5% NaCl aqueous solution. Bode phase angle (phase angle *vs.* logarithmic frequency) and frequency (logarithmic total impedance *vs.* logarithmic frequency).

The higher the charge transfer resistance is, the higher the blocking behavior is. The *SAM*s of 8C and 18C+Cl shows slightly larger semicircle compared to bare samples which indicates moderate blocking ability of these films on Al samples. These results are in good agreement with

potentiodynamic results discussed earlier. It was explained that the diameter of a semicircle obtained in an impedance plot is a measure for the charge transfer resistance, R_{ct}, which is higher in the case of *SAMs* modified samples compared to a bare electrode. This is due to inhibition of ET by formation of films on Al samples [202]. Finally, the impedance data are fitted to a standard Randle's equivalent circuit model (Fig.5.11) comprising a parallel combination of a constant phase element (CPE) and R_{ct} in series with the uncompensated solution resistance, R_s. Charge transfer resistance represents a diffusional parameter [202]. By an equivalent circuit fitting procedure using impedance data, the R_{ct} values of bare and *SAM*s modified Al electrodes can be determined. These values are shown in Table 5.3. It is obvious that the R_{ct} values of *SAMs* modified samples, as expected, are much higher when compared to that of a bare Al sample. This change in R_{ct} values implies a better blocking behavior of 18C-*SAMs* towards electrochemical reactions. Changes in the double layer capacitance and interfacial capacitance have been found to correlate to *SAMs* formation [48, 49]. The capacitance should decrease as the *SAMs* coverage increases, since the capacitance is inversely proportional to the distance between the charges. In addition, the polarization resistance, which corresponds to the charge transfer resistance in the pores of the monolayer or bare surface, increases as the coverage increases [48, 49]. The *SAMs* modified surfaces have larger impedance and a faster increase in phase angle than the bare substrates. These changes are associated with *SAMs* thin film formation. A multiple layer thin film assembled from hydrocarbon compounds may certainly acts as a better barrier for corrosion accelerants compared to a single monolayer [48].

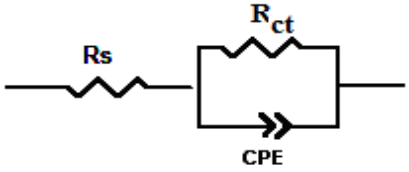

Fig.5.11. The equivalent circuit used to model EIS data. R_s is the solution resistance, R_{ct} is the polarization resistance and CPE is a constant phase element.

The potentiodynamic polarization test as well as the electrochemical impedance spectroscopic studies revealed that corrosion resistance of the 18C-*SAMs* coated samples improved compared to both 8C- and 18C+Cl-*SAMs* coated samples. It can be seen that *SAMs* of 18C exhibited higher R_{ct}

values compared to that of 8C and 18C+Cl and both films of 8C and 18C+Cl showed higher R_{ct} values when compared to bare AA2024 electrode. The Bode plots of phase angle versus frequency are nearly the same while impedance plot still have some differences (localized corrosion) in AA2024 [284]. It was explained that two main approaches were used to analyze EIS data. First involved looking at values found directly from impedance spectra and second involved equivalent circuit modeling. The EIS data was modeled with a *Randle's circuit* modified with a constant phase element (CPE) in place of a capacitor, as shown in Fig.5.11. The impedance of a CPE depends on the frequency via following equation: $Z_{CPE} = 1/C(j\omega)^n$, where C is capacitance. As "n" approaches 1, the impedance of CPE reduces to that of a true capacitor. After immersion in a saline solution, the R_{ct} values for *SAM* modified surfaces are larger than for a bare surface which indicates that R_{ct} increased. The blocking property of 18C-*SAMs* is higher as this layer exhibit higher R_{ct} value and the barrier property towards the ET is moderate in the case of *SAM*s of 8C and 18C+Cl as their corresponding R_{ct} values are smaller [183, 202, 284]. Using these R_{ct} values, the surface coverage of *SAM*s films (Θ) on Al electrodes can be calculated by applying the corresponding equation as follows [284]:

$$\Theta_{imp} = 1- [R_{ct} (STAA2024) / R_{ct} (coated\ aluminum\ with\ SAMs)] \qquad \mathbf{5.1}$$

Surface coverage was calculated with the assumption that the current is due to presence of holes and defects within the layer [284].

Table 5.3. ElS parameters data obtained for bare and coated Al samples after 2-h immersion in 0.1 M $NaHCO_3$ + 3.5% NaCl solution.

Sample	**AA2024**	**8C-*SAMs* Coating**	**18C+Cl *SAMs* Coating**	**18C-*SAMs* Coating**
R_s (Ωcm^2)	10.08 (±1.41%)	11.27 (±1.20%)	11.03 (±1.20%)	12.50 (±1.22%)
CPE (Fcm^{-2})	$4.35X10^{-5}$ (±1.03%)	$1.02X10^{-5}$ (±1.01%)	$4.97X10^{-6}$ (±1.15%)	$6.84X10^{-7}$ (±1.09%)
R_{ct} (Ωcm^2)	3750 (±0.30%)	22961 (±0.28%)	41500 (±0.26%)	214500 (±0.21%)

The surface coverage calculated for 18C-*SAMs* is ~98%, implying a formation of a well-ordered and dense film on Al sample and exhibiting an improved insulating property. In the case

of 8C and 18C+Cl *SAM*s, however, the surface coverage values were found to be ~83% and 91%, respectively. This indicates that these films were formed on the aluminum surface with a larger number of holes and defects (Table 5.4). Immediately after sample immersion in saline solution, the *SAMs* film behaves as a barrier to redox activity, as is evidenced by larger R_{ct} values. Meanwhile, as the capacitance, modeled by an equivalent circuit, is affected by *SAMs* type more than R_{ct} values [202, 284], then, it is possible to say that the redox activity occurs much on Cu-enriched particles on Al surface. Therefore, these particles are not covered completely by *SAMs coating*. Although there is a reasonable coverage on Al surface, however, the defects are probably centered on Cu-enriched particles, which are distributed throughout the alloy surface [202]. From R_{ct} and corresponding Θ values of impedance studies, it is clear that the blocking ability and barrier property of these films on Al samples follows the following order: 18C-*SAMs* > 18C+Cl *SAMs* > 8C-*SAMs*.

Table 5.4. Charge transfer resistance and surface coverage values calculated for bare and *SAMs* modified aluminum.

Sample	**AA2024**	**8C-*SAMs* Coating**	**18C+Cl *SAMs* Coating**	**18C-*SAMs* Coating**
R_{ct} (Ωcm^2)	3750 (±0.30%)	22961 (±0.28%)	41500 (±0.26%)	214500 (±0.21%)
Surface coverage (Θ_{imp})	---	83.7%	91.0 %	98.26%

This is in consistency with the results observed in potentiodynamic studies. The interfacial capacitance values of various coated Al samples can be calculated theoretically as $C=\varepsilon\varepsilon_o A/d$, where C is the capacitance, ε is the dielectric constant of the film, ε_o is the relative permittivity of vacuum, A is the area of electrode used and d is the thickness of the layer. If the measured capacitance is higher than what is measured theoretically, it can be understood that the thickness of layers is small [285, 286]. These three *SAMs* molecules were, in fact, selected in a way to have variation in electron transport domain (spacer region), alkyl change and terminal functionalities. As it can be observed from these results, the presence of a long aliphatic chain in the case of 18C-*SAMs* prevents ET to a larger extent in comparison with shorter aliphatic chains (8C-*SAMs*), where

ET can occur by tunneling [285]. Therefore, ET process can be tuned by the proper choice of *SAMs* molecules.

5.2.5 Corrosion Resistance of Single Layer *SAMs* Coatings after UV-ageing Test

Since dissimilar integrity was obtained by EIS studies for different *SAMs* used in this study, potentiodynamic polarization was carried out, in addition, on coated Al samples immediately after UV-aging test to study their anti-corrosive performance (Fig.5.12). The electrochemical parameters including E_{corr} and j_{corr} values are presented in Table 5.5. It is obvious that the corrosion current density, j_{corr}, of all hydrophobic *SAMs* coatings decreased after the test as compared to those before.

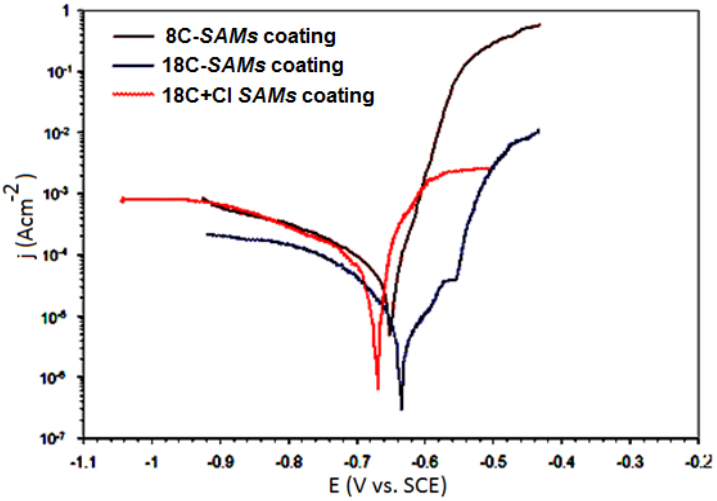

Fig.5.12. Potential and current density of bare and coated AA2024 with different *SAMs* after UV-ageing Test with condensation step.

These results confirm that these single layer *SAMs* coatings were not dense enough, but permeable to electrolytes and underwent dissolution in aggressive media leading to an accelerated corrosion rate. However, it is obvious that the barrier property of coated Al sample with 18C-*SAMs* was somewhat better with respect to E_{corr} and j_{corr} values. In the case of 8C and 18C+Cl *SAMs*, however, the situation was worse if compared to 18C-*SAMs* which definitely is due to the presence of imperfection or defects in silane films. This leads to the creation of a non-well-uniform *SAMs* on an Al substrate.

Table 5.5. Potentiodynamic results of coated Al after UV-aging test.

Specimen	$E_{corr.}$ (V *vs.* SCE)	$j_{corr.}$ (μAcm^{-2})	E_b-E_{corr} (V *vs.* SCE)
8C-*SAMs*	-0.65 (±0.05)	111.8 (±8.3)	0.03
18C+Cl *SAM*s	-0.67 (±0.03)	94.0 (±6.5)	-
18C-*SAM*s	-0.63 (±0.07)	12.18 (±3.4)	0.09

5.3 Conclusions

The corrosion resistance of bare and coated AA2024 substrates demonstrated that the value of $E_{corr.}$ positively increased for hydrophobic 18C-*SAM*s coating. However, it shifts slightly to positive values for Al sample coated with 8C-*SAM*s and 18C+Cl *SAM*s. This is obviously due to improved protective performance of a hydrophobic coating formed on an Al substrate. Meanwhile, the cyclic corrosion test exposure showed that the bare Al samples exhibited extensive corrosion after only 8 cycles of exposure with appearance of numerous black dots (pits) in micrometer scale. However, the earlier stage of corrosion observable in the case of hydrophobic Al samples coated with 8C-*SAM*s was after 12 cycles of exposure and a trace of corrosion was observed in the case of 18C-*SAM*s-modified samples even after 18 cycles of exposure. The most promising result again was obtained for the Al substrates coated with 18C-*SAMs*, where after 42 cycles of exposure, a surface corroded area of about ~9% was observed. A higher phase angle in the case of sample coated with 18C-*SAMs* suggested lower ionic permeation and therefore better insulating property. The impedance data were fitted to a standard Randle's equivalent circuit model. The R_{ct} values of coated samples with 18C-*SAMs* were much higher when compared to that of 8C-*SAMs*, 18C+Cl *SAMs* and bare Al sample (a better blocking behavior of 18C-*SAMs* towards electrochemical reactions). The surface coverage calculated for 18C-*SAMs* is ~98%, implying a formation of a well-ordered and dense film on Al (improved insulating property). In the case of 8C and 18C+Cl *SAM*s, however, the surface coverage values were found to be ~83% and 91%, respectively.

CHAPTER VI

HYDROPHOBICITY, ICEPHOBICITY AND DURABILITY OF DOUBLE LAYER COATING SYSTEM ON ALUMINUM SUBSTRATE

6.1 Introduction

Coating a surface with stable and environmentally friendly anti-ice materials can be an effective way to reduce and prevent ice accretion [34]. Meanwhile, anticorrosive performance becomes an important issue of coating durability and stability when we deal with metallic substrates such as high strength Al alloys. However, since the majority of anti-corrosive coatings are not hydrophobic, but rather hydrophilic, the selection of materials is seriously narrowed if hydrophobicity and icephobicity are among our objectives too. Therefore, another layer(s) is inevitably required to achieve this aim and obtain an anticorrosive property. Corrosion inhibition is a complex phenomenon which depends on the simultaneous effect of a variety of parameters, e.g. surface pre-treatment, ability of silanes to form highly cross-linked network, etc [34, 49, 172, 259]. Coupling agents such as 1, 2-bis-trioxymethyl-silyl-ethane or tetraethyl orthosilicate are among the best compromise solutions for corrosion inhibition due to their high cross-linking. They covalently bond to a hydroxylated surface substrate with one of the end groups, and to an organic molecule with the other end [260]. Such an "*anchoring layer*" can be then covered by a *SAM*s top layer, forming a thicker and denser coating.

The objective of this chapter is the detailed investigation on double layer coating systems consisting of a dense under layer providing anticorrosive performance and a top layer (alkylsilane-based layer) on AA2024.

6.2 Wetting Property and Coating Stability

6.2.1 Hydrophobicity of Double Layers Coating System

The liquid phase method was used to fabricate under layer(s) as a facile and cheap method and to increase the surface density of hydroxyl groups. This results in improving the surface density of subsequently grafted alkyl groups [50, 167, 172] and finally the anti-corrosive performance of the coatings. The thin layer tested as an anticorrosive under layer was an organosilane coupling agent of bis-1, 2-(triethoxysilyl) ethane (BTSE, $C_{14}H_{34}O_6Si_2$)) based on the *SAMs* coating deposition method. Curing of the silane layer has the potential for improving the barrier properties of the film [48, 50, 51, 172]. These silanes possess hydrolysable Si-O-C bonds on both ends of the carbon chain, known also as cross-linking agents [51, 52]. The BTSE layer is more efficient as a corrosion inhibitor because of its thickness that noticeably hinders penetration of aggressive solutions [51] and seems to be an interesting alternative system for replacing the toxic chromates [261]. Further cross-linking can lead to formation of Si–O–Si siloxane bonds by condensation of two silanols on which the protective action of these coatings will increase [48, 51, 172]:

$$\text{-Si-OH} + \text{HO-Si-} \rightarrow \text{Si-O-Si} + H_2O \qquad \textbf{6.1}$$

The optimum conditions reported by other researchers [52, 172, 229, 262, 263] were used in these series of tests. Attention was paid to maintain pH of the solution in the range of 4.5 to 5.0 at which a maximum amount of reactive silanol groups can interact with Al surface [52, 172, 229, 262, 263]. In the meantime, dense and more compact BTSE layer was obtained by curing step as BTSE films are dependent on deposition conditions, e.g. immersion time, curing etc [52, 172, 229, 263]. Organosilanes can be easily grafted to a surface by Si-O-Al bond. However, a challenge in modification of Al is to avoid using Cl^- ion releasing materials either as *SAMs* precursors or in subsequent manipulations. These ions can cause chloride-induced pitting corrosion [50]. Bare Al alloy is a hydrophilic substance with water contact angle and surface energy of ~ 41.5 ± 3^o and 46.36 ± 1.64 (mNm^{-1}), respectively. Aluminum is extremely reactive with atmospheric oxygen, and a thin layer of Al_xO_y forms on exposed Al surfaces [48, 52, 172]. The freshly formed Al_xO_y

layer on Al substrate was then reacted with BTSE molecules to form a covalently bound coating on Al surface. The values of contact angle and free surface energy in this step measured after BTSE deposition were ~ 62^{o} and 33.68 ± 1.11 (mNm^{-1}), respectively. However, after 18C-*SAMs* coating deposition for 5 min, both samples of 18C-*SAM*s alone and BTSE/18C-*SAMs* coatings demonstrate initial values of CA ≥ 110 ^{o} (Figures 6.1-6.3 and 6.4a) which indicates well-coated flat hydrophobic Al surfaces with 18C-*SAMs* thin film. Different immersion times were also applied; however, contact angle values correspond to immersion time of 5 min demonstrated superior wetting properties. Meanwhile, samples which underwent ~10 s sonication demonstrated more surface uniformity appearance in comparison with non-sonicated samples. The procedures to prepare single and double layer coatings were explained in more detail in chapter 3.

Fig.6.1. Contact angle values (deg.) of prepared single 18C-*SAM*s and double layer BTSE/18C-*SAM*s coatings on AA2024 samples (bare samples as reference).

6.2.2 Coating Thickness and Surface Energy Calculation

The optical property, refractive index of n, measured by MILTON ROY Co. refractometer at 20 ^{o}C were ~1.55 and ~1.56 for BTSE and 18C-*SAMs* solutions (both in isopropyl alcohol),

respectively. The thickness of BTSE coating, 18C-*SAMs* and BTSE/18C-*SAMs* thin films deposited on AA2024 substrate measured via spectroscopic ellipsometry were ~119 nm (n=1.36), ~10 nm (n=1.46) and ~108 nm (n=1.42), respectively. The wavelength range used to measure coating thickness was 400-1700 nm and in low incidence angles of 20, 25, 30, 35 degrees in order to further reduce depolarization. In fact, a multiple layer film could be formed on the Al surface between each layer, and the functional groups can polymerize together through hydrolysis/condensation reactions [51, 52, 172]. This polymer network provides denser layer with extra strength on Al surface to protect the substrate surface against water molecules, moisture, or any other aggressive molecules which may lead to accelerated corrosion. Free surface energy values of coated Al samples with single hydrophobic 18C-*SAM*s coating as well as double layer coating system of BTSE/18C-*SAM*s were calculated according to proper method. It is well known that the free surface energy of a surface is a characteristic related to surface chemistry, depending on its chemical composition and atomic arrangements near the surface [41, 172] and therefore, the smaller the surface energy is, the more water repellent it will be [32]. Tables 6.1 presents the surface energy values of prepared single and double layer coatings obtained from contact angle measurements. As is obvious, the values of contact angle and free surface energy for Al sample coated by BTSE layer were ~ 62.3^{o} and 33.68 ± 1.11 (mNm^{-1}), respectively. However, after 18C-*SAMs* deposition, the BTSE/18C-*SAMs* sample demonstrates initial values of contact angle and free surface energy of ~111.6^{o} and 6.03 ± 1.06 (mNm^{-1}), indicating well-coated flat hydrophobic Al surfaces [40, 172, 173, 190, 191].

Table 6.1. Contact angle (degree) and free surface energy [ε (mNm^{-1})] of AA2024 coated with single and double layer *SAM*s coatings.

	As-received AA2024	**Mirror polished AA2024**	**BTSE coating**	**18C-*SAMs* coating**	**BTSE/18C-*SAMs***
Contact angle and free surface energy values	41.5 ± 3^{o} ε: 46.36 (±1.64)	80.6 ± 2^{o} ε: 23.27 (±1.25)	62.3 ± 2^{o} ε: 33.68 (±1.11)	111.3 ± 2^{o} ε: 6.03 (±1.14)	111.6 ± 1^{o} ε: 6.03 (±1.06)

It is clear that for double layer coating system, the surface energy value is much smaller than for a sample coated with BTSE layer alone (i.e. 33.68 ± 1.11 (mNm^{-1}). Moreover, the free surface energy values of both single and double layer *SAM*s coatings are quite similar and close to each other, i.e. 6.03 ± 1.14 and 6.03 ± 1.06 (mNm^{-1}) for single and double layer *SAM*s coatings respectively. Overall, in both cases, the surface energies are much smaller than those obtained on bare samples, i.e. 46.36 ± 1.64 and 23.27 ± 1.25 (mNm^{-1}) for as-received and mirror-polished AA2024, respectively.

6.2.3 Coating Stability and Durability in Different Conditions

The stability of the coatings is an essential factor in the lifetime of a coating under extreme environmental conditions. Acidic rain with a pH in a range of 4 to 6 is an environmental problem in urban and industrial areas, and it can have harmful effects on outdoor infrastructure. Consequently, the study of the stability of a coating in acidic outdoor conditions is necessary. In addition, in order to apply the double layer hydrophobic coatings to industrial fields, it is critical to know the chemical stability of the coatings in different pH solutions [264]. Therefore, in order to evaluate the stability of the coatings against rainwater in outdoor conditions and other applications, coated surfaces were exposed to different pH solutions including acidic, basic and neutral solutions, and the resistance of the coating against different buffers at different pH levels was investigated. Figures 6.2 and 6.3 present contact angle values of AA2024 samples coated with 18C-*SAMs* alone or with BTSE/18C-*SAMs* layers as a function of immersion time in nano-pure and tap water with water conductivity of ~0.26 and 89.3 μScm^{-1} at 20 ^{o}C, respectively as well as basic and acidic media. While these samples demonstrated hydrophobic properties (CA ≥ 110 ^{o}), however, it can be observed that the contact angle values decrease over immersion time. A large contact angle can be considered as a characteristic for well-covered, complete and homogeneous hydrophobic *SAMs* coatings. The coated samples were found to gradually lose their hydrophobic properties completely after ~1100-h of immersion in different media, which was

associated with the decrease of water contact angle values (Figure 6.4b). This tendency to lose hydrophobicity is most likely due to R'Si-O-SiR bond rupture between 18C-*SAMs* molecules and BTSE layer caused by hydrolysis of corresponding bonds. Hydrolysis of Al-O-Si-R bonds leads to formation of Al-OH and RSi-OH components (-OH groups), a fairly hydrophilic functional group on Al surface samples [49, 172]. Therefore, more a hydrophilic property presented by decrease of water contact angle (CA) was observed.

It can be seen in Figure 6.3 that the contact angle values of double layer coating systems decreased slightly from ~ 110 ° to ~ 97 º after an immersion time of 320 hours. After that, the contact angle decreased significantly after 710 hours of immersion in water when it reached about 88 º and as the immersion time increased to 1100 hours, the contact angle decreased to 84 º. It should be noted that 18C-*SAMs* layer (~10 nm) degraded initially in comparison with BTSE layer which is thicker (~119 nm). The coatings degrade, in fact, within several days of immersion in aggressive media. Loss of hydrophobicity as a decrease of contact angle values was slightly faster for samples immersed in tab water compared to samples immersed in nano-pure water which is probably due to the influence of salts dissolved in tap water, a reason for the accelerated rate of coating deterioration. A decrease in surface hydrophobicity can also be observed clearly in Figure 6.4b, implying the decay of coatings. These results show that for the first 200 hours of immersion, pH values had small effect on the contact angle of these coatings. However, immersion in acidic or basic solutions for more immersion time (>200 hours) decreased the contact angle more significantly if compared to nano-pure water (pH~7) which shows the effect of pH and the buffer compositions on coating performances. Meanwhile, the contact angle results showed a reasonable resistance in neutral solutions. The contact angle decrease (hydrophobicity) was faster for samples immersed in basic media compared to samples immersed in acidic and/or neutral solutions. This observation is attributed to the influence of basic conditions on Al oxide layer stability and therefore the rate of Al corrosion in basic media [202] which leads to accelerated coating deterioration.

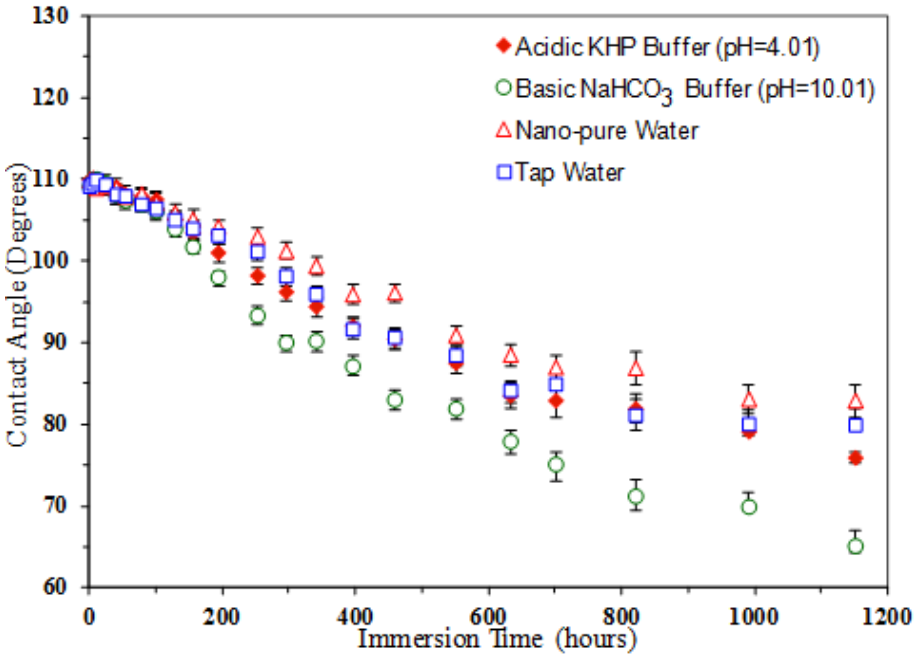

Fig.6.2. Contact angle *vs.* immersion time in different pH conditions for Al sample coated with 18C-*SAMs* coating.

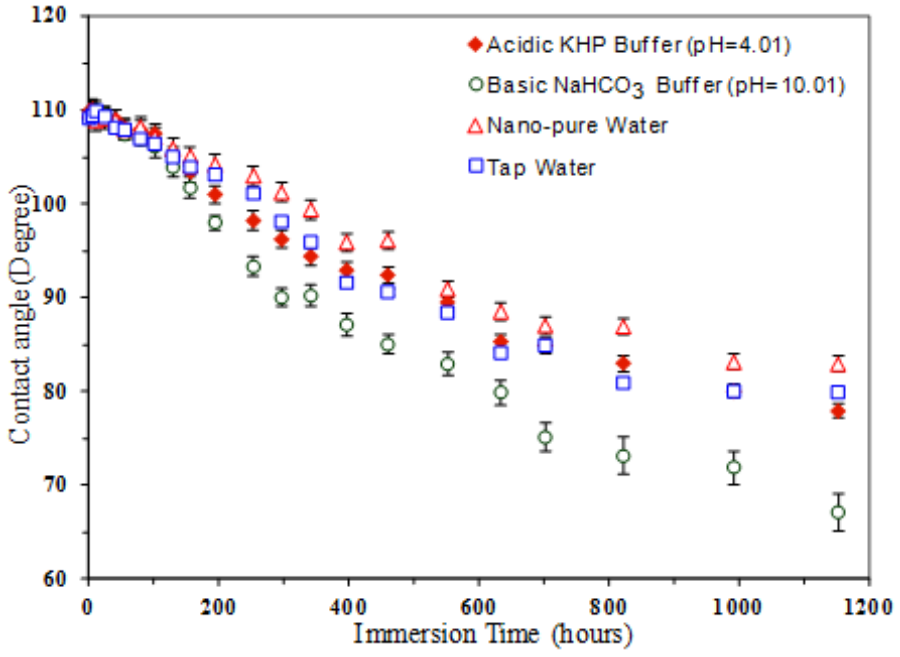

Fig.6.3. Contact angle *vs.* immersion time in different pH conditions for Al sample coated with BTSE/18C-*SAMs* layers.

Figure 6.4 presents water droplet images on a coated AA2024 sample with BTSE/18C-*SAMs* before (a) and after a ~820-h immersion in nano-pure water (b). By immersing Al substrate in aggressive conditions, the thin 18C-*SAMs* layer undergoes some degree of degradation initially, compared to the thicker BTSE layer [48]. As a result, alkylsilane molecules were removed from the surface, resulting in a decrease of surface hydrophobicity. The top *SAM*s layer, indeed, is believed to be not dense enough or too thin and not sufficiently cross-linked to prevent water molecules or other aggressive ions from penetrating through the coating to the surface beneath.

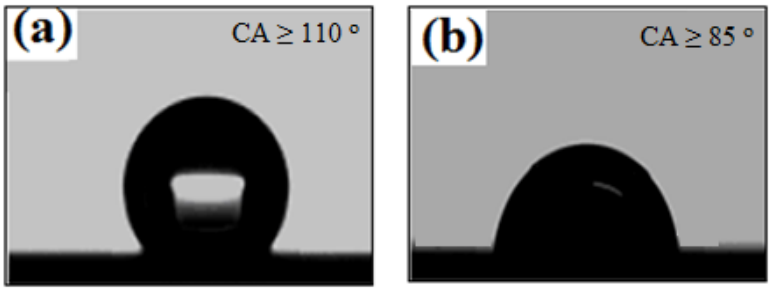

Fig.6.4. Water droplet images on a coated Al sample with BTSE/18C-*SAMs* before (a) and after (b) an ~820-h immersion in nano-pure water.

It is worthy to mention that the acidic and alkaline buffer solutions used in the present study were color-coded "*Thermo Scientific™ Orion™ pH Buffers"* contained potassium hydrogen phthalate ($C_8H_5KO_4$, KHP), sodium carbonate (Na_2CO_3)/bicarbonate ($NaHCO_3$) and Methylparaben ($C_8H_8O_3$), respectively (Figure 6.5).

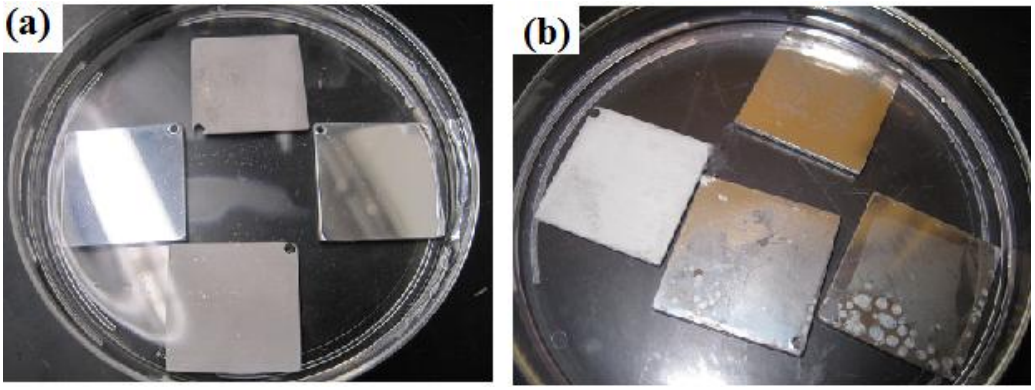

Fig.6.5. Al samples immersed in basic solution (a) initially and (b) after finishing the stability test.

6.2.4 Surface Chemical Composition Analysis via X-ray Photoelectron Spectroscopy (XPS)

Figures 6.6 to 6.9 show the XPS spectra of AA substrates coated with BTSE, 18C-*SAMs* and BTSE/18C-*SAMs* layers, respectively. The high-binding-energy peaks at 284.6 and ~281 (eV) correspond to the existence of C-H, C-C and C-Si bonds, respectively, with high concentration implying on presence of alkylsilanes molecules on Al surfaces. Accordingly, the XPS signals of C, O and Si, as presented in Figures 6.6 to 6.9, showed covered Al substrates with corresponding molecules (layer).

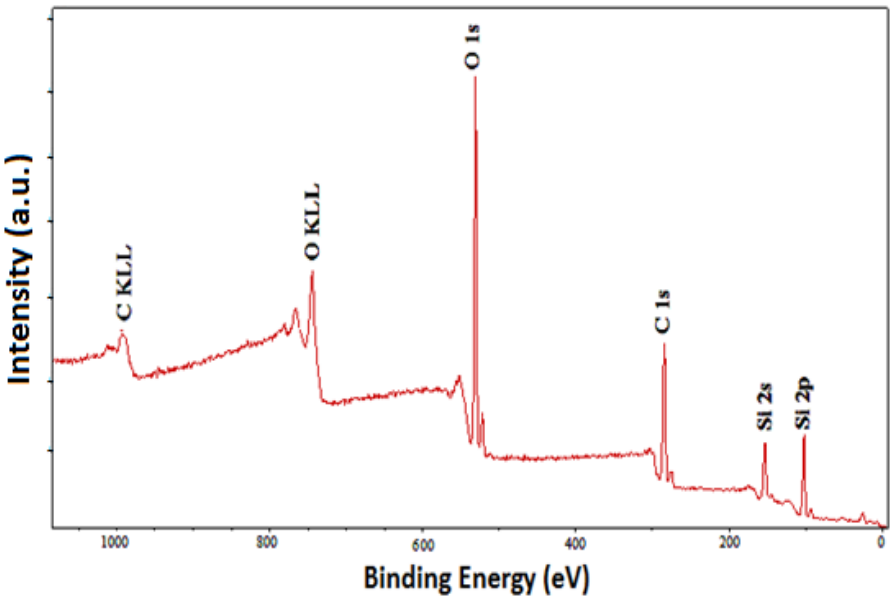

Fig.6.6. XPS spectra of Al sample coated with BTSE layer [Al Kα X-ray source, 1486.6 (eV)].

The BTSE under layer is thicker than the analysis depth of the XPS, so that, in the BTSE and BTSE/18C-*SAMs* samples, as presented in Figs. 6.6 and 6.9, no trace of Al peak is observed. However, the 18C-*SAMs* upper layer is not as thick as the BTSE under layer, which is why the Al peak is visible in the spectrum for 18C-*SAMs* alone (Figure 6.7). The XPS spectra can be obtained at high resolution, focusing on the specific binding energy of the C 1s fitting components, as shown in Figure 6.9 for BTSE/18C-*SAMs* coating. The spectrum can be satisfactorily fitted with a combination of four distinct peaks: the peak at 284.6eV corresponds to C-C or C-H species, the

peak at 286,2eV to C-O or C-OH groups, the peak at 288.3eV corresponds to O-C=O, and the peak at 282eV to C-Si.

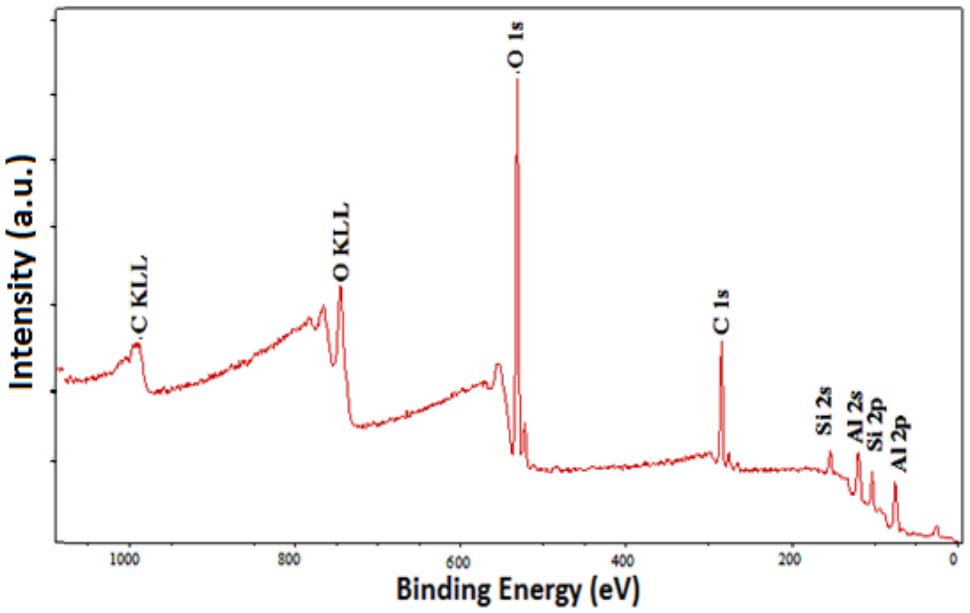

Fig.6.7. XPS spectra of Al coated with 18C-*SAM*s alone [Al Kα X-ray source, 1486.6 (eV)].

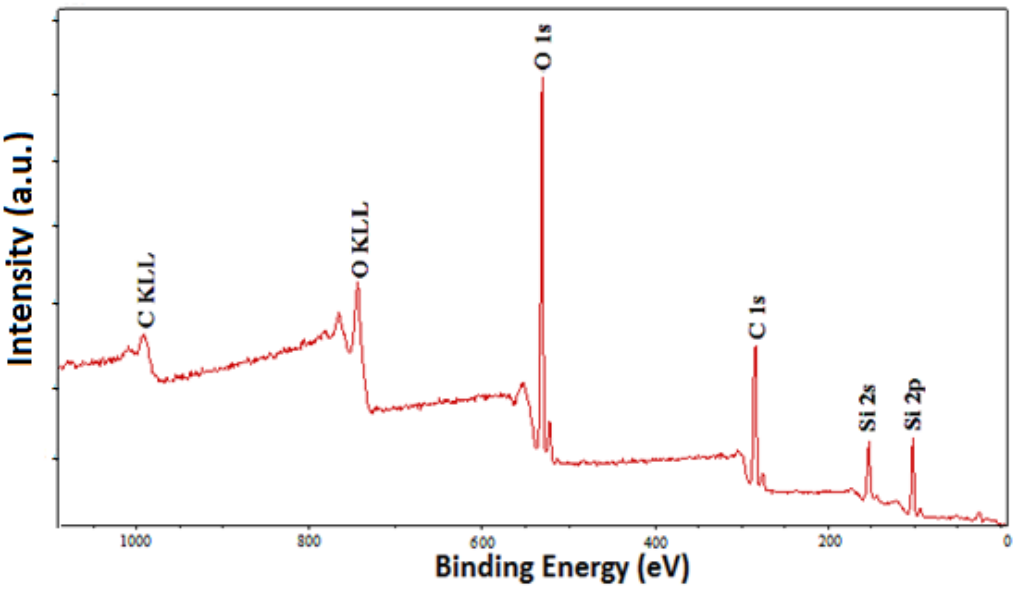

Fig.6.8. XPS spectra of Al coated with BTSE/18C-*SAM*s coating [Al Kα X-ray source, 1486.6 (eV)].

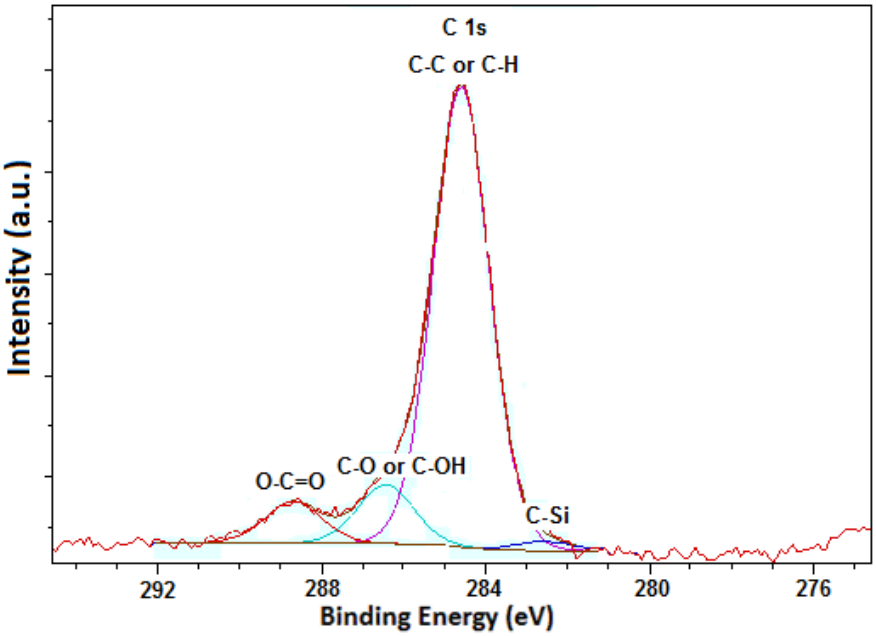

Fig.6.9. C1s spectra of Al sample coated with as-prepared BTSE/18C-*SAM*s.

Therefore, based on the XPS analysis results, it is possible to conclude that the Al substrates were covered with their corresponding alkylsilane molecules. In fact, when the silanol (R-Si-OH) groups are in contact with the hydroxylated surface of Al, this accelerates the formation of interface bonding of Al-O-Si in two steps, conversion to silanol followed by condensation on Al surface. The silanol undergoes a condensation reaction with a hydroxide group on the surface forming the siloxane linkage (X-O-Si).

6.2.5 Surface Characterizations (Prior to Test)

Figures 6.10 to 6.6.12 present the AFM images, optical microscope images and SEM survey of both series of bare and coated AA2024 surfaces with 18C-*SAMs* and BTSE/18C-*SAMs*, demonstrated flat uniform surfaces. It is obvious from the optical microscopy presented in Figure 6.11 below that the Al substrates after coating and before subjecting to the test environment (aggressive media) are quite similar, without any sign of corrosion or even removing or dissolving the inter-metallic second phase particles (inert particles) and/or pitting on the substrate surface.

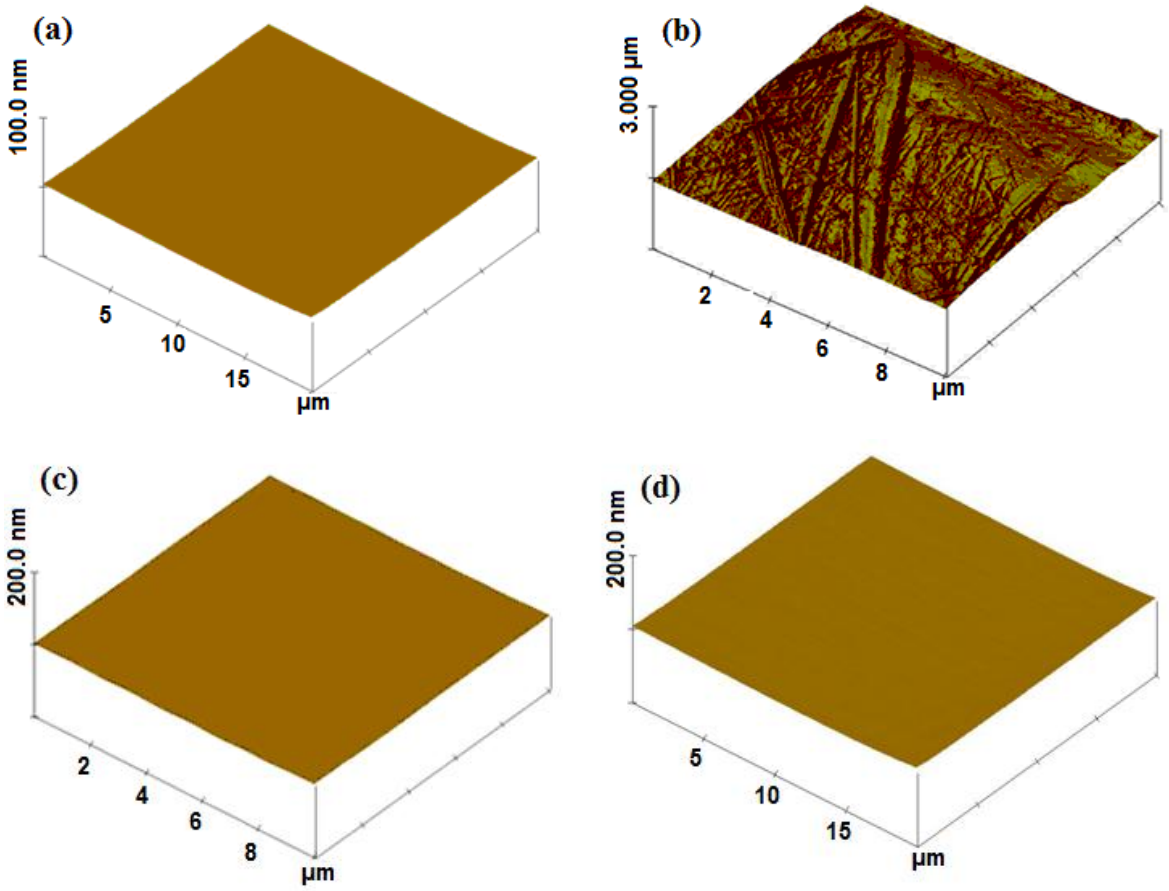

Fig.6.10. AFM images of: (a) bare standard AA2024 (R_{rms}: ~ 28 nm), (b) as-received AA2024 (R_{rms}: ~ 177 nm) and Al surface coated with (c) single 18C-*SAM*s (R_{rms}: ~ 25 nm) and (d) BTSE/18C-*SAM*s (R_{rms}: ~ 33 nm) prior to test.

The morphology and chemical composition of prepared coatings before and after stability tests were studied to find any changes in sample surface and coating composition (Figs. 6.10-6.12). The BTSE coating, indeed, forms a layer with more closely packed and dense than 18C-*SAMs* top layer (more defective domains). Coating with less defective domains provides better corrosion protection.

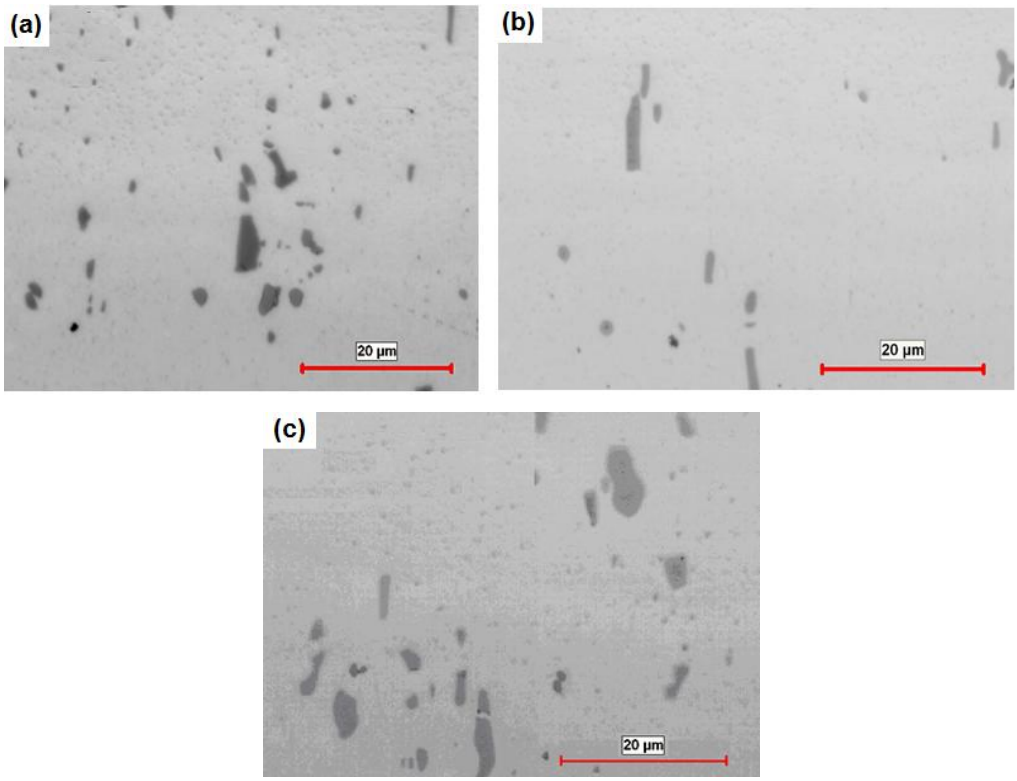

Fig.6.11. Microscopic images of: (a) bare standard AA2024 (x1000) and as-prepared coated Al surface with (b) 18C-*SAMs* (x1000) and (c) BTSE/18C-*SAMs* (x1000), prior to test.

6.2.6 Surface Characterizations (After Stability Test)

Surface morphology obtained from optical microscopy and SEM observations for Al samples coated with single 18C-*SAMs* and double layer BTSE/18C-*SAMs* after 700-h immersion in water is presented in Figs.6.12 and 6.13. It is evident here that signs of corrosion and corrosion products around second-phase inter-metallic particles which are nobler, compared to the surrounding Al matrix, can be clearly observed in sample coated with single 18C-*SAMs*. This explains well the contact angle measurements presented in Figure 6.2. The 18C-*SAMs* layer is not believed to be dense enough to prevent water molecules from penetrating through the coating and reaching to the coating-substrate interface. This caused both the corrosion processes, whose effects are seen in Figure 6.13b, and the hydrolysis of the Si-O-Si bond, through which the 18C-*SAMs* molecules were attached to the surface.

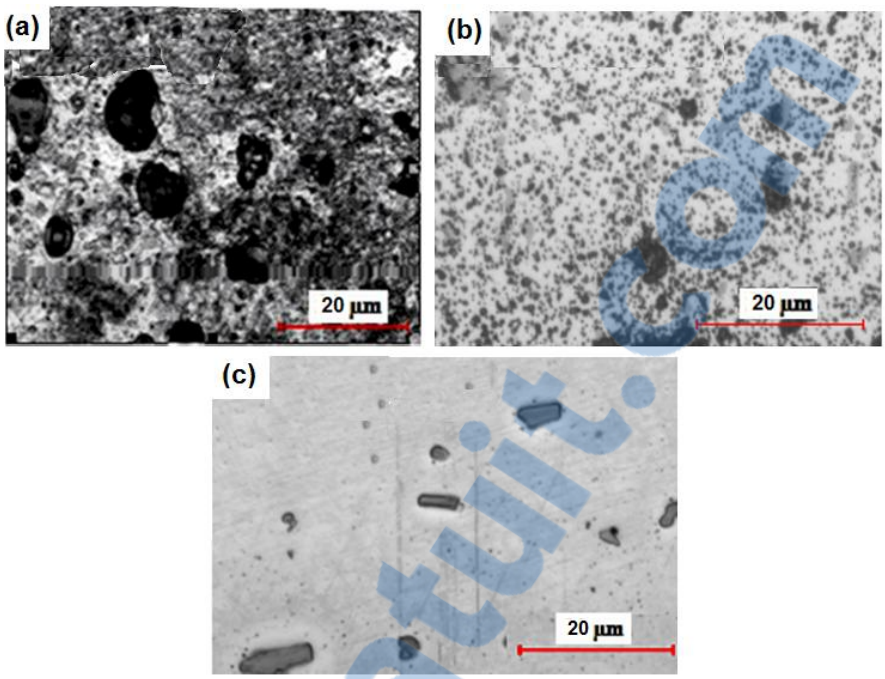

Fig.6.12. Optical microscope images of (a) bare standard AA2024 (x1000) and coated surface with (b) 18C-*SAMs* (x1000) and (c) BTSE/18C-*SAMs* (x1000), after 700-h immersion in water.

Some alkylsilane molecules were thus removed from the surface, resulting in a decrease of hydrophobicity. A film with less defective domains will result in better corrosion protection of the Al surface substrate. The AA2024 contains Cu-enriched second-phase inter-metallic particles, confirmed by EDX analysis during SEM survey (see Fig.6.14). Therefore a large number of these particles can influence the film performance. In other words, the corrosion products are also believed to contribute to the decrease of contact angles observed in Figure 6.1. However, in the case of AA surfaces coated with BTSE/18C-*SAMs*, corrosion and corrosion products around second-phase inter-metallic particles are significantly less compared to single layer 18C-*SAMs* coating. The BTSE under layer, in fact, provided a dense coating on Al substrate which prevents penetration of water or any other aggressive molecules through coating to the underlying metallic substrate. Optical microscope and SEM analysis revealed that while the earliest corrosion products came into sight on bare samples after only ~20 hrs of immersion in an aqueous media, local corrosion and pitting in the matrix regions or around second-phase particles

was observed after ~310 and ~700 hrs exposure to aqueous media in the case of 18C-*SAMs* and BTSE/18C-*SAMs* coatings, respectively (Figs.6.12 and 6.13).

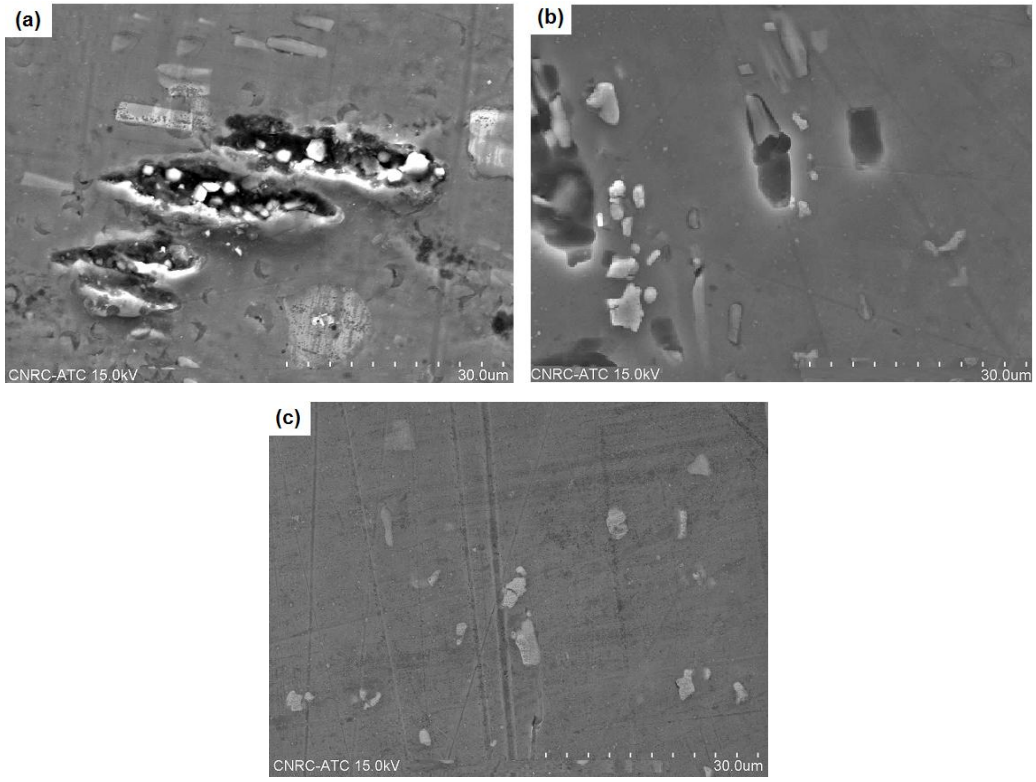

Fig.6.13. Backscattered SEM images of (a) bare and coated Al surface with (b) 18C-*SAMs* and (c) BTSE/18C-*SAMs* after 700-h immersion in water.

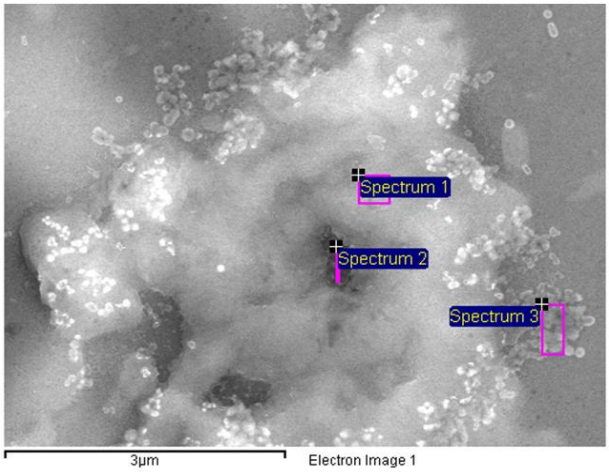

Spectrum	O	Mg	Al	Si	Mn	Cu
Spectrum 1			77.16		1.72	18.40
Spectrum 2	5.59	0.87	79.36		0.79	12.29
Spectrum 3	7.23	1.63	85.89	1.68	0.23	3.34
Max.	7.23	1.63	85.89	1.68	1.72	18.40
Min.	5.59	0.87	77.16	1.68	0.23	3.34

Fig.6.14. EDX results and SEM images of bare standard AA2024 after stability test (immersion in water).

For an Al substrate coated with 18C-*SAMs*, a number of inter-metallic particles were dissolved and removed from the matrix (see Figs.6.12 and 6.13). This is due to rapid dissolution and corrosion rate occurred by immersion in aggressive media. Following corrosion distribution, the coating layer finally loses adhesion with the metal surface, making the substrate more vulnerable to the corrosion process.

6.2.7 X-ray Photoelectron Spectroscopy Results (After Stability Test)

The X-ray photoelectron spectroscopy analysis was used to study the chemical composition of tested Al samples (Table 6.2), demonstrating altering coating chemistry. While the 18C-*SAMs* coating showed a significant peak of Si 2p before the test (silane layer on Al surface), its atomic concentration decreased remarkably after immersion in acidic media. This confirms the hypothesis that aggressive molecules hydrolyze the -O-Si-R bond and gradually destroy the silane layer on the Al substrate. However, in the case of a double layer coating of BTSE/18C-*SAMs*, the Si 2p peak does not change much after the test. Similar processes are expected in the case of samples immersed in other media.

Table 6.2. XPS results of Al surface coated with 18C-*SAMs* and BTSE/18C-*SAMs* coating before and after stability test.

Element	18C-*SAM* coating		BTSE/18C-*SAM* coating	
	% At. Concentration		% At. Concentration	
	Before	After	Before	After
C 1s	44.08	29.95	47.32	56.92
O 1s	30.10	42.07	29.70	21.44
Si 2p	13.15	2.18	22.98	16.84
Al 2p	12.67	25.15	n/a	3.16
Na 1s	n/a	0.65	n/a	1.64

6.3 Durability of Single and Double Layer Coatings at Ambient Conditions

A series of Al samples coated with 18C-*SAMs* and BTSE/18C-*SAMs* layers was kept at ambient conditions of T: (18-21 ^{o}C) and humidity of 30 to 53 % RH to evaluate their stability over long period of time, as shown in Figure 6.15.

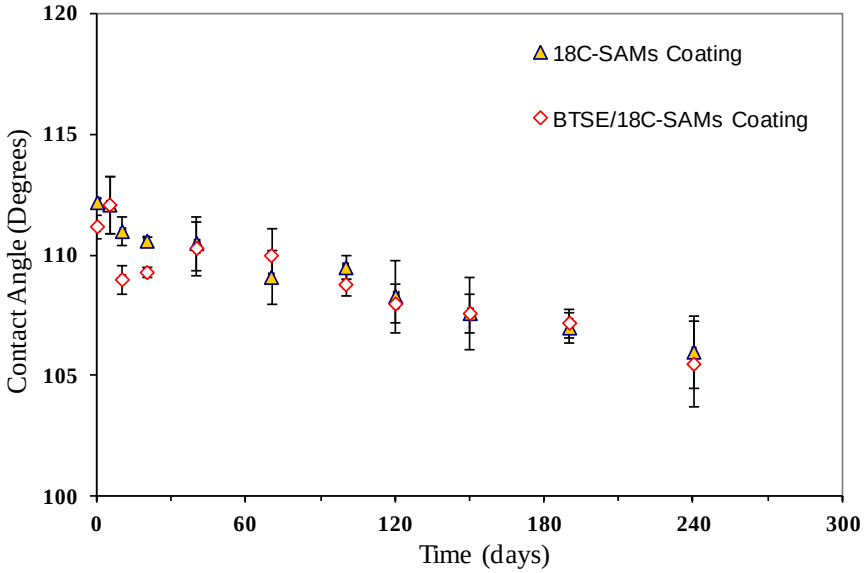

Fig.6.15. Stability of flat AA2024 sample coated with 18C-*SAM*s and BTSE/18C-*SAM*s coatings kept at ambient condition.

A reasonable stability was observed for coated Al samples with these *SAM*s coatings in all cases at ambient conditions and over time. As it is obvious in Figure 6.15, no considerable changes were observed after 240-days of keeping at ambient conditions. Both single and double layer *SAM*s coatings demonstrated slight degradations over time.

6.4 Effect of UV Radiation on Hydrophobic Properties of single and double layer *SAM*s Coatings

The stability of the coatings is an essential factor in the lifetime of a coating under extreme environmental conditions. In order to study and evaluate coating stability in a simulated natural weathering process for potential outdoor applications, their aging performance was examined against UV exposure. In several studies, superhydrophobic coatings were fabricated via different methods; however, few of them investigated the stability of such coatings under simulated environmental conditions, e.g. UV degradation, rainwater and ice-accumulation. UV-degradation is an important aging process when coatings are exposed to atmospheric weathering

conditions. These icephobic coatings, indeed, must essentially accomplish both of the following requirements: first, they must efficiently reduce snow or ice adhesion force; and second, they must have a reasonably long service life or stability. For the second requirement, the prepared single and double layer *SAM*s coatings were examined under different conditions, in various pH solutions and UV degradation. Stability against various pH solutions was studied in the above sections. Long service life or durability of the coatings is an important factor in the lifetime of a coating under extreme environmental conditions. Sunlight or ultraviolet UVA/B light is considered to be one of the most important reasons for coating degradation. Consequently, the accelerated UV weathering was used to simulate and then assess damage of outdoor conditions in a controlled environment. The Al samples were exposed to a UVA-340 fluorescent lamp according to ASTM G154. The test cycle was 8-hours with 0.89 Wm^{-2} irradiance and a temperature of 60 ºC in the QUV accelerated weathering tester. The water contact angle of each sample was measured before and after UV cycles. It was mentioned earlier that almost each 537-h of artificial UV exposure is equal to one year of sunlight exposure in Canada [256]. Therefore, this section focuses on the stability of different prepared *SAM*s coatings against UV degradation. Figure 6.16 presents sample wettability of coated Al samples with single and double layer coatings following UV exposure without (upper figure) and with (lower figure) a 4 hours condensation step. It can be seen that both samples lost their hydrophobic properties associated with decrease of water contact angle while the number of UV cycles increased. Coating degradation was worse when the condensation step was applied. However, no considerable difference was observed between the samples. Meanwhile, after 38 cycles, their hydrophobic properties reduced noticeably, to the extent that they became hydrophilic surfaces with contact angles of ~88.8^{o} to 89.2^{o} obtained. The sample wetting property remains approximately constant between 12 and 20 cycles (Fig.6.16, top) where their contact angle slightly decreased. Overall and based on UV exposure results, thus, a realistic stability was observed for both coated Al samples over almost six months of natural sunlight exposure [256].

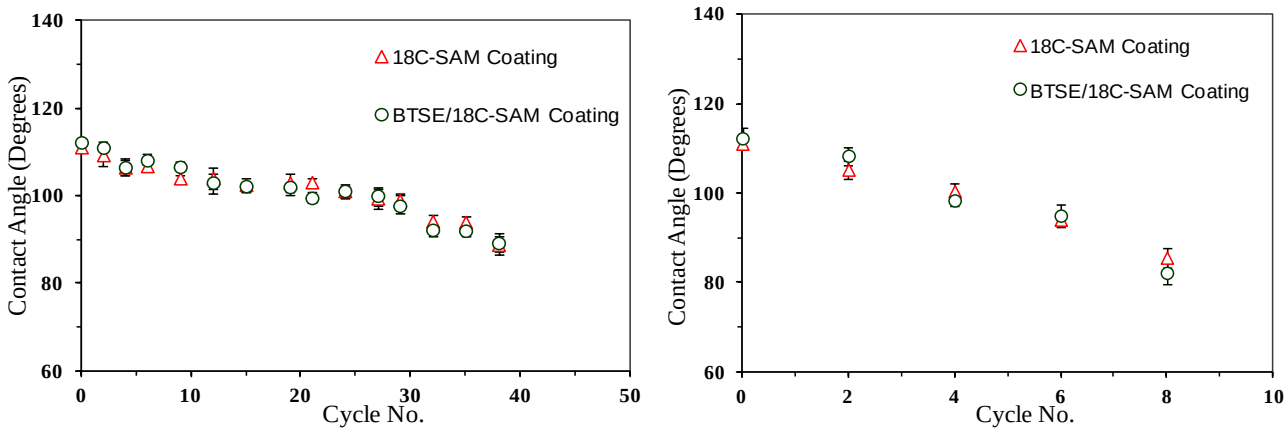

Fig.6.16. Coating stability (CA *vs.* UV cycle) for flat AA2024 coated with 18C-*SAM*s and BTSE/18C-*SAM*s (left) without condensation step and (right) with 4-h condensation.

6.4.1 X-ray Photoelectron Spectroscopy Results after UV Exposure

In order to study chemical composition of samples before and after UV exposure, an XPS analysis was used. The results of this analysis for both coated samples before and after UV exposure test are summarized in Table 6.3. It is evident that the Si 2p atomic concentration remains almost the same before and after the test, although this value is remarkably large for double layer coating. However, for a single 18C-*SAM*s coating, atomic concentrations of C 1s decreased from 44.08% to 28.20% and O 1s increased from 30.10% to 45.66%. In the case of a double layer BTSE/18C-*SAM*s coating, atomic concentrations of C 1s decreased from 47.32% to 39.71% and O 1s increased from 29.70% to 38.33%. This is due to the difference in atomic bond strength in *SAM*s molecules. This difference results in the gradual loss of the deposited 18C-*SAMs* layer on an Al substrate after UV exposure (decrease of water contact angle). In other words, the hydroxyl groups adsorbed on defective sites can be replaced gradually by O atoms when samples are UV-irradiated. This is the reason why the water contact angle decreased over repeated UV cycles. In fact, a decrease of water contact angle was observed due to gradual loss of the deposited top layer coating following UV exposure. In the case of UV-induced

degradation, UV irradiation can generate electron-hole pairs in the coated surface, some of the holes reacting with oxygen to form surface oxygen vacancies.

Table 6.3. XPS analysis of coated Al samples with 18C-*SAM*s and BTSE/18C-*SAM*s before and after UV exposure test.

Element	18C-*SAMs* coating		BTSE/18C-*SAMs* coating	
	% At. Concentration		% At. Concentration	
	Before	After	Before	After
C 1s	44.08	28.20	47.32	39.71
O 1s	30.10	45.66	29.70	38.33
Si 2p	13.15	11.53	22.98	20.19
Al 2p	12.67	13.09	n/a	0.77
Na 1s	n/a	1.52	n/a	1.0

Meanwhile, water and oxygen may compete to dissociatively adsorb onto these vacancies. The defective sites are kinetically more favorable for hydroxyl adsorption than oxygen adsorption. As a result, the surface hydrophilicity is improved, and the water contact angle can significantly be reduced. It has also been demonstrated that the surface becomes energetically unstable after the hydroxyl adsorption. Since the oxygen adsorption is thermodynamically favored, it is more strongly bonded on the defect sites than the hydroxyl group [257]. Therefore, the hydroxyl groups adsorbed on the defective sites can be replaced gradually by oxygen atoms when the samples are UV-irradiated [129].

6.5 Icephobic Performance and Durability of Single and Double Layer *SAMS* Coatings

6.5.1 Ice Adhesion Strength

The stability of the coating after several icing/de-icing cycles was considered as an important factor in cold regions. Table 6.4 presents the initial values of shear stress of ice detachment and the ice adhesion reduction factor (*ARF*) as well for aluminum samples coated with 18C-*SAMs* and BTSE/18C-*SAMs* layers.

Table 6.4. The ice adhesion strength and *ARF* values of Al sample coated with BTSE/18C-*SAMs* layers.

Sample	Ice adhesion strength	*ARF*
Mirror-polished AA2024	270 ± 20	~ 1.37
As-received AA2024	370 ± 30	1
18C-*SAM* Coating	190 ± 15	~ 1.94
BTSE/18C-*SAM* Coating	195 ± 12	~ 1.90

In the meantime, sample stability and durability in terms of ice-repellent performance over time and repeated icing/de-icing cycles similar to natural atmospheric icing were studied. Figure 6.17 presents the shear stress of ice detachment as a function of icing/de-icing cycles for bare and coated Al samples. Each sample was subjected to 9 successive de-icing cycles. As-received and mirror-polished bare Al was used as a standard reference showing the initial values of shear stress of ice detachment of ~370 ± 30 kPa and ~270 ± 20 kPa, respectively. It is evident in Figure 6.17 that while a bare flat sample showed average shear stress of ice detachment of ~370 ± 30 kPa, its coated counterparts showed a reduced value of ~195 kPa. This reduction is attributed to the presence of the low surface energy coating, 18C-*SAM*s, on Al samples.

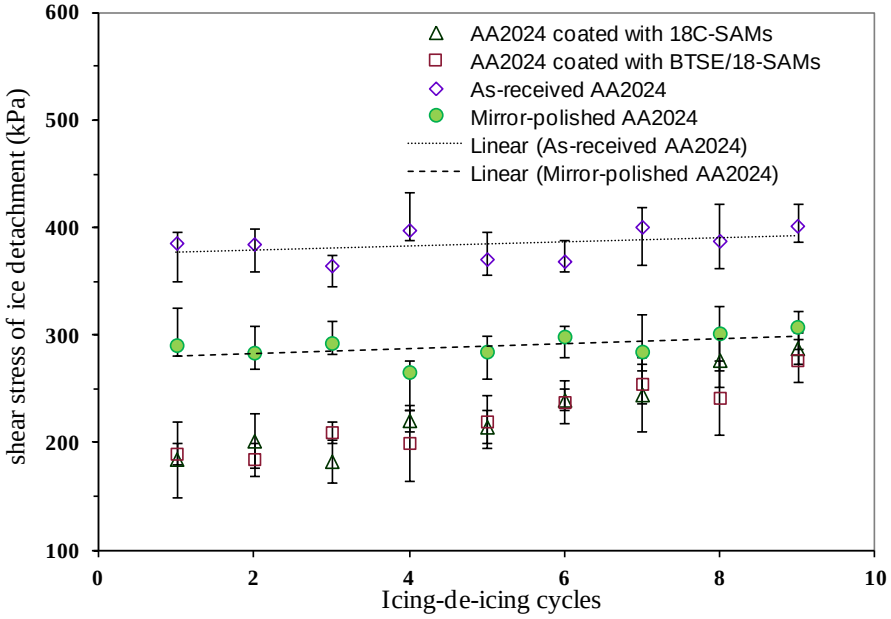

Fig.6.17. Shear stress of ice detachment *vs.* icing/de-icing cycle for coated Al surface with 18C-*SAM*s and BTSE/18C-*SAM*s layers.

In fact, coated Al with single and double layer *SAM*s coatings demonstrated ice adhesion strength values of ~ 2 times lower than as-received Al surfaces and about ~1.5 times lower than those observed on mirror-polished Al. Meanwhile, it was observed that a thick homogeneous glaze ice layer was accumulated on bare Al surfaces (no-coated substrate) compared to a hydrophobic surface where the heterogeneous freezing of water droplets on the hydrophobic surface was observed. However, the shear stress of ice adhesion of both coated samples increased after as many as 9 icing/de-icing cycles, as shown in Fig.6.15, from ~190-195 kPa (*ARF* ~ 1.9-1.94) to ~260 kPa (*ARF* ~ 1.42). This increase in ice adhesion strength values is believed to be associated with the partial decay of both coatings caused by contact with water. It is believed that the 18C-*SAMs* layer degraded on the BTSE under layer in a way similar to that on a polished Al substrate. Consequently, water could attack the R-Si-O- bond, hydrolyzing it and thus resulting in loose silanol species and the hydrophilic -OH group on the surface.

6.5.2 Sample Hydrophobic Property Following Ice Detachment

In order to assess the longevity of such coatings and their potential outdoor applications as well as to better understand our observations obtained during ice adhesion strength tests, their durability was studied following several icing/de-icing cycles. An "*icephobic*" coating can indeed reduce ice adhesion. However, to study whether hydrophobicity of a coating remains following ice detachment, the contact angle measurements after each icing/de-icing cycle were done in order to reduce extensive maintenance and operating costs. As is evident in Figure 6.18, sample hydrophobicity slightly decreased following each icing/de-icing cycle associated with small decreases in water contact angle values. More precisely, the contact angle value decreased from 110.4^{o} to 88.8^{o} after 9 successive icing/de-icing cycles. This is probably due to partial elimination of the hydrophobic coating (low surface energy coating) on the Al alloy surfaces during or after several icing/de-icing cycles. In fact, by hydrolyzing R-Si-O- bonds and loss of silanol species, hydrophilic surface with -OH group atop will obtain [172]. Decrease of water contact angle values after ice removal, therefore, is an additional proof for partial loss of hydrophobic coating on Al substrate.

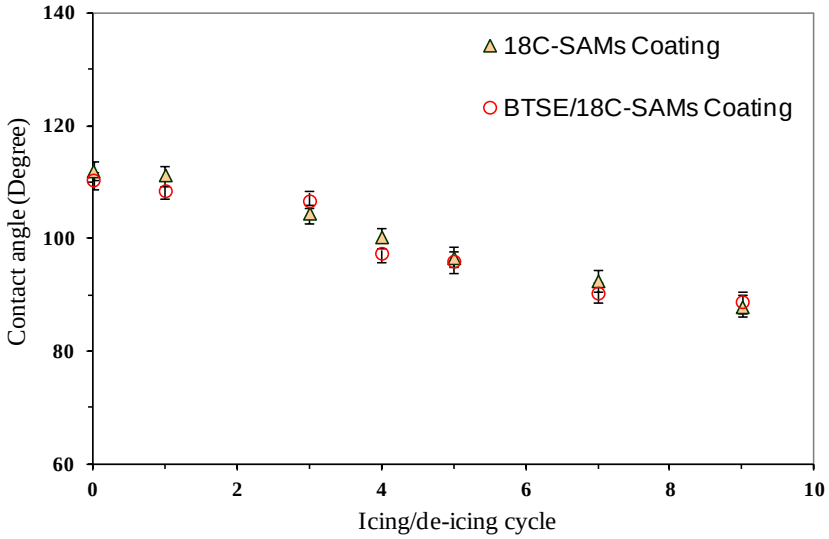

Fig.6.18. Contact angle values as a function of icing/de-icing cycles for coated aluminum samples with 18C-*SAM*s and BTSE/18C-*SAM*s layers.

6.5.3 X-ray Photoelectron Spectroscopy (XPS) Results (Prior and Following Ice Detachment)

X-ray Photoelectron Spectroscopy (XPS) analysis was used to investigate the chemical composition of Al substrates coated with single 18C-*SAMs* and double layer BTSE/18C-*SAMs* coatings prior and following icing/de-icing cycles (Table 6.5). It is obvious in Table 6.5 that while both single and double layer *SAMs* coatings showed a peak of Si 2p (at 103.1 eV) before the test, indicating silane layer(s) on the Al surface, its atomic concentration decreased after ice detachment. As is evident, this decrease is even worse in the case of an Al sample coated with single layer 18C-*SAM*s. This supports the assumption mentioned above, that water molecules hydrolyze the -O-Si-R bond and gradually destroy silane layers on an Al substrate. The presence of more Si 2p (at 103.1 eV) after the test in the case of a double layer coating (BTSE/18C-*SAM*s) improves the property that the under layer BTSE coating still presents somewhat after several icing/de-icing cycles. Meanwhile, after ice detachment, the atomic concentrations of C 1s (at 285 eV) decreased and the atomic concentrations of Al 2p (at 75.1eV) and O 1s (at 533eV) increased.

The presence of Al on the surfaces, in fact, indicates that these surfaces are not fully covered by *SAM*s coatings anymore.

Table 6.5. The elemental composition of aluminum samples coated with 18C-*SAM*s and BTSE/18C-*SAM*s before and after icing/de-icing cycles.

Element	18C-*SAMs* coating		BTSE/18C-*SAMs* coating	
	% At. Concentration		% At. Concentration	
	Before	After	Before	After
C 1s	44.08	26.16	47.32	40.96
O 1s	30.10	38.02	29.70	33.48
Si 2p	13.15	4.09	22.98	14.17
Al 2p	12.67	29.95	n/a	8.66
Na 1s	n/a	1.78	n/a	2.73

However, this percentage is different, 29.95% and 8.66% for 18C-*SAM*s and BTSE/18C-*SAM*s coating respectively, as the underlying structure, bare aluminum (Al_2O_3) or 18C-*SAM*s coating, is dissimilar. In the meantime, the XPS results confirm the obtained results of contact angle measurement following ice adhesion strength too. The presence of carbon component of the coating before icing/de-icing showed the presence of an organic film on the surfaces. The amount of carbon and silicone groups decreased after several icing/de-icing cycles. At the same time, the ratio of C to Si (C/Si) as a concentration of organic to inorganic function before and following icing/de-icing cycles increased from 3.35 to 6.39 for 18C-*SAM*s and from 2.05 to 2.89 for BTSE/18C-*SAM*s. It is clear that the increase in the organic to inorganic function ratio (C/Si), indeed, is remarkably larger (almost two times) for 18C-*SAM*s compared to BTSE/18C-*SAM*s. The results indicate that the top layer of Al surface (BTSE/18C-*SAM*s) was probably removed following icing/de-icing cycles. Despite the partial loss of coatings on both single and double layer coated Al surface after icing/de-icing cycles, however, the percentage of Si as well as the amount of C/Si for double layer coatings over repeated icing/de-icing cycles (14.17% and 2.89, respectively) is more than its value for single layer before icing/de-icing cycles (13.15%). This implies the presence of under layer coating on Al surface after icing/de-icing cycles, which in

turn is a promising sign for good adhesion of this coating to the substrate. This fact, in turn, can protect the sample substrate against further corrosion or any other surface changes.

6.6 Conclusions

In this chapter, alkyl-terminated Al surface substrates were prepared by depositing layers of 18C-*SAMs* on BTSE-grafted AA2024 or bare mirror-polished AA2024 surfaces to study the hydrophobic and ice phobic properties of double layer *SAM*s thin films on an Al surface. The influence of experimental parameters on coating properties and performances was investigated in order to optimize the conditions.

The hydrophobicity, ice-phobicity and durability of single and double layer coatings in different conditions were investigated by means of contact angle measurements, demonstrating gradual loss of hydrophobicity over ~1100-h-long immersion in water, associated with decreasing water contact angles. Ice-releasing properties of the same coated surfaces were also investigated by accumulating glaze ice in a wind tunnel at subzero temperature and by spraying supercooled micrometer-sized water droplets, similar to what exists in nature. Both surfaces initially demonstrated shear stress of ice detachment values about ~2 times lower than as-received aluminum surfaces and ~1.5 times lower than those observed on mirror-polished Al surfaces, as references. The ice adhesion strength values gradually increased after as many as 9 successive icing/de-icing cycles. The observed increase in ice adhesion strength can be ascribed to degradation of coatings upon their contact with water. In addition, hydrophobic properties of coated surfaces were investigated after icing/de-icing cycle to study their stability after ice removal, illustrating decreases in contact angle values.

The SEM and optical microscopy observations demonstrated that the double layer coating system, however, provided dense coating on Al substrate compared to single layer which prevents penetration of aggressive molecules through coating to the underneath metallic substrate. This was approved by presenting significantly less corrosion or corrosion products

around second-phase inter-metallic particles or dissolving and removing inter-metallic particles from matrix for double layer coating system compared to single layer 18C-*SAMs* coating after stability tests. Meanwhile, it was revealed that while the earliest corrosion products came into sight on bare Al after only ~20 hrs of immersion in an aqueous media, corrosion products, local corrosion and pitting in either matrix region or around second-phase particles was observed after ~310 and 700 hrs exposure to aggressive media in the case of 18C-*SAM*s and BTSE/18C-*SAM*s coatings, respectively. The XPS analysis showed that while 18C-*SAMs* coating demonstrated a significant peak of Si 2p before test, however, its atomic concentration decreased remarkably after a stability test (hydrolyzing the -O-Si-R bond and destroying the silane layer on Al surface). However, in the case of double layer BTSE/18C-*SAMs* coating, the Si 2p peak does not change much after the test, implying the existence of a dense BTSE layer on the Al surface.

CHAPTER VII

ANTI-CORROSIVE PERFORMANCE OF DOUBLE LAYER *SAMS* COATING SYSTEMS: POTENTIODYNAMIC POLARIZATION, ELECTROCHEMICAL IMPEDANCE SPECTROSCOPY AND CYCLIC CORROSION TESTING

7.1 Introduction

The hydrophobic and ice-phobic properties of double layer *SAMs* coated Al substrates as well as their stability and durability in different conditions were discussed in detail in the previous chapter. The objective of this chapter is to study anti-corrosive properties of prepared double layer self-assembled monolayer/multilayer thin film on an Al surface by means of appropriate instruments and measurement methods. The potentiodynamic measurements were used to evaluate the corrosion behavior of coated samples by using a standard three-electrode flat cell as the working cell. The electrochemical impedance spectroscopy plots and fitted results of surfaces immersed in saline solution were used as a final step of electrochemical study. Anti-corrosive performance of bare and coated Al samples was further investigated by *Cyclic Corrosion Exposure Testing* in accordance with ISO14993 [271]. More details can be found in chapter V.

7.2 Corrosion Resistance of Prepared Double layer *SAM*s Coatings

7.2.1 Anti-corrosive Performance of Double Layer Coatings

The corrosion resistance of the bare and coated AA2024 substrates was initially evaluated by potentiodynamic polarization test in 3.5 wt.% NaCl solution (pH: ~7.9). The PDP curves of (a) bare AA2024 and hydrophobic coatings of (b) 18C-*SAMs* and (c) BTSE/18C-*SAMs* on AA2024 are presented in Fig. 7.1. The E_{corr}, j_{corr} and R_p values derived from corresponding polarization curves using *Tafel* extrapolation are summarized in Table 7.1. It is evident in Fig.7.1 and Table 7.1 that

the value of E_{corr} positively increases from -0.68±0.03V and -0.69±0.04V for the bare standard and control AA2024, respectively, to -0.60±0.03V and -0.54±0.04V in the case of hydrophobic 18C-*SAMs* and BTSE/18C-*SAMs* coating, respectively. As a reminder, the cleaned bare Al samples with and without immersing in iso-propanol for 15 min, as solvent, were labeled as "*Control*" and "*Standard*" reference samples, respectively.

Table 7.1. Potentiodynamic results of bare and coated AA2024 with 18C-*SAM*s and BTSE/18C-*SAMs* thin films in 3.5 wt.% NaCl solution.

Specimen	$E_{corr.}$ (V *vs.* SCE)	$j_{corr.}$ (μAcm^{-2})	R_p ($k\Omega cm^2$)	E_b-E_{corr} (V *vs.* SCE)
Control AA2024	-0.69 (±0.04)	9.78 (±0.63)	15.57 (±2.20)	-
Standard AA2024	-0.68 (±0.03)	22.89 (±9.06)	2.96 (±2.71)	-
18C-*SAMs* coating	-0.60 (±0.03)	0.90 (±0.11)	248.11 (±2.55)	0.12
BTSE/18C-*SAMs* coating	-0.54 (±0.04)	0.008 (0.00)	521.14 (±1.83)	0.20

The positive shift observed in E_{corr} values is apparently due to improvement in barrier and protective performance of hydrophobic coating formed on Al substrates. The corrosion current density, $j_{corr.}$, of hydrophobic coating of BTSE/18C-*SAMs* ($0.008\mu Acm^{-2}$) decreased about 4 orders of magnitude as compared to that of bare standard ($22.89\mu Acm^{-2}$) and 2 orders of magnitude as compared to 18C-*SAMs* ($0.90\mu Acm^{-2}$). In other words, the potentiodynamic polarization curves demonstrated that the corrosion inhibition of BTSE/18C-*SAMs* thin film was superior to that of 18C-*SAMs* coating. Moreover, the double layer coated samples demonstrated increased resistance to initiation of corrosion attack revealed by the presence of a breakdown potential (E_b) and a larger passive potential range (E_b-$E_{corr.}$). It is well-known that the larger the E_b-$E_{corr.}$, the higher resistance of the sample toward pitting corrosion which is a measure of film integrity and protectiveness as well. The double layer coating system of BSTE/18C-*SAMs* also showed a decrease in $j_{corr.}$ in the cathodic and anodic regions, which suggested packed and tight silane layers formed on Al, thereby protecting the Al substrate more effectively against corrosion

[268]. Corrosion inhibition is a complex phenomenon depending on surface pre-treatment, ability of coatings to form highly cross-linked network, and coating-aluminum interface bonding. The Al_xO_y layer is permeable to electrolytes/moisture and is prone to undergo dissolution in a humid environment, leading to an accelerated corrosion rate. In contrast and based on the $E_{corr.}$ and $j_{corr.}$ values, the BTSE/18C-*SAMs* thin film is more impermeable to corrosion accelerants compared to unmodified sample or even coated Al with 18C-*SAMs* thin film, offering improved barrier property and insulating. Decrease in jcorr. suggests, indeed, a closely packed barrier film on Al surface with less disorder or defect. In other words, the BTSE layer forms a dense layer with fewer defects over the entire Al substrate as a complete layer.

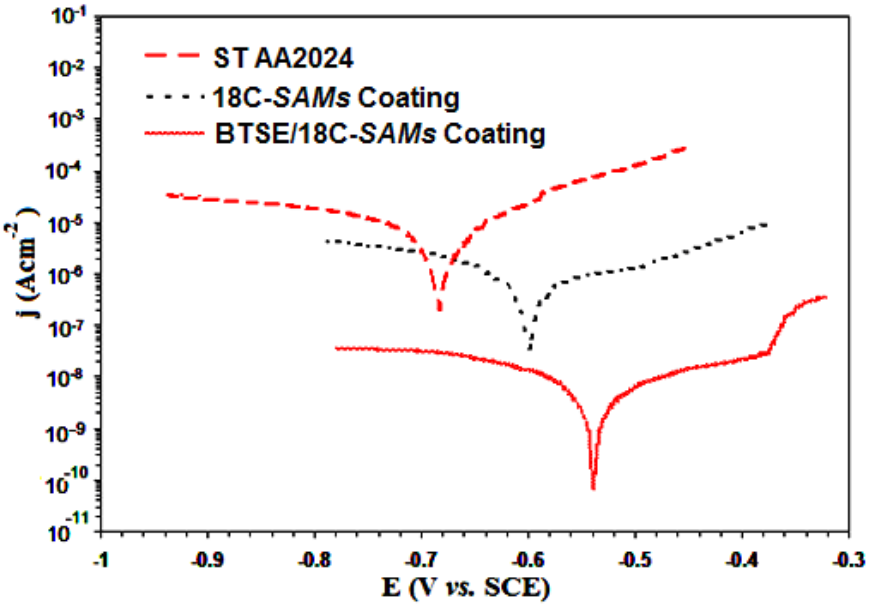

Fig.7.1. Polarization curves of bare and coated AA2024 with 18C-*SAMs* and BTSE/18C-*SAMs* thin films in 3.5 wt.% NaCl solution.

Meanwhile, Fig. 7.1 shows that the slope of anodic current versus E curve was smaller for double layer coated Al surface than for 18C-*SAMs* and bare samples. It is worth mentioning that the $E_{corr.}$ and $j_{corr.}$ values for BTSE coating alone are ~-0.6 (V) and at the orders of ×10-6 Acm^{-2}, respectively [202, 212, 237]. As explained before, hydrophobicity is claimed to be the most important property against corrosion as it controls the access of water to the metal-coating

interface. However, a sufficiently cross-linked network firmly attached to the metallic substrate should be formed to protect the surface against corrosion. According to the results obtained from potentiodynamic polarization tests, the BTSE under layer, indeed, showed a good coverage of Al surface, more particularly on Cu-enriched parts of alloy and therefore, less localized corrosion was observed. Localized corrosion is the weakest point of corrosion inhibition of 18C-*SAMs* alone. The pitting corrosion is less likely to take place on BTSE/18C-*SAMs* coated surface. Therefore, the BTSE under layer can significantly improve the corrosion resistance. Even though bare samples also present high $E_{corr.}$, however, it is due to the presence of an insulating Al_2O_3 layer on the Al surface. In addition, according to the results reported in the literature for the $j_{corr.}$ values for toxic chromate coatings (in the order of 10^{-7} to $10^{-8}Acm^{-2}$) [287-292], the presented double layer system provides excellent anti-corrosive performance with few environmental legislation issues. The Oxidation-reduction reactions in the electrolyte can only occur when defects are present in the structure of the coatings, allowing electron transfer at the aluminum-coating interface. Oxidation of aluminum is balanced by simultaneous reduction of ions in solution. In aqueous media with pH close to 7 (fresh water), only two reduction reactions can occur: (i) reduction of protons (H^+) or (ii) reduction of oxygen (O_2) dissolved in water. It was explained that corrosion inhibition is a multifaceted phenomenon depending on the simultaneous effect of various parameters such as surface pretreatment, ability of coatings to form a highly cross-linked network, its inherent hydrophobicity etc.

The potentiodynamic polarization studies revealed that the corrosion resistance of the double layer coated Al substrates improved significantly compared to single layer *SAM*s-modified samples. However, the 18C-*SAM*s single layer on Al surface also exhibited better corrosion resistance as compared to the bare and control panels. Even though the bare samples also have high corrosion potential, this is perhaps due to the presence of an insulating Al_2O_3 layer on Al surface. Upon cathodic polarization, there is a difference between what observed for coated samples with single and double layer *SAM*s and those observed for bare surfaces. Indeed a higher redox activity was found over Cu-enriched particles regarding the matrix oxide surface, indicating

that cathodic reaction should occur mainly on the Cu-enriched particles [172]. The BTSE under layer, indeed, inhibited remarkably the cathodic process, and thus, the O_2 diffusion to the metal surface was suppressed. Therefore, it is possible to conclude that the BTSE under layer were fabricated over the entire Al surface (a complete layer) while the molecules in the coating were densely packed to provide a packed barrier layer. In fact, a large dissimilarity in cathodic behavior of single and double layer coated samples as well as their extreme values of $j_{corr.}$ to bare samples supports our conclusion that there was a packed barrier layer cover on Cu-enriched particles. For this reason, if these sites were left open, suppression of the cathodic current would not be expected. In addition, the obtained contact angle results presented in the previous chapter, are consistent with a well ordered and densely packed 18C-*SAMs* film on Al surface. Meanwhile, the slope of anodic i *vs.* E is less for BTSE/18C-*SAMs* modified samples than for a bare surface. Therefore, the anodic current density is considerably suppressed on this coated surface. The Al oxide layer, indeed, is permeable to electrolytes and moisture and is prone to undergo dissolution in humid environment, leading to an accelerated corrosion rate. In contrast, the thin film formed from under layer BTSE along with upper layer 18C-*SAMs* provides a double layer thin film on Al surface with few if any defects. This leads to more impermeable film to corrosion accelerants and thus more insulating (with respect to $E_{corr.}$ and $j_{corr.}$ values).

7.2.2 Cyclic Corrosion Tests of Prepared Double Layer Coatings

The anti-corrosive performance of modified and unmodified AA2024 samples was further studied by cyclic corrosion exposure testing. Cyclic corrosion test offers controlled accelerated corrosive condition to evaluate relative corrosion resistance of any coating. As presented in Figures 7.2-7.4, the unmodified flat Al samples exhibited extensive corrosion after only 8 cycles of cyclic corrosion exposure with appearance of numerous black dots (pits) in micrometer scale revealed under an optical microscope. Meanwhile, the size and density of the black dots increased as the cyclic corrosion test cycle number increased which is due to localized corrosion continually expanding. However, the earlier stage of corrosion observable in the case of hydrophobic Al

samples modified by 18C-*SAMs* was observed after 18 cycles of exposure and only small traces of corrosion were observed in the case of BTSE/18C-*SAMs*-modified samples even after 81 cycles of exposure (Fig.7.2). It is worth recalling that the earlier stage of corrosion in the case of Al samples coated with 8C-*SAMs* was observed after 12 cycles of exposure. Meanwhile, the optical images of 18C+Cl *SAM*s modified samples after cyclic corrosion exposure bear a very close likeness to 8C-*SAM*s modified samples. A closer look at these black dots via optical microscope revealed locally corroded areas on a micrometer scale. Pitting corrosion seemed to be the typical mode of surface degradation. In Figures 7.2-7.4, the optical images (taken by a digital camera) and SEM observations of bare and coated modified (*SAM*s coated) samples are presented.

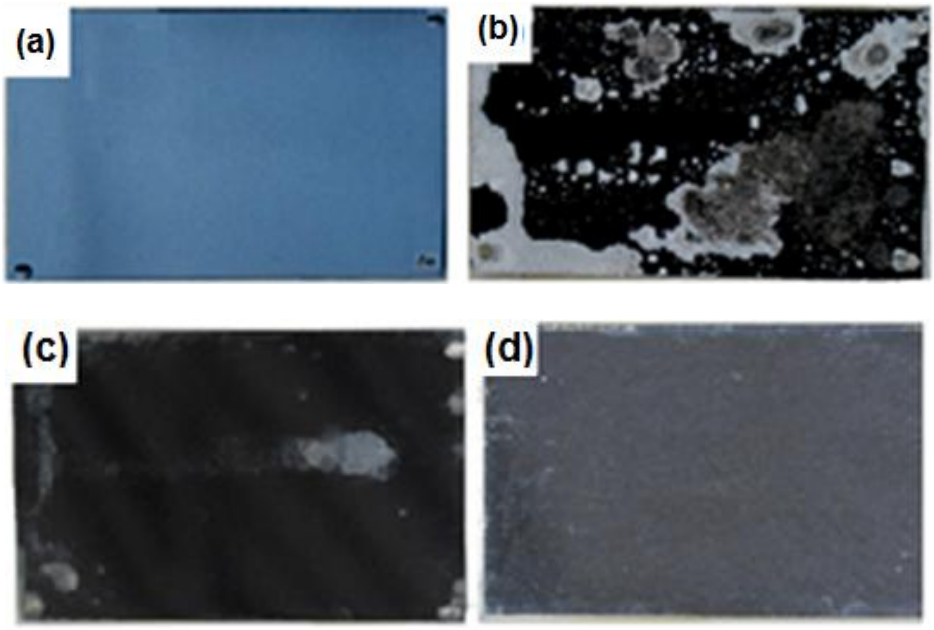

Fig.7.2. Optical images of unmodified AA2024 a) before and b) after 85 cycles of cyclic corrosion test and modified AA2024 with c) 18C-*SAMs* and d) BTSE/18C-*SAMs* after cyclic corrosion cycles.

These observations revealed by the cyclic corrosion test confirmed again the results presented earlier in Figure 7.1 by potentiodynamic polarization curves, which imply an improvement in the corrosion resistance and barrier property of coated samples with BTSE/18C-*SAMs*. In other words, the cyclic corrosion tests validate the fact that the BTSE under layer was

formed on an Al substrate with fewer defect areas and significant density compared to the 18C-*SAMs* layer alone. As a result, this layer acts as a superior barrier to prevent easy penetration of corrosion accelerants, e.g. electrolytes and water, to the metallic Al substrate beneath. Consequently, a decreasing corrosion rate or further expansion of corrosion to the surrounding areas was observed. Pitting corrosion seemed to be a typical mode of surface degradation.

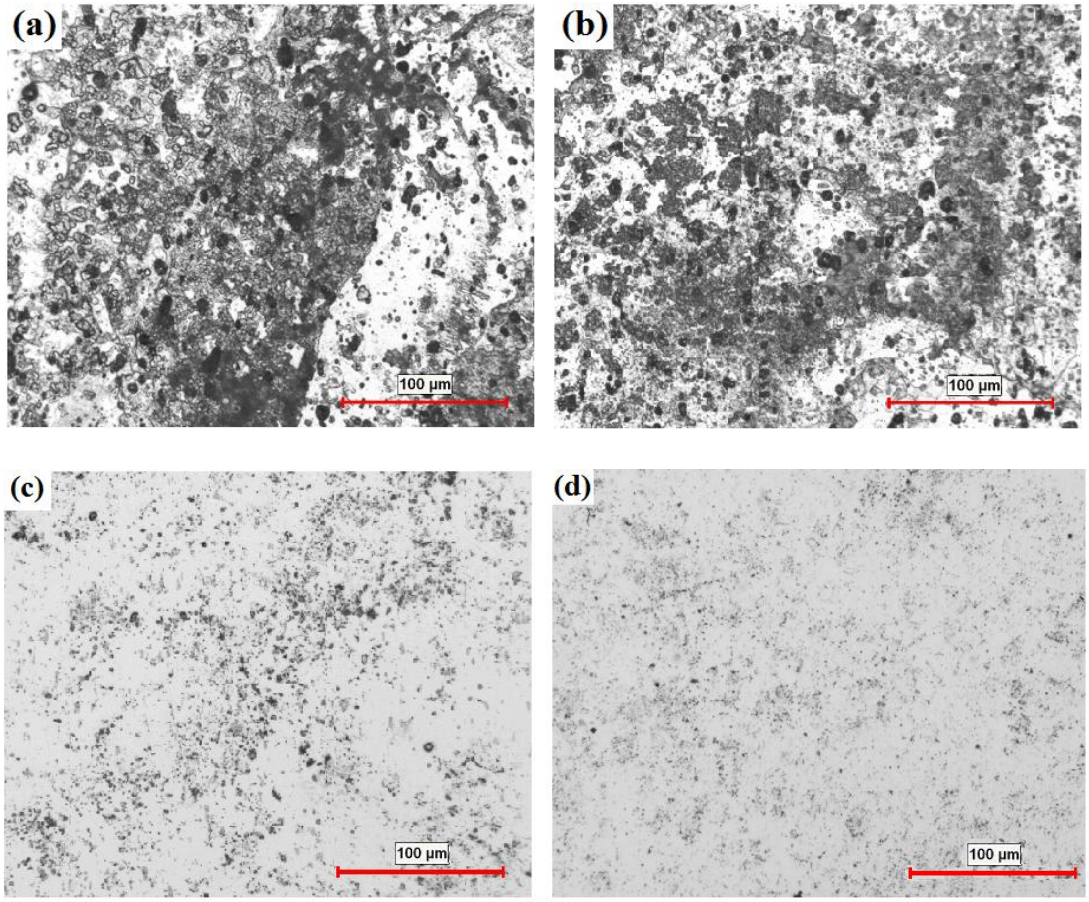

Fig.7.3. Optical images of bare and coated AA2024 with single and double layer *SAM*s thin film after 120 cycles of cyclic corrosion test: a) standard AA2024, b) control AA2024, c) 18C-*SAM*s and d) BTSE/18C-*SAM*s coatings.

In this double layer system, the BTSE under layer blocked more effectively active sites on Al from penetration of corrosion accelerants due to the combined effect of cross-linking and formation of Al-O-Si and Si-O-Si interface bondings with the Al substrate in addition to the hydrophobicity of the alkyl chains. In the meantime, the 18C-*SAMs* top layer also provides

hydrophobicity and therefore, more barrier property. However, as it is obvious, corrosion resistance for 18C-*SAMs* alone does not improve as much as for the BTSE/18C-*SAMs* coating. In contrast to the BTSE/18C-*SAM*s-modified samples, the Al panels coated with 18C-*SAM*s exhibited obvious corrosion after 18 cycles of exposure. Because of the improved barrier property of Al surface coated with double layer BTSE/18C-*SAMs*, the corrosion resistance of these samples, as a result, improved compared to the bare samples. This prevents electrolytes and water molecules penetration to the metal substrate to prevent further expansion of corrosion to surrounding areas.

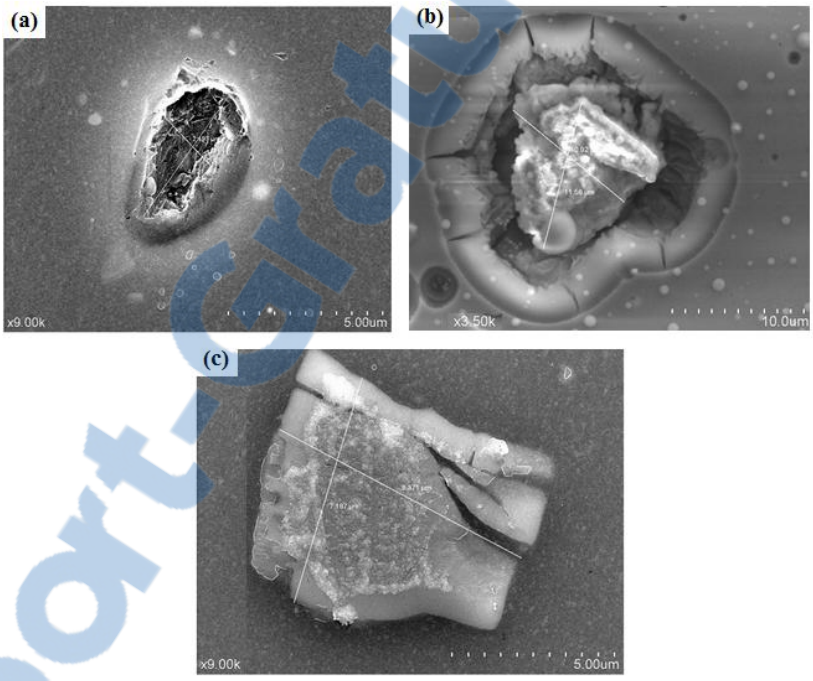

Fig.7.4. SEM images of a) bare Al and coated Al with *SAM*s of b)18C and c) BTSE/18C coatings after 85 cycles of cyclic corrosion test.

Figure 7.5 presents corroded area percentage of the bare and coated Al samples over 120 cycles of cyclic corrosion exposure obtained by using CLEMEX Vision PE (Olympus BX51M) Mosaic Images Feature with a magnification of ×50 over a surface area of ~1631±35 mm^2 (28*24-frames). The image magnification is ×50 over a surface area of ~1631±35 mm^2. The gray cast corresponding to the corrosion product was defined. The share of the corroded area was calculated by dividing the dots having a white-to-gray cast by the whole number of dots

representing the sample. It is shown in Fig.7.5 that by increasing the cycle number of cyclic corrosion exposure, the percentage of corroded area increased for all samples, bare and coated Al substrate, as was also observed in Fig.7.2. However, in the case of bare standard and control AA2024, after 42 cycles of exposure, a substrate surface percentage of about ~50% was corroded and completely destroyed. As was shown in a previous chapter, for coated Al samples with 8C-*SAMs*, 18C+Cl *SAMs* and 18C-*SAMs* thin films, however, this percentage was lower, i.e. ~19, ~28 and ~9%, respectively. The most promising result was obtained for the Al substrates coated with BTSE/18C-*SAMs*, where even after 120 cycles of exposure, a surface corroded portion of only ~16.4% was observed.

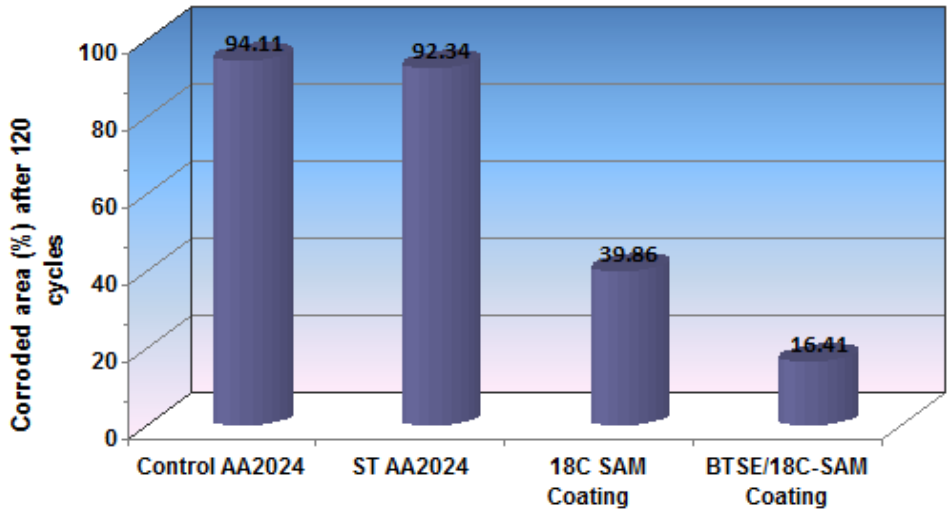

Fig.7.5. Portion of the corroded area of modified and unmodified Al samples exposed to the cyclic corrosion test.

Meanwhile, it is obvious that standard and control AA2024 both show a high corrosion rate in all stages: the slopes of the curves are greater when compared to coated Al samples. In addition, it was shown that the depth of the corroded area measured on standard AA2024 after cyclic corrosion tests via optical profilometry and AFM techniques measured 2µm to 4µm (see Fig.5.5 in chapter 5). This means that during cyclic corrosion exposure, the Al substrate was exposed to being corroded not only by spreading on the outermost layer of the surface, but also by digging throughout the surface.

7.2.3 Corrosion Resistance of Double Layer *SAMs* Coatings on Al Surface after One Week of Immersion in Saline Solution

A series of bare and coated Al samples with single and double layer *SAMs* thin films were kept for one week in a 3.5% NaCl solution and their anti-corrosive performances were measured immediately via potentiodynamic polarization curves, as shown in Figure 7.6. Consequently, the values of $E_{corr.}$ and $j_{corr.}$ derived from corresponding polarization curves using Tafel extrapolation were obtained, see Table 7.2. It is evident that the corrosion current density, $j_{corr.}$, of both single (18C-*SAMs*) and double layer (BTSE/18C-*SAMs*) hydrophobic coatings on Al substrate decreased about one order of magnitude compared to similar as-prepared samples.

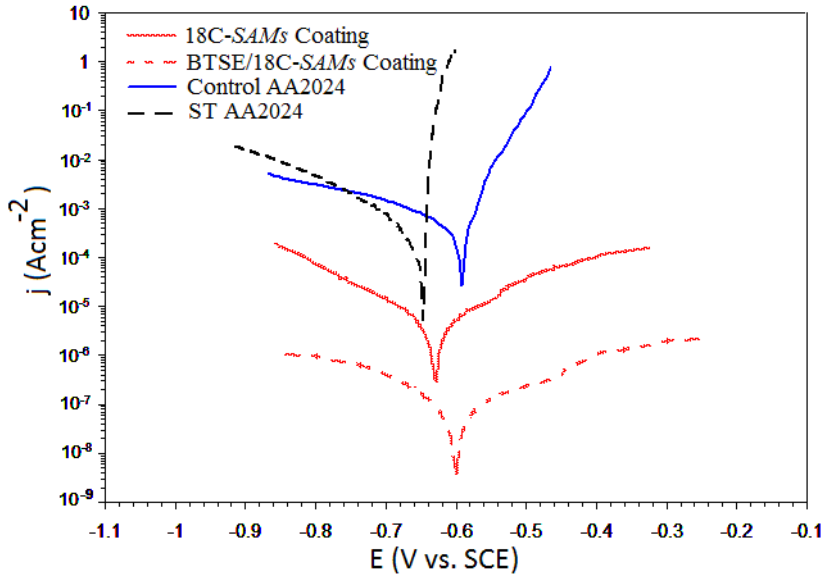

Fig.7.6. Potential and current density of bare and coated AA2024 samples with single and double layer *SAM*s thin films after one week immersion in 3.5% NaCl solution.

However, the anti-corrosive performance of double layer thin film is still reasonable while exposed to aggressive condition containing Cl^- ions (accelerated corrosion rate). The barrier property of *SAMs*-modified Al alone dropped off greatly following immersion in a saline solution ($E_{corr.}$ and $j_{corr.}$) which is due to presence of defects, holes and imperfection in the film. These results proved that the single layer hydrophobic coating on Al surfaces is more permeable to electrolytes and moisture and thus is prone to undergo dissolution in salted environment with

aggressive ions of Cl^-. On the other hand, in the case of a double layer coating system, it showed better anti-corrosive performance compared to bare samples as well as single layer *SAMs*-modified Al samples (compact and dense film). However, in both cases and based on observed results, it is possible to conclude that their barrier property decreased as they underwent a saline test (with respect to $E_{corr.}$ and $j_{corr.}$ values). In both cases, however, the coated Al samples exhibited better anti-corrosive performance compared to the bare (standard and control AA2024) samples.

Table 7.2. Potentiodynamic results of bare and coated AA2024 samples with single and double layer *SAMs* thin films after one week of immersion in 3.5% NaCl solution.

Specimen	$E_{corr.}$ (V *vs.* SCE)	$j_{corr.}$ (μAcm^{-2})	E_b-E_{corr} (V *vs.* SCE)
Control AA2024	-0.61 (±0.02)	878 (±121)	-
Standard AA2024	-0.65 (±0.03)	528 (±107)	-
18C-*SAM*s coating	-0.63 (±0.02)	17.0 (±6.1)	0.09
BTSE/18C-*SAMs* coating	-0.60 (±0.08)	0.09 (±0.01)	0.13

7.2.4 Electrochemical Impedance Spectroscopy of Double Layer Coatings

Electrochemical impedance spectroscopy (EIS) is used to study and understand the electron transfer (ET) and corrosion behaviors of a silane-coated-aluminum alloy. Useful parameters can be determined from EIS curves by fitting them to an appropriate equivalent circuit model. The charge transfer resistance (R_{ct}) of the film to the ET process across coated electrode-electrolyte interface is calculated from impedance data and equivalent circuit fitting. In fact, understanding details of structural arrangement and orientation of organic molecules on the substrate is necessary, from both the fundamental and the applications points of view, to investigate their blocking behavior (barrier property), ET behavior across the electrode-electrolyte interface as well as the presence of holes and defects in the films on Al surfaces. By using the R_{ct}

values, the surface coverage (Θ) value of the corresponding thin film and other kinetics parameters associated with film formation can be calculated. Impedance measurements were carried out using an AC signal of ±10 mV amplitude versus OCP in a wide frequency ranging from 100 kHz to 0.1 Hz via an electrochemical impedance analyzer at room temperature. Typical EIS spectra (Nyquist and Bode plots) of bare and coated Al samples immediately after exposure to 3.5% NaCl supporting electrolyte are presented in Fig.7.7. The NaCl solution was used in order to evaluate ionic permeation of prepared coatings to ions via electrochemical impedance spectroscopy [48, 49, 55, 261]. Meanwhile, it is well-known that more rapid formation of corrosion products occurs in the aerated solution. The Bode plots of phase angle and impedance *versus* frequency demonstrates characteristic differences between coated samples, single and double layer, and bare surfaces. Therefore, it is possible to classify them into pure and leaky capacitors (difference in phase angle). A higher phase angle in the case of Al sample coated with BTSE/18C-*SAMs* suggests lower ionic permeation and therefore better insulating, as seen in Fig.7.7 [48, 49, 202, 239, 261]. The phase angles values confirm that the BTSE/18C-*SAMs* film behaves much more like an ideal capacitor compared to an 18C-*SAMs* coating. This is due to a more packed and cross-linked film with fewer defects. For the bare samples, however, it acts as a leaky capacitor, arising mainly from the presence of defects within the natural Al oxide layer [48, 49, 261]. Meanwhile, based on total impedance ($|Z|(\Omega cm^2)$) *vs.* frequency (*f*), it can be seen that the impedance values are higher, showing a better capacitive behavior for double layer BTSE/18C-*SAMs* coatings than for single layer 18C-*SAMs*. The higher phase angle values were obtained even at lower frequencies for the BTSE/18C-*SAMs* coating, where ionic permeation is generally favored [48, 49, 202, 239, 261]. This observation points to the fact that the under layer BTSE molecules form a compact and dense layer with few holes and defects [48]. The Bode plots of phase angle *versus* frequency are nearly the same while the impedance plot still has some differences. Nyquist plots of bare AA2024 as well as coated Al samples with 8C and 18C+Cl *SAMs* (chapter V) show very small semicircles throughout the frequency region. This indicates that the ET process is reversible and essentially diffusion controlled [48, 49, 183, 202].

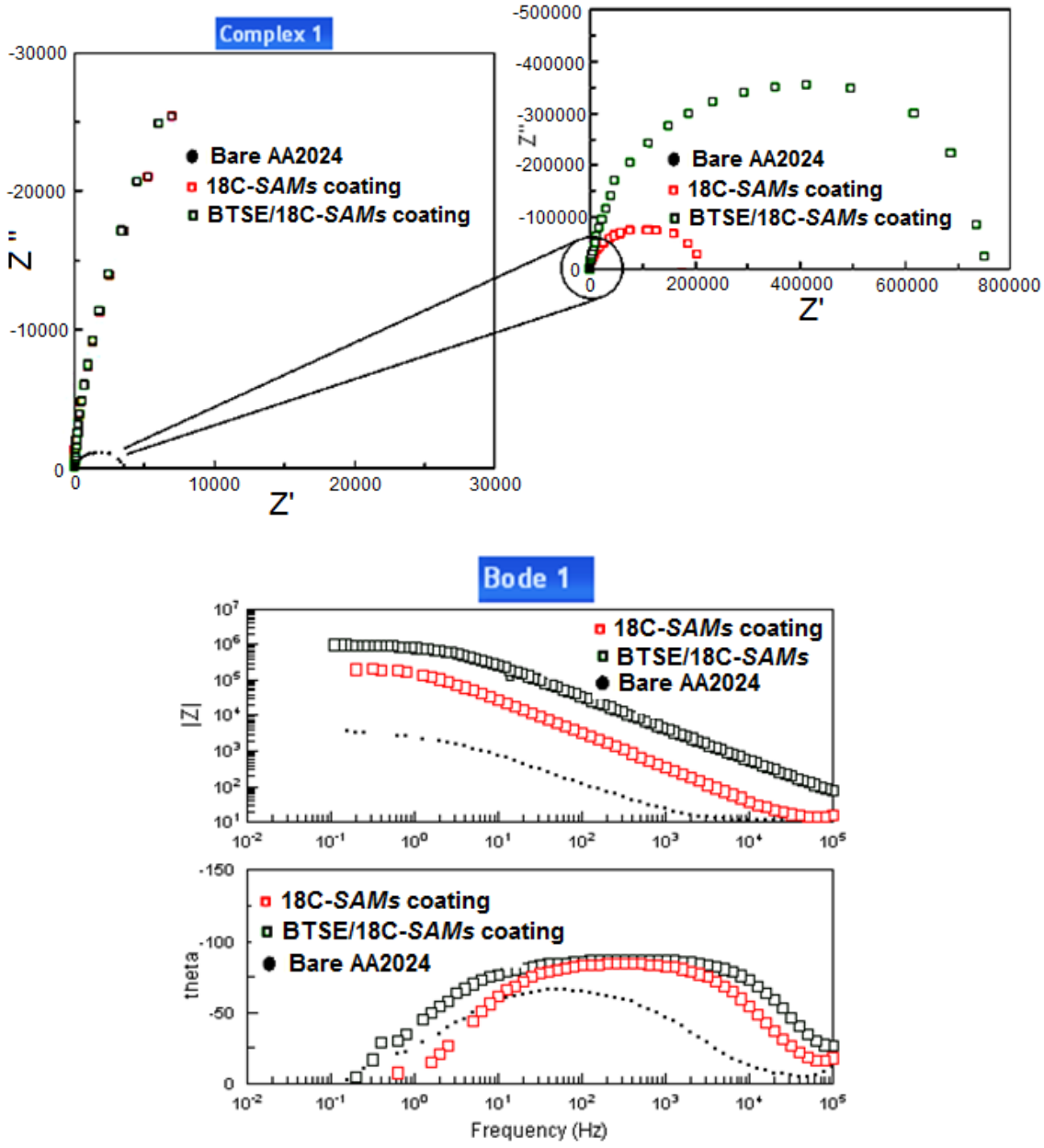

Fig.7.7. Impedance plots of bare and coated AA2024 with 18C-*SAM*s and BTSE/18C-*SAMs* in 3.5% NaCl aqueous solution. Bode phase angle (phase angle *vs.* logarithmic frequency) and frequency (logarithmic total impedance *vs.* logarithmic frequency).

On the contrary, the BTSE/18C-*SAMs* coatings exhibit quite large semicircles over the entire frequency range, indicating that the ET reaction is inhibited by displaying improved blocking behavior against diffusion of aggressive molecules. Consequently, in such cases, the

process of ET is considered as a charge transfer control process [48, 49, 183, 202, 239, 261]. For the bare AA2024, the low frequency impedance log|Z| (Ωcm^2) at 0.1 Hz decreased to ~3.5, indicating the corrosion process [202, 293-295]. However, the log|Z|(Ωcm^2) was at higher values of ~5.3 and 9.3 for 18C-*SAMs* and BTSE/18C-*SAMs* coatings, respectively. Decrease of low frequency impedance is often an indication of a more permeable barrier towards electrolyte ions and also the beginning of the corrosion process [48, 183, 202, 293-295]. These results are in good agreement with potentiodynamic results discussed earlier. It was explained that the higher the charge transfer resistance is, the higher the blocking behavior is [183, 202]. The diameter of a semicircle obtained in an impedance plot is a measure for the charge transfer resistance, R_{ct}, which is higher in the case of coated samples compared to a bare electrode. This is due to inhibition of ET by formation of films on Al samples [202]. In other words, the formation of a semicircle with a higher charge transfer resistance (R_{ct}) during EIS studies suggests that the film is compact with few defects (superior blocking property) [48, 49]. The coated Al samples showed, indeed, larger impedance and quicker increase in phase angle than bare substrates which are associated with coating formation. In the next step, the impedance data are fitted to a standard Randle's equivalent circuit model (Fig.7.8) comprising a parallel combination of a constant phase element (CPE) and R_{ct} in series with the uncompensated solution resistance, R_s. Charge transfer resistance represents a diffusional parameter [202, 293]. By an equivalent circuit fitting procedure using impedance data, the R_{ct} values of bare as well as single and double layer coated Al electrodes can be determined. These values are shown in Table 7.3. Two methods were used to analyze EIS data: first looking at values found directly from impedance spectra, and second, from equivalent circuit modeling (Fig.7.8). The impedance of a CPE depends on the frequency via the following equation: $Z_{CPE} = 1/C(j\omega)^n$, where C is capacitance. As "n" approaches 1, the impedance of CPE reduces to that of a true capacitor [293-295]. It is obvious that the R_{ct} values of coated Al samples, as expected, are much higher when compared to those of a bare Al sample. This change in R_{ct} values implies a better blocking behavior of BTSE/18C-*SAMs* towards electrochemical reactions.

Table 7.3. ElS parameters data obtained for bare and coated aluminum samples after 2-h immersion in 0.1 M $NaHCO_3$ + 3.5% NaCl solution.

Sample	AA2024	18C-*SAMs* Coating	BTSE/18C-*SAMs* Coating
R_s (Ωcm^2)	10.08 (±1.41%)	12.50 (±1.22%)	11.27 (±1.20%)
CPE 1 (Fcm^{-2})	$4.35X10^{-5}$ (±1.03%)	$6.84X10^{-7}$ (±1.09%)	$9.74X10^{-8}$ (±1.00%)
CPE 2 (Fcm^{-2})	n/a	n/a	$4.45X10^{-7}$ (±1.18%)
R_{ct} (Ωcm^2)	3750 (±0.30%)	214500 (±0.21%)	595000 (±0.27%)
R_p (Ωcm^2)	-	-	136602 (±1.19%)

Changes in the double layer capacitance and interfacial capacitance have been found to correlate to film formation [48, 49]. The capacitance should decrease as the film coverage increases, since the capacitance is inversely proportional to the distance between the charges. In addition, the polarization resistance, which corresponds to the charge transfer resistance, R_{ct}, in the pores of the film or bare surface, increases as the coverage increases [48, 49]. A multiple layer film assembled from hydrocarbon compounds may certainly act as a better barrier for corrosion accelerants compared to a single monolayer [48]. The EIS data was modeled with a *Randle's circuit* modified with constant phase elements (CPE1 and 2) in place of capacitors (Fig. 7.8).

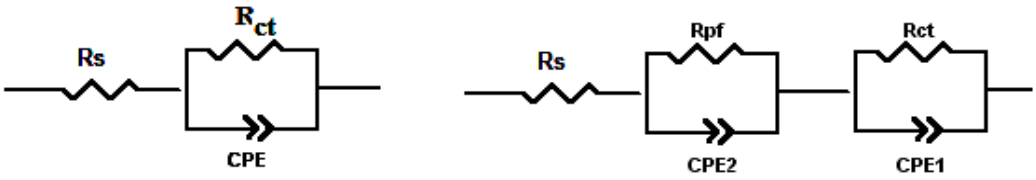

Fig.7.8. The Randle's equivalent circuit used to model EIS data of single (left) and double layers (right). R_s is the solution resistance, CPE1 and CPE2 are constant phase elements corresponding to under and top layers, respectively and R_{ct} and R_{pf} are the charge transfer and polarization resistances, respectively.

After immersion in a saline solution, it is evident that the R_{ct} values for BTSE/18C-*SAMs* are larger than for 18C-*SAMs* or bare AA2024 electrodes. This indicates better blocking by a double

layer coating (higher R_{ct} value), compared to a single layer, from the ET process (blocking degree) [183, 202, 284]. Using these R_{ct} values, the surface coverage of single and double layer thin films (Θ) on Al electrodes can be calculated by applying the corresponding equation as follows [284]:

$$\Theta_{imp} = 1 - [R_{ct} (STAA2024) / R_{ct} (coated\ aluminum\ with\ SAMs)] \quad \textbf{7.1}$$

Surface coverage was calculated with the assumption that the current is due to the presence of holes and defects within the layer [284]. The surface coverage percentage calculated for BTSE/18C-*SAMs* is 99.37%, suggesting the formation of a well-packed and dense film centered on an Al sample, especially on Cu-enriched particles distributed throughout alloy surface with few holes/defects (Table 7.4). This exhibits an improved insulating property of double layer coating on an Al substrate. As a reminder, in the case of 8C and 18C+Cl *SAM*s, however, the surface coverage values were found to be ~83% and 91%, respectively. This indicated that these films were formed on the Al surface with a larger number of holes and defects. Immediately after sample immersion in saline solution, the coating behaves as a barrier to redox activity, as is evidenced by larger R_{ct} values.

Table 7.4. Charge transfer resistance and surface coverage values calculated for bare, single and double layer coatings on Al substrate.

Sample	**AA2024**	**18C-*SAMs* Coating**	**BTSE/18C-*SAMs* Coating**
R_{ct} (Ωcm^2)	3750 (±0.30%)	214500 (±0.21%)	595000 (±0.27%)
Surface coverage (Θ_{imp})	-	98.26%	99.37%

These results show the presence of a long aliphatic chain (top layer) in a double layer coating (on the under layer) which also helps to prevent ET to a larger extent in comparison with single layer coating or shorter aliphatic chains. From R_{ct} and corresponding Θ values of impedance studies, it is clear that the prepared single and double layer coatings on Al samples are ordered as follows, with respect to the blocking ability and barrier property:

BTSE/18C-*SAMs* > 18C-*SAMs* > 18C+Cl *SAMs* > 8C-*SAMs*

This is consistent with the results observed earlier in potentiodynamic studies. In other words, coating integrity and the blocking behavior order of prepared coatings in this study are further confirmations for the results obtained so far. The potentiodynamic polarization test as well as electrochemical impedance spectroscopy revealed that the corrosion resistance of the double layer coating BTSE/18C-*SAMs* improved significantly compared to bare as well as to the 8C, 18C+Cl-*SAMs* and even 18C-*SAMs* coated samples. In fact, electrochemical measurements highlight the fact that *SAMs* coatings alone on metallic substrates do not provide a great deal of protection against localized corrosion since the Cu-rich particles were not protected. These particles must be protected to have considerable corrosion protection on AA2024. This aim was achieved, herein, by applying a BTSE under layer that bonds to both particles and oxide surface. Coating integrity and blocking behavior order of prepared coatings are another confirmation for the results obtained so far.

7.2.5 Corrosion Resistance of Double Layer *SAMs* Coatings After the UV-aging Test

Potentiodynamic polarization of coated Al samples with single 18C-*SAMs* and double layer BTSE/18C-*SAMs* thin films was performed immediately after the UV-aging test to study their anti-corrosive performance. The electrochemical parameters including E_{corr} and j_{corr} values are presented in Table 7.5. It is obvious that the corrosion current density, j_{corr}, of both samples decreased after the test as compared to those before. However, it is obvious that the barrier property of coated Al sample with double layer BTSE/18C-*SAMs* coating was better with respect to E_{corr} and j_{corr} values. Comparing the obtained results for single and double layer coatings, indeed, proved that the silane layer alone (top layer) was not as dense as the BTSE under layer (presence of more defects), but permeable to electrolytes. Therefore, it underwent dissolution in aggressive media leading to an accelerated corrosion rate. However, in both cases, the *SAMs*-modified samples overall exhibited better anti-corrosive performance compared to bare sample.

Table 7.5. Potentiodynamic results of coated AA2024 with single and double layer thin films after UV-aging test.

Specimen	$E_{corr.}$ (V *vs.* SCE)	$j_{corr.}$ (μAcm^{-2})	E_b-E_{corr} (V *vs.* SCE)
Standard AA2024	-0.69 (±0.04)	618 (±46)	-
BTSE/18C-*SAMs* coating	-0.61 (±0.02)	2.5 (±1.2)	0.11
18C-*SAM*s coating	-0.63 (±0.07)	12.18 (±3.4)	0.09

With respect to $E_{corr.}$ and $j_{corr.}$ values, it is evident that some under layer molecules are still present on an Al surface, even after the test. Finally, the electrochemical studies suggest that a double layer BTSE/18C-*SAMs* coating can provide good protection from localized corrosion on an Al substrate.

7.3 Conclusions

The corrosion resistance of bare and coated AA2024 substrates as well, was evaluated by the potentiodynamic polarization test in 3.5 wt.% NaCl solution. This test pointed out that the value of $E_{corr.}$ significantly increased positively for hydrophobic BTSE/18C-*SAM*s coatings and its $j_{corr.}$ decreased about 4 orders of magnitude as compared to that of bare standard and 2 orders of magnitude as compared to 18C-*SAMs*. This is obviously due to superior protective performance of a double layer hydrophobic coating formed on an Al substrate compared to 18C-*SAMs* coating. The double layer coating system also showed a decrease in $j_{corr.}$ in the cathodic and anodic regions, which suggested a packed and tight silane layer formed on Al and hence, protecting Al substrate more effectively against corrosion.

Meanwhile, the cyclic corrosion test exposure showed that the bare Al samples exhibited extensive corrosion after only 8 cycles of exposure with the appearance of numerous black dots (pits) in micrometer scale revealed under an optical microscope. Meanwhile, the size and density of the black dots increased as the number of cycles increased (localized corrosion continually

expanding). However, the earlier stage of corrosion in the case of single layer coating was observed after 18 cycles of exposure and only small traces of corrosion were observed in the case of double layer coated samples even after 81 cycles of exposure. In addition, for the bare standard and control AA2024, after 42 cycles of exposure, a substrate surface area of about ~50% was corroded and completely destroyed. For coated Al samples with 8C-*SAMs*, 18C+Cl *SAMs* and 18C-*SAMs* thin films, however, this percentage was ~19, ~28 and ~9%, respectively. The most promising result was obtained for the Al substrates coated with BTSE/18C-*SAMs*, where even after 120 cycles of exposure, a surface corroded area of about ~16.4% was observed. These observations confirmed again the results obtained by the PD test, implying an improvement in corrosion resistance of coated samples with BTSE/18C-*SAMs* coating.

The j_{corr}. of both single and double layer hydrophobic coatings on Al decreased about one order of magnitude each as compared to similar samples, before being kept for one week in a 3.5% NaCl solution. However, the anti-corrosive performance of double layer thin film is still reasonable (compact and dense film) while exposed to an aggressive condition containing Cl^- ions compared to single layer (presence of defects, holes and imperfections in the film). Electrochemical impedance spectroscopy, Nyquist and Bode plots, were used to study and understand the electron transfer (ET) and corrosion behaviors of silane-coated-aluminum alloys. The Bode plots of phase angle and impedance versus frequency showed characteristic differences between coated samples, single and double layer, and bare surfaces. A higher phase angle in the case of Al sample coated with BTSE/18C-*SAMs* suggested lower ionic permeation and therefore better insulating. The impedance data were fitted to a standard Randle's equivalent circuit model. The R_{ct} values of coated Al samples were much higher when compared to that of a bare Al sample. This change in R_{ct} values implies a better blocking behavior of BTSE/18C-*SAMs* towards electrochemical reactions. The surface coverage percentage calculated for BTSE/18C-*SAMs* was 99.37%, suggesting the formation of a well-packed and dense film centered on the Al sample (improved insulating property of double layer coating on Al substrate). The corresponding values for 8C, 18C-*SAMs* and 18C+Cl *SAMs* were found to be ~83%, 98.26% and 91%, respectively.

From R_{ct} and the corresponding Θ values of impedance studies, the blocking ability and barrier property of the prepared single and double layer coatings on Al samples is ordered in the following manner:

BTSE/18C-*SAMs* > 18C-*SAMs* > 18C+Cl *SAMs* > 8C-*SAMs*

Potentiodynamic polarization of coated Al samples with single 18C-*SAMs* and double layer BTSE/18C-*SAMs* thin films was performed immediately after the UV-aging test, showing that the barrier property of coated Al sample with double layer BTSE/18C-*SAMs* coating was better with respect to E_{corr} and j_{corr} values. This proved that the silane layer alone (top layer) was not as dense as the BTSE under layer (presence of more defects), but permeable to electrolytes. With respect to E_{corr} and j_{corr} values, it was evident that some under layer molecules were still present on an Al surface, even after the test. Finally, these results showed that the BTSE under layer on an AA2024 provide particularly enhanced corrosion resistance.

CHAPTER VIII

CONCLUSIONS AND RECOMMENDATIONS

8.1 Conclusions

Ice and snow accretion on outdoor structures is a severe challenge for cold climate countries. Passive approaches, e.g. ice-phobic coatings, are gaining in popularity. On the other hand and in connection with the subject of the present study, it should be remembered that corrosion is always a serious issue when it comes to using metallic substrates outdoors. This research work was focused for the first time on the preparation and systematic study of new environmentally friendly ice-phobic coatings with anti-corrosive properties, especially on flat AA2024 surfaces, by a unique, cheap and easy-to-use method with reasonable stability. A combination of both low surface energy and good anticorrosive performance on an AA2024 metallic substrate was expected to be achieved by preparing double layer coating systems, where each layer plays its own role. Such coatings would be a very interesting alternative to replacing the well-studied and toxic Cr-coatings. On the basis of the experimental results the following conclusions can be drawn**:**

1. A series of experiments was conducted to study hydrophobic and ice phobic properties of coated AA2024 substrates by three dissimilar alkyl-terminated *SAM*s thin films (8C, 18C and 18C+Cl *SAM*s). The hydrophobic, icephobic and durability of such prepared coatings in different conditions (accelerated aging, e.g. UV degradation, immersion in different pH solutions to simulate rainwater conditions and exposure to an environment) were tested, clearly demonstrating gradual loss of hydrophobicity over time. This was associated with a decrease in contact angle values of coated samples. Regardless of the type of coating, they did, however, decay either partially or completely after several hours of immersion in different media.

2. Ice-releasing performance of the same surfaces was also examined by accumulating glaze ice in a wind tunnel at subzero temperature to simulate the conditions of natural outdoor atmospheric icing. All coated surfaces demonstrated initially the shear stress of ice detachment values of ~ 1.68 to 2 times lower than as-received Al surfaces with a rougher finish and about ~ 1.22 to 1.5 times lower than those observed on mirror-polished substrates. It means that the ice accreted on these coated samples can be much more easily detached from them than from bare samples. The ice adhesion strength values gradually increased after as many as 5 to 9 successive icing/de-icing cycles. This can be ascribed to degradation of the coatings upon contact with water.

3. In addition, hydrophobic properties of coated surfaces were investigated after the icing/de-icing cycle to study their stability after ice releasing. They showed decreases in CA values. According to the results obtained, the most efficient alkylsilane coating as candidate for the top layer is octadecyltrimethoxysilane (18C) *SAM*s.

4. Loss of hydrophobicity and increase of ice adhesion were dramatically and completely different for coated samples with 8C and 18C+Cl *SAM*s compared to 18C-*SAM*s thin films. This was due to a significant *"steric effect"* on surface properties.

5. The corrosion resistance of bare and coated AA2024 substrates, evaluated by the potentiodynamic polarization test in 3.5 wt.% NaCl solution, demonstrated that the value of E_{corr}. positively increased for hydrophobic 18C-*SAM*s coatings. However, it shifts slightly to positive values for Al samples coated with 8C-*SAM*s and 18C+Cl *SAM*s. This is obviously due to the improved protective performance of a hydrophobic coating formed on an Al substrate.

6. The cyclic corrosion test exposure showed that the bare Al samples exhibited extensive corrosion after only 8 cycles of exposure, with the appearance of numerous black dots (pits) in micrometer scale. Meanwhile, the size and density of the black dots increased as the number of cycles increased (localized corrosion). However, the earlier stage of corrosion observable in the case of hydrophobic Al samples coated with 8C-*SAM*s was after 12 cycles of exposure and a trace of corrosion was observed in the case of 18C-*SAM*s-modified samples even after 18 cycles

of exposure. Pitting corrosion seemed to be a typical mode of surface degradation. A closer look at black dots under an optical microscope for C18+Cl *SAM*s (even before exposure) revealed that there was a micrometer scale locally corroded area due to the release of corrosive Cl^- ions.

7. As in the case of 8C-*SAM*s coated samples, it is believed that this thin film contains more defect areas compared to 18C-*SAM*s thin film. Meanwhile, in the case of bare standard and control AA2024, after 42 cycles of exposure, a substrate surface area of about ~50% was corroded and completely destroyed. For coated Al samples with 8C-*SAMs* and 18C+Cl *SAMs* coatings, however, this percentage was lower, e.g. ~19 and ~28%, respectively. The most promising result again was obtained for the Al substrates coated with 18C-*SAMs*, where after 42 cycles of exposure, a surface corroded area of about ~9% was observed. The corrosion depth measured on standard AA2024 after cyclic corrosion test was about 2µm to 4µm.

8. The corrosion current density of hydrophobic 18C-*SAM*s coating decreased about one order of magnitude as compared to similar samples before being kept for one week in a 3.5% NaCl solution.

9. Electrochemical impedance spectroscopy was used to study the electron transfer and corrosion behaviors of silane-coated Al substrates. The Bode plots of phase angle and impedance versus frequency show characteristic differences between *SAM*s-modified and bare surfaces. A higher phase angle in the case of samples coated with 18C-*SAMs* suggested lower ionic permeation and therefore better insulating properties. The impedance data were fitted to a standard Randle's equivalent circuit model. The R_{ct} values of coated samples with 18C-*SAMs* were much higher when compared to those of 8C-*SAMs*, 18C+Cl *SAMs* and bare Al samples (a better blocking behavior of 18C-*SAMs* towards electrochemical reactions). The higher the charge transfer resistance is, the higher the blocking behavior is. These values showed that the *SAM*s of 8C and 18C+Cl act as a leaky capacitor (very small semicircles throughout the frequency region).

10. The surface coverage calculated for 18C-*SAMs* is ~98%, implying the formation of a well-ordered and dense film on Al samples (improved insulating property). In the case of 8C and 18C+Cl *SAM*s, however, the surface coverage values were found to be ~83% and 91%,

respectively. This indicates that these films were formed on the Al with a larger number of holes and defects. From R_{ct} and corresponding Ɵ values of impedance studies, the blocking ability and barrier property of these films on Al samples is ordered as follows: 18C-*SAMs*>18C+Cl*SAMs*>8C-*SAMs*.

11. The potentiodynamic polarization test was carried out on coated samples immediately after the UV-aging test, with the condensation step showing a decrease in the current corrosion density of all hydrophobic *SAMs* coatings. These results confirm that the single layer *SAMs* coatings were not dense enough, but were permeable to electrolytes, undergoing dissolution in aggressive media and leading to an accelerated corrosion rate.

12. Finally, alkyl-terminated Al surface substrates were prepared by depositing layers of 18C-*SAMs* on BTSE-grafted AA2024 or bare mirror-polished AA2024 surfaces. The influence of experimental parameters on coating properties and performances was investigated in order to optimize the conditions.

13. The hydrophobicity, ice-phobicity and durability of single and double layer coatings in different conditions were investigated, demonstrating gradual loss of hydrophobicity over ~1100-h-long immersion in water, associated with decreasing water contact angles. Both surfaces initially demonstrated ice detachment shear stress values about ~2 times lower than as-received Al and ~1.5 times lower than those observed on mirror-polished Al surfaces, as references. The ice adhesion strength values gradually increased after as many as 9 successive icing/de-icing cycles. The observed increase in ice adhesion strength can be ascribed to degradation of coatings upon their contact with water. In addition, hydrophobic properties of coated surfaces were investigated after the icing/de-icing cycle, in order to study their stability after ice removal. Decreases in contact angle values were generally observed.

14. The SEM and optical microscopy observations demonstrated that the double layer coating system provided a dense coating on Al substrates, (compared to a single layer), which prevents the penetration of aggressive molecules through the coating to the metallic substrate underneath. This was shown by significantly less corrosion or corrosion products around second-

phase inter-metallic particles, and by dissolving and removing inter-metallic particles from the matrix for double layer coating systems compared to single layer 18C-*SAMs* coatings after stability tests. It was observed that while the earliest corrosion products came into sight on bare Al after only ~20 hrs of immersion in an aqueous media, corrosion products, local corrosion and pitting in either the matrix region or around second-phase particles occurred after ~310 and ~700 hrs exposure to aggressive media in the case of 18C-*SAM*s and BTSE/18C-*SAM*s coatings, respectively.

15. The XPS analysis showed that while the 18C-*SAMs* coating showed a significant peak of Si 2p before testing, however, its atomic concentration decreased remarkably after a stability test (hydrolyzing the -O-Si-R bond and destroying the silane layer on the Al surface). However, in the case of double layer BTSE/18C-*SAMs* coatings, the Si 2p peak does not change much after the test, implying the existence of a dense BTSE layer on the Al surface.

16. According to these observations, the double layer BTSE/18C-*SAM*s coating could be considered as a good alkylsilane candidate to protect an Al surface against corrosion.

17. The corrosion resistance of bare and coated AA2024 substrates as well, was evaluated by the potentiodynamic polarization test in 3.5 wt.% NaCl solution. This test pointed out that the value of E_{corr}. significantly increased positively for hydrophobic BTSE/18C-*SAM*s coatings and its j_{corr}. decreased about 4 orders of magnitude as compared to that of bare standard and 2 orders of magnitude as compared to 18C-*SAMs*. This is obviously due to superior protective performance of a double layer hydrophobic coating formed on an Al substrate compared to 18C-*SAMs* coating. The double layer coating system also showed a decrease in j_{corr}. in the cathodic and anodic regions, which suggested a packed and tight silane layer formed on Al and hence, protecting Al substrate more effectively against corrosion.

18. Meanwhile, the cyclic corrosion test exposure showed that the bare Al samples exhibited extensive corrosion after only 8 cycles of exposure with the appearance of numerous black dots (pits) in micrometer scale revealed under an optical microscope. However, the earlier stage of corrosion in the case of single layer coating was observed after 18 cycles of exposure and

only small traces of corrosion were observed in the case of double layer coated samples even after 81 cycles of exposure. In addition, for the bare standard and control AA2024, after 42 cycles of exposure, a substrate surface area of about ~50% was corroded and completely destroyed. For coated Al with 8C-*SAMs*, 18C+Cl *SAMs* and 18C-*SAMs* thin films, however, this percentage was ~19, ~28 and ~9%, respectively. The most promising result was obtained for the Al substrates coated with BTSE/18C-*SAMs*, where even after 120 cycles of exposure, a corroded surface portion of about ~16.4% was observed. These observations confirmed again the results obtained by the PD test, implying an improvement in corrosion resistance of coated samples with BTSE/18C-*SAMs* coating.

19. The j_{corr}. of both single and double layer hydrophobic coatings on Al decreased about one order of magnitude each as compared to similar samples, before being kept for one week in a 3.5% NaCl solution. However, the anti-corrosive performance of double layer thin film is still reasonable (compact and dense film) while exposed to an aggressive condition containing Cl^- ions compared to single layer (presence of defects, holes and imperfections in the film).

20. Electrochemical impedance spectroscopy, Nyquist and Bode plots, were used to study and understand the electron transfer (ET) and corrosion behaviors of silane-coated-aluminum alloys. A higher phase angle in the case of Al sample coated with BTSE/18C-*SAMs* suggested lower ionic permeation and therefore better insulating. The R_{ct} values of coated Al samples were much higher when compared to that of a bare Al sample. This change in R_{ct} values implies a better blocking behavior of BTSE/18C-*SAMs* towards electrochemical reactions.

21. The surface coverage percentage calculated for BTSE/18C-*SAMs* was 99.37%, suggesting the formation of a well-packed and dense film centered on the Al sample (improved insulating property of double layer coating on Al substrate). The corresponding values for 8C, 18C-*SAMs* and 18C+Cl *SAMs* were found to be ~83%, 98.26% and 91%, respectively. From R_{ct} and the corresponding Θ values of impedance studies, the blocking ability and barrier property of the prepared single and double layer coatings on Al is ordered in the following manner:

BTSE/18C-*SAMs* > 18C-*SAMs* > 18C+Cl *SAMs* > 8C-*SAMs*

25. Potentiodynamic polarization of coated Al with single 18C-*SAMs* and double layer BTSE/18C-*SAMs* thin films was performed immediately after the UV-aging test, showing that the barrier property of coated Al sample with double layer BTSE/18C-*SAMs* coating was better with respect to E_{corr} and j_{corr} values. This proved that the silane layer alone (top layer) was not as dense as the BTSE under layer (presence of more defects), but permeable to electrolytes. With respect to E_{corr} and j_{corr} values, it was evident that some under layer molecules were still present on an Al surface, even after the test.

26. Finally, these results showed that the BTSE under layer on an AA2024 provide particularly enhanced corrosion resistance. This would be an excellent approach to improve anti-corrosive performance of metallic surfaces for outdoor application, instead of the current use of toxic chromate-based coatings.

8.2 Recommendations for Future Works

In light of the results obtained, the following can be recommended for future study:

- Since the BTSE under layer was shown to be a promising coupling agent (cross-linking agent) for corrosion resistance, it would be worthwhile to prepare and characterize other coupling agents, such as tetraethyl orthosilicate, as under layers, in order to compare them with the results of the BTSE used in this thesis. As an under layer, an inorganic coating such as a permanganate-based coating can be applied as well.

- As the top layer, in this study, alkylsilanes with short and long alkyl chains were studied. However, it was not possible to expand our study to alkylsilane with different chains, e.g. aromatic chains, due to a time limitation. It is recommended to apply a number of harder materials as the top layer, in order to weather icing/de-icing cycles more effectively, e.g. DLC. Their performances, e.g. corrosion resistance, hydrophobicity and icephobicity as well as durability, must be considered in order to evaluate the stability of the coatings in real-world conditions. Some tests could be performed under natural conditions to evaluate their hydro/ice-

phobicity in the real world. This direction requires further research.

- The great advantage of this research work, compared to the existing research available to date, was introducing an anti-ice double layer coating system with enhanced anti-corrosive properties and sufficient stability against UV-irradiation or in various pH solutions. Therefore, it can be considered as an initial standard system for comparison purposes. However, further studies will be required in order to apply these coatings on large scale application. Meanwhile, it may be interesting to perform further experiments to study the influence of temperature and types of water on coating stability and performance. Also, the influence of temperature, the liquid water content and droplet size on ice-repellent property of coated surfaces, could be studied.

- It would be of interest if the prepared double layer coating in this study extends to various types of substrate, e.g. AA6061 (busbar and connectors) or AA5052 (boats) or AA5083 (autos), rough finished or anodized Al surfaces, in order to evaluate their icerepellent property, hydrophobicity, stability as well as corrosion resistance performance.

- Additional tests could investigate how the electric field, corona, intensity and polarity of the applied voltage, affect the ice accretion on coated substrates subjected to an electric field.

- It is proposed to run more experiments to study how different saline media and salt concentrations [0% (Fresh waters), 1% (Estuary waters) and 5% (Brine waters)] affect the anti-corrosive performance of double layer coating systems prepared in this study.

REFERENCES

[1] M. Farzaneh, "Atmospheric Icing of Power Networks", Dordrecht, Netherlands: Springer 2008.

[2] R. Menini and M. Farzaneh, "Elaboration of Al_2O_3/PTFE icephobic coatings for protecting Al surfaces", Surf. Coat. Technol. 2009.

[3] M. Farzaneh, Ed., "Atmospheric Icing of Power", Springer, Berlin. 2008.

[4] M. Farzaneh, "Ice Accretion on H.V. conductors and Insulators and Related Phenomena," Philos. Trans. R. Soc. London, Ser. A. 2000.

[5] M. R. Kasaai and M. Farzaneh, "Analytical Evaluation of Existing Mechanisms of Ice Adhesion on Power Network Equipment," American Society of Mechanical Engineers (ASME), Canada, 2004.

[6] M. R. Kasaai and M. Farzaneh, "A Critical Evaluation of the Existing Methods to Determine Ice Adhesion Strength," Proceedings of the 23rd International Conference on Offshore Mechanics and Arctic Engineering, Canada, 2004.

[7] http://www.ec.gc.ca/adsc-cmda/default.asp?lang=En&n=931AB89B-1.

[8] M. Farzaneh, J. Zhang and C. Volat, "Effect of Insulator Diameter on AC Flashover Voltage of an Ice-covered Insulator String", IEEE Trans. Diel. El. Ins., 2006.

[9] G. Poots, "Ice and snow accretion on structures", John Willy & Sons Inc., 1996.

[10] G. McClure, K. C. Johns, F. Knoll and G. Pichette, "Lessons from the ice storm of 1998", Proceeding of IWAIS 2002.

[11] M. Farzaneh, "IEEE standard 1783-guide for test methods and procedures to evaluate the electrical performance of insulators in freezing conditions". IEEE Press, New York, 2009.

[12] M. Farzaneh, W.A. Chisholm, "Insulators for icing and polluted environments", IEEE Press series on Power Engineering, IEEE/John Wiley, New York, 2009.

[13] V. K. Croutch and R. A. Hartley, "Adhesion of ice to coatings and the performance of ice release coatings", J. Coat. Technol. 1992.

[14] M. Farzaneh. "Systems for prediction and monitoring of ice shedding, anti-icing and de-icing for overhead lines", CIGRÉ WGB2.29, Technical Brochure, 2010.

[15] D. Sarkar and M. Farzaneh, "Superhydrophobic coatings with reduced ice adhesion", J. Adhes. Sci. Technol., 2009.

[16] D. Kuroiwa, "Icing and snow accretion", Monograph Series of Research, Institute of Applied Electricity, Japan, 1958.

[17] I. Imai and L. Chiro, "Studies on ice accretion", Researches on Snow and Ice, 1953.

[18] H. Oguchi, "Icing on Electric Wires", Researches on Snow and Ice, 1953.

[19] J. Druez, P. McComber and M. Farzaneh, "Atmospheric icing on a test power line". T. Can. Soc. Mech. Eng., C.S.M.E., 2000.

[20] M. Farzaneh and C. Volat and C. Leblond, "Anti-icing and De-icing Techniques for Overhead Lines," Atmospheric Icing of Power Networks, ed., Elsevier, 2008.

[21] R. Menini, Z. Ghalmi and M. Farzaneh, 2011, "Highly resistant icephobic coatings on aluminum alloys," Cold Reg. Sci. Technol. 2011.

[22] R. Jafari, R. Menini and M. Farzaneh, "Superhydrophobic and Icephobic Surfaces Prepared by RF-sputtered polytetrafluoroethylene coatings," Appl. Surf. Sci. 2010.

[23] S. Farhadi, M. Farzaneh and S. Kulinich, "Nanostructured Superhydrophobic Surfaces with Anti-Ice Properties," 2010.

[24] F. Arianpour, M. Farzaneh and S. A. Kulinich, “Nanopowder-Doped Silicone Rubber Coatings for Anti-Ice Applications,” Scanning Electron Microscopy, 2010.
[25] V. F. Petrenko and S. Qi, “Reduction of ice adhesion to stainless steel by ice electrolysis”, J. Appl. Phys., 1999.
[26] I. A. Ryzhkin and V. F. Petrenko, “Physical Mechanisms Responsible for Ice Adhesion”, J. Phys. Chem. B, 1997.
[27] M. Farzaneh, J. Zhang and M. Frechette, “Effects of High Altitude and Atmospheric Icing on the Performance of Outdoor Insulators”, IEEE PES Conference, Caracas, 2006.
[28] M. Javan-Mashmool, C. Volat, and M. Farzaneh, “A new method for measuring ice adhesion strength at an ice/substrate interface”, Hydrol. Process., 2006.
[29] Minimizing Effects from Highway Deicing”, EPA 832-F-99-016 (1999).
[30] Airplane Deicing Fluid Recovery Systems, EPA 832-F-99-043 (1999).
[31] http://water.epa.gov/scitech/wastetech/upload/2002_06_28_mtb_airplnde.pdf: “Storm Water Technology Fact Sheet Airplane De-icing Fluid Recovery Systems”, EPA 1999.
[32] B. Y. Yang and R. Montgomery, “De-icers derived from corn steep water”, Bioresour. Technol., 2003.
[33] A. Nakajima, K. Hashimoto and T. Watanabe, “Invited review recent studies on superhydrophobic films’’, Monatsh. Chem., 2001.
[34] B. Somlo and V. Gupta, “A hydrophobic self-assembled monolayer with improved adhesion to aluminium for de-icing application’’, Mech. Mater., 2001.
[35] C. Laforte, J. L. Laforte and J. C. Carrier, “How a solid coating can reduce the adhesion of ice on a structure”, Proceedings of the *IWAIS*, 2002.
[36] V. F. Petrenko and S. Peng, “Reduction of ice adhesion to metal by using self-assembling monolayers (SAMs)”, Can. J. Phys. 2003.
[37] J. L. Laforte, M. A. Allaire and J. Laflamme, “State-of-the-art on power line de-icing”, Atm. Res. 1998.
[38] S. Kulinich and M. Farzaneh, “How wetting hysteresis influences ice adhesion strength on superhydrophobic surfaces”, Langmuir 2009.
[39] F. Arianpour, M. Farzaneh and S. A. Kulinich, “Hydrophobic and ice-retarding proper-ties of doped silicone rubber coatings”, Appl. Surf. Sci. 2013.
[40] S. Farhadi, M. Farzaneh and S.A. Kulinich, “Anti-icing performance of superhydrophobic surfaces”, Appl. Surf. Sci., 2011.
[41] G. Momen and M. Farzaneh, “Facile approach in the development of icephobic hierarchicallytextured coatings as corrosion barrier”, Appl. Surf. Sci. 2014.
[42] L. Foroughi Mobarakech, R. Jafari and M. Farzaneh, “The ice repellency of plasma polymerized hexamethyldisiloxane coating”, Appl. Surf. Sci. 2013.
[43] P. Tourkine, M. Le Merrer and D. Quéré, “Delayed freezing on water repellent mate-rials”, Langmuir 2009.
[44] S. Jung, M. Dorrestijn, D. Raps, A. Das, C. M. Megaridis and D. Poulikakos, “Are Superhydrophobic Surfaces Best for Icephobicity?,” Langmuir , 2011.
[45] S. Kulinich, S. Farhadi, K. Nose and X. W. Du, “Superhydrophobic Surfaces: Are They Really Ice-Repellent?”, Langmuir 2011.
[46] A.B.D. Cassie and S. Baxter, “Large contact angles Of plant and animal surfaces”, Nature 1945.
[47] R. G. Buchheit, R. P. Grant and P. F. Hlava, “Local dissolution phenomena associated with S phase (AlCuMg) particles in AA2024-T32”, J. Electrochem. Soc., 1997.

[48] A. Frignani, F. Zucchi and G. Trabanelli,"Protective action towards aluminium corrosion by silanes with a long aliphatic chain Growth of corrosion-resistant manganese oxide coatings on an aluminium alloy", Corros. Sci., 2006.
[49] D. H. Wang, Y. H. Ni and Q. Huo, "Self-assembled monolayer and multilayer thin films on AA2024-T3 and their corrosion resistance study", Thin Solid Films, 2005.
[50] S. Meth and C. N. Sukenik, "Siloxane-anchored thin films on silicon dioxide-modified stainless steel", Thin Solid Films, 2003.
[51] A. Franquet, H. Terryn, C. Le Pen and J. Vereecken, "Characterization of protection behaviour of aluminium alloys by silane coatings", Eurocorr., 2001.
[52] A. Franquet, J. De Laet, T. Schram et al., "Determination of the thickness of thin silane films on Al surfaces by means of spectroscopic ellipsometry", Thin Solid Films, 2001.
[53] J. W. Bibber, "Chromate-free conversion coatings for aluminium", Plat. Surf. Finish., 2003.
[54] F. Delaunois, V. Poulain and J. P. Petitjean, "The trivalent chromium pretreatment applied to Aluminium 1050", Mater. Sci. Forum, 1997.
[55] S. A. Kulinich, M. Farzaneh and XW. Du, "Growth of corrosion-resistant manganese oxide coatings on an aluminium alloy", Inorg. Mater. 2007.
[56] T. Yip, "Estimating icing amounts caused by freezing precipitation in Canada", Atmospheric Research, 1995.
[57] Atmospheric Icing on Structures, COST-727 Action. ISO12494, ISO/TC 98/SC3, 2000.
[58] C. Ryerson, "Ice protection of offshore platforms", Cold Reg. Sci. Technol., 2011.
[59] J. Levine, "Statistical Explanation of Spontaneous Freezing of Water Droplets", NASA Center: Glenn Research Center, Report NACA-TN-2234, 1950.
[60] S. Fikke, G. Ronsten, A. Heimo, *et al.* "Atmospheric icing on structures measurements and data collection on icing: State of the Art", COST-727, 2006.
[61] N. Dalili, A. Edrisy and R. Carriveau, "A review of surface engineering issues critical to wind turbine performance", Renewable and Sustainable Energy Reviews 2009.
[62] R. Cattin, S. Kunz, A. Heimo, R. Oechslin and M. Russi, "An improved approach for the determination of in-cloud icing at wind turbine sites", Federal Office of Meteorology and Climatology Meteo-Swiss COST Action 727.
[63] D. Kuroiwa, "Icing and Snow Accretion on Electric Wires", CRREL Res. Report, 1965.
[64] C. Ryerson, "Assessment of Superstructure Ice Protection as Applied to Offshore Oil Operations Safety", ERDC/CRRELTR-08-14, 2008.
[65] http://amsglossary.allenpress.com/glossary/search7icNrime-icel: "Rime Ice in the Glossary of Meteorology".
[66] http://amsglossary.allenpress.com/glossary/search7icNglazel: "Glaze in the Glossary of Meteorology".
[67] F. Kiessling, P. Nefzger, J. F. Nolasco and U. Kaintzyk, "Overhead Power Lines: Planning, Design, Construction", 2003.
[68] C. Ryerson and K. Claffey, "Efficacy of ice detector hoarfrost observations", Proceedings of the Fourth Annual Washington Observatory Symposium 2000, 1995.
[69] C. Ryerson, "Assessment of Superstructure Ice Protection as Applied to Offshore Oil Operations Safety", U.S. Army Cold Regions Research and Engineering Lab., 2009.
[70] T. Haavasoja, V. Haavisto, M. J. Turunen, P. Nylander, and Y. Pilli-Sihvola, "A field trial of vehicle grip compared to RWS data", Vaisala News, 2002.
[71] M. Farzaneh, "Insulator Icing Test Methods and Procedures", IEEE Pow. Delivery, 2003.

[72] M. Farzaneh, “Selection of station insulators with respect to ice or snow-part I: Technical context and environmental exposure”, IEEE T. Power Delivery, 2005.
[73] M. Farzaneh, “Selection of station insulators with respect to ice or snow-part II: Methods of selection and options for mitigation”, IEEE T. Power Delivery, 2005.
[74] M. Farzaneh, “Selection of line insulators with respect to ice and snow-Part I: Context and stresses”, IEEE T. Power Delivery, 2007.
[75] M. Farzaneh, “Selection of line insulators with respect to ice and snow-Part II: Selection methods and mitigation options”, IEEE T. Power Delivery, 2007.
[76] https://www.rms.com/Publications/1998-Ice-Storm-Retrospective.pdf: “The 1998 Ice Storm: 10-Years Retrospective”.
[77] M. Landry, R. Beauchemin and A. Venne, “De-icing EHV overhead transmission lines using electromagnetic forces generated by moderate short-circuit currents”, IEEE Conference, 2000.
[78] C.Manuzio, “An Investigation of the Forces on Bundle Conductor Spacers under Fault Conditions,” IEEE Transactions on Power Apparatus and Systems, 1967.
[79] M. Landy and A. Freiberger, “Studies of Ice Adhesion, I: Adhesion of Ice to Plastics”, J. Colloid Interface Sci., 1967.
[80] V. F. Petrenko and R. W. Whitworth, “Physics of Ice”, Oxford university press, Oxford, 1999.
[81] U. Bovensiepen, “Ultrafast Electron Transfer, Localization and Solvation at Ice-Metal Interfaces: Correlation of Structure and Dynamics”, Prog. Surf. Sci., 2005.
[82] I. A. Ryzhkin and V. F. Petrenko, “Proton Ordering in Ice at an Ice-Metal Interface”, J. Exp. Theor. Phys., 2005.
[83] G. Salomon, “Adhesion and adhesives”, Amsterdam. Elsevier, 1965.
[84] L. A. Wilen, J. S. Wettlaufer, M. Elbaum and M. Schick, “Dispersion-force effects in interfacial premelting of ice”, Phys. Rev. B, 1995.
[85] W. I. Dunning, “Thermodynamics and imperfections of solid surfaces in adhesion”, London oxford university press, 1961.
[86] A. W. Adamson, “Physical chemistry of surfaces”, New York inter-science, second edition, 1967.
[87] J. M. Sayward, “Seeking low ice adhesion”, Special Report AD-A071-040, US Army Regions Research and Engineering Laboratory, Hanover, NH, 1979.
[88] G. R. Desiraju, “Hydrogen Bridges in Crystal Engineering: Interactions without Borders”, Ace. Chem. Res., 2002.
[89] D. Eley, “Thermodynamic adhesion, concluding remarks In Adhesion”, London Oxford University Press, 1961.
[90] J. Gregg, “The surface chemistry of solids”, 2nd ed., Reinhold Publishing Corp, New York, 1961.
[91] K. R. Wilson et al., “Surface Relaxation in Liquid Water and Methanol Studied by X-Ray Absorption Spectroscopy”, J. Chem. Phys., 2002.
[92] X. Wang, “The Calculation of the Surface Energy of High-Index Surfaces in Metals at Zero Temperature”, Surf. Sci., 2004.
[93] J. M. Zhang, F. Ma and K. W. Xu, “Calculation of the Surface Energy of FCC Metals with Modified Embedded-Atom Method”, Chinese Phys., 2004.
[94] K. F. Wojciechowski, “Surface Energy of Metals: Theory and Experiment”, Surf. Sci., 1999.
[95] P. Archer and V. Gupta, “Measurement and Control of Ice Adhesion to Aluminium 6061 Alloy”, J. Mech. Phys. Solids, 1998.

[96] J. Ahn, L. K. Mittal, and R. H. McQueen, "Hardness and Adhesion of Filmed Structures as Determined by the Scratch Techniques", Thick Films and Bulk Coatings, L. K. Mittal, Ed.: American Society for Testing and Materials, 1978.
[97] S. Krongelb, "Electromagnetic Tensile Adhesion Tests Methods", in Adhesion Measurements of Thin Films, Thick Films and Bulk Coatings, L. K. Mittal, Ed.: American Society for Testing and Materials, 1978.
[98] J. W. McBain and W. B. Lee, "Third and Final Report of the Adhesives Research Committee", J. Phys. Chem., 1933.
[99] D. L. Loughborough and E. G. Hass, "Reduction of the Adhesion of Ice to De-icer Surfaces", J. Aero. Sci., 1946.
[100] J. W. Beams, J. B. Breazeale and W. L. Bart, "Mechanical Strength of Thin Film of Metals", Phys. Rev., 1983.
[101] L. E. Raraty and D. Tabor, "The Adhesion and Strength properties of Ice", Proc. R. Soc. Lond. A, 1958.
[102] L. Cao, A. K. Jones, V. K. Sikka, J. Wu and D. Gao, "Anti-icing superhydrophobic coatings", Langmuir, 2009.
[103] D. Sarkar and M. Farzaneh, "Superhydrophobic coatings with reduced ice adhesion". Journal of Adhesion Science and Technology, 2009.
[104] M. He, J. Wang, H. Li, X. Jin, J. Wang, B. Liu and Y. Song, "Superhydrophobic film retards frost formation", Soft Matter, 2010.
[105] S. Mantovani and S. Valen, "Mechanical behavior at ice metal interfaces", Philos. Mag. A., 1978.
[106] A. W. Adamson, F.P. Shirley and K.T. Kunichika, "Contact angles on molecular solids", J. Colloid Interface Sci., 1970.
[107] W. A. Zisman, "Relation of the Equilibrium Contact Angle to Liquid and Solid Constitution", U. S. Naval Research Laboratory Washington, Chapter 1, 2009.
[108] J. R. Huntsberger, "The relationship between wetting and adhesion in advances Chemistry", J. Am. Chem. Soc, Washington DC, 1964.
[109] N. K. Adam, "Principles of Water-Repellency, in Water-Proofing and Water-Repellency", Elsevier Publishing Co., Amsterdam, 1963.
[110] J. Davies and E. K. Rideal, "Interfacial phenomena", Academic Press, New York, 1961.
[111] X. Zhang, F. Shi, J. Niu, Y. Jiang and Z. Wang, "Superhydrophobic surfaces: from structural control to functional Application", J. Mater. Chem, 2008.
[112] B. Bhushan, "Biomimetics: lessons from nature-an overview", Phil. Trans. R. Soc. 2009.
[113] B. Bhushan, Y. C. Jung and K. Koch, "Micro-, nano- and hierarchical structures for super-hydrophobicity, self-cleaning and low adhesion", Phil. Trans. R. Soc. A., 2009.
[114] P. Wagner, R. Furstner, W. Barthlott and C. Neinhuis, "Quantitative assessment to the structural basis of water repellency innatural and technical surfaces", J. Exp. Bot. 2003.
[115] K. Koch, B. Bhushan and W. Barthlott, "Diversity of structure, morphology, and wetting of plant surfaces (invited)", Soft. Matter. 2008.
[116] W. Barthlott and C. Neinhuis, "Purity of the sacred lotus, or escape from contamination in biological surfaces", Planta. 1997.
[117] Z. Burton and B. Bhushan,"Surface characterization and adhesion and friction properties of hydrophobic leaf surfaces", Ultramicroscopy. 2006.
[118] B. Bhushan and Y. C. Jung, "Micro and nanoscale characterization of hydrophobic and hydrophilic leaf surface", Nanotechnolgy. 2006.

[119] C. Neinhuis and W. Barthlott, "Characterization and distribution of water-repellent, self-cleaning plant surfaces", Ann. Bot. 1997.
[120] D. J. Crisp, "Waterproofing mechanisms in animals and plants", in: water-proofing and water- repellency, In J. L. Molliet, 1963.
[121] K. Koch, B. Bhushan and W. Barthlott, "Fabrication of artificial lotus leaves and significance of hierarchical structure for super-hydrophobicity and low adhesion", Soft. Matter. 2009.
[122] K. Koch, B. Bhushan and W. Barthlott, "Multifunctional surface structures of plants: an inspiration for biomimetics (invited)", Prog. Mater. Sci. 2009.
[123] X. F. Gao and L. Jiang, "Biophysics: water-repellent legs of water striders", Nature. 2004.
[124] H. J. Busscher, I. Stokroos, J. Golverdingen and J. M. Schakenraad, "Adhesion and spreading of human fibroblast on superhydrophobic FEP-Teflon," Cells Mater., 1991.
[125] W. H. Coghill and C. O. Anderson, "Certain interfacial tension equilibria important in flotation", U. S. Bur. Mines Tech. Pap., 1923.
[126] J. A. Jaber and J. B. Schlenoff, "Recent developments in the properties and applications of polyelectrolyte multilayers", Colloid Interface Sci., 2006.
[127] A. Cassie and S. Baxter, "Wettability of porous surfaces", Trans. Faraday Soc., 1944.
[128] L. Feng and L. Jiang, "Biomimic and Smart Nano-Interface Materials", Chemical Industry Press, Beijing, 2007.
[129] M. Ma and R. M. Hill, "Superhydrophobic surfaces", Colloid Interface Sci., 2006.
[130] F. Bartell and J. Shepard, "The Effect of Surface Roughness on Apparent CA and on Contact Angle Hysteresis, The system Paraffin–Water–Air", J. Phys. Chem., 1953.
[131] H. Ollivier, "Initial understanding of wetting-repellent Phenomena", Ann. Chim. Phys., 1907.
[132] J. J. Bikerman, in Surface Chemistry, 2nd edn, Academic Press, New York, 1958.
[133] N. K. Adam, "Physics and Chemistry of Surfaces", 3rd edn, Humphrey Milford, Oxford University Press, London, 1941.
[134] C. Neinhuis and W. Barthlott, "Characterization and Distribution of Water-repellent, Self-cleaning Plant Surfaces", Ann. Bot., 1997.
[135] R. Wenzel, "Resistance of Solid Surfaces to Wetting by Water", Ind. Eng. Chem. 1936.
[136] F. Reick, "Substrate coated with superhydrophobic layers", US Pat., US 3931428, 1976.
[137] Y. Chong and N. Watanabe, "Fabrication of self-cleaning superhydrophobic surface on aluminum alloys with excellent corrosion resistance", J. Fluorine Chem., 1991.
[138] T. S. Lin, C. F. Wu, C. T. Hsieh, "Enhancement of water-repellent performance on functional coating by using the Taguchi method", Surf. Coat. Technol, 2006.
[139] X.-M. Li, D. Reinhoudt and M. Crego-Calama, "What do we need for a superhydrophobic surface?", Chem. Soc. Rev., 2007.
[140] K. Ogawa, M. Soga, Y. Takada and I. Nakayama, "Development of a Transparent and Ultrahydrophobic Glass Plate", Jpn. J. Appl. Phys., 1993.
[141] M. W. Holdgate, "The Wetting of Insect Cuticles by Water", J. Exp. Biol., 1955.
[142] N. K. Adam, "Physics and Chemistry of Surfaces", Clarendon Press, Oxford, 1930.
[143] D. Quéré, "Non-sticking drops", Rep. Prog. Phys. 2005.
[144] D. Oner and T. J. McCarthy, "Ultrahydrophobic surfaces. Effects of topography length scales on wettability", Langmuir, 2000.
[145] T. Onda, S. Shibuichi, N. Satoh and K. Tsujii, "Super-Water-Repellent Fractal Surfaces", Langmuir, 1996.
[146] J. Y. Shiu, C. W. Kuo, P. Chen and C. Y. Mou, "Surface and Interfacial Aspects of Cell Adhesion", Chem. Mater., 2004.

[147] S. Wang, L. Feng and L. Jiang, "One-Step Solution-Immersion Process for the Fabrication of Stable Bionic Superhydrophobic Surfaces", Adv. Mater., 2006.
[148] T. Baldacchini, J. E. Carey, M. Zhou and E. Mazur, "Superhydrophobic surfaces prepared by microstructuring of silicon using a femtosecond laser", Langmuir, 2006.
[149] F. Shi, X. Chen, L. Wang, J. Niu and X. Zhang, "Accelerating the healing of superhydrophobicity through photothermogenesi", Chem. Mater., 2005.
[150] B. Qian and Z. Shen, "Fabrication of Superhydrophobic Surfaces by Dislocation-Selective Chemical Etching on Aluminum, Copper, and Zinc Substrates", Langmuir, 21(2005)9007.
[151] Y. Wu, H. Sugimura, Y. Inoue and O. Takai, „Fabrication of superhydrophobic and oleophobic Al surfaces by chemical etching and surface fluorination", Chem. Vap. Deposition,2002.
[152] A. Pozzato, S. D. Zilio, et al. "Facile approach to prepare a quasi-one-dimensional anisotropic wetting surface on copper substrate and its wetting properties", Microelectron. Eng., 2006.
[153] J. Sagiv, "Fabrication of stable superoleophobic surface based on copper oxide with micro-nanoscale hierarchical roughness", J. Am. Chem. Soc., 1980.
[154] H. Tavana, A. Amirfazli and A. W. Neumann, "Fabrication of superhydrophobic surfaces of n-hexatriacontane", Langmuir, 2006.
[155] L. Jiang, Y. Zhao and J. Zhai, "Design of micro-textures to induce superhydrophobic behavior on hydrophilic materials", Angew. Chem., Int. Ed., 2003.
[156] Y. Wu, M. Bekke, et al. "Wetting behaviour during evaporation and condensation of water microdroplets", Thin Solid Films, 2004.
[157] B. D. Washo, "Mimicking superhydrophobic surfaces: a review on recent progress in preparing superhydrophobic surfaces", Org. Coat. Appl. Polym. Sci. Proc., 1982.
[158] X. Zhang, F. Shi, X. Yu, *et al.* "Dynamic effects of bouncing water droplets on superhydrophobic surfaces", J. Am. Chem. Soc., 2004.
[159] S. Lau, J. Bico, K. B. K. Teo, et al., "Adsorption of polar molecules on alkali-fluorides", Nano Lett., 2003.
[160] A. Nakajima, A. Fujishima, K. Hashimoto and T. Watanabe, "Wetting study of patterned surfaces for superhydrophobicity", Adv. Mater., 1999.
[161] Zisman and W. A, "Relation of the equilibrium contact angle to liquid and solid constitution" , Am.Chem.Soc., 1964.
[162] M. Miwa, A. Nakajima, et al., "Effects of the surface roughness on sliding angles of water droplets on superhydrophobic surfaces", Langmuir 2000.
[163] K. Tadanaga, N. Katata and T. Minami, "Super-water-repellent Al_2O_3 coating films with high transparency", J. Am. Ceram. Soc., 1997.
[164] M. Qu, G. Zhao, Q. Wang, X. Cao and J. Zhang, "Chemical Deposition of Al2O3 Thin Films on Si Substrates", Nanotechnology 2008.
[165] S. T. Wang, Y. L. Sun and L. Jiang, "Recent studies on super-hydrophobic films", J. Photochem. Photobiol., 2007.
[166] L. Gao and T. McCarthy, "A Perfectly Hydrophobic Surface", J. Am. Chem. Soc., 2006.
[167] L. Feng, S. Li, Y. Li, et al. , "Preparation of Water-Repellent Glass by Sol–Gel Process Using Perfluoroalkylsilane and Tetraethoxysilane", Adv. Mater., 2002.
[168] A.C Zettlemoyer, "Hydrophobic surfaces", J. Colloid Interface Sci., 1968.
[169] D. Richard, C. Clanet and D. Quéré, "Contact time of a bouncing drop", Nature, 2002.
[170] D. Richard and D. Quéré, "Bouncing water drops", Europhys. Lett., 2000.

[171] S. Shibuichi, T. Onda, N. Satoh and K. Tsujii, "Super water-repellent surfaces resulting from fractal structure", J. Phys. Chem, 1996.
[172] S. Farhadi, M. Farzaneh and S. A. kulinich, "Preventing Corrosion and Ice Accretion on Aluminium Surfaces Applying Organic and Inorganic Thin Films", MSc thesis, 2010.
[173] S. Kulinich and M. Farzaneh, "Hydrophobic properties of surfaces coated with fluoroalkylsiloxane and alkylsiloxane monolayers", Surf. Sci., 2004.
[174] T. Nishino, M. Meguro, K. Nakamae, M. Matsushita, and Y. Ueda, "The Lowest Surface Free Energy Based on -CF3 Alignment", Langmuir, 1999.
[175] J. N. Israelachvili, "Intermolecular and Surface Forces", Academic Press: 1991.
[176] W. J. Dohaney and J. D. Innes, "ice-free pavement-evaluation of verglimit as a de- icing agent", Mater. Performance., 1981.
[177] E. F. Hare, E. G. Shafrin, and W. A. Zisman, "Properties of Films of Adsorbed Fluorinated Acids", J. Phys. Chem., 1954.
[178] S. Zanini, C. Riccardi, M. Orlandi, et al., "Wood coated with plasma-polymer for water repellence," Wood Science and Technology, 2008.
[179] M. Lúcia, N. Raymond, D. D. S. Eletrônicos, et al., "Hydrophobic Plasma Polymerized Hexamethyldisilazane Thin Films : Characterization and Uses," 2006.
[180] T. T. Isimjan, T. Wang and S. Rohani, "A novel method to prepare superhydrophobic, UV resistance and anti-corrosion steel surface," Chemical Engineering Journal, 2012.
[181] A. Irzh, L. Ghindes and A. Gedanken, "Rapid deposition of transparent super-hydrophobic layers on various surfaces using microwave plasma.," applied materials, 2011.
[182] C. Huang, C. H. Pan and C. H. Liu, "Deposition of hydrophobic nano-coatings with low-pressure radio frequency CH_2F_2/Ar plasma processing," Thin Solid Films, 2010.
[183] T. Ishizaki, Y. Masuda and M. Sakamoto, "Corrosion resistance and durability of superhydrophobic surface formed on Mg alloy coated with nanostructured cerium oxide film and fluoroalkylsilane molecules in corrosive NaCl aqueous solution", Langmuir, 2011.
[184] X. Xu, Z. Zhang, F. Guo, J. Yang, X. Zhu and Q. Xue, "Superamphiphobic self-assembled monolayer of thiol on the structured Zn surface," Colloids and Surfaces A: Physicochemical and Engineering Aspects, 2012.
[185] S. Zanini, E. Grimoldi and C. Riccardi, "Development of controlled releasing surfaces by plasma deposited multilayers," 2013.
[186] M. Touzin, P. Chevallier, F. Lewis, S. Turgeon, S. Holvoet, G. Laroche and D. Mantovani, "Study on the stability of plasma-polymerized fluorocarbon ultra-thin coatings on stainless steel in water," Surface and Coatings Technology, 2008.
[187] A. K. Gnanappa, C. O'Murchu, O. Slattery, F. Peters, B. Aszalós-Kiss and S. Tofail, "Effect of annealing on hydrophobic stability of plasma deposited fluoropolymer coatings," Polymer Degradation and Stability, 2008.
[188] J. L. Parker, P. M. Claesson, J. H. Wang and H. K. Yasuda, "Surface Forces between Plasma Polymer Films," Langmuir, 1994.
[189] Y. Yin, T. Liu, S. Chen and S. Cheng, "Structure stability and corrosion inhibition of super-hydrophobic film on aluminum in seawater," Applied Surface Science, 2008.
[190] S. Farhadi, M. Farzaneh and S. Simard "On Stability and Ice-Releasing Performance of Nanostructured Fluoro-Alkylsilane-Based Superhydrophobic AA2024 Surfaces", Inter. J. Theor. and Appl. Nanotechnology, 2012.

[191] S. Farhadi, M. Farzaneh and S. Simard, "Organosilane Thin Films Technology in Coating Applications: Comparative Investigation of UV Ageing Features, Anticorrosive Properties and Ice-releasing Performance", Functional Coatings and Surface Engineering, 2014.
[192] S. Farhadi, M. Farzaneh and S. Simard, "Corrosion resistance, ice-releasing performance and stability of nanostructured AA2024-T3 superhydrophobic surfaces", IWAIS Conference, Canada, 2013.
[193] S. Farhadi, M. Farzaneh and S. Simard, "A novel approach to fabricate anti-corrosive coatings with hydrophobic properties on an aluminium alloy surface", IWAIS Conference, Canada, 2013.
[194] S. Farhadi, M. Farzaneh and S. Simard, "Nanostructured ultra superhydrophobic Al surfaces: stability and icephobic properties", Inter. conference on nanotechnology: Fundamentals and Applications, Canada, 2012.
[195] http://www.corrosion-club.com/costs.htm.
[196] Y. Huang, D. Sarkar, D. Gallant and X. G. Chen, "Corrosion resistance properties of superhydrophobic copper surfaces fabricated by one-step electrochemical modification process," Applied surface science, 2013.
[197] S. Wernick and R. Pinner, "The Surface Treatment and Finishing of Aluminum and its Alloys", Robert Draper, Ltd.; Teddington 1, 1972.
[198] W. P. Callister, "Materials Science and Engineering An Introduction", John Wiley and Sons; Toronto, 1997.
[199] Galvele. J. R., "Methods for Fabricating Nanostructures", Corros. Sci. 1981.
[200] Wood, G. C., Sutton, W. H., Richardson, J. A., Riley, T. N . K., Malherbe, A. G., Proceeding Conference on Localized Corrosion, 1974.
[201] Thompson, G. E., Doherty, P. E., Wood, G. C , J. Electrochem. Soc, 1982.
[202] E. Ghali, "Corrosion Resistance of Aluminum and Magnesium Alloys Understanding, Performance, and Testing", 2010.
[203] S. L. Chawla, R. K. Gupta, "Materials Selection for Corrosion Control", A S M International; 1993.
[204] D. A. Jones, "Principles and Prevention of Corrosion", Prentice-Hall; New Jersey 1996.
[205] M. Pourbaix, "Atlas of Electrochemical Equilibria in Aqueous Solutions", NACE; 1974.
[206] X. Wu and K. Hebert, "Orthogonal self-assembled monolayers: alkanethiols on gold and alkane carboxylic acids on alumina", J. Electrochem. Soc, 1996.
[207] A. P. Bond, G. F. Boiling, H. A. Domian and H. Biloni, "Patterning self-assembled monolayers: applications in material science", J. Electrochem. Soc. 1966.
[208] L. Shier, "Microcontact printing of alkanethiols on silver and its application in microfabrication", Corrosion, Butterworth-Heinmann, 1994.
[209] T. Blestek and J. Webber, "Conversion Coatings", C. R. Draper, Portcullis Press; 1976.
[210] R. Stricklen, "Lithographically patterned self-assembled films", Mater.and Meth.. 1952.
[211] T. Foster, G. N. Blenkinsop, P. Blattler and M. Szandorowski, J. Coatings Technol., 1991.
[212] W. J. Van Ooij, "Silanes and Other Coupling Agents", J. Surf. Eng., 2000.
[213] P. Puomi and H. M. Fagerholm, "self-assembled monolayer electron beam resist on GaAs and SiO_2", J. Adhes. Sci. Technol., 2001.
[214] L. J. Matienzo, D. K. Shaffer, W. C. Moshier, and G. D. Davis, "Patterned self-assembled monolayers and meso-scale phenomena", J. Mat. Sci., 1986.
[215] A. Sabata, W. J. Van Ooij, and R. J. Koch, "The interphase in painted metals pretreated by functional silanes", J. Adhes. Sci. Technol.,1993.

[216] E. P. Plueddemann, “Silane Coupling Agents”, Plenum Publishing Corp.; New York (1991) 2nd ed.
[217] B. A.Waldman, “Evaluation of the influence of various nanofillers on the AC breakdown of epoxy-based nanocomposites”, Modern Paint and Coatings. 1996.
[218] P. G. Pape and E. P. Plueddemann, “Photoelectrochemical Study of Inorganic Inhibitor Films Formed on Mild Steel in Aerated Municipal Water”, Eng. Plast., 1993.
[219] F. J. Boerio, C. A. Gosselin, R. G. Dillingham and H. W. Liu, “Molecular Characterization of Composite Interfaces”, J. Adhes., 1981.
[220] Plato, Timaeus, R. D. Archer Hinds, ed., McMillan; London 1888.
[221] E. P. Plueddemann, H. A. Clark, L. E. Nelson and K. R. Hoffmann, “XPS studies of adhesion at organosilane/aluminum interfaces”, Mod. Plast, 1962.
[222] S. E. Hornstrom, J. Karlsson, W. J. Van Ooij, N. Tang and H. J. Klang, “XPS studies of adhesion at organosilane/aluminum interfaces”, Adhes. Sci, Technol., 1996.
[223] F. Lu and W. J. Van Ooii, “Recent advances in superhydrophobic nanomaterials and nanoscale systems”, Acta Metall. Sin., 1999.
[224] V. Subramanian and W. J. Van Ooij, Corrosion, “Effect of the Amine Functional Group on Corrosion Rate of Iron Coated with Films of Organofunctional Silanes”, 1998.
[225] M. Kono, X. Sun, R. Li, K. C. Wong, K. A. Mitchell and T. Foster, “Role of Transient Iron Sulfide Films in Microbial Corrosion of Steel”, Surf Rev. Lett., 2001.
[226] M. Ghiazza, A. M. Beccaria, G. Poggi and G. Castello, “Corrosion protection properties of organofunctional silanes”, Br. Corros. J., 1994.
[227] W. J. Van Ooij, C. Zhang, J. Zhang and W. Yuan, “Corrosion protection of metals by water-based silane mixtures of bis-[trimethoxysilylpropyl] amine and vinyltriacetoxysilane”, Electrochemical Society Proceedings, 1998.
[228] N. Tang, W. J. Van Ooij and G. Gorecki, “Corrosion protection with synergistic LBL/Ormosil nanostructured thin films”, Prog. Org. Coat., 1997.
[229] W. J. Van Ooij and T. Child, “Coating silicon compounds on steels to improve adhesion and provide corrosion resistance”, Chemtech, 1998.
[230] T. F. Child and W. J. Van Ooij, “Progess in superhydrophobic surface development”, Trans. IMF, 1999.
[231] J. A. Treverton and M. P. Thomas, “A Study of Preparation and Properties of BTESPT Silane-Rare Earth Composite Coating on Aluminum-Tube Surface”, Int. J . Adhes. Adhes.. 1989.
[232] J. Bishopp, E. K. Sim, G. E. Thompson and G. C. Wood, Adhesion 13, Ed. K. W. Allen, 1989.
[233] A. Sabata and B. A. Knueppel, “Preparation and Performance of Ceramic Coating on Cold-Rolled Steel Sheet”, J . Test. Eval., 1995.
[234] L. Kozma and I. Olefjord, “Characterization and Electrochemical Analysis of a Silanizing Film on Aluminum Alloy”, Mater. Sci. Technol. 1987.
[235] R. L. De Rosa, J. T. Grant, L. Katsen, M. Donley and G. P. Bierwagen, “Effect of Saline Treatment on Corrosion of Coating/Metal System”, Corrosion, 2000.
[236] G. W. Critchlow and D. M. Brewis, “Cerium Conversion Coating on Al and its Alloys”, Int. J . Adhes. Adhes. 1996.
[237] I. Pires, L. Quintino, C. M. Rangel, G. E. Thompson and X. Zhou, “Pretreatments of Al-2024 T3 Alloy for BTSE Silane Deposition”, Trans IMF. 2000.

[238] P. Hulser, U. A. Kruger and F. Beck, "Organic/inorganic multilayer coating system", Corr. Sci., 1996.
[239] C.A. Smith, "The corrosion story", Part 3, "Zinc, lead and Al", Anti-Corrosion, 1977.
[240] D. Wang, Y. Ni, Q. Huo and D. E. Tallman, "Electrodeposition of Organofunctional Silanes for Improved Corrosion Protection of Metals", Thin Solid Films 2005.
[241] W. Thompson and J. Pemberton, "Characterization of octadecylsilane and stearic-acid layers on Al_2O_3 surfaces by Raman-Spectroscopy", langmuir, 1995.
[242] A. E. Hughes, R.J. Taylor and B. R. Hinton, "Chromate Conversion Coatings on 2024 Al Alloy", Surf. Interface Anal., 1997.
[243] G. P. Sundararaian and W. J. Van Ooij, "Nanostructure of Materials and Corrosion Resistance", J. Surf Eng. 2000.
[244] X. T. Zhang, O. Stao and A. Fujishima, "Water Ultrarepellency Induced by Nanocolumnar ZnO Surface", Langmuir, 2004.
[245] A. Safaee, "Nanostructured metal surfaces and their passivation for superhydrophobic and antiicing applications", PhD thesis in Engineering, UQAC, 2008.
[246] S. Noormohammed, "Nanostructured Thin Films for Icephobic Applications", PhD thesis in Engineering, UQAC, 2009.
[247] M. J. Pellerite, T. D. Dunbar, L. D. Boardman et al., "Effects of Fluorination on Self-Assembled Monolayer Formation from Alkanephosphonic Acids on Aluminum: Kinetics and Structure", J. Phys. Chem., 2003.
[248] W. Limbut, P. Kanatharana, B. Mattiasson et al., "A comparative study of capacitive immunosensors based on self-assembled monolayers formed from thiourea, thioctic acid, and 3-mercaptopropionic acid" , J. Biosens. Bioelectron., 2006.
[249] V. Lakshminarayanan and U. K. Sur, "Hydrophobicity-induced drying transition in alkanethiol self-assembled monolayer–water interface", J. Phys., 2003.
[250] C. R. Kessel and S. Granick, "Formation and Characterization of a Highly Ordered and Well- Anchored Alkylsilane Monolayer on Mica by Self –Assembly", Langmuir.,1991.
[251] M. Jin, S. Li, J. Wanga, et al., "Photoinduced Surface Wettability Conversion of ZnO Thin Films", Appl. Surf. Sci., 2012.
[252] S. Ram, "Preparation of hybrid film with superhydrophobic surfaces", Infrared Phys. Technol. 2001.
[253] K. Nishikida, R. Hannah, "A modified Wenzel model for hydrophobic behavior of nanostructured surfaces", Appl. Spectrosc. 1992.
[254] M. D. Porter, T. B. Bright, D. L. Allara, C. E. D. Chidsey, "Hydrophobic surfaces", J. Am. Chem. Soc. 1987.
[255] ATLAS Weathering Testing Guidebook.
[256] R. Sun, A. Nakajima, A. Fujishima, T. Wanatabe, K. Hashimoto, "Fabrication of nonaging superhydrophobic surfaces by packing flowerlike hematite particles", J. Phys. Chem. B, 2001.
[257] V. Pophristic and L. Goodman, "Fabrication of super hydrophobic coating based on modified nano-sized calcium carbonate and ordinary polyacrylate", L. Nature, 2001.
[258] A. Franquet, C. Le Pen, H. Terryn, et al., "Effect of bath concentration and curing time on the structure of nonfunctional thin organosilane layers on aluminium", Electrochim. Acta, 2003.
[259] J. K. Nelson and C.W. Reed, "Dielectric Polymer Nanocomposites", Science, 2010.

[260] B. Hong, J. Han, S. Kim, Y. Cho, M. Park, T. Dolukh, C. Sung, "Super hydrophobic property of PVDF nanocomposite coatings", Thin Solid Films, 1999.
[261] A. Cabral, R. Duarte, M. Montemor and M. Ferreira, "Analytical characterisation and corrosion behaviour of bis-[triethoxysilylpropyl]tetrasulphide pre-treated AA2024-T3", Corrosion Science, 2005.
[262] D. Zhu and W. Ooij, "A comparative study on the corrosion resistance of AA2024-T3 substrates pre-treated with different silane solutions: Composition of the films formed", Electrochimica Acta., 2004.
[263] T. Ishizaki, S. Lee, and K. Teshima, "High Functionalization of Magnesium Alloy Surface by Superhydrophobic Treatment", 2010.
[264] G. Sposito, "The Environmental Chemistry of Aluminum, Second Edition", Second edition, LEWIS PUBLISHERS, 1995.
[265] L. F Mondolfo, "Aluminum alloys: Structure and properties", Butterworths, 1976.
[266] http://asm.matweb.com/search/SpecificMaterial.asp?bassnum=MA2024T3.
[267] http://asm.matweb.com/search/SpecificMaterial.asp?bassnum=MA6061t6.
[268] www.matweb.com/search/DataSheet.aspx?MatGUID=57483b4d782940faaf12964a1821fb61.
[269] L. Palomino, Z. Pászti, I. Aoki and H. Melo De, "Ultrahydrophobic surfaces. Effects of topography length scales on wettability ", Materials Research, 2007.
[270] L. Thomsen, B. Watts, D. Cotton, J. Quinton and P. Dastoor, "Drop evaporation on surfaces: contact angle mode", Surf. Interface Anal., 2005.
[271] X. Yao, Q. W. Chen, et al. "analysis of evaporating thick liquid films on solids", Adv. Funct. Mater., 2010.
[272] W. R. Thompson and J. E. Pemberton, "Combustion and Self-assembly of Nanoenergetic Materials", Langmuir, 1995.
[273] www.samwells.com/document/NITON/8-217_0108_XL3t900_Alloy_Spec sheet_low.pdf.
[274] M. Callies, Y. Chen, F. Marty, A. Pépin, and D. Quéré, "Microfabricated Textured Surfaces for Superhydrophobicity Investigations", Microelectron. Eng., 2005.
[275] "User Manual for drop shape analyzer", Kruss GmbH, DSA 100, Vl.9-03.
[276] L.E. Kollar and M. Farzaneh, "Wind-Tunnel Investigation of Icing of an Inclined Cylinder", Int. J. Heat Mass Trans., 2010.
[277] L. Kollar, M. Farzaneh and A. Karev, "Modeling Droplet-Size Distribution near a Nozzle Outlet in an Icing Wind Tunnel", Atomization Spray, 2006.
[278] A.R. Karev, M. Farzaneh and L.E. Kollar, "Measuring Temperature of the Ice Surface During its Formation by Using Infrared Instrumentation". Int. J. Heat Mass Trans., 2007.
[279] A. Karev and M. Farzaneh, "Evolution of Droplet Size Distribution in an Icing Wind Tunnel", IWAIS 2002, Czech Republic, 2002.
[280] C. Laforte, A. Beisswenger, "Icephobic Material Centrifuge Adhesion Test", Proceedings of the IWAIS 2005.
[281] QUV /Accelerated Weathering Tester catalogue.
[282] G. Grossman, "Correlation of laboratory to natural weathering", J. Coat. Tech., 1977.
[283] T. Leitner, H. Hoffmann, "Formation of Self-Assembled Octadecylsiloxane Monolayers on Mica and Silicon Surfaces Studied by Atomic Force Microscopy and Infrared Spectroscopy", Langmuir, 2002.
[284] F. Mansfeld, Y. Wang, et al., "Electrochemical Impedance: Analysis and Interpretation, ASTM STP 1188", ASTM, Philadelphia, USA, 1993.

[285] V. Ganesh, V. Lakshminarayanan, "Self-Assembled Monolayers of Alkanethiols on Gold Prepared in a Hexagonal Lyotropic Liquid Crystalline Phase of Triton X-100/Water System", Langmuir, 2006.
[286] S. Slawomir, P. Barbara, R. Bilewicz, "Structural Influences on the Fast Dynamics of Alkylsiloxane Monolayers on Si Surfaces Measured with 2D IR Spectroscopy", J. Phys. Chem. B, 2002.
[287] S. Survilienė, O. Nivinskienė, A. Cesuniene and A. Selskis, "Silane based pretreatments for automotive steels", J. Appl. Electrochem, 2006.
[288] F. Kandemirli and S. Sagdinc, "Organic–inorganic hybrid sol–gel coatings for metal corrosion protection", Corros. Sci., 2007.
[289] S. Survilienė, V. Jasulaitiene, A. Cesuniene and A. L. Oleksiak, "Characterization of Corrosion Interfaces by the Scanning Kelvin Probe Force Microscopy Technique", Solid State Ionics, 2008.
[290] I. Lukovits, I. Bako, A. Shaban and E. Kalman, "Effect of solution heat treatment on galvanic coupling between intermetallics and matrix in AA7075-T6", Electrochim. Acta, 1998.
[291] Y. Huicheng, C. Baizhen, W. Haiying and L. Bin, "The use of quantitative microscopy in studying the localised corrosion of aluminium 7075", Electrochimica Acta, 2008.
[292] C. Kun, B. Yuan, L. Ming, L. Sung and W. Haiying, "Microstructures of the commercial 6061 Al alloy", Applied Surface Science, 2010.
[293] T. Liu, L. Dong, T. Liu and Y. Yin, "Mechanism of localized corrosion of 7075 alloy plate", Electrochimica Acta, 2010.
[294] K.F. Khaled, "Guanidine derivative as a new corrosion inhibitor for copper in 3% NaCl solution", Mater. Chem. Phys., 2008.
[295] B. Yin, L. Fang, A. Tang, G. Bai, H. Bai, "Novel strategy in increasing stability and corrosion resistance for super-hydrophobic coating on aluminum alloy surfaces", Applied Surface Science, 2011.